Intercalibration of 40AR/39AR geochronology and in situ terrestrial cosmogenic 3HE

Schneider, B.S.H.

2012

document version
Publisher's PDF, also known as Version of record

VRIJE UNIVERSITEIT

INTERCALIBRATION OF ^{40}AR/^{39}AR GEOCHRONOLOGY AND IN SITU TERRESTRIAL COSMOGENIC ^{3}HE

Two scientific methods join at Earth's surface

ACADEMISCH PROEFSCHRIFT

ter verkrijging van de graad Doctor aan
de Vrije Universiteit Amsterdam,
op gezag van de rector magnificus
prof.dr. L.M. Bouter,
in het openbaar te verdedigen
ten overstaan van de promotiecommissie
van de faculteit der Aard- en Levenswetenschappen
op woensdag 11 april 2012 om 11.45 uur
in het auditorium van de universiteit,
De Boelelaan 1105

door

Björn Sven Harald Schneider

geboren te Huerth, Duitsland

promotor:	prof.dr. P.A.M. Andriessen
copromotor:	prof.dr. J.R. Wijbrans

Für Daniel…Du bist nicht vergessen…

The Reading Committee

Dr. L.A. Morgan
Dr. F.M. Stuart
Dr. T.J. Dunai
Dr. J.M. O'Connor
Dr. A. Hildenbrand

This research was carried out at the

Vrije Universiteit Amsterdam
Department of Isotope Geochemistry, Faculty of Earth and Life Sciences
De Boelelaan 1085
1081 HV Amsterdam, The Netherlands

and the

Scottish Universities Environmental Research Centre
NERC Cosmogenic Isotope Analysis Facility
Rankine Avenue
Scottish Enterprise Technology Park
East Kilbride G75 0QF, Scotland

The project was kindly supported by the

Marie Curie Initial Training Network CRONUS-EU
Project number 511927

and

The Netherlands Research Centre for Integrated Solid Earth Science (ISES).

Table of content

Chronos, the god of time (sculpture by Franz Ignaz Gunther, 1765 – 1770, Bayerisches Nationalmuseum, Munich, Germany)

Introduction, rationale and outline of this study

One of the great challenges in Earth Sciences is to date ever younger events and processes with satisfactory precision and accuracy. This is an important step towards linking past and present behaviour of processes and potentially predicting future trends. Geochronology needs therefore refinement of existing methods and development of new ones, including intercalibration of methods, and their validation and testing. Radiometric dating is based on the fact that by knowing the production or decay of an isotope an age of a sample containing the isotope can be made. One of the challenges is that it is not possible to use a single dating method as all depend on suitable material and only achieve satisfactory precision within certain time intervals. For example, the radiocarbon method depends on the decay of ^{14}C in a specimen over time. It is effectively extinct in 10 half-lives, one half- life being 5730 ka. Most other isotopic dating techniques are accumulation methods, i.e. they rely on the in-growth of the radiogenic daughter isotope by in situ decay of a radioactive isotope, or as will be shown, by continued exposure to a field of cosmic rays at the interface between the lithosphere and the atmosphere. All isotopic dating techniques relying on accumulation are also constrained by a detection limit of their daughter isotope at the younger end of their range of applicability.

This study was initiated to improve our knowledge about the production rate of *in situ* terrestrial cosmogenic nuclides (TCN) within the framework of the CRONUS-EU Research Training Network. The primary aims of this network were to improve our understanding of TCN systematics and to train the next generation of scientists in using the TCN technique. CRONUS-EU and the parallel United States based network initiative CRONUS-Earth also aimed to unify the various existing scaling methods and production rates. Prior to these initiatives the best characterized calibration sites for the Holocene where clustered on Hawaii and for the Pleistocene in the Western USA and on the Canary Islands (Dunai, 2001 and references therein). During the CRONUS-EU initiative new sites emerged as potential calibration sites, e.g. Mt Etna and Stromboli in Italy and the Canary and Cape Verde Islands in the Atlantic Ocean.

The research described in this thesis focused on calibration of the cosmogenic ^{3}He exposure dating method using $^{40}Ar/^{39}Ar$ dated lava flows from the Canary Islands. It re-evaluated the Canary Islands as a low latitude and low altitude calibration site for cosmogenic nuclides by changing the sampling area from Lanzarote to Fuerteventura. This site was part of a natural target network spanning a wide range of latitudes from Mt Kilimanjaro at 3 degrees South to Iceland at 64

degrees N. It provided also an opportunity for testing new approaches in measuring argon isotopes for $^{40}Ar/^{39}Ar$ geochronology and extracting helium from olivine phenocrysts. With the successful calibration of the cosmogenic ^{3}He exposure dating improvements in production rate knowledge would be possible and help to decrease the uncertainties involved in cosmogenic nuclide applications.

Technical improvements for dating younger rock samples

Both the K/Ar and $^{40}Ar/^{39}Ar$ techniques are well established dating methods. This study uses the $^{40}Ar/^{39}Ar$ method as an independent dating tool to validate the results of cosmogenic nuclide measurements.

Since its development from the K/Ar method, the $^{40}Ar/^{39}Ar$ technique (Merrihue & Turner, 1966) has been used to date rocks spanning a wide age range extending from the earliest geological records to palaeoanthropological timescales and even the history of Rome in the Classic Era (Renne et al., 1997; Ludwig & Renne, 2000). As ongoing analytical improvements in mass spectrometry reduce the uncertainties in isotope measurements the uncertainties in K/Ar standard ages and irradiation and decay constants have become increasingly important in $^{40}Ar/^{39}Ar$ geochronology (Kuiper et al., 2008; Renne et al., 2008; Min et al., 2000). These analytical improvements were necessary because dating increasingly younger samples was hindered by their low radiogenic ^{40}Ar content. This problem is particularly accute with ages less than a few 100 ka. An additional problem is that the $^{40}Ar/^{39}Ar$ plateau method assumes the trapped non-radiogenic argon component has an atmospheric isotopic composition. Thus, a very good measure of this composition is important for dating upper Pleistocene and younger samples (Renne et al., 2009 and this study).

The same instrumentation for analysis of noble gases is necessary for $^{40}Ar/^{39}Ar$ and cosmogenic ^{3}He geochronology with a furnace or laser commonly used to degas and melt the solid sample material. The released gas is normally cleaned using metal sinter or filament getters[1] within stainless steel pipework at pressures of 10^{-9} mbar. A magnetic sector mass spectrometer equipped with electron multipliers and Faraday cup detectors is used for isotope analysis. Multi-collector detection systems are now used routinely in $^{40}Ar/^{39}Ar$ geochronology because measuring multiple

[1] Gas cleanup by adsorption of reactive gasses at activated metal surfaces: e.g. a Zr-AL alloy or a Fe-V-Zr alloy has the property of binding N_2, O_2, H_2, CO and CO_2 by adsorption.

isotopes simultaneously improves precision due to faster data collection and results in increased sample throughput (Coble et al., 2011 and references therein; Mark et al., 2009; Mark et al, 2011). While the $^{40}Ar/^{39}Ar$ technique is used to date volcanic rock formation or metamorphic mineral crystallization, cosmogenic nuclides are generated by secondary cosmic ray particles in exposed rock surfaces and hence date how long the surface has been exposed. It is some 25 years since the first publications utilising TCNs for dating and reconstructing Earth surface processes (Kurz, 1986; Nishiizumi et al., 1986; Phillips et al., 1986). The pace of method development and application have in the meantime increased rapidly. Due to the variety of cosmogenic isotopes many minerals and rocks can be dated. In situ cosmogenic ^{3}He is widely used to date the eruption of young volcanic rocks. Recent work demonstrates that rocks of Holocene age are datable (Foeken et al., 2009). Factors such as erosion and accumulation of non-cosmogenic helium isotopes over time usually limit the application of cosmogenic ^{3}He to samples to an age of a few 100 ka, and in rare circumstances up to a few 10s Myr.

TCN production rates and scaling models

The production of TCNs (discussed in detail in Chapter IV) in a given rock surface is primarily a function of the host mineral and rock chemical composition, and location (principally latitude and elevation). Production rates for suites of minerals and rocks are determined on calibration sites. Production rates can not, however, be compared directly to each other and need to be scaled to a reference position with known geomagnetic and atmosphere attenuation characteristics (i.e. geographical latitude and elevation). In the past two decades several scaling models and production rates have been developed and improved. The pioneering work was done by Lal (Lal, 1991). Improved scaling methods have been developed (Stone, 2000; Dunai, 2000, 2001; Desilets and Zreda, 2003; Pigati and Lifton, 2004; Lifton et al., 2008). Lal (1991) proposed a scaling model using an axial dipole field as an approximation of the geomagnetic field. The first review of Lal's model was undertaken by Dunai (2000) who proposed using a more detailed parameterization of the geomagnetic field. This improved the model by incorporating temporal changes in the geomagnetic field in order to better assess behaviour of TCN production rates in the geological past (Dunai, 2001; Masarik et al., 2001; Desilets & Zreda, 2003; Pigati & Lifton, 2004; Lifton, 2008). Furthermore, the database of neutron flux measurements was increased and solar modulation was included as an important factor (Desilets & Zreda, 2003; Lifton et al., 2005). A lot

of production rate calibration work has concentrated on cosmogenic ^{3}He as production rates in suitable targets are high. Production is primarily from O and Si as well as Mg and Al and to a lesser extent from Fe. All elements are abundant in olivine and pyroxene phenocrysts in basalts. The host rock can be independently dated using ^{40}Ar/^{39}Ar or ^{14}C techniques.

For cosmogenic nuclide applications analytical uncertainties are less important compared to other factors. Intensity of the geomagnetic field since exposure, sample location and composition, local shielding and geomorphology need to be constrained in order determine the TCN production rate. No complete empirical dataset of cosmogenic nuclide measurements has been assembled yet that can test the existing models which are based on mathematical modelling and neutron flux monitor datasets. This study was part of a natural calibration network to obtain production rate data over a wide range of latitudes. These data would serve as a validation of existing scaling models or a base for new ones.

^{40}Ar/^{39}Ar technique and ^{3}He exposure dating

Both the ^{40}Ar/^{39}Ar and ^{3}He exposure dating techniques are applicable to basaltic rocks. However the application age ranges of the two methods are very different and overlap only partially. Depending on sample characteristics such as e.g. potassium content, the ^{40}Ar/^{39}Ar technique is applicable to samples from the upper Pleistocene or older. Cosmogenic ^{3}He on the other hand is commonly used on samples of upper Pleistocene age or younger although exposure ages of Miocene age have been obtained in old landscapes. In ideal cases partial overlap in the Pleistocene makes intercalibration between the two methods possible. The basis for the intercalibration work in this study is the fact that the ^{40}Ar/^{39}Ar technique is not easily applicable to young samples while the cosmogenic ^{3}He method still needs major refinement. It will be shown that the quest for perfectly preserved basalt flow tops is central to the success of any intercalibration effort.

Intercalibration in Fuerteventura

Many studies already have focused on cosmogenic ^{3}He calibration: Dunai & Wijbrans, 2000; Ackert et al., 2003; Blard et al., 2005; Amidon et al., 2009; Fenton et al., 2009. For samples as young as the Holocene intercalibration of cosmogenic 3He with the ^{14}C-method is very common, especially for volcanic rocks as they conserve old datable wood material (Kurz, 1986; Liccardi et al., 1999; Amidon et al., 2008).

This study aimed at calibration of cosmogenic ^{3}He at seal level and was also used as a basis for calibration of cosmogenic ^{36}Cl (Mai, 2009). Fuerteventura was chosen as study area because of the abundance of well preserved lava flows suitable for both exposure and absolute dating. Its location at low latitude and its low relief made it a potential candidate for a sea level calibration site within the CRONUS-EU natural target network. Furthermore its latest volcanic history below 400 ka was still lacking a complete geochronological record (Coello et al., 1992) apart from some constraints on Holocene volcanism (Coello et al., 1999). Similar calibration work has been carried out on the neighbouring island of Lanzarote (Dunai & Wijbrans, 2000), which could be directly compared with our results but uses an older set of scaling factors (Dunai, 2000). Our study also aimed to test a novel instrumental approach for ^{40}Ar/^{39}Ar geochronology.

Chapter I of this thesis introduces the geology of the Canary Islands and Fuerteventura. First it summarizes the different models for the formation of the island: mantle plume, extension, uplift and relaxation, or a propagating fracture linked to the Atlas and finally a unifying model addressing all aspects of the other models. The focus is on Fuerteventura and its geology and geochronology: seamount stage, pre- and post-erosional sub-aerial stages. Finally this chapter addresses the geomorphological and climatic aspects important for the part of this study utilizing terrestrial cosmogenic nuclides.

Chapter II starts by describing sampling strategy including satellite image analysis and sampling techniques for ^{40}Ar/^{39}Ar geochronology and cosmogenic ^{3}He exposure dating. The sample sites and sampled flows are described in detail, followed by petrographic descriptions of the samples.

Chapter III discusses the theory of K/Ar and ^{40}Ar/^{39}Ar geochronology and highlights the recent achievements and discussions concerning K/Ar and ^{40}Ar/^{39}Ar geochronology, especially developments and progress on decay constants, standard ages and data interpretation. The main focus of this chapter is the description of the novel quadrupole mass spectrometer line used for ^{40}Ar/^{39}Ar geochronology. It involves instrument testing and intercalibration with the in-house magnetic sector instrument as well as other instruments.

Chapter IV starts with a summary of the theory on terrestrial cosmogenic nuclides and the different models proposed for scaling. This is followed by a description of the commonly used methods when using cosmogenic ^{3}He for exposure dating and the approach taken at the noble gas laboratory of SUERC when analysing olivine.

Chapter V shows the results of the dating of Fuerteventura basalts. $^{40}Ar/^{39}Ar$ data show that volcanism on Fuerteventura continued from the upper Pleistocene to 52.0 ± 21.6 ka. $^{40}Ar/^{39}Ar$ data treatment is also discussed with a focus on latest developments in decay constants and standard ages as well as redetermination of the composition of atmospheric argon. Exposure ages using in situ terrestrial cosmogenic ^{3}He support the younger radiogenic ages from younger than 200 ka.

Chapter VI concludes with a summary of this study's results and their implications and a perspective on the work necessary in the future to improve current methods and timescale precisions.

Introductie, uitgangspunten en schets van dit onderzoek

Een van de grote uitdagingen in de aardwetenschappen is het dateren van steeds jongere gebeurtenissen met voldoende nauwkeurigheid. Dat is een belangrijke stap in het kunnen verbinden van het gedrag van processen in verleden en heden en in het kunnen voorspellen van mogelijke ontwikkelingen in de toekomst. In de geochronologie moeten wij daartoe bestaande methoden verfijnen en nieuwe ontwikkelen, met inbegrip van hun intercalibratie, validering en beproeving. Radiometrische datering berust er op dat productie of verval van een isotoop ons de ouderdom leert van het monster waarin het isotoop voorkomt. Een van de uitdagingen daarbij is dat het niet mogelijk is om één enkele dateringsmethode te gebruiken, daar alle methoden beperkt zijn tot daartoe geschikt materiaal en alleen voldoende precisie behalen over bepaalde, beperkte delen van de geologische tijd. De radiokoolstofmethode berust bijvoorbeeld op het verval van ^{14}C in een monster met de tijd. Het is praktisch uitgestorven na 10 halveringstijden, waarbij een halveringstijd 5730 ka lang is. De meeste andere isotopische dateringsmethoden berusten op accumulatie, d.w.z. op de aangroei van het radiogene dochterisotoop tijdens in-situ verval van een radioactieve moeder, of, zoals in het onderhavige werk, door voortdurende blootstelling aan kosmische straling op het grensvlak van lithosfeer en atmosfeer. Alle isotopische dateringsmethoden die op accumulatie berusten worden ook beperkt door de detectiegrens van hun dochterisotoop aan de lage, jonge kant van hun toepassingsbereik.

Dit onderzoek is opgezet om onze kennis te verbeteren van het aanmaaktempo van terrestrische cosmogene nucliden (TCN) binnen het raamwerk van het CRONUS-EU Research Training Network. De belangrijkste doelen van dit netwerk zijn de verbetering van ons begrip van TCN-systematieken en de opleiding van de volgende generatie van wetenschappers in het gebruik van de TCN-techniek. CRONUS-EU en zijn pendant in de Verenigde Staten, CRONUS-Earth, beogen ook om verschillende bestaande schaalmethoden en productietempi met elkaar te verenigen. Voorafgaand aan deze initiatieven dienden vindplaatsen op Hawaii als de beste locaties voor calibratie voor het Holoceen, en sites in de westelijke VS en op de Canarische eilanden voor het Pleistoceen (Dunai, 2001, en referenties daarin). Tijdens het CRONUS-EU-initiatief zagen nieuwe locaties voor calibratie het licht, bijv. de Etna en Stromboli in Italië en de Canarische en Kaapverdische eilanden in de Atlantische oceaan.

Het onderzoek dat in dit proefschift wordt beschreven richt zich op de calibratie van de cosmogene ^{3}He-methode voor datering van de exposieouderdom met behulp van met $^{40}Ar/^{39}Ar$ gedateerde

lavastromen van de Canarische eilanden. Het werk behelst een herwaardering van de Canarische eilanden als calibratie-site voor cosmogene nucliden op lage breedte en geringe hoogte, door Lanzarote als monsterlocatie te vervangen door Fuenteventura. Deze locatie maakte deel uit van een net van natuurlijke richtpunten met een groot bereik aan geografische breedten, van de Kilimanjaro op 3 graden zuiderbreedte tot IJsland op 64 graden noorderbreedte. Het bood ook de mogelijkheid om nieuwe methoden te beproeven om argonisotopen te meten en om helium uit olivijnfenokristen te extraheren. Een geslaagde calibratie van de cosmogene ^{3}He-exposiedatering zou onze kennis kunnen verbeteren van het productietempo, alsook de onzekerheden verminderen in toepassingen van cosmogene nucliden.

Technische verbeteringen bij datering van jongere gesteentemonsters

De K/Ar- en de ^{40}Ar/^{39}Ar-techniek zijn welbekende dateringsmethoden. In dit onderzoek wordt de ^{40}Ar/^{39}Ar-methode gebruikt als onafhankelijk middel om de resultaten te valideren van metingen van cosmogene nucliden. Sinds zijn ontwikkeling uit de K/Ar-methode is de ^{40}Ar/^{39}Ar-techniek gebruikt voor de datering van gesteenten over een breed ouderdomsspectrum, van de vroegste geologische geschiedenis tot paleoanthropologische tijdschalen en zelfs de geschiedenis van Rome in de Klassieke Periode (Renne et al., 1997; Ludwig & Renne, 2000). Terwijl voortdurende analytische verbeteringen van de massaspectrometrie de onzekerheden in isotopische metingen verkleinen, zijn onzekerheden in de ouderdom van K/Ar-standaarden en in de bestralings- en vervalconstanten steeds belangrijker geworden in de ^{40}Ar/^{39}Ar-geochronologie (Kuiper et al., 2008; Renne et al., 2008; Min et al., 2000). Deze analytische verbeteringen waren noodzakelijk omdat het dateren van steeds jongere monsters stuitte op hun lage gehalte aan radiogeen ^{40}Ar. Dit problem geldt in het bijzonder ouderdommen van minder dan enkele 100 ka. Een bijkomend problem is dat de ^{40}Ar/^{39}Ar-plateaumethode er van uit gaat dat de non-radiogene argoncomponent de atmosferische isotopensamenstelling heeft. Daarom is het belangrijk om bij het dateren van bovenpleistocene en jongere monsters te beschikken over een zeer goede meting van die samenstelling (Renne et al., 2009 en dit onderzoek).

^{40}Ar/^{39}Ar- en cosmogene ^{3}He-geochronologie maakt gebruik van hetzelfde instrumentarium voor analyse van edelgassen, gewoonlijk met gebruik van een oven of laser voor het ontgassen en smelten van vast monstermateriaal. Het vrijgemaakte gas wordt gewoonlijk schoongemaakt met

metaalsinter of 'getter'-filamenten[2] in roestvrijstalen pijpen onder een druk van 10^{-9} mbar. Voor isotopenanalyse gebruikt men een magneetsector-massaspectrometer uitgerust met detectoren voor ionenbundels die berusten op het principe van secundaire electronenversterking en op stroommeting van directe bundels met een Faradaydetector. Multicollector-detectiesystemen zijn nu gemeengoed in de $^{40}Ar/^{39}Ar$-geochronologie, omdat het simultaan meten van verschillende isotopen dankzij snellere meting leidt tot betere precisie en hogere productie (Coble et al., 2011 and referenties daarin; Mark et al., 2009; Mark et al, 2011).

Terwijl de $^{40}Ar/^{39}Ar$-techniek gebruikt wordt voor datering van vorming van vulkanische gesteenten of kristallisatie van metamorfe mineralen, ontstaan cosmogene nucliden door secundaire deeltjes uit kosmische straling in ontsloten gesteenteoppervlakken; de techniek dateert derhalve hoe lang het oppervlak ontsloten is geweest. De eerste publicaties over het gebruik van TCNs voor datering en reconstructie van processen aan het aardoppervlak verschenen zo'n 25 jaar geleden. Inmiddels is tempo van methodeontwikkeling en toepassing snel gestegen. Dankzij de veelheid aan cosmogene isotopen kunnen veel mineralen en gesteenten gedateerd worden. In-situ cosmogeen ^{3}He wordt alom gebruikt voor datering van eruptie van jonge vulkanische gesteenten. Recent werk toont aan dat gesteenten van Holocene ouderdom dateerbaar zijn (Foeken et al., 2009). Factoren als erosie en accumulatie met de tijd van niet-cosmogeen ^{3}He beperken gewoonlijk de toepassing van cosmogeen ^{3}He tot ouderdommen van enkele 100 ka en in zeldzame gevallen tot enkele tientallen Myr.

Productietempi van TCN en schalingsmodellen

De productie van TCNs (in detail behandeld in Hoofdstuk IV) in een gegeven gesteenteoppervlak is primair een functie van het gastmineraal en van de chemische samenstelling van het gesteente, en van de locatie (vnl. breedte en hoogte). Productietempi voor mineraal- en gesteentegezelschappen worden bepaald op calibratiesites. Men kan productietempi echter niet direct met elkaar vergelijken; zij moeten geschaald worden naar een referentiepositie met bekende geomagnetische en atmosferische verzwakkings-eigenschappen (d.w.z. geografische breedte en hoogte). In de afgelopen twee decennia zijn er verschillende schalingsmodellen en productietempi

[2] Gasreiniging door middel van adsorptie van reactieve gassen aan geactiveerd metaaloppervlak: bijvoorbeeld een Zr-Al legering, of een Fe-V-Zr legering heeft de eigenschap N_2, O_2, H_2, CO en CO_2 te binden door adsorptie.

vastgesteld en verbeterd. Het pionierswerk is verricht door Lal (Lal, 1991). Er zijn verbeterde schalingsmodellen ontwikkeld (Stone, 2000; Dunai, 2000, 2001; Desilets and Zreda, 2003; Pigati and Lifton, 2004; Lifton et al., 2008). Lal (1991) stelde een schalingsmodel op m.b.v. een axiaal dipoolveld als benadering van het aardmagnetische veld. De eerste kritische beschouwing van het model van Lal was die van Dunai (2000), die een meer gedetailleerde parametrisatie van het aardmagnetisch veld voorstelde. Dit verbeterde het model door tijdafhankelijke veranderingen van het magnetisch veld te incorporeren en daarmee het gedrag van productietempi van TCN in het verleden beter te kunnen vaststellen. Bovendien werd de database van metingen van de neutronenflux uitgebreid en werd modulering door de zon als belangrijke factor meegenomen (Desilets & Zreda, 2003; Lifton et al., 2005). Veel werk m.b.t. de calibratie van het productietempo heeft zich geconcentreerd op cosmogeen ^{3}He, vanwege zijn hoge productietempo in geschikte materialen. Het wordt primair geproduceerd uit O en Si, alsook uit Mg en Al en in mindere mate uit Fe. Het moedergesteente kan onafhankelijk gedateerd worden met de ^{40}Ar/^{39}Ar- of ^{14}C-technieken.

Bij toepassing van cosmogene nucliden zijn analytische onzekerheden van minder belang dan andere factoren. Men dient goed inzicht te hebben in de intensiteit van het aardmagnetisch veld gedurende de exposie, de locatie en samenstelling van het monster en de locale afscherming en geomorfologie. Er is nog geen volledig empirisch gegevensbestand van metingen van cosmogene nucliden samengesteld dat als test kan dienen voor bestaande modellen gebaseerd op mathematische modellering en op gegevens van neutronenfluxmonitoren. Dit onderzoek maakte deel uit van een netwerk voor natuurlijke calibratie van productietempi over een groot bereik van geografische breedten. De gegevens dienen ter validering van bestaande schalingsmodellen of als basis voor nieuwe.

De ^{40}Ar/^{39}Ar-techniek en de ^{3}He exposiedatering

Zowel de ^{40}Ar/^{39}Ar- als de ^{3}He-exposiedateringstechniek zijn toepasbaar op bazaltische gesteenten. Het leeftijdsbereik waarop de twee methoden van toepassing zijn verschilt echter aanzienlijk en overlapt slechts ten dele. Afhankelijk van monstereigenschappen als bijv. kaliumgehalte is de ^{40}Ar/^{39}Ar- techniek toepasbaar op monsters uit het Boven Pleistoceen of ouder. Cosmogeen ^{3}He wordt daarentegen gewoonlijk gebruikt voor monsters van bovenpleistocene op jongere ouderdom, alhoewel er miocene exposieouderdommen verkregen zijn in oude

landschappen. In ideale gevallen maakt gedeeltelijke overlap in het Pleistoceen intercalibratie mogelijk van de twee methoden. De basis van het intercalibratiewerk in dit onderzoek is het feit dat de $^{40}Ar/^{39}Ar$-techniek niet makkelijk toepasbaar is op jonge gesteenten, terwijl de cosmogene ^{3}He-methode nog steeds belangrijke verfijning behoeft. Er wordt aangetoond dat het vinden van perfect bewaarde bovenoppervlakken van bazaltstromen de sleutel is tot het succes van elke poging tot intercalibratie.

Intercalibratie in Fuenteventura

Er zijn al veel studies gericht naar de calibratie van cosmogeen ^{3}He: Dunai & Wijbrans, 2000; Ackert et al., 2003; Blard et al., 2005; Amidon et al., 2009; Fenton et al., 2009. Voor jonge, holocene monsters is intercalibratie van cosmogeen ^{3}He met de ^{14}C-methode heel gebruikelijk, vooral voor vulkanische gesteenten die oud, dateerbaar hout bevatten (Kurz, 1986; Liccardi et al., 1999; Amidon et al., 2008).

Dit onderzoek richtte zich op calibratie van cosmogeen ^{3}He op zeeniveau en fungeerde ook als basis voor calibratie van cosmogeen ^{36}Cl (Mai, 2009). Fuenteventura is als onderzoeksgebied gekozen vanwege het voorkomen van veel goed bewaarde lavastromen, geschikt voor bepaling van de exposieouderdom zowel als voor absolute datering. Zijn ligging op lage breedte en zijn lage reliëf maken het een potentiële kandidaat voor een calibratiesite op zeeniveau binnen het CRONUS-EU netwerk voor natuurlijke richtpunten. Bovendien ontbrak het er nog aan een volledige geochronologische documentatie van de laatste 400 ka van zijn vulkanische geschiedenis (Coello et al., 1992), afgezien van enige gegevens over holoceen vulkanisme (Coello et al., 1999). Soortgelijk calibratiewerk is verricht op het naburige eiland Lanzarote (Dunai & Wijbrans, 2000), wat direct vergeleken kon worden met onze resultaten maar dat een ouder stel schalingsfactoren gebruikt (Dunai, 2000). Ons onderzoek had ook ten doel om een nieuwe instrumentele aanpak van de $^{40}Ar/^{39}Ar$-geochronologie te beproeven.

Hoofdstuk I van dit proefschrift geeft een inleiding in de geologie van de Canarische eilanden en Fuenteventura. Allereerst vat het de verschillende modellen samen van vorming van het eiland: mantelpluim, rek, opheffing en relaxatie, of een voortschrijdende breuk gelieerd aan de Atlas, en tenslotte een alomvattend model dat toeziet op alle aspecten van de andere modellen. De aandacht gaat vooral uit naar Fuenteventura en zijn geologie en geochronologie: het seamount-stadium en

de pre- en post-erosieve subaerische stadia. Tenslotte besteedt dit hoofdstuk aandacht aan de geomorfologische en klimatologische aspecten die van belang zijn voor het deel van dit onderzoek dat terrestrische cosmogene nucliden betreft.

Hoofdstuk II begint met een beschrijving van de bemonsteringsstrategie, waarbij inbegrepen de analyse van satellietbeelden, en van de bemonsteringstechnieken voor $^{40}Ar/^{39}Ar$-geochronologie en cosmogene ^{3}He-exposiedatering. De monsterlocaties en bemonsterde lavastromen worden in detail beschreven, gevolgd door petrografische beschrijvingen van de monsters.

Hoofdstuk III bespreekt de theorie van K/Ar- en $^{40}Ar/^{39}Ar$-geochronologie en richt zich speciaal op recente vorderingen en discussies betreffende de K/Ar- en $^{40}Ar/^{39}Ar$-geochronologie. Het belangrijkste punt van aandacht van dit hoofdstuk is de beschrijving van de nieuwe quadrupool-massaspectrometrische lijn voor $^{40}Ar/^{39}Ar$-geochronologie. Het omvat het testen van de apparatuur en de intercalibratie met het al aanwezige magneetsectorinstrument en met andere instrumenten.

Hoofdstuk IV begint met een samenvatting van de theorie van terrestrische cosmogene nucliden en de verschillende schalingsmodellen. Dit wordt gevolgd door een beschrijving van gebruikelijke methoden voor cosmogene ^{3}He-exposiedatering en van de aanpak van het edelgaslaboratorium van het SUERC voor de analyse van olivijn.

Hoofdstuk V laat de resultaten zien van de datering van bazalten van Fuenteventura. $^{40}Ar/^{39}Ar$-gegevens tonen aan dat er vulkanisme op Fuenteventura optrad van het Boven Pleistoceen tot 52.0 ± 21.6 ka. Ook wordt de bewerking van $^{40}Ar/^{39}Ar$-gegevens besproken met speciale aandacht voor de laatste ontwikkelingen op het gebied van de vervalconstanten en de ouderdommen van standaarden, alsook van herbepaling van de samenstelling van atmosferisch argon. Exposieouderdommen gebaseerd op in-situ terrestrisch cosmogeen ^{3}He bevestigen de radiometrische dateringen jonger dan 200 ka.

Hoofdstuk VI geeft tenslotte een samenvatting van de resultaten van dit onderzoek en hun implicaties, alsook een vooruitblik op toekomstig werk ter verbetering van huidige methoden en van de nauwkeurigheid van de tijdschaal.


View of Montana de Arena from the East

I. Geological Setting

1. Geology of the Canary Islands

Fig. 1: Location of the Canary Islands off the coast of Africa and location of Fuerteventura on the eastern side of the Canary archipelago (images taken from Google Earth).

The Canary Islands are located in the eastern central Atlantic Ocean, on the edge of the continental shelf off the coast of northwest Africa (Figure 1). They form an archipelago of seven main, inhabited volcanic islands ordered in an E-W oriented chain nearly 500 km long. The eastern sides of the easternmost islands of Fuerteventura and Lanzarote are located on the continental shelf apron, their western sides and all the islands to the west are all on oceanic crust (Coello et al., 1992). Vertical tectonic movements during the Pleistocene and Holocene have been small in the archipelago as indicated by fossil shorelines (Zazo et al., 2002; Rothe, 1996). Volcanism in the Canary Islands started as early as 68 Myrs ago (Geldmacher et al., 2005). It is a predominantly alkaline suite and forms stratovolcanoes (Roque Nublo on Gran Canaria and Teide on Tenerife).

The different theories are now summarised that have been proposed to explain the formation of the islands in a chain but nevertheless lacking of a clear age-progression. More thorough summaries

Setting of the Study area

and description of the geological setting are found in Anguita & Hernan (2000) and Geldmacher et al. (2005).

Inspired by the work of Morgan (1971) a mantle plume model has been proposed based largely on isotopic age and trace element geochemical data indicating an enriched deep mantle material source (Holik et al., 1991; Hoernle & Schmincke, 1993; Carracedo et al., 1998).

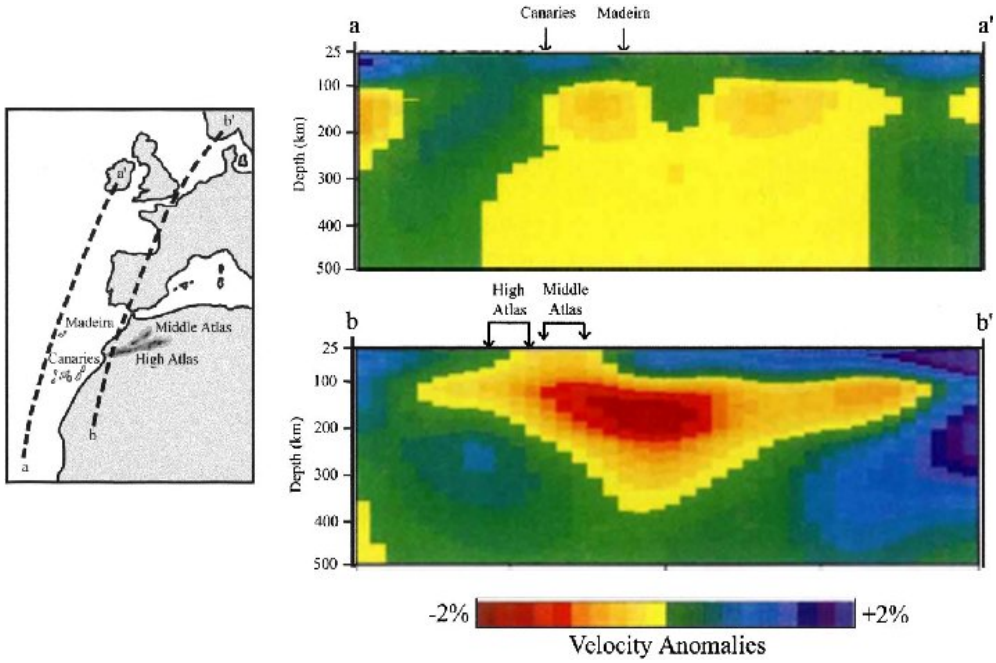

Fig. 2: Map and seismic tomography profiles showing velocity anomalies (Fig. 4 in Anguita & Hernan (2000), after Hoernle et al., (1995)). The dashed lines in the map show the locations of the seismic profiles.

Hoernle et al. (1995) show seismic and tomographic evidence for large scale slow upwelling of a sheet like body in the upper mantle under western and central Europe and the eastern Atlantic

Ocean. The existence of a mantle plume is further reinforced by Geldmacher et al. (2005) finding that shield-stage volcanism is age progressive. Alternative tectonic models are supported by the presence of an extensional ridge by dilation in basement rocks (Fuster, 1975), uplifting and relaxation inferred from uplift (Arana & Ortiz, 1986) and a propagating fracture linked to the Atlas mountain system that would have caused volcanism in the archipelago during periods of relaxation that would have been suppressed during compressive phases (Anguita & Hernan, 1975).A unifying theory (Anguita & Hernan, 2000) tries combine the main aspects of the aforementioned models into one model. Based on tomographic and isotopic data in Hoernle et al. (1995, Fig. 2) this model proposes a shared mantle source beneath the Canary Islands and the Atlas Mountains in the form of a fossil plume, which can be tapped during extensional tectonic activity in the area.

Lead isotopic data summarized by Geldmacher et al. (2005, and references therein; Fig. 3) show that the composition of Canary and Madeira basalts is similar to that of African subcontinental lithosphere and N-MORB. This shallow non-hotspot MORB composition makes it very difficult to define a typical mantle plume enriched composition for the Canary and nearby Madeira Islands and seamounts. The existence of seamounts which continue the progressive formation ages of the basal parts of the archipelago towards the North east supports the plume hotspot model (Geldmacher et al., 2005).

Setting of the Study area

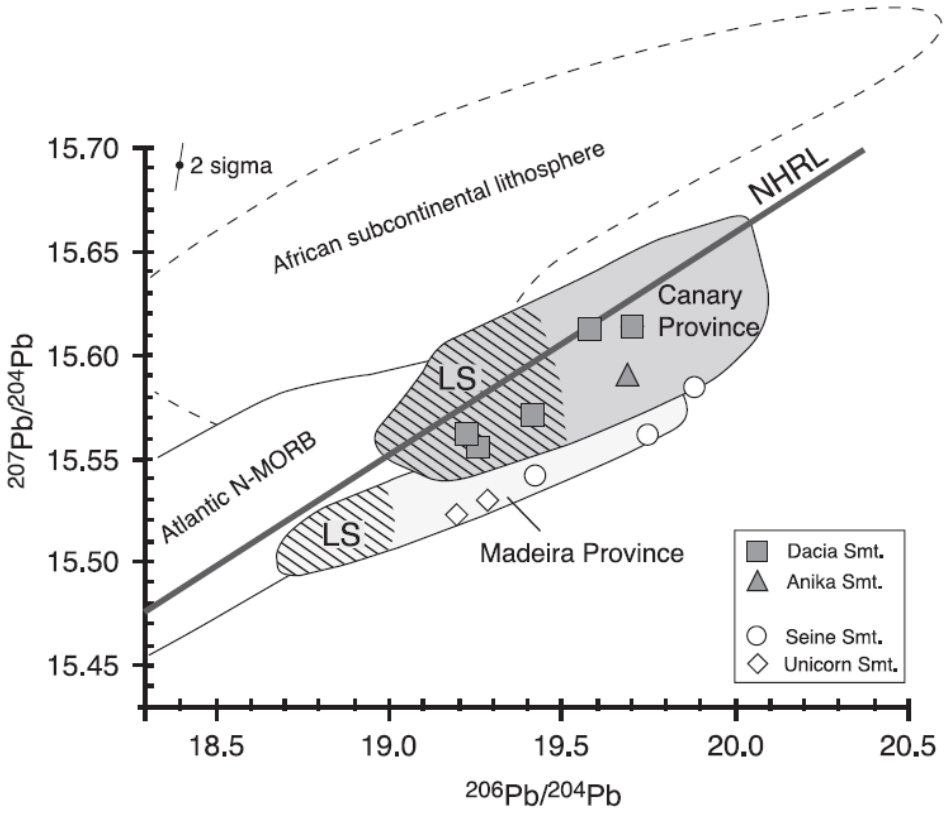

Fig. 3: Lead isotopic composition of Unicorn and Seine Seamounts overlap the field for the Canary and Madeira Province (Geldmacher et al., 2005 and references therein). NHRL is the Northern Hemisphere Reference Line. LS marks the isotopic composition of late stage volcanism in the Canary and Madeira provinces.

2. Fuerteventura

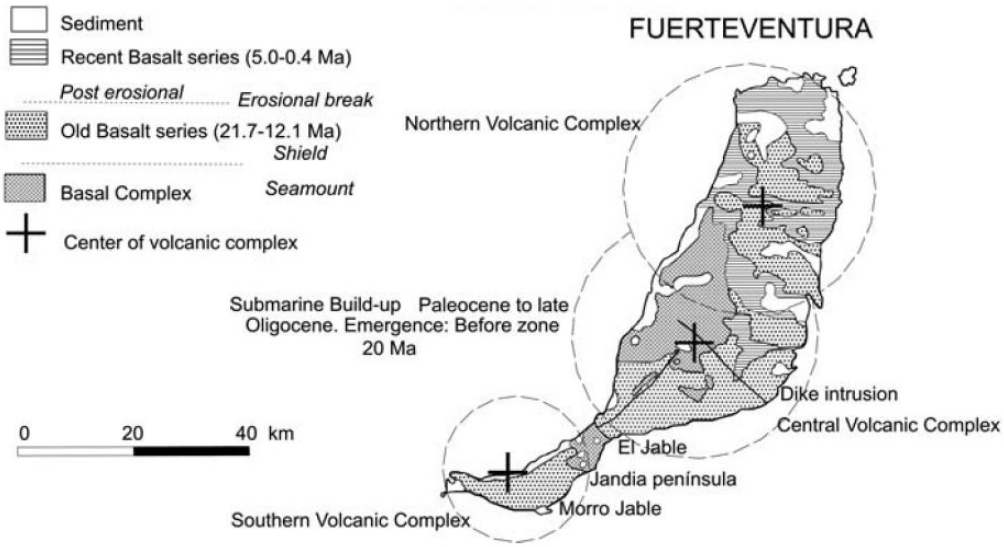

Fig. 4: Geological overview of Fuerteventura. After Acosta et al. (2003), compiled from Coello et al. (1992), Carracedo and Rodríguez-Badiola (1993), Ancochea et al. (1996) and Stillman (1999).

Fuerteventura is divided into a basal complex, which represents the mainly oceanic basement of the island edifice and the Northern, Central and Southern Volcanic Complexes (Figure 4, furthermore NVC, CVC and SVC respectively) divided into Series I to IV. The basal complex is exposed only below the CVC and NVC. It consists of turbidites covered by interbedded sediments, submarine volcanic and plutonic rocks (Coello et al., 1992, Stillman, 1999). A dense dyke network intrudes into this series. Series I is a series of bedded volcanic and pyroclastic deposits that lie unconformably on the basal complex. It is largely of Miocene age and is characterized mainly by basalts and a few, mostly alkaline, trachybasalts. Towards the end of the Miocene alkali volcanism

increased and trachybasalts and trachyandesites become more abundant (Ancochea et al., 1996). The post-Miocene Series II to IV consist exclusively of basaltic rocks and are separated from the underlying Series I by an unconformity (Coello et al., 1992).

3. Geochronological framework

3.1 Canary Islands

The geochronology of the Canary Islands is summarised in Geldmacher et al., (2005), Carracedo (1994) and references therein. A notable aspect of volcanism in the Canary Islands is the time gap between the shield stage and the late volcanic activity. On Fuerteventra this time gap is approximately 7 Myr (Coello et al., 1992). A similar hiatus of 4 - 7 Myr occurs on Vlinder Seamount (West Pacific) between the formation of the older pedestal and the younger main shield (Koppers, 1998). On the Hawaiian and Marquesas islands the largest recorded time gap are 1 - 2.3 Myr and 2.3 - 3.5 Myr, respectively (Woodhead, 1992). Hotspot volcanism is believed to occur with shorter gaps for up to roughly 5 Myr on Hawaii so such large time gaps suggest that tectonics played a role with or possibly without the presence of mantle plume (Anguita & Hernan, 2000) The islands of Tenerife, La Palma, Lanzarote and El Hierro (Fig. 1) have been active in historical times. The youngest volcanism on Fuerteventura and Gran Canaria is Late Pleistocene (Coello et al., 1992 and references therein), while on La Gomera only Late Pliocene activity is found (Cantagrel et al., 1984).

Because the above mentioned large time gap and widespread activity volcanism throughout the archipelago differ from what is found in Hawaiian Islands it is argued that the Canary Islands were not formed by a plume driven ‘hot spot’ (Anguita & Hernan, 2000).

However the slower relative movement of the African plate at the latitude of the Canary Islands (Geldmacher et al., 2005) provides a simple explanation for widespread volcanism across Canary archipelago.

3.2 Fuerteventura

The geochronology of Fuerteventura is summarized by Stillman (1999) and references therein, and a particularly detailed description is given in Coello et al. (1992). The volcanic history of the island can be divided into three stages (Fig. 4): (1) the submarine seamount stage or basal complex, (2) the subaerial shield stage sitting on the lower Miocene (20.4 ± 0.4 Ma and lasting for 3.5 Myr until the end of the middle Miocene (Coello et al., 1992), (3) the post-erosional, late stage volcanism, which started around the Miocene/Pliocene boundary and continued until well into the Pleistocene The onset of the subaerial shield stage was not the same for the three volcanic centres on Fuerteventura. Main activity of the CVC occurred from 20 to 18 Ma while NVC and SVC were built up mostly between 14 - 12 Ma and 16 - 14 Ma respectively (Coello et al., 1992).

The last directly dated episode of volcanism on Fuerteventura was in the upper Pleistocene (Coello et al., 1992). K/Ar dating of basaltic rocks yielded an age of 400 ± 100 ka (Coello et al., 1992), however stratigraphical constraints using radiocarbon dating in combination with sedimentary and palaeoclimatological records show evidence of volcanism younger than 9280 ± 370 a (Coello et al., 1999).

4. Geomorphology and climate

Potential TCN calibration samples sites need to have been stable since eruption. Weathered and eroded samples need to be avoided because their cosmogenic isotope contents have been

influenced by factors other than actual cosmogenic production. Correct assessment of geomorphological and climatic factors and their interactions is essential when choosing a calibration site. Fuerteventura is very dry just like Lanzarote. The favourable characteristics are outlined in Dunai & Wijbrans (2000, and references therein). It has low relief (apart from a few single peaks or ridges, the highest being Pico de la Zarza with 807 m), which ensures that clouds do not form with ensuing precipitation,

This contrasts with, for example, Tenerife where the NE trade winds blow moist air against the 3718 m high mountains of Teide volcano dividing the island into a wet, heavily vegetated and eroded northern half and a well preserved dry southern half.

Due to its low latitude location (29º N) and low relief snowfall is considered to be absent on Fuerteventura. The dry climate supports only a little vegetation so the surface consists mostly of bare crystalline rocks and unconsolidated sediments. Fuerteventura's relief is defined by low volcanic ridges and cones in the centre of the island which flatten out abruptly into broad concave valleys and rolling hills towards the coast, suggesting some degree of erosion since the creation of the middle Miocene volcanic edifices. In these valleys volcanic rocks dominate but close to sedimentary infill mostly in the form of sedimentary fans, is found on the flanks of the Miocene ridges. As a result, the valleys are often cultivated and inhabited.

Fig. 5: Photos showing the local geomorphology of flows VF (near Valle de Fimapaire, right) and MQ (near Montana Quemada, left). The flows represent local highs in the geomorphology.

Some cinder cones associated with dark brown or black basalt flows represent the last stage of volcanic activity in the middle and the north of the island. These lava flows often form morphological highs by themselves given the very flat topography of the valleys (Figure 5). Due to heavy erosion of its old edifices and rather small volumes of late Neogene volcanism Fuerteventura has a very low relief compared to other islands of the archipelago. Most importantly, the most recent volcanic rocks appear to be well preserved.

A sample in situ (top) and a jaw crusher at the Vrije Universiteit Amsterdam (bottom)

II. Sampling strategy, description and preparation

Fig. 1: Satellite image of Fuerteventura. The most recent units stand out in the picture due to their dark colour. The sampling locations are: Valle de Fimapaire (VF), Montana Quemada (MQ), Caldera de Gairia (CG), Montana de la Mancha (MM), Montana de Arena (MA), Montana Negra (MN), Caldera de los Arrables (CA), Malpais Chico (MC), Malpais de Roja (MR). Satellite images were taken from Google Earth.

Sampling strategy, description and preparation

1. Sampling strategy

To ensure a simple exposure history without any episodes of erosion it is necessary to find lava flow tops with well preserved surface structures. This is often reflected in the ropey appearance of pahoehoe flows or the cauliflower structures found on aa flows. The semi-arid climate on Fuerteventura ensures the lack of extensive cover by plants. However, it is not a straightforward task to ensure that a lava flow has not been covered by another lava flow, ash, sediment or soil. Airborne and satellite based images were studied to find good sampling sites by locating fresh looking lava flows without vegetation.

As can be seen from a satellite image, fresh lava flows are dark brown to black in colour and so are in strong contrast to the older light brown lavas or green vegetated surfaces (Figure 1). Flows identified were closely examined in the field. Only samples with clearly recognizable cauliflower or ropey surface structures were chosen to ensure minimal erosion. Sample sites on local highs were preferred as they have a lower probability of being covered by ash. At sample sites chosen for cosmogenic helium analysis 7 or 8 mostly disk shaped surface boulders of about 20 to 40 cm diameter and half of that in height, preferably with flat surface, were taken as complete pieces within a an area 20 m in diameter. Samples for $^{40}Ar/^{39}Ar$ analysis were taken wherever possible from deeper and less vesicular parts of the flows using a hammer and chisel. The positions of sample sites were recorded by GPS measurements and the height of relief on the horizon line was measured in 10 degree increments for a full circle using a handheld clinometer. This horizon line would be used for geomorphological shielding correction later.

2. Sampling sites and sample field characteristics

Coordinates of the sample locations are in Table 1 in Appendix A and photographs of the sample sites are in Figure 2. We now summarize the characteristics of the sample sites.

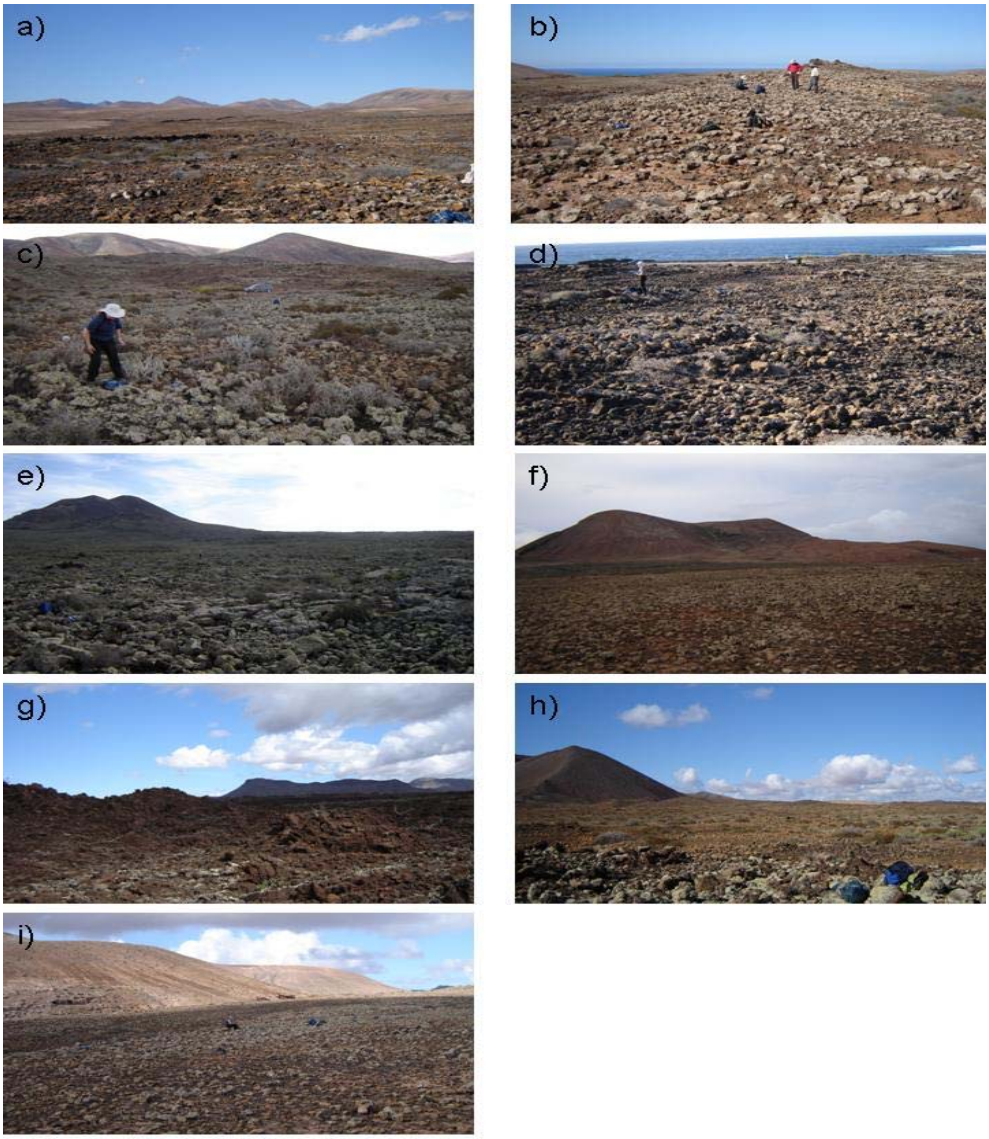

Fig. 2: Photographs of the sample locations showing the immediate geomorphological characteristics. The locations are: a) Valle de Fimapaire (VF), b) Montana Quemada (MQ), c) Caldera de Gairia (CG), d) Montana de la Mancha (MM), e) Montana de Arena (MA), f) Montana Negra (MN), g) Caldera de los Arrables (CA), h) Malpais Chico (MC), i) Malpais de Roja (MR).

Sampling strategy, description and preparation

Sample VF (Valle de Fimapaire, Figure 2a) is a pahoehoe flow, which is in a transitional stage towards becoming a desert pavement and so is eroded in some parts while others are better preserved. No vegetation was on this lava flow. The sampling site was on a morphological high, located close to the sea, and no geomorphological obstacle was located close by minimizing effects of topographic shielding.

Sample MQ (Montana Quemada, Figure 2b) is a lava flow, now transformed into a desert pavement, with large clasts lying on top of the finer grained material. There is no evidence of recent vegetation. The sample site is located on a morphological high making it unlikely that it was covered by sediment that eroded later. No hills or cones are located close to this site that could have caused significant topographic shielding.

Sample CG (Caldera de Gairia, Figure 2c) is an aa flow. The only vegetation growing are very small bushes scattered about, some in small groups. The sampling site is in a shallow trough surrounded by other lava flows that might contribute to topographic shielding.

Sample MM (Montana de la Mancha, Figure 2d) is an aa flow. The only vegetation consists of some small single plants. Being close to the sea this sampling site has only a volcanic cone in the neighbourhood, which does not contribute greatly to topographic shielding.

Sample MA (Montana de Arena, Figure 2e) is a pahoehoe flow. Vegetation consists mostly of single low plants and a few smallgroups. The sampling site is at the foot of a cone.

Sample MN (Montana Negra, Figure 2f) is a former lava flow now converted into a desert pavement. No vegetation is present. Located between two nearby cones this sampling site might be subjected to considerable topographic shielding. The site is surrounded by agricultural fields and could therefore be disturbed.

Sample CA (Caldera de los Arrables, Figure 2g) is an aa flow with no vegetation. The shape of the flow top is a bit irregular, which together with some local heights surrounding the sample site, might cause some topographic shielding.

Sample MC (Malpais Chico, Figure 2h) is an aa flow with only very few small individual plants. The sampling site is located on a local high and only one cone is close enough to possibly cause any shielding.

Sample MR (Malpais de Roja, Figure 2i) is an aa flow in transition to a desert pavement. It is vegetated by single low plants. A volcanic cone is close by.

3. Sample petrographyy

All samples show a very fine grained dark blue-grey to black matrix with varying degrees of vesicularity. In the most vesicular samples soil has filled some of the vesicles indicating vesicle network extending fromthe sample surface. Phenocrysts are very small, mostly smaller than 0.5 mm. In thin section the rock matrices are characterized by varying amounts of plagioclase needles and pyroxene developed in a cryptocrystalline to glassy matrix. Most phenocrysts are subeuhedral to euhedral; fragmentary olivines and clinopyroxenes are present with the exception of sample VF where the majority of phenocrysts are clinopyroxenes. Most phenocrysts show alteration in the form of embayments indicating partial assimilation of the phenocryst by surrounding melt.

	phenocrysts	**matrix**
CG	olivine (subeuhedral to rounded), clinopyroxene (subeuhedral)	very fine grained with pyroxene
MM	olivine (subeuhedral to embayed), clinopyroxene (subeuhedral to embayed)	very fine grained with feldspar needles and pyroxene
MN	olivine (subeuhedral), clinopyroxene (subeuhedral)	very fine grained with pyroxene and feldspar needles
MQ	olivine (subeuhedral to embayed), clinopyroxene (euhedral to subeuhedral)	very fine grained with pyroxene and feldspar needles
MR	olivine (subeuhedral), clinopyroxene (euhedral to subeuhedral)	fine grained with feldspar needles
CA	clinopyroxene (euhedral to subeuhedral), olivine (subeuhedral to embayed)	glassy with feldspar and pyroxene needles
MA	clinopyroxene (euhedral to subeuhedral), olivine (subeuhedral to embayed)	glassy with feldspar and pyroxene needles
VF	plagioclase needles, clinopyroxene (euhedral to subeuhedral), olivine (rounded)	glassy with pyroxene
MC	clinopyroxene (subeuhedral to embayed), olivine (subeuherdal to rounded)	glassy with pyroxene

Table 1: Summary of thin-section analysis.

4. Sample preparation

Samples were cleaned with a metal brush to remove dust, lichen and soil and subsequently split in pieces small enough for the jaw crusher. Uncrushed pieces were weighed and then their volume was determined in a glass of water to determine their density (see Appendix F). This procedure also accounted for vesicularity and sedimentation in vesicles. For cosmogenic helium analyses most samples where crushed completely assuming and promoting homogeneous mixing of the crushed material. Some cosmogenic samples were cut from the topmost 5 cm of a boulder and the rest was discarded (see Chapter V for surface samples). These two sample sets should allow for obtaining a production rate profile. After crushing samples were sieved to fractions of > 1 mm, 0.5-1 mm, 0.25-0.5 mm, 0.125-0.25 mm and <0.125 mm and then washed to clean them of dust and any leftover floating components such as remaining plant material.

For $^{40}Ar/^{39}Ar$ analysis a 0.5-1 mm size fraction was separated by density using a methylene-iodide-dichlorobenzene solution of 2.9 g/cm^3 density and an overflow centrifuge in order to separate the groundmass from heavy minerals. The float was then handpicked for groundmass and the groundmass separates were leached in 15 minute baths of dilute HNO_3, HF and HNO_3 again before 1 g per sample was packed in aluminium foil packages together with Drachenfels sanidine used as an internal laboratory standard. After packing the samples were irradiated at the HFR reactor in Petten, The Netherlands, and irradiated for one hour in the rotating Cd-shielded RODEO facility in the pool of the reactor.

Thin section analysis showed that most olivine phenocrysts suitable for cosmogenic ^{3}He analysis have a diameter of 0.25-0.5 mm. Olivine was separated from this size fraction using heavy liquid separation with a 3.2 g/cm^3 density methylene-iodide-dichlorobenzene solution and then, if necessary, again with a density of 3.3 g/cm^3.

The olivine separates were hand picked to minimise adhering basalt and then etched in a solution of 10% HNO_3 and 10% HF at 35ºC to remove the outermost few 10´s µm in order to minimise the implanted ^{4}He (Farley et al., 1996).

5. Geochemistry

Knowledge of the geochemistry of the analysed samples was beneficial and, in some cases, essential for this project. For example, $^{40}Ar/^{39}Ar$ analysis can be better planned when the concentrations of calcium, potassium and also chlorine in the samples are known as these elements contribute most to the production of argon isotopes in nature and in the reactor. In situ cosmogenic ^{36}Cl is produced by many elements so when performing ^{36}Cl analysis on whole rock samples (another part) of this study (Mai, 2009) a complete knowledge of major and trace element concentrations is essential both for sample preparation and analysis.. It is important to know also the Th and U concentrations in the host rock when analysing cosmogenic ^{3}He in olivine in order to determine the amount of implantation of radiogenic helium into the phenocryst grain if it was not etched. Implantation effects are normally reduced if these elements are concentrated in only a few mineral phases rather than distributed homogeneously in a sample. The effects of compositional zonation of target minerals are discussed in detail in Chapter V. Whole rock major element geochemistry of the samples was determined by X-ray fluorescence analysis. Trace elements were measured using ICP-MS. Both measurement series were undertaken at the Faculty of Geosciences, Utrecht University. Whole rock major and trace element oxide concentrations are given in Tables 1 and 2 in Appendix A. The chemical compositions of the individual flows show two major correlations. While SiO_2 correlates positively with Al_2O_3, they correlate negatively with Fe_2O_3, MgO and P_2O_5 indicating magmatic differentiation trends. The K_2O concentrations are all around 1 wt%.

Sampling strategy, description and preparation

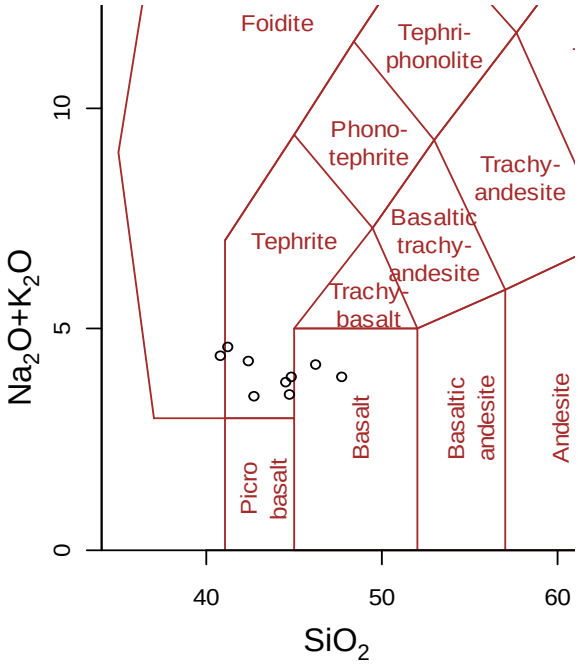

Fig. 3: TAS classification diagram (after Middlemost, 1994) showing the 9 Fuerteventura basaltic samples (circles) clustered from foiditic to basaltic composition. Axes are in wt%.

In the TAS classification diagram (Figure 3) the samples span a linear compositional array from slightly foiditic over tephritic to basaltic composition. From the major element discrimination diagrams (Figure 4) the Fuerteventura basalts have the signature of an ocean island setting. The trace element pattern (Figure 5) shows an enriched signature compared to primitive mantle and also compared to N-MORB (Sun & McDonough, 1989; Geldmacher, 2005). This composition is commonly associated with ocean island or intraplate volcanism (Geldmacher et al., 2005). The missing Eu anomaly indicates that no plagioclase was fractionated out of the melt. This in turn implies a melt generation at greater depths than a few 10's of km. A negative K anomaly similar to HIMU basalts from the Canary Islands (Geldmacher et al., 2005) points towards a mantle source originating from recycled crust which might have mixed with enriched mantle in order to produce the melt of the analysed Fuerteventura basalts.

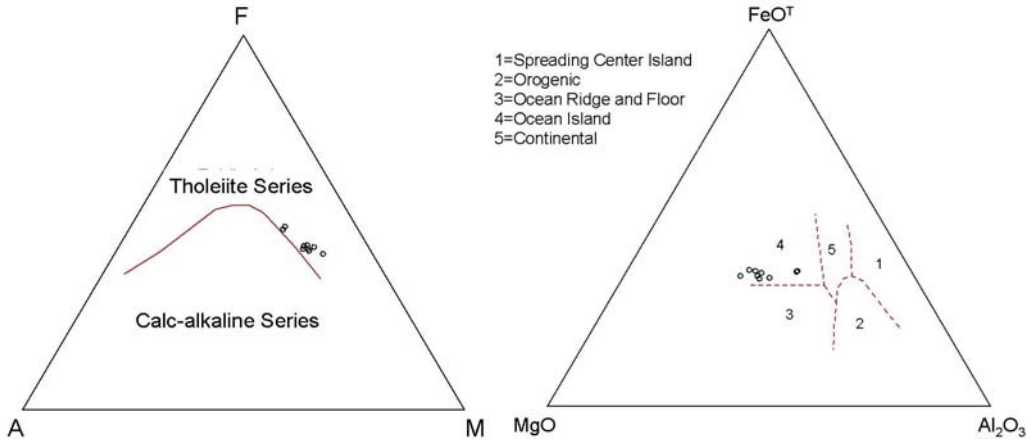

Fig. 4: The AFM diagram (left, Irvine and Baragar, 1971) shows the primitive composition of the basaltic lava flows of this study. The diagram on the right (Pearce et al., 1977) demonstrates Fuerteventura lavas plot in the Ocean Island Basalts close to the Ocean Ridge composition.

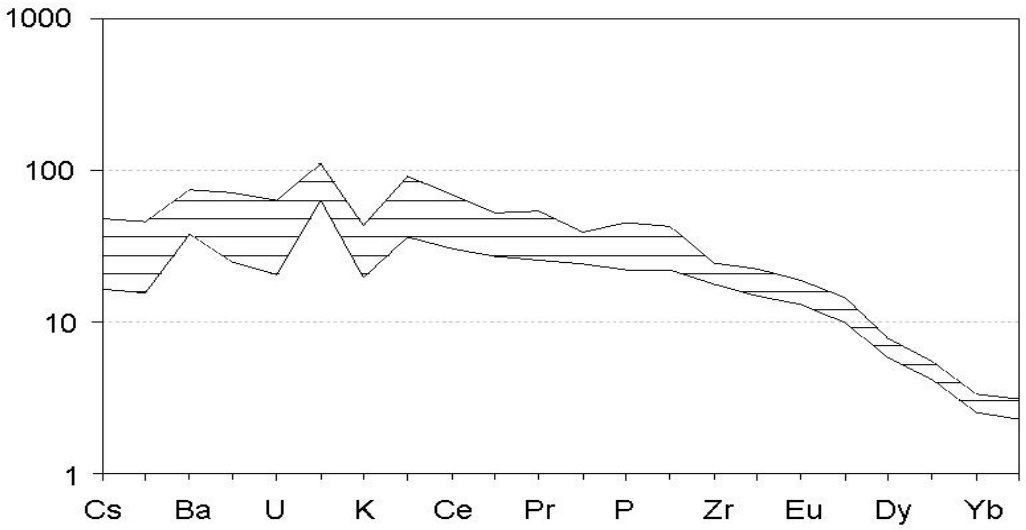

Fig. 5: Spider diagram normalized to primitive mantle composition (after Sun & McDonough, 1989). The horizontally lined area spans the range of values for all the Fuerteventura basalts analysed here.

6. Summary

The dry climate on Fuerteventura provides an environment with little chemical or mechanical weathering and the collected samples show very good preservation even in thin section. The aphanitic matrix of the basalts contains only very small phenocrysts. Major and trace element compositions of the samples cluster tightly in the area of primitive basalts. The data suggests a typical ocean island suite for these samples. In summary it is possible to use these samples for the intercalibration of $^{40}Ar/^{39}Ar$ geochronology and cosmogenic ^{3}He exposure dating. Erosion was sometimes present, but minimal. The small olivine phenocrysts made separation difficult and additional steps were necessary to minimise the influence of implanted ^{4}He.

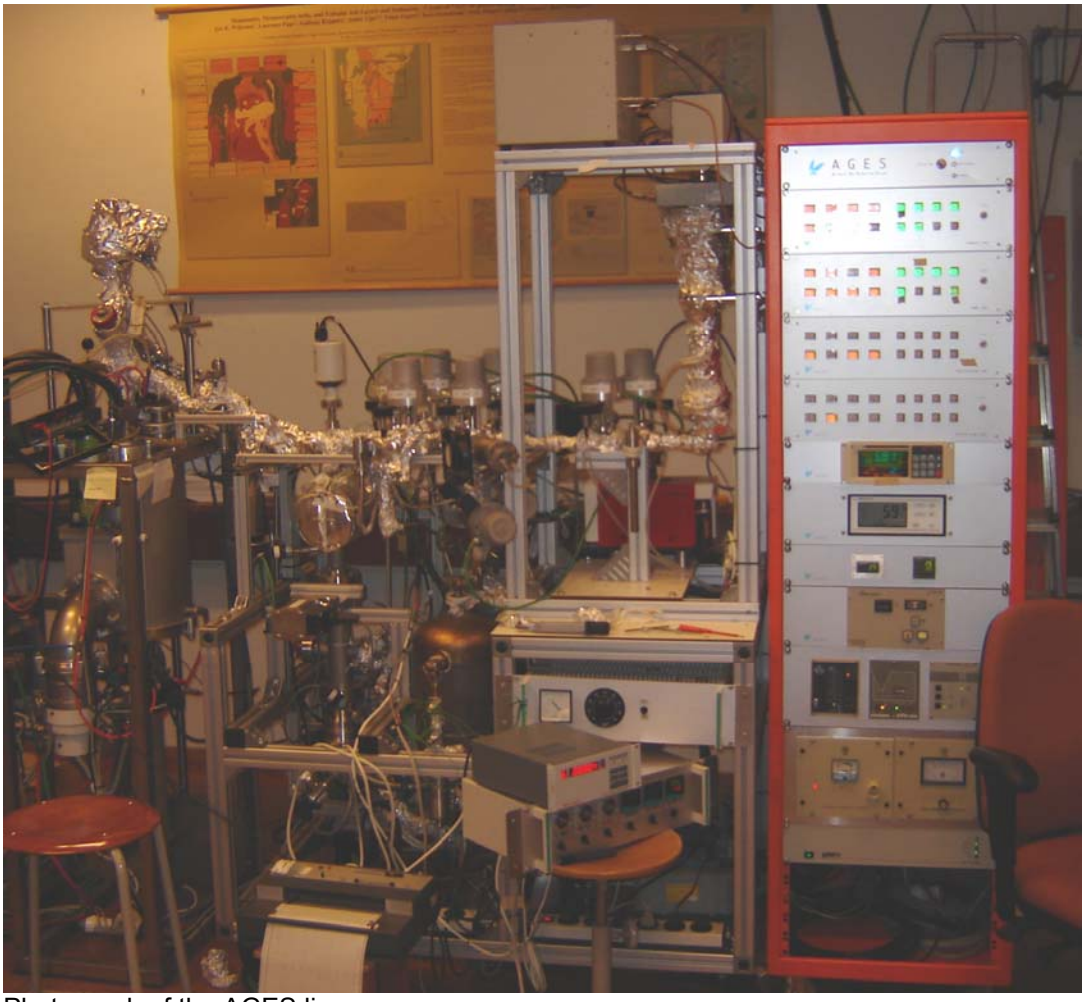

Photograph of the AGES line

III. $^{40}Ar/^{39}Ar$ dating with a commercial grade triple filter quadrupole mass spectrometer

(Published as: Schneider, B., Kuiper, K.F., Postma, O., Wijbrans, J.R. (2009). $^{40}Ar/^{39}Ar$ geochronology using a quadrupole mass spectrometer. Quaternary Geochronology 4 (6), 508-516.)

Introduction

Noble gas mass spectrometers are generally developments from the machine originally described by Nier (1947). They are characterized by an electron impact gas source, magnetic sector mass filter with first-order direction focusing, and a Faraday cup as beam detector. In the 1950's and 60's several different types of mass spectrometers were tested: The Reynolds-type (Reynolds, 1956), the Omegatron (Grasty & Miller, 1965), and small sized permanent magnet instruments such as the Varian GD150 and the AEI MS10 (Rex & Hudson, 1970) mass spectrometers are the most prominent examples. The all-glass design of Reynolds was a modification of the Nier type mass spectrometer. It led to greatly enhanced sensitivity for measurements of noble gases in a time when high purity steel and reliable gaskets for vacuum seals were not yet available. Most mass spectrometers today use a source that dates back to the design of Nier (1947), although ionisation sources designs have proven successful, e.g. the Baur-Signer (Baur & Signer, 1980) and the modified compressor source (Baur, 1999).

Since the 1980's quadrupole mass spectrometers (QMS) have been used moderately for determining noble gas abundance in fluids and rocks (Kulongoski & Hilton, 2002; Sano & Takahata, 2005; Marty et al., 1995; Hamme & Emerson, 2004; Pinti et al., 2001), ^{4}He content in apatite and zircon in U/Th-He thermochronology (Persano et al., 2002) and more recently for K-Ar age determinations (Rouchon et al., 2008).

Isotope ratio measurements for the $^{40}Ar/^{39}Ar$ dating technique have been carried out routinely on magnetic sector magnet mass spectrometers of the Reynolds and Nier types since the introduction of the technique (Merrihue and Turner, 1966). At that time these instruments achieved better sensitivity and resolution compared to quadrupole instruments. Measurements were initially carried out using Faraday cups as detectors at first and later discrete dynode electron multipliers were used to measure low signals with better precision (Layer et al 1987, Dalrymple, 1989). The most recent development is the use of multi-collector instruments which can measure all argon isotopes simultaneously (Stacey et al., 1981; Coulie et al., 2004; Storey et al., 2007; Mark et al.,

2009). Quadrupole mass spectrometer improvements in resolution and abundance sensitivity (by factors of up to 1000 and more while still maintaining low peak base widths, Konenkov et al., 2001) are such that complete peak separation at high intensity can now be achieved (e.g. Hamme & Emerson, 2004) and the application of these instruments in the $^{40}Ar/^{39}Ar$ dating technique now becomes possible. Compared to sector magnet instruments quadrupole instruments are less expensive and smaller in size making them easier to acquire and maintain. This chapter describes the fully automated facility used at the VUA for $^{40}Ar/^{39}Ar$ dating using a modern triple filter quadrupole mass spectrometer with pulse counting channeltron beam detection connected to a furnace extraction system. This chapter presents the characteristics of this facility, which was originally designed for $^{40}Ar/^{39}Ar$ incremental heating analysis of large volumes of young volcanic rocks. .The theoretical basis of $^{40}Ar/^{39}Ar$ dating and general practical application is summarized first together with some basics about mass spectrometry. Next is a description of the furnace extraction line and mass spectrometer. Then the performance of the system is described and the development of the measurement routine is outlined. Finally the **A**utomated **G**as **E**xtraction **S**ystem (furthermore AGES) line is compared to the 'Vulkaan' laser probe in use for many years at the Vrije Universiteit Amsterdam (VUA) (Wijbrans et al., 1995) and a quadrupole system in use at the Laboratoire de Geochronologie Multi-Techniques (Universite Paris Sud) for K-Ar dating (Rouchon et a., 2008).

1. $^{40}Ar/^{39}Ar$ geochronology: theory and application

The $^{40}Ar/^{39}Ar$ technique is based on the K-Ar technique which utilizes the decay of ^{40}K to ^{40}Ar via electron capture and positron decay to calculate ages of high potassium phases. The basis for this and other radio-isotopic dating techniques is the exponential decay of a radioactive isotope over time

$$N = N_0 e^{-\lambda t} \qquad (1.1)$$

with N being the amount of radioactive isotope at present, N_0 the amount of isotope at time zero, λ the decay constant and t the time elapsed since the rock forming event. However only the present day concentrations of the parent and daughter isotopes in a sample can be measured so the original concentration of the parent isotope is:

$$N_0 = N + D \tag{1.2}$$

where D is the concentration of the daughter isotope.

Combining these equations yields:

$$N = (N + D)e^{-\lambda t} \tag{1.3}$$

which can be rearranged to

$$t = \frac{1}{\lambda} \ln\left(\frac{D}{N} + 1\right) \tag{1.4}$$

For the K-Ar decay system the basic age equation is

$$t = \frac{1}{\lambda_{Ca} + \lambda_{Ar}} \ln\left(\frac{\lambda_{Ca} + \lambda_{Ar}}{\lambda_{Ar}} \frac{^{40}Ar}{^{40}K} + 1\right) \tag{1.5}$$

with $^{40}Ar^*$ being the amount of ^{40}Ar generated by in situ decay of ^{40}K, λ_{Ar} the proportion of ^{40}K decaying to $^{40}Ar^*$, λ_{Ca} the proportion of ^{40}K decaying to $^{40}Ca^*$. The $^{40}Ar/^{39}Ar$ technique utilizes the fact that neutron irradiation converts ^{39}K into ^{39}Ar which can be used as a proxy for the potassium concentration to calculate an age. For this purpose the conversion constant J has to be determined using standards of a known age (see McDougall & Harrison, 1999)

$$J = \left(e^{\lambda T} - 1\right) \times \left(\frac{^{40}Ar}{^{39}Ar_K}\right)^{-1} \tag{1.6}$$

where T is the age of the standard and $^{39}Ar_K$ is the ^{39}Ar generated by neutron irradiation in the reactor. The age of an unknown sample can then be calculated from:

$$t = \frac{1}{\lambda} \ln\left(1 + J \times \left(\frac{^{40}Ar}{^{39}Ar_K}\right)\right) \tag{1.7}$$

where $^{40}Ar^*/^{39}Ar_K$ is the measured ratio in the unknown sample.

Both the K-Ar technique and the $^{40}Ar/^{39}Ar$ technique are based on three basic assumptions:

1. The natural abundance of potassium isotopes in nature is homogenous. In particular the $^{40}K/K$ ratio has to be constant. Natural potassium isotopes include 93.2581 ± 0.0029 % ^{39}K, 0.01167 ± 0.00004 % ^{40}K, 6.7302 ± 0.0029 % ^{41}K (Garner et al., 1975) and no abundance differences greater than ~1.3% have been reported (McDougall & Harrison, 1999).

2. Decay constants do not vary with time and are independent of chemical state or P-T conditions.
3. The argon trapped in a sample is a mixture of radiogenic ^{40}Ar and atmospheric derived Ar.

The K-Ar method relies on the separation of two aliquots of the same sample, one for K measurement and the other for argon isotope measurement. Consequently highly homogenous sample material is required. Another disadvantage is that the absolute amount of argon should be extracted from the mineral phase which can be difficult for e.g. sanidine. The $^{40}Ar/^{39}Ar$ dating technique requires only one aliquot and incremental heating can assess whether argon loss or gain has occurred in the sample, hence provide an assessment of thermal history (McDougall & Harrison, 1999).The $^{40}Ar/^{39}Ar$ method requires samples to be neutron irradiated in order to produce ^{39}Ar from ^{39}K via neutron capture.

$^{39}K(n,p)^{39}Ar$

Moreover, interfering nuclear reactions produce 5 additional unwanted argon isotopes. It is essential to characterise nuclear interference correction factors, which are specific to a nuclear reactor, by irradiating and analysing zero age salts or glasses. The following reactions are most important:

$^{42}Ca(n,\alpha)^{39}Ar$
$^{40}Ca(n,\alpha)^{37}Ar$
$^{40}Ca(n,n,\alpha)^{36}Ar$

These reactions are monitored using high purity Ca salts such as fluorite (CaF_2).

$^{40}K(n,p)^{40}Ar$
$^{41}K(n, \alpha)^{38}Cl(e)^{38}Ar$

These reactions are monitored using high purity potassium salts (K_2SO_4) or synthesized potassium rich glasses.

Age calculations are based on the equation of McDougall and Harrison (1999) for calculating the $^{40}Ar^{*}/^{39}Ar_K$ ratio F and the corresponding age t

$$F = \frac{^{40}Ar}{^{39}Ar_K} = \frac{^{40}Ar_m - 295.5\times{}^{36}Ar_m + 295.5\times\left[^{36}Ar^{37}Ar\right]_{Ca}\times{}^{37}Ar_m}{^{39}Ar_m - \left[^{39}Ar^{37}Ar\right]_{Ca}\times{}^{37}Ar_m} - \left[^{40}Ar^{39}Ar\right]_K \tag{1.8}$$

$$t = \frac{1}{\lambda}\ln\left[\frac{F_u}{F_{st}}\left(e^{\lambda T} - 1\right) + 1\right] \tag{1.9}$$

where $^{X}Ar_m$ is the measured signal for isotope X corrected for blank, mass discrimination and ^{37}Ar or ^{39}Ar decay, $[^{36}Ar/^{37}Ar]_{Ca}$, $[^{39}Ar/^{37}Ar]_{Ca}$ and $[^{40}Ar/^{39}Ar]_K$ are correction factors for neutron interference reactions. λ is the decay constant ($5.543 \pm 0.010*10^{-10}$, Steiger & Jäger, 1977). F_u and F_{st} are the $^{40}Ar^{*}/^{39}Ar_K$ ratios for the unknown sample and the standard respectively and T is the age of the standard.

The VUA age equation based on this is

$$F = \frac{\left\{\left(^{40}Ar_m - {}^{40}Ar_{bl}\right) - D\times\left(^{36}Ar_m - {}^{36}Ar_{bl}\right) + \frac{E\times\left[^{36}Ar^{37}Ar\right]_{Ca}\times\left(^{37}Ar_m - {}^{37}Ar_{bl}\right)\times C_{37}}{\frac{0.75E}{D} + 0.25} + \frac{E\times\left[\frac{^{36}Cl}{^{38}Cl}\right]_P\times\lambda_{^{36}Cl}\times t_e\left(^{38}Ar_m - {}^{38}Ar_{bl}\right)}{\frac{0.5E}{D} + 0.5}\right\}}{\left\{\frac{\left(^{39}Ar_m - {}^{39}Ar_{bl}\right)C_{39}}{\frac{0.25E}{D} + 0.75} - \frac{\left[^{39}Ar^{37}Ar\right]_{Ca}\left(^{37}Ar_m - {}^{37}Ar_{bl}\right)C_{37}}{\frac{0.75E}{D} + 0.25}\right\}} - \left[^{40}Ar^{39}Ar\right]_K \tag{1.10}$$

where $^{X}Ar_m$ is the uncorrected measured signal for isotope X. $^{X}Ar_{bl}$ is the measured blank signal for isotope X, D is the $^{40}Ar/^{36}Ar$ ratio measured on air and E is the literature value for the $^{40}Ar/^{36}Ar$ ratio of air. $[^{36}Ar/^{37}Ar]_{Ca}$, $[^{39}Ar/^{37}Ar]_{Ca}$ and $[^{40}Ar/^{39}Ar]_K$ are correction factors for neutron interference reactions. $[^{36}Cl/^{38}Cl]_P$ is the production ratio of the Cl isotopes from ^{35}Cl and ^{37}Cl, ~316 reported by Roddick (1983) and 262.8 ± 1.7 and 252.7 ± 1.8 for NaCl and KCl respectively reported by Renne et al. (2008). λ_{36Cl} is the decay constant for decay ^{36}Cl to ^{36}Ar and t_e is time elapsed between irradiation and measurement. C_{37} and C_{39} are the correction factors for ^{37}Ar and ^{39}Ar decay and are defined as:

$$C_{37} = \frac{\lambda_{37} \times d \times e^{\lambda_{37} t_e}}{\left(1 - e^{-\lambda_{37} t_e}\right)} \quad (1.11)$$

$$C_{39} = \frac{\lambda_{39} \times d \times e^{\lambda_{39} t_e}}{\left(1 - e^{-\lambda_{39} t_e}\right)} \quad (1.12)$$

with λ_{37} and λ_{39} being the decay constants of ^{37}Ar (half life 35.1 days) and ^{39}Ar (half life 269.0 years) respectively and d the duration of the irradiation.

It is important to analyse enough sample material and to choose an irradiation time to yield a ^{40}Ar*/^{39}Ar ratio which is low enough (less than 300, Turner, 1971) to be measured with appropriate precision. However irradiation time also needs to take into account the expected ^{40}Ar* of a sample which is proportional to its age. Irradiation produces ^{39}Ar and therefore the irradiation time should not be too long or the ^{40}Ar*/^{39}Ar ratio becomes too small to be measured precisely.

As the enrichment in radiogenic ^{40}Ar in very young samples down to Holocene ages is extremely low, successful measurement also relies on the precise determination of the atmospheric component, $^{40}Ar_{atm}$, in the sample and hence on the precise measurement of $^{36}Ar_{atm}$. To measure ^{36}Ar precisely one needs to work with large amounts of sample material in order to get a beam intensity that is sufficiently high to be measured precisely.

2. Mass spectrometer line setup and methods

2.1 Hardware

Many laser extraction systems are dedicated to the measurement of small amounts of argon. The recently developed furnace and extraction line with a large gettering (i.e., gas purification) capacity has become a viable option for dating young rocks with high contents of air and alteration phases.

^{40}Ar/^{39}Ar dating is still carried out predominantly using magnetic sector instruments. In a magnetic sector instrument a high voltage (usually around 3 kV) is applied to the source ion optics to accelerate the ionized phase towards a static or sometimes electric magnet which bends the ion

trajectories according to their mass over charge ratio (m/z). Ion beams are focussed onto detectors by changing the accelerating voltage, the magnetic field properties or the detector positions.
A basic quadrupole mass analyzer consists of 4 metal rods arranged in rotational symmetry around the path of the ions (Figure 1).

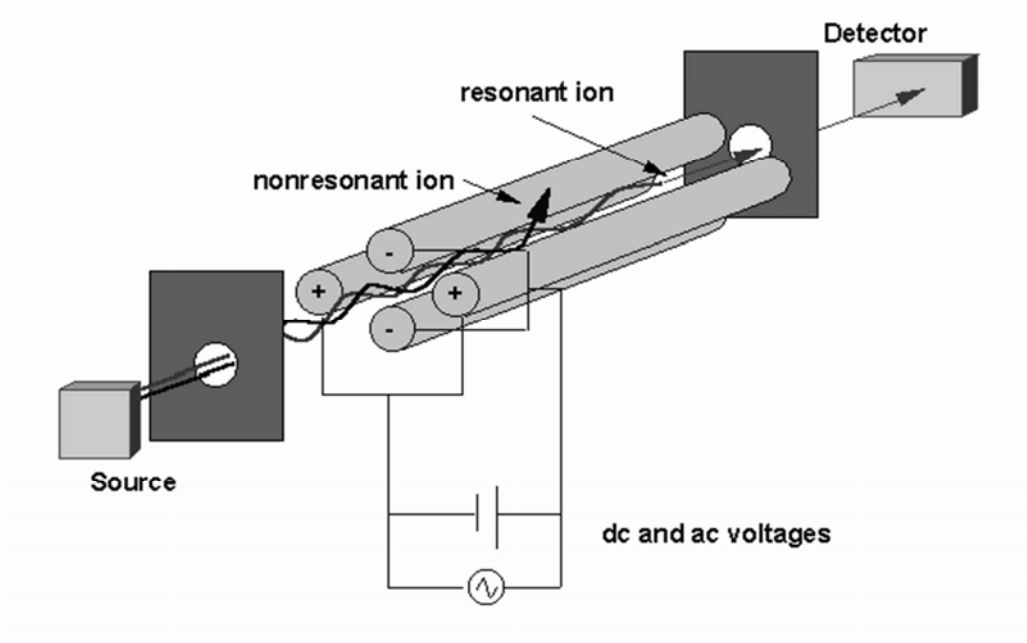

Fig. 1: Scheme showing the working principle of a quadrupole mass filter
(Diagram from the Chemistry Hypermedia Project: http://www.files.chem.vt.edu/chem-ed/ms/quadrupo.html).

Ion acceleration towards the detector is achieved by a voltage applied to the ion optics similar to a sector instrument. However, the voltage applied can be much lower (usually a few 100 V or less) than in magnetic sector instruments as the quadrupole mass analyser does not use ion acceleration in the ion separation process. Instead a radio frequency/direct current combination is applied on the rods giving opposite facing rods the same polarity. This AC/DC combination lets the ions' flight paths resonate and sorts out undesired ions by simply making them leave the path to the detector. Desired ions are detected by applying the appropriate acceleration voltage and/or radio frequency.

The AGES is a noble gas extraction system dedicated to $^{40}Ar/^{39}Ar$ incremental heating analysis of young igneous rocks (Figure 2). It features a revolving sample holder able to store 23 *ca* 500 mg-sized samples, a double vacuum resistance furnace for gas extraction linked to a pumping line able to maintain ultra high vacuum (UHV), a purification line with large getter capacity, and two reference gas vessels linked to the line via air actuated pipette systems. Gas analysis is performed on a Hiden HAL Series 1000 triple filter instrument fitted with a dual detector setup including a Faraday cup and a channeltron electron multiplier.

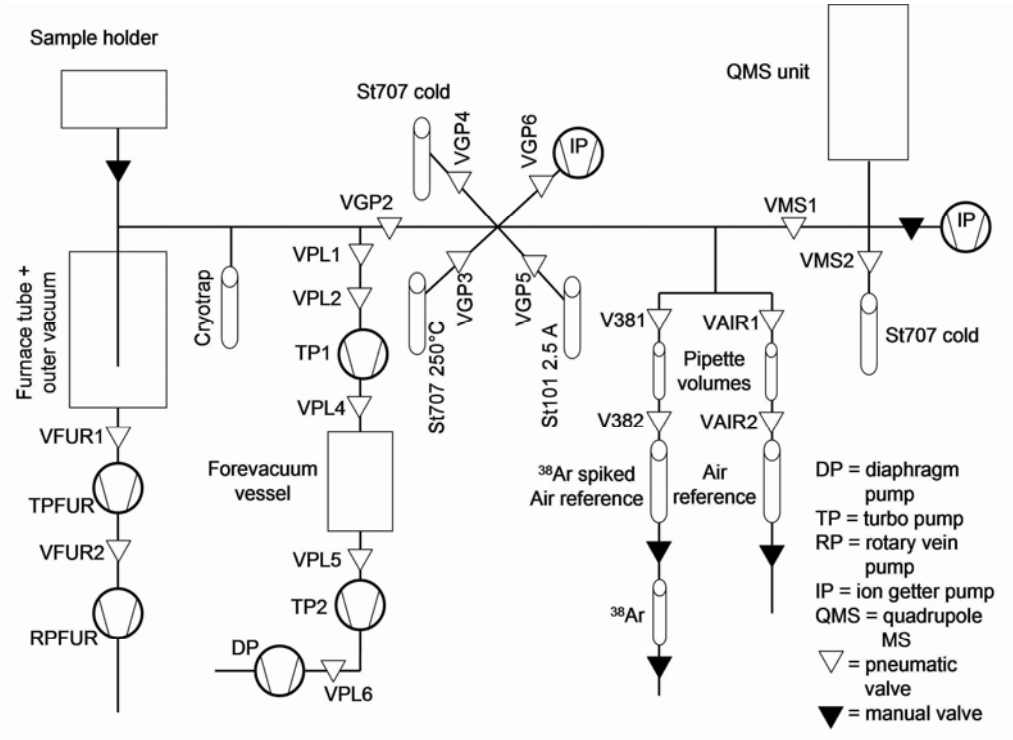

Fig. 2: A simplified scheme of the setup of the AGES argon extraction line.

The tubing of the system is made of stainless steel and all components in contact with UHV are bakeable to 250˚C. All valves are all-metal type, operated pneumatically, fitted with status indicators and can be switched manually using the control unit or remotely under computer control. The extraction line uses Nupro SS8BG valves with vented Cu-tips and neutral-closed air actuators. For pumping a turbopump (Pfeiffer-Balzers TPH 062), a 10 l expansion vessel, a drag

pump (Adixen-Alcatel MDP 5011) and a diaphragm pump (Vacuubrand MD4) are used. The turbo pump is fitted with a large aperture gate valve (VAT series 108) to the extraction line.

Extraction furnace

Gas extraction takes place in an in-house designed double vacuum high capacity resistor furnace with an isolating outer vacuum around the inner molybdenum alloy tube. The design is based on that of Staudacher et al. (1978). Heating is achieved using a GE™ wire mesh tungsten heating element fitted into 5 cm diameter Cu-block electrodes. The operating current to a maximum of *ca* 1000 A is generated using a single phase 12 kVA transformer. The temperature of the furnace is regulated using a Eurotherm™ 2400 series PID controller fitted with a W-WRe thermocouple. The electrical feedthroughs (2 per electrode) are water cooled to allow high currents (maximum ca 500 A/feed-through). During the testing stages of the furnace temperatures of ca 2200˚C were achieved. At these high temperatures the Mo furnace tube becomes vulnerable to cracking because the metal recrystallizes, leading to micro-cracks between the newly formed crystals. For safety reasons the maximum temperature of the furnace has been limited to 1600°C at the bottom of the oven tube, which is quite sufficient to fully degas molten basalt groundmass and glass (Winkler, 1962). To avoid damaging reactions between melts and the inner tube a thin walled molybdenum liner is inserted in the tube. The furnace is separated from the revolving sample holder using a manual gate valve to decrease the effective volume of the oven and to lower blanks in the furnace line during operation. A trap that can be cooled with liquid nitrogen is used in the furnace line to trap volatiles such as e.g. CO_2, H_2O, H_2S. The trap consists of a Cu-tube fitted with a sintered stainless steel filter to expand the internal surface of the trap. Argon is not trapped in it as it does not condensate on stainless steel at temperatures in the range ~ -190°C. The outer vacuum of the furnace is pumped using a rotary vein pump (Edwards 3 RV3) – turbo pump (Pfeiffer TPH 170) combination and is monitored using a thermocouple and cold cathode vacuum gauge.

UHV Pumping system and gas purification

The main pump line (Figure 2) is configured serially starting from the furnace with two gate valves, one of which (VPL2) is closed only during maintenance, while the other (VPL1) is used regularly for pumping between experiments. Next is a turbo pump which is the main UHV pump in the system used to pump residual gas out of the furnace line after each experiment. The gas

pumped out by the main turbo pump is expanded into a 10 l expansion reservoir at ~10^{-4} mbar. The expansion vessel is pumped out regularly when its pressure rises above a preset trip level. The pumping routine is set up so that the two valves (VPL4, VPL5) isolating the expansion reservoir from the turbo pump and the foreline pumps are never opened at the same time, thus preventing a direct open connection between the UHV line and atmosphere. The expansion volume is pumped by a drag pump and a diaphragm pump separated by another valve (VPL6). Extracted gas is purified in a separate section of the facility by two SAES St707 (Fe-V-Zr alloy) getters one of which is operated at room temperature and the other one at 250°C by heating externally with a thermocouple controlled pipe heater. A filament heated SAES AP50 getter operating at 2.5 A (St101, Zr-Al alloy, NEG) is used as a second stage getter. These getters adsorb N_2, O_2, H_2, CO and CO_2. Residual gases are pumped out of the purification line and the mass spectrometer with Starcell® ion pumps. An additional SAES St707 getter finger operating at room temperature is used on samples with exceptionally high content of volatiles.

Two reference gas vessels containing air and ^{38}Ar spiked air, respectively, are linked to the purification line. Each vessel consists of a 10 l reservoir fitted with a SAES St707 getter tube for purification and an air actuated gas pipette. The gas pipettes are built in-house by welding together two Nupro SS8BG valves each fitted with a neutral-closed air actuator. The volume contained between the two valves is ca 2.7 ml. The mass spectrometer segment hosts an ion getter pump and another SAES St707 getter operated at room temperature. The quadrupole mass spectrometer itself has an additional SAES St707 getter for further gas purification. These last two getters are included in order to reduce the hydrogen background in the analyser section of the line.

Triple Filter Quadrupole Mass Spectrometer

The Hiden HAL 3F Series 1000 Pulse Ion Counting Triple Filter Quadrupole Mass Spectrometer was set up to detect masses up to 100 amu. It is equipped with a radial symmetrical platinum electron impact ion source with twin Th-oxide coated iridium filaments operated at an electron energy of 85 eV and a trap current of 200 μA. A triple filter quadrupole minimizes contamination from unwanted ionized phases: In addition to the main mass filter, where a direct current and an RF current are applied to four parallel metal rod electrodes to accelerate and filter ions respectively, two RF-only filters are fitted before and after the main filter. The RF-only filters work at a different frequency than the mass filters RF current. The pre-filter stage greatly

decreases the number of unwanted ions that would normally be implanted in the mass filter electrodes and disturb the DC and RF fields. The two RF-only filters compensate for the fringing electric field of the central mass filter which would defocus the ion beam to some extent. They increase the overall filter length, which together with the smoothened mass filter electric fields result in higher mass transmission. Reducing these problems results in an overall higher sensitivity, steeper peak flanks and a broader peak top. Neighbouring peaks overlap less in the triple filter instrument so achieving a higher resolution compared to the single filter instrument - when both are operated at the same 50 % peak height width. A dual detector from Burleigh consisting of an ion counting single channeltron continuous dynode electron multiplier and a Faraday cup are fitted for beam detection.

2.2 Automation/Software

The AGES line can be operated in 3 modes: manual, semi-automatic and fully automatic. In manual mode all valves and pumps are operated manually by buttons on the control unit and no control mechanisms are active. This mode is normally used only for maintenance or testing protocols as it potentially allows contamination of the system with atmosphere and damage of components sensitive to high pressure. The only safety available in this mode is the power failure safety. In the case of a power failure all air actuated valves will shut and the whole system stays shut down until started up again under operator control.

In semi-automatic mode all valve actions are still carried out by the operator, but the safety protocols of the control units' microprocessors are functional. This means that potentially dangerous valve actions are prevented. For example, in semi-automatic mode it is not possible to open all valves on both sides of the fore vacuum expansion vessel, thus preventing a direct connection to the atmosphere, or open both valves of a reference gas vessel expanding the whole vessel to the purification line, or to open the two valves of the air pipette systems at the same time (a full listing of allowed and forbidden valve configurations is given in Appendix B). Furthermore, the status of pressure gauges and pumps throughout the system are continuously checked and if one sensor in a part of the system (furnace, cooling water, pump line, purification line, pipette system and QMS) reports critical values and goes into alarm condition, closing all valves and stopping all pumps. In the case of a forbidden condition on the furnace the power

supply for the heating elements also cut. All actions are logged by the automated control software in the background allowing for efficient error recovery.

In fully-automated mode the microprocessors in the system are instructed by the central process control platform to run pre-programmed experiment protocols. Experiment schedules are created using single step templates or self made protocols (heating step, blank step, reference gas measurement), which are put together in an online experiment editor. Typically an experiment consists of 10 or more furnace extraction steps at increasing temperatures between 650°C and 1300°C, with system blanks run before and after the experiment. Air and reference gas (^{38}Ar spiked air) calibration runs can be programmed at any point in the sequence. Hot blanks are measured before and after every cycle of 10 to a maximum of 23 experiments.

Automation is organized in such a way that the four main system components furnace (1), pump line (2), purification line and pipette system (3) and QMS (4) function as separate units each fitted with a PIC-processor based valve operating and policing protocol and a process state engine hosted on a miniature computer. The state engine of one unit is prompted for a particular experiment (in most cases the furnace or pipette system) on the basis of the edited protocol. Then the control software proceeds with the operations required on the basis of the parameters that it has received from the experiment protocol and prompts the next sub-system controlling the next segment; usually the purification line. Finally the gas is expanded into the mass spectrometer. In this subsystem the control software prompts the LabVIEW® module used to run the quadrupole mass spectrometer using pre-selected data collection protocols, as explained in the next section. The LabVIEW® module stores generated data on the local computer and on the network drive after the measurement has been completed. Experiment progress and system status can be monitored online via a dedicated webpage. Regression of stored peak intensity data are undertaken with ArArCALC 2.40 (Koppers, 2002) following analysis.

3. Procedure development

3.1 Peak shapes

Figure 3 illustrates a semi-continuous mass spectrum obtained by single channel electron multiplier measurements on a sample of air reference gas within a mass range of m/z=35 to 41 at 0.01 increments with a measurement time of 1 second per increment.

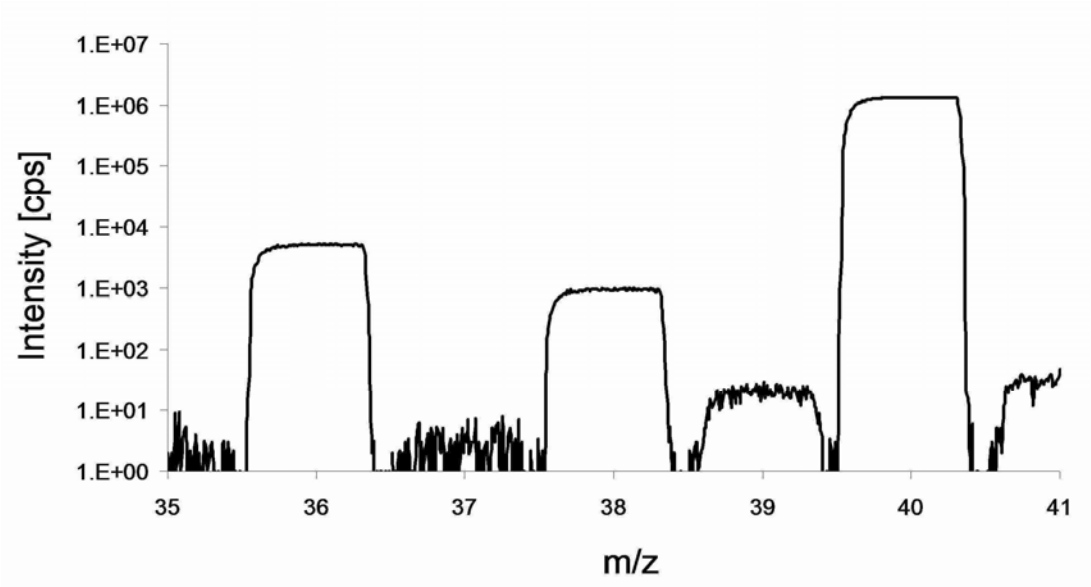

Fig. 3: Semi-continuous mass scan from m/z=35 to m/z=41 with a measurement interval of 0.01 m/z between points with a measurement time of 1 second per increment. Note that the abscissa is in logarithmic scale.

It shows well defined peaks at m/z=36, 38 and 40 as well as a much smaller peak at m/z=39 which is caused by a very small memory effect in the mass spectrometer and only a very low signal at m/z=37 with valleys between the peaks at baseline values. Note that the scale on the Y-axis is logarithmic. Peak shapes are not symmetric, showing first a very steep increase followed by a mildly increasing section to the nearly flat peak centre. On the high mass side the peak top is cut off very abruptly and at high intensities even showing a little tail of increasing values again (Figure 4) comparable to the peak shape achieved by Rouchon et al. (2008). The width of the peak base increases only very slightly with increasing beam intensity and never fully reaches 1 amu in the measurable intensity range ensuring complete resolution of all argon peaks because in the valleys baseline intensities are only 0 to 2 counts per second.

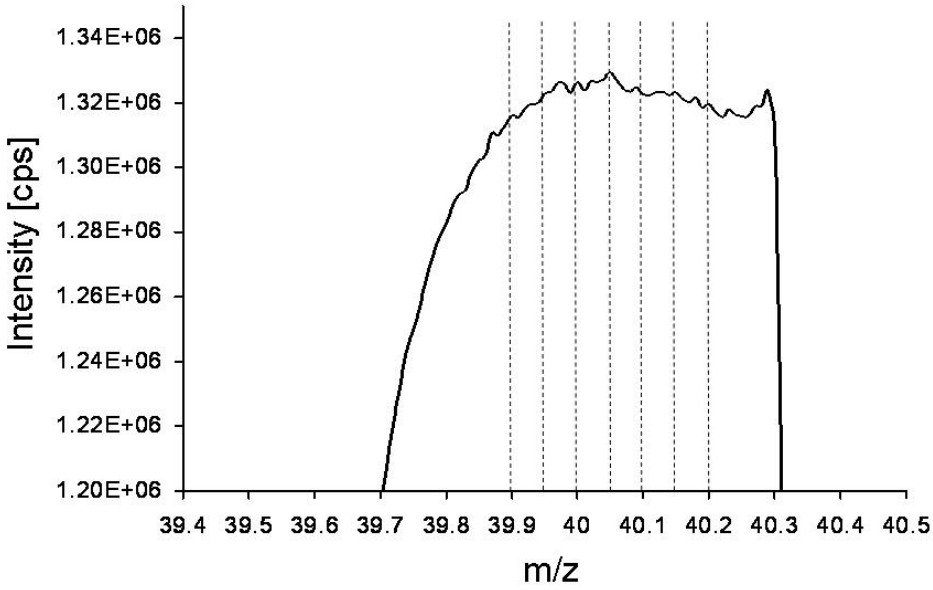

Fig. 4: Detailed linearly-scaled view of the peak at m/z=40 shown in Figure 3. Dashed lines indicate the positions measured over this peak during sample measurements.

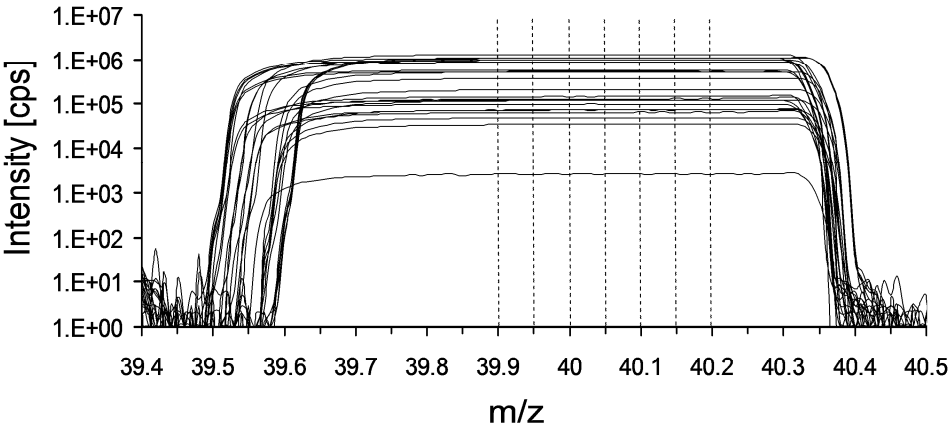

Fig. 5: Collection of peak shapes for m/z=40 over two years showing reference gas at different intensities. The abscissa is in logarithmic scale. Dashed lines indicate the positions measured over this peak during sample measurements.

Over the course of two years peak shifting occurred only within a range of 0.1 m/z and 0.05 m/z in the before and after peak slopes, respectively, showing high peak position stability, even after maintenance events (Figure 5). Because the peak is stable and has a peak shape with a plateau like top, the measurements sample the centre of the peak plateaus for each isotope (see 3.2).

3.2 Blanks

As mentioned in 3.1 the baseline of this instrument is 0 to 2 counts per second at the given measurement settings so it is negligible with respect to signal contribution. Furnace blanks on the other hand make a significant contribution to the measured signal for samples yielding low intensities and at high furnace temperatures. Figure 6 shows the blank levels of the different isotopes as a function of temperature.

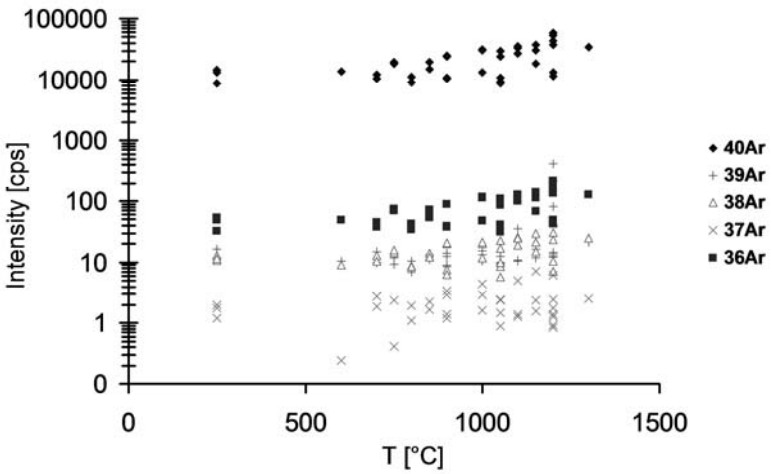

Fig. 6: Blank data for all argon isotopes from 2007 and 2008. Note that the abscissa is in logarithmic scale so all isotopes can be shown. As shown in section 3.6 of this chapter 1 count per second is equal to 1.663×10^{-18} mol or 3.725×10^{-14} cc.

The ^{40}Ar signal shows an especially large spread from 1000ºC upward, which tends to rapidly increase from 1200ºC. Because blank levels for ^{37}Ar and ^{39}Ar are generally very low, they are easily affected by undegassed residue remaining in the furnace. ^{36}Ar, ^{38}Ar and ^{40}Ar show nearly

identical distribution patterns in the blank data resulting from the fact that these isotopes come mainly from an air component in the blank, although ^{40}Ar is also influenced by residual sample gas.

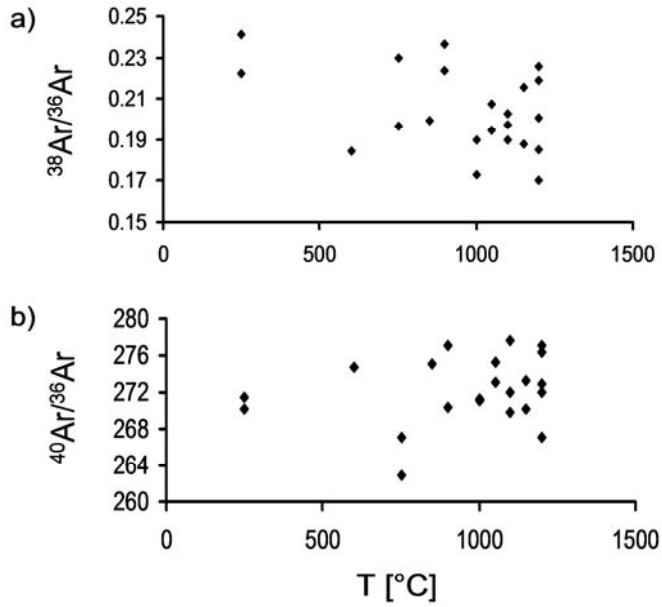

Fig. 7: Argon isotope ratios of blanks. In diagram (a) $^{38}Ar/^{36}Ar$ cluster around 0.21, the ratio obtained from air reference gas in this system. The $^{40}Ar/^{36}Ar$ ratios in diagram (b) are higher than the measured air ratio of 257.9 ± 1.3 obtained from reference gas, indicating residual radiogenic ^{40}Ar in the furnace. The uncertainty of the ratios is lower than the abscissa spread of the datapoints and therefore omitted.

This is supported by the $^{38}Ar/^{36}Ar$ and $^{40}Ar/^{36}Ar$ ratios in Figure 7 (a and b respectively): The $^{40}Ar/^{36}Ar$ ratios spread from 260 to 285 for high temperature blanks. A value of 260 is close to the measured air ratio because of the inherently high mass discrimination of the quadrupole mass spectrometer. The higher ratios indicate a slight enrichment in radiogenic ^{40}Ar. The $^{38}Ar/^{36}Ar$ ratio remains fairly constant at around 0.21, the ratio obtained in air reference gas. This indicates the presence of residual sample in the furnace and a non atmospheric ^{40}Ar concentration of up to 10 %

of the total blank signal at high furnace temperatures. The furnace blank is the main factor limiting the precision of the system. Blank signals for ^{40}Ar and ^{36}Ar range from 20,000 to about 60,000 cps and 40 to 220 cps, respectively. Samples without a lot of radiogenic argon shave decreased precision due to the high error contribution from the blank making high sample volumes of at least 200 mg (depending on sample quality) a necessity for dating young samples. It is important to apply a higher final bake out at a temperature level higher that that of the highest sample heating step to ensure effective degassing of argon from the melt residue before starting a new experiment. While basaltic groundmass experiments are typically degassed completely at around 1200ºC, a cleaning bake-out was applied at 1500ºC for 30 minutes. This ensured low blanks which increase nearly linearly until 1200ºC (Figure 6). The degassing routine proved particularly effective after analysis on the ca 25.26 Ma old Drachenfels (DRA) sanidine internal laboratory standard. Sanidine has a melting temperature in excess of 1700°C. The Fe-rich glass of previously degassed groundmass experiments acted as a flux that dissolved the sanidine at 1500ºC therefore effectively removing the argon from the sanidine.

3.3 Peak counting

The standard measurement procedure for argon isotopes depends on the impact of the different isotopes on the final results. ^{40}Ar and ^{39}Ar are sampled by measuring seven points over each peak starting at m/z=39.9 and 38.9 respectively, with increments of 0.05 amu and a dwell time of 3 s at each position. As ^{36}Ar generally yields low intensities, but is vital to the correction for air contamination, its peak is sampled at seven points starting with m/z=35.9 with 0.05 amu increments, at a dwell time of 7 s per point to improve counting statistics.

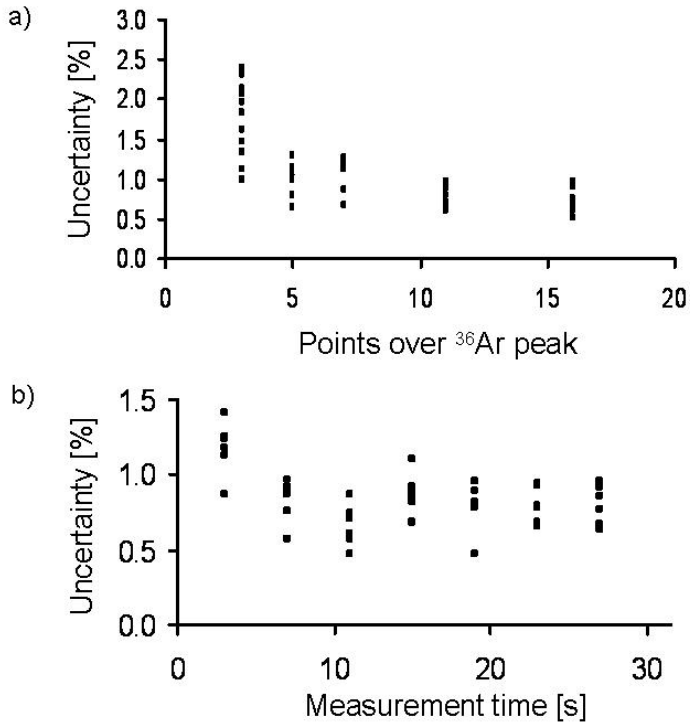

Fig. 8: Diagram (a) shows uncertainties over the sampled peak area resulting from using a different number of sample points over the m/z=36 peak ranging from m/z=35.9 to 36.2 with increments of 0.05 amu. There is no improvement in the analytical uncertainty with measurement of more than 7 points. Diagram (b) shows the uncertainties resulting from different measurement times over a sample point. A measurement time of 7 ms was chosen in the end for the regular measurement procedure as further increase in time did not decrease the analytical uncertainty.

This approach was chosen based on two experiments. In the first experiment shown in Figure 8 (a) the interval from m/z=35.9 to m/z=36.2 was sampled using different numbers of points but with a dwell time of 3 seconds for each measurement. The maximum ^{36}Ar peak measurement uncertainty is plotted against the number of points and shows a trend of decreasing uncertainty from nearly 2.5 % using 3 measurement points to 1 % using 16 measurement points. Although there is still a small improvement using more than 7 points over the peak 7 points where chosen in order to keep

the measurement cycle as short as possible to reduce the workload on the electron multiplier. In the second experiment the peak was sampled over the same interval but with different dwell times from 3 to 27 seconds (Figure 8b). A dwell time of 3 seconds yields maximum uncertainty of up to 1.45 %. Increasing it to more than 7 seconds does not reduce uncertainties to less than 0.8 %. ^{37}Ar and ^{38}Ar are sampled by taking measurements over m/z=37.1 and 38.1 respectively for 3 s each. The baseline is sampled at m/z=35.45. Measurements are undertaken in a peak jumping mode increasing in mass in a cycle that is repeated 15 times.

Output files are made compatible with the in-house data reduction package ArArCALC (Koppers, 2002) using an Excel macro that calculates the average number of counts and standard deviations for each scan over the 7 mass positions of the ^{36}Ar, ^{39}Ar and ^{40}Ar peaks. For the baseline ^{37}Ar and ^{38}Ar the peak intensity is stored (standard deviation cannot be calculated because sampling is at only one position for these isotopes). Data from the 15 cycles is then regressed to inlet time in ArArCALC to obtain the peak intensities used in the age calculation.

3.4 Measurement routine

The measurement routine for a single step starts with heating of the sample to the desired temperature for 25 minutes followed by 10 minutes of cooling to 250°C. The cold trap removes already most of the volatiles during the heating and cooling cycle.

The residual gas is first expanded (2 minutes expansion time) into the purification stage where it is exposed to the SAES St707 getter at 250°C for 10 minutes. After 10 minutes the gas is exposed to the SAES AP50 St101 getter for 5 minutes. Finally, the purified gas is expanded into the mass spectrometer for 3 minutes. Residual gas is pumped from the furnace with the turbo pump, from the purification section using Starcell® ion pumps, and from the mass spectrometer section.

Measurements of reference gases follow a slightly modified procedure. The gas is expanded directly from the reference gas pipette systems into the cleaning line without exposure to the furnace. It is preferable to keep the connection time between the furnace and the purification line to a minimum in order to maintain a high getter capacity for longer than might result from frequent and prolonged exposure to the furnace. A gas calibration measurement first involves expanding the reference gas to the pipette volume for 5 minutes. Then the pipette volume is expanded into the purification line where the gas is exposed to the heated SAES St707 getter for

10 minutes, then the SAES AP50 St101 getter for 5 minutes. The measurement procedure is the same.

3.5 Mass discrimination (MD)

Measurements of one pipette volume of air reference gas gave a $^{40}Ar/^{36}Ar = 257.9 \pm 1.3$ over two years (1 sigma, n=34, the relatively low number of measurements (Figure 9, black dots) is due downtime related to testing automation of the system and maintenance). Rouchon et al. (2008) report an air ratio of 262.5 ± 0.36 (monthly standard deviation) on their quadrupole instrument. Both findings suggest that these low $^{40}Ar/^{36}Ar$ ratios may be a common characteristic of quadrupole mass spectrometers. The now generally adopted air $^{40}Ar/^{36}Ar$ ratio is 298.56 ± 0.31 (Lee et al., 2006) so this instrument discriminates heavily in favour of the lighter isotopes. Standard sector instruments generally display $^{40}Ar/^{36}Ar$ ratios between 280 and 300 (MAP 215-50, Figure 9, grey dots).

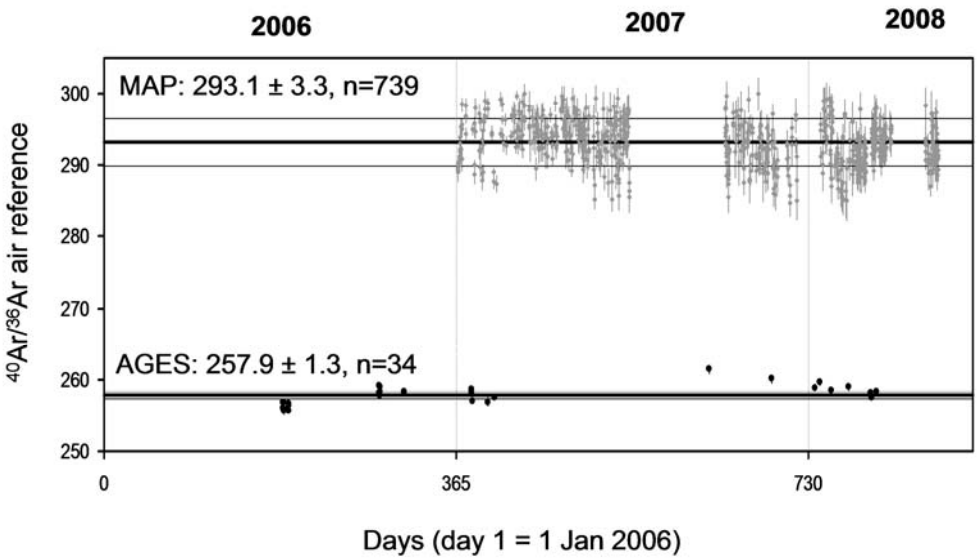

Fig. 9: Comparison of measurements of $^{40}Ar/^{36}Ar$ of $1.6*10^{-12}$ mole of air reference gas between the MAP 215-50 instrument (grey dots) and the quadrupole instrument (black dots).

Furthermore, measurements of combined aliquots of air reference gas show an intensity dependent change of the $^{40}Ar/^{36}Ar$ ratio, with a gradual, but substantial change at ^{40}Ar signals higher than 1 million counts per second (Figure 10 (a)). At the same time the $^{38}Ar/^{36}Ar$ ratio is unaffected until an observed range maximum of ~4 million cps (Figure 10 (b)).

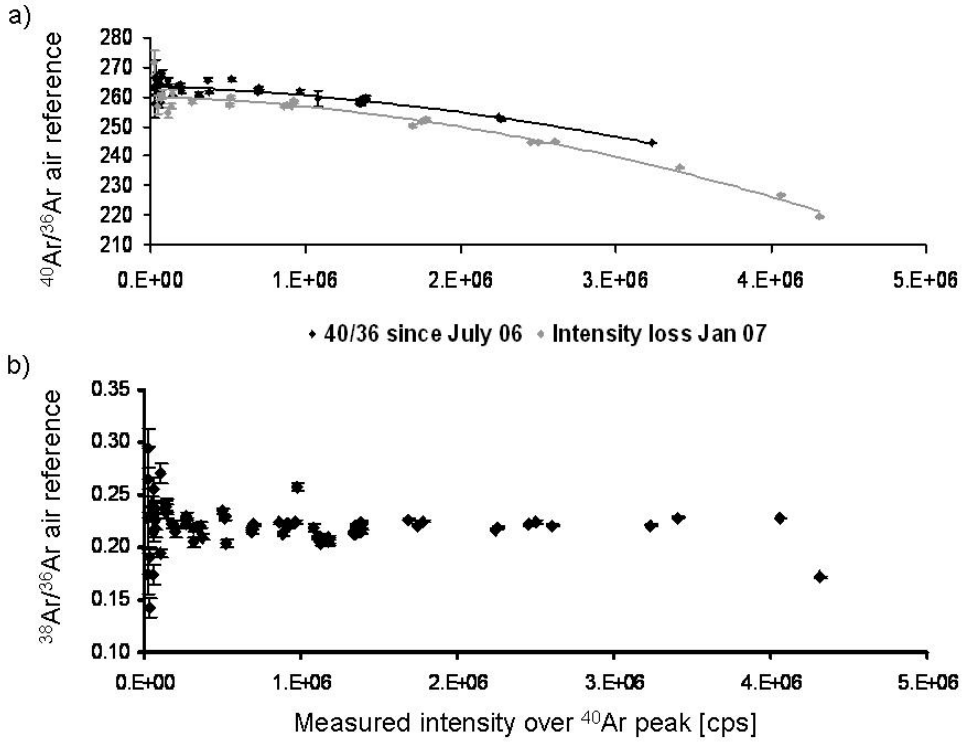

Fig. 10: Argon isotope ratios plotted against measured intensity of ^{40}Ar. Diagram (a) shows the change of $^{40}Ar/^{36}Ar$ since July 2006 (black diamonds) and the effect of an intensity loss when restarting in early 2007. Diagram (b) shows the development of $^{38}Ar/^{36}Ar$ with increasing intensity of ^{40}Ar.

The observed non-linear behaviour at high beam intensities is caused by the dead time factor in the channeltron multiplier. At high beam intensities the pulse counting electron multiplier misses incoming ions as the pulses come too fast after each other to be separated. To monitor this non-

linear effect reference gas of known isotopic ratios is measured over the whole range of expected intensities and the resulting data is used as basis for an empiric function describing the mass discrimination factor trend as a function of intensity (Figure 11).

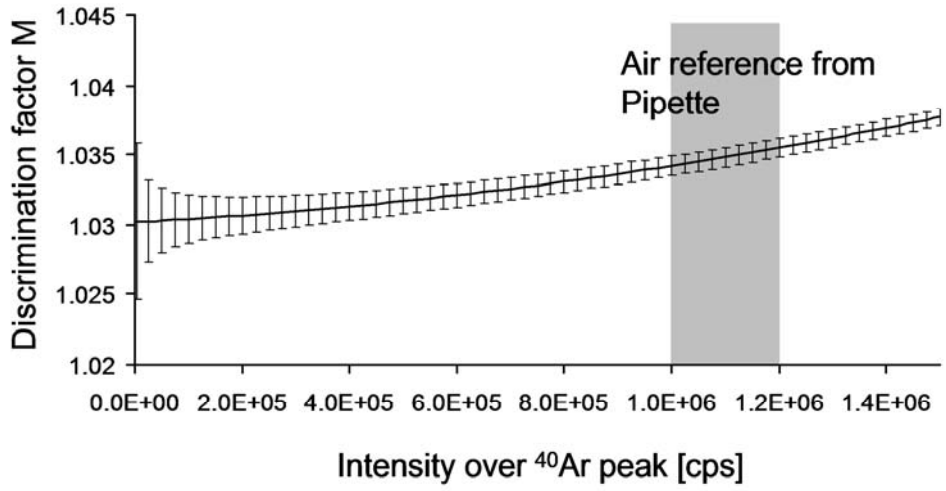

Fig. 11: Diagram showing the modeled discrimination factor between ^{40}Ar and ^{36}Ar plotted against measured intensity of ^{40}Ar. The highlighted area represents measurements of one pipette volume or $1.6*10^{-12}$ mole of air reference gas.

For this purpose the mass discrimination factor is determined over a wide range of intensities by diluting and enriching pipette volumes of air reference gas. Second order polynomial fits are used to obtain a continuous function of the mass discrimination depending on the ^{40}Ar intensity. This correction procedure is required, because the pipette system yields intensities of 1.1 million cps of ^{40}Ar while sample measurements span a wide range of intensities (Figure 11).

Varying the amount of Drachenfels sanidine (internal laboratory standard DRA-1; 25.26 Ma, intercalibrated against TCR-1 sanidine at 28.34 Ma; Renne et al., 1998) demonstrates the impact of intensity-dependent MD (Figure 12).

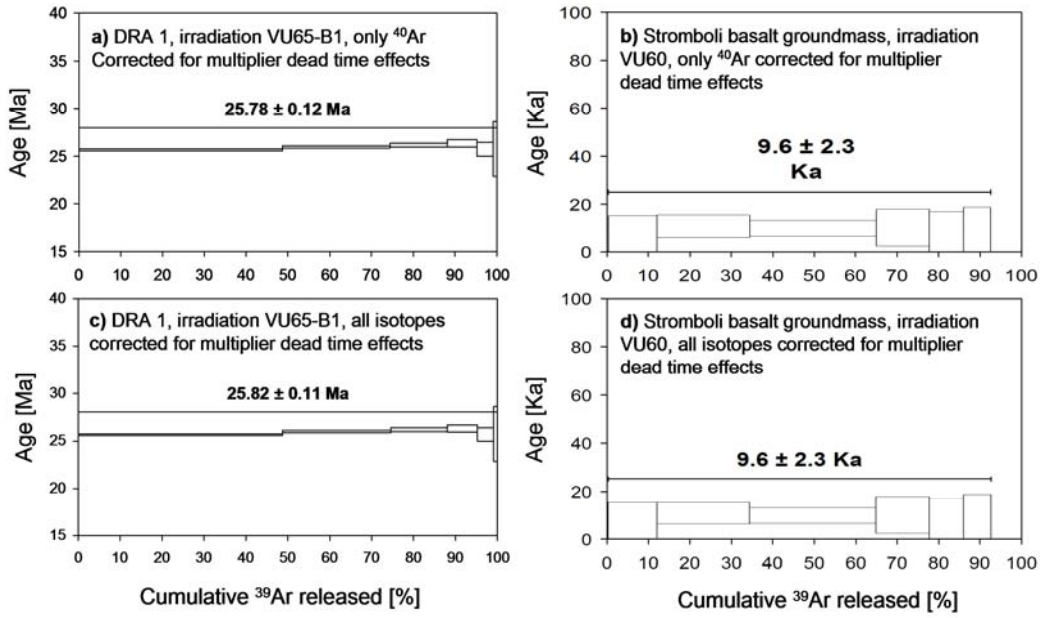

Fig. 12: A DRA-1 sanidine and a Stromboli basalt groundmass sample (Nel Canestra unit) before ((a) and (b)) and after ((c) and (d)) intensity dependent fractionation correction for all isotopes. Errors are 1 sigma. The Stromboli sample's age does not change in the visibly from (b) to (d) due to the low intensities measured and the resulting lower effects on the multiplier.

The results are displayed in plateaus, but represent different dilution steps. In Figure 12(a) the weighted mean age was calculated after correction for dead time effects on ^{40}Ar only while the age in Figure 12(c) was corrected for dead time on all Ar isotopes. The two ages are identical within analytical uncertainty as the intensities yielded on isotopes other than ^{40}Ar are simply not high enough to cause a significant dead time effect on the multiplier to affect the measurement. Note that the ages of these sanidine experiments of ~25.8 Ma are slightly higher than the age determined for the DRA-1 of 25.26 Ma due to the fact that the mass spectrometers fractionation behaviour was still re-equilibrating after a major maintenance event earlier on.

Figure 12(b) shows the same experiment done with Holocene basalt from the Nel Cannestra unit from Stromboli (Wijbrans et al., 2011). Predictably the intensities of the argon isotopes are not

high enough to cause any difference in the second age calculation (Figure 12(d)) correcting all argon isotopes for dead time effects. Both experiments show that correcting only of ^{40}Ar for multiplier dead time is sufficient provided that no isotope apart from ^{40}Ar yields signals in excess of about 200,000 cps.

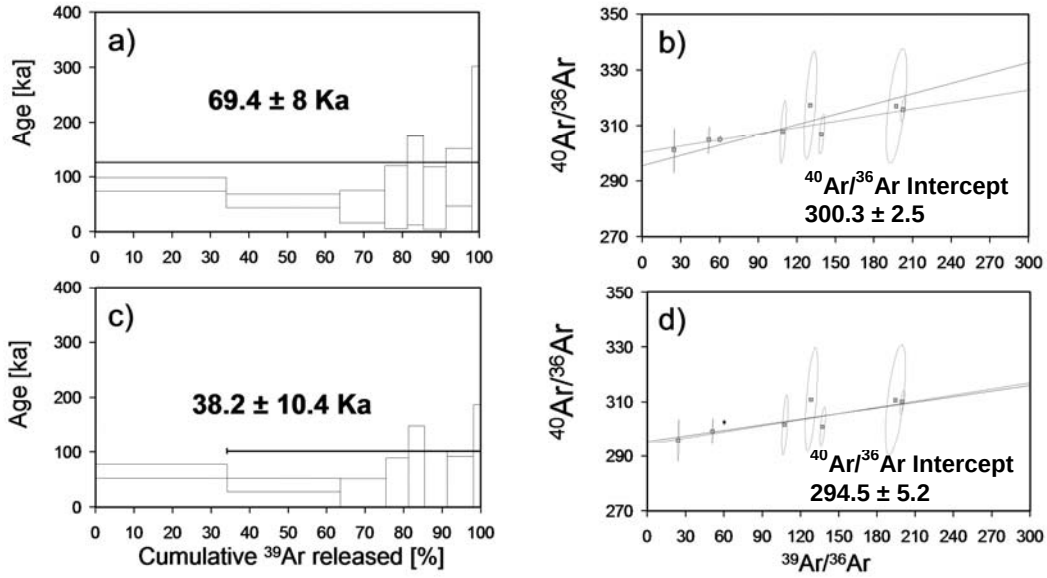

Fig. 13: Measurement of a groundmass from a basalt from Mt Etnea (sample location 37°50'59.49"N, 14°50'18.89"E, see samples SI28, SI29 and SI41 in Blard et al., 2005). The sample was dated by K-Ar as 33 ± 2 ka by Blard et al. (2005). The upper diagrams show plateau (a) and isochron (b) before correction for intensity dependent fractionation while the lower diagrams (c) + (d) show the same after correction. Errors are 1 sigma. Figures (b) and (d) show two isochrones as ArArCALC calculates one isochrone fit through the ordinate intercept of $^{40}Ar/^{36}Ar$=295.5 and another isochron based on a true best fit through the selected data points. In Figures (b) and (d) the value for the best fit $^{40}Ar/^{36}Ar$ intercept is given.

Figure 13 shows the effect of applying this intensity-dependent fractionation correction on a young sample. A basalt groundmass sample from Mt. Etna, dated by K-Ar 33 ± 2 ka (Blard et al., 2005), was used for this experiment. The discrimination correction based on the $^{40}Ar/^{36}Ar$ of one pipette volume of air reference gas yields a reasonably well-developed plateau (Figure 13(a)), but the $^{40}Ar/^{36}Ar$ isochron intercept of 300.3 ± 2.3 is not air composition (Figure 13(b)). Applying the intensity-dependent mass discrimination factor on every heating step drastically changes the plateau age from 69.4 ± 8.0 ka to 38 ± 10.4 ka (Figure 13(c)) bringing it close to the already obtained age from Blard et al. (2005).

3.6 Sensitivity

The sensitivity of the system was measured using unirradiated aliquots of HD-B1 assuming a radiogenic ^{40}Ar concentration of 7.536 ± 0.104 nl/g or $3.364*10^{-10}$ mol/g from Hess and Lippolt (1994). The measurements were corrected for blank and mass discrimination and plotted for radiogenic ^{40}Ar content against signal intensity (Figure 14) and shown in Table 1.

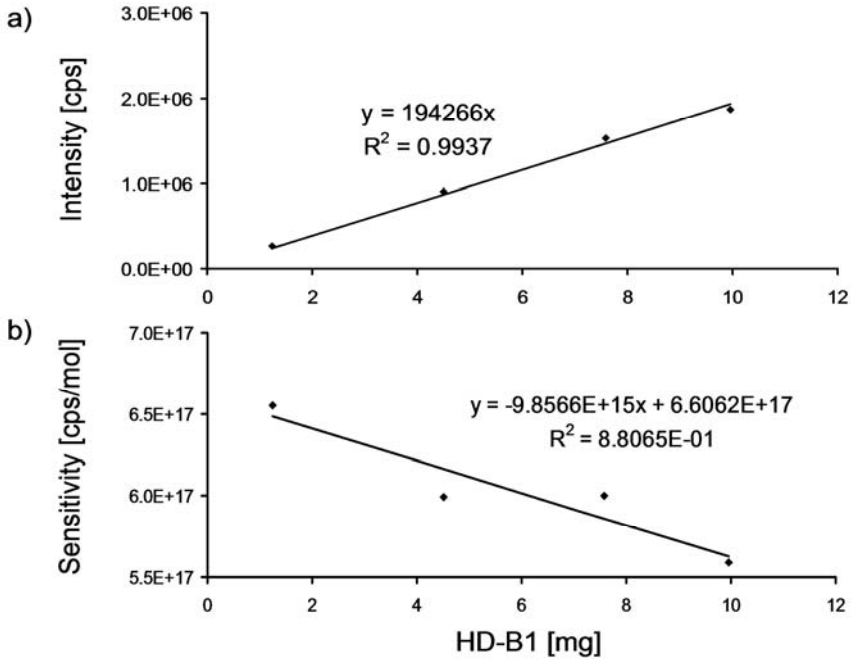

Fig. 14: Plot of intensity against mass of HD-B1 biotite (Hess & Lippolt, 1994) (a) and calculated sensitivity against used HD-B1 biotite (b). Although intensity correlates linearly, sensitivity is still a function of amount of sample used.

Standard	40Ar* ± 1SD (cps)		Sample weight (mg)	40Ar* ± 1SD (in cps/g)		Sensitivity ± 1SD using 40Ar* content from Hess and Lipopolt(1994) (mol/cps)		error %
1	273381	429	1.24	220468548	345968	1.526E-18	2.148E-20	1.4%
2	906834	543	4.5	201518667	120667	1.669E-18	2.337E-20	1.4%
3	1530466	767	7.58	201908443	101187	1.666E-18	2.332E-20	1.4%
4	1870003	846	9.95	187940000	85025	1.790E-18	2.505E-20	1.4%
					Average:	**1.663E-18**	**1.080E-19**	**6.5%**

Table 1: Sensitivity data for the ^{40}Ar signal of non irradiated HD-B1 biotite samples. To convert the sensitivity from cps/mol into A/mol the charge of a single charged ion of $1.602x10^{-19}$ Coulomb (elementary charge, National Institute of Standards and Technology, USA) was used.

This experiment yields a sensitivity of $6.033x10^{17}$ cps/mol or 0.09664 A/mol (±6.6%, 1 sigma). Although the intensity response to sample size linearly correlated (Figure 14 (a)) the calculated sensitivity decreases with the amount of sample (Figure 14 (b)) showing the effect of multiplier dead time. Increasing sensitivity causes a non-linear correlation of yielded intensity with sample amount but due to the low number of measurements this is not evident in the data.

3.7 Intercalibration with a MAP 215-50 sector magnet mass spectrometer

The noble gas laboratory at the Vrije Universiteit Amsterdam is also equipped with a MAP 215-50 magnetic sector mass spectrometer with a discrete dynode Balzers multiplier (SEV217) detector for $^{40}Ar/^{39}Ar$ analyses (Wijbrans et al., 1995). This allows a direct comparison between a magnetic sector instrument and a quadrupole instrument. For this purpose a series of the in-house standard DRA-1 sanidine was compared on both instruments and air reference gas was monitored on both systems over longer periods of time.

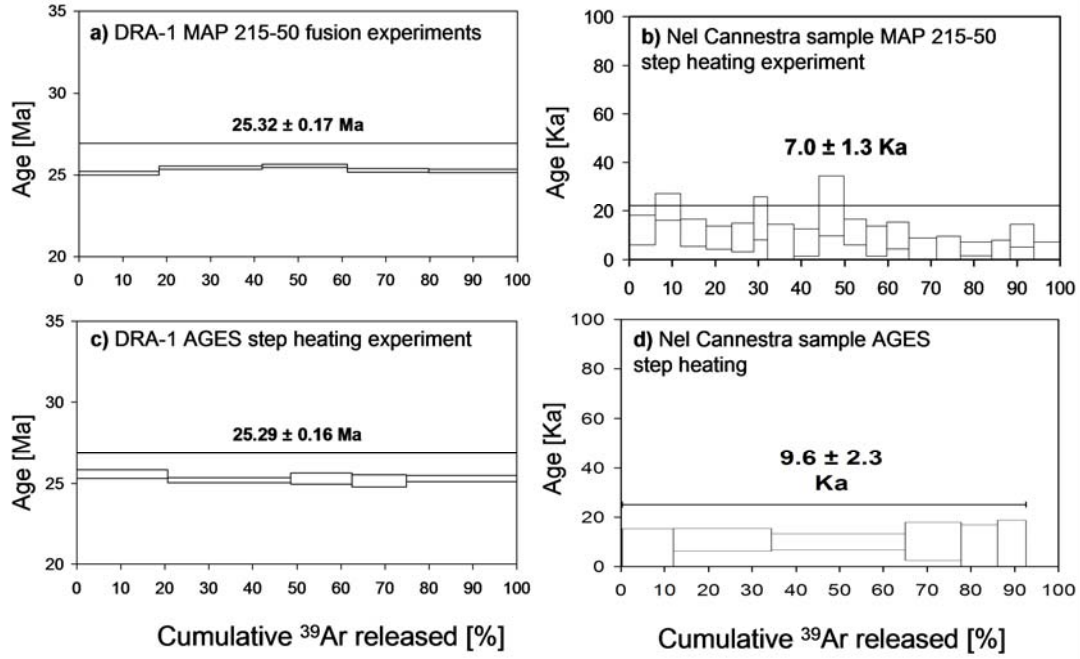

Fig. 15: Comparison between a single fusion experiment on the MAP 215-50 (a) and a step heating experiment on the quadrupole line (c) of DRA-1. J-factors were determined separately on each instrument. On the right side is a similar comparison for the young basaltic groundmass sample from Stromboli, single fusion experiment on the MAP 215-50 (b) step heating experiment on the quadrupole line (d). In this experiment J-factors were determined on the magnetic sector instrument only. Errors are 1 sigma.

In a first attempt, three DRA-1 samples were analysed. Two were used to bracketas flux monitors, one was treated as unknown. On the MAP 215-50 replicate multi-grain fusion experiments were performed with ~5 grains per fusion using a CO_2 laser. On the QMS an incremental heating experiment was performed on ~15 grains using the furnace. Figures 15 (a) and (c) for the MAP and the AGES respectively shows that both measurements yield identical ages. Analytical uncertainties of the QMS system are slightly higher for single measurements because of larger blank uncertainties. The same experiment was performed on young basaltic groundmass from the Nel Cannestra flow, Stromboli (Figures 15 (b) and (d) for the MAP and the

AGES respectively). Within uncertainty the two ages overlap. The superior sensitivity of the MAP 215-50 allows for many more steps in that experiment when compared to the AGES.

To compare the stability of both systems the measured $^{40}Ar/^{36}Ar$ of air reference gas are shown in Figure 9. The pipettes on both systems are of identical design so a reasonable comparison can be made showing a $^{40}Ar/^{36}Ar$ for the quadrupole system of 257.9 ± 1.3 (n=34 since July 2006) and for the magnetic sector instrument 293.1 ± 3.3 (n=739 since beginning of 2007). A sensitivity test using HD-B1 on the sector instrument was compared to the test on the quadrupole instrument (Table 1). The MAP 215-50 achieved a sensitivity of 2.86723 A/mol using the laser extraction part of the line, 30 times higher then the 0.09664 A/mol (Table 1) of the furnace section of the QMS.

3.8 Difficult samples

Figure 16 shows two samples which were particularly difficult to date.

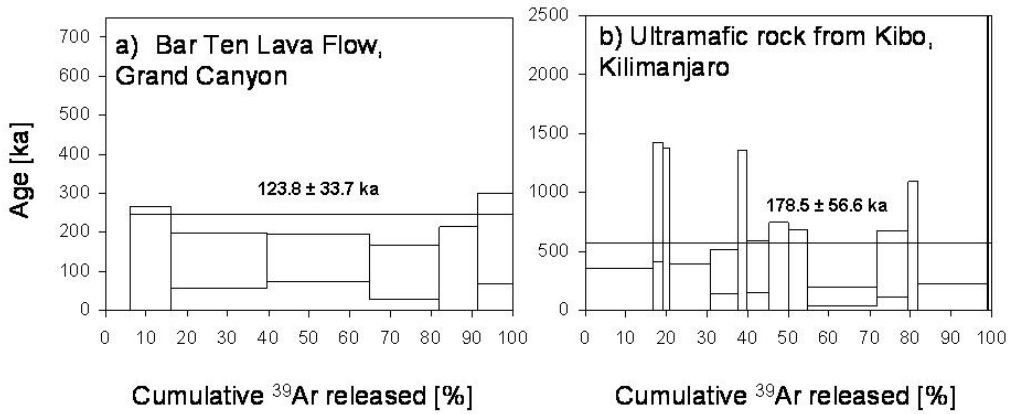

Fig. 16: Two cases of problematic ages. (a) Bar Ten lava flow, Grand Canyon, USA. This sample yielded less than 1% of radiogenic ^{40}Ar but 20 times that amount of trapped ^{40}Ar. (b) Ultramafic lava flow Kibo, Kilimanjaro, Tanzania. This sample had a ratio of atmospheric ^{40}Ar to radiogenic ^{40}Ar of 30 or even higher.

The Bar Ten lava flow in the western Grand Canyon, Arizona (USA) was analysed with different geochronological methods (88 ± 6 ka, cosmogenic ^{3}He Fenton et al., 2001; 108 ± 29 ka,

thermoluminescence, Holmes et al., 1978) but none yielded ages of satisfactory precision or accuracy. An age determination using the AGES yielded similar results (Figure 16 (a)). Ultramafic rocks low in potassium are similarly hard to analyse. One of a series of samples from Kibo (Kilimanjaro, Tanzania; age obtained on one of the samples discussed in Schimmelpfennig et al., 2011) also yielded a surprisingly high uncertainty compared to the normal performance of the AGES in this age range (Figure 16 (b)). Both samples share one important similarities: low potassium concentrations (K_2O less than 1 wt%) and a low content in radiogenic ^{40}Ar compared to either trapped argon (Bar Ten) or blank (Kibo).

3.9 Comparison to argon isotope measurements on other quadrupole systems

Rouchon et al. (2008) were the first to describe a quadrupole mass spectrometer fitted with an electron multiplier for argon isotopes analyses. The system was developed for non-spiked quantitative ^{40}Ar and $^{40}Ar/^{36}Ar$ measurements in minerals, calibrated and validated against several international geochronological standards. It is a single filter instrument with many characteristics similar to those of the triple filter quadrupole mass spectrometer used in our study. Peak shapes are asymmetric on both instruments and show the same tip at peak centre and a tail before the slope towards higher m/z although the data collection procedure of Rouchon et al. (2008) is able to work around this tailing effect. On the triple filter instrument used in our study peak tops are much flatter and more stable allowing measurements over an interval of 0.3 m/z over the peak. The measured $^{40}Ar/^{36}Ar$ ratios for air composition for both instruments are in the same range. In this study the ratios of air reference gas measurements of 257.9 ± 1.3 for $^{40}Ar/^{36}Ar$ that were obtained at low intensity (Figure 10 (a)) are very similar to the value of 262.5 ± 0.36 obtained by Rouchon et al. (2008). Both quadrupole instruments show also much better stability over long timescales (Rouchon et al., 2008 and Figure 9) compared to e.g. the MAP 215-50 instrument at the VU Amsterdam.

However, while Rouchon et al. (2008) use their quadrupole instrument to determine absolute amounts of radiogenic ^{40}Ar after the nonspiked Cassignol-Gillot technique (Cassignol & Gillot, 1982), in this study the $^{40}Ar/^{39}Ar$ incremental heating technique is used, which only utilizes isotope ratios. This results in very distinct approach to assessing the fractionation behaviour of the quadrupole mass spectrometers. Rouchon et al. (2008) measure an air reference gas sample of similar intensity just after the mineral sample to measure the fractionation behaviour of the

instrument close to time of sample measurement. In our study a diluted air reference gas series is used to characterize the fractionation behaviour over an intensity range at intervals including several sample measurements. Also the approach in this study of measuring several points overpeak intervals for most isotopes rather than over a single point helps to counter noise effects at low intensities.

4. Conclusions

The new quadrupole mass spectrometer system shows a long term stable performance. Peak shapes and positions have been stable for more than two years without the need for major readjustments. Broad peak tops make measurements less prone to peak shifting when compared to magnetic sector mass spectrometers and choosing a greater measurement interval instead of a single point on the peaks of the more crucial isotopes improves counting statistics as does cycling over the peak several times. This is supported by the reproducibility of air reference measurements and standards.

While dead time effects on the single channel electron multiplier when exposed to high intensity beams are predictable and accounted for, they need to be monitored regularly to prevent erroneous corrections for multiplier dead time over long periods.

Blank control is achieved by baking out the furnace tube at a much higher temperature than used for fusion of samples. This eliminates the sample residue component of the blank leaving only background and air components. The background component is constant so the air component is easily taken into account.

Intercalibration with a magnetic sector instrument shows greater stability and a very reasonable sensitivity suitable for $^{40}Ar/^{39}Ar$ dating of samples as young as the Holocene. In summary, a triple filter quadrupole mass spectrometer can serve as an economical alternative for magnetic sector (multi-collector) instruments when small sample size or very high precision measurements are not first priority.

Earth is under constant bombardment by cosmic radiation

IV. Theory and application of *in situ* Terrestrial Cosmogenic Nuclides

Introduction

Research history of *in situ* Terrestrial Cosmogenic Nuclides (furthermore TCNs) has been summarized in the introduction of this thesis. The following review focuses on the cosmogenic noble gas ^{3}He and to lesser extent ^{21}Ne. For a full review of TCN systematics for all nuclides (stable and radionuclides), the reader is referred to Gosse and Phillips (2001), Niedermann (2002), Lifton et al. (2008) and Dunai (2010). This chapter is structured in three main parts. In the first section, the principles of *in situ* TCN application are summarized. Section two provides application and methodological background of noble gas TCNs. Finally section three focuses on the measurement of in situ cosmogenic ^{3}He at SUERC and in this thesis**.**

1. Principle of Cosmogenic Nuclide applications

1.1 Basic concepts

In situ TCNs are continuously produced in the uppermost layer of the Earth's surface by interactions of cosmic rays with matter. Upon approaching the Earth, the primary cosmic ray particles (predominantly protons) induce a nuclear reaction cascade in the upper atmosphere producing secondary particles. Cosmic ray flux decreases rapidly with depth in soils and rocks, with more than 99% of the TCNs formed in the uppermost 3 metres of the Earth (Gosse & Phillips, 2001).

Due to the interaction of primary protons and secondary neutrons with the Earth's magnetic field and the atmosphere, the cosmic ray flux varies with latitude and altitude. Production rates for each TCN vary, but are generally between a few atoms and several hundred atoms per gram of rock per year. For TCNs to be useful, their natural background concentration must be low in geological material not exposed to cosmic rays. This limits the commonly used TCNs to ^{3}He, ^{21}Ne (stable, noble gas isotopes), ^{10}Be, ^{26}Al and ^{36}Cl (radionuclides with half-lives of 1.5, 0.7 and 0.3 Myr, respectively).

1.2 Terrestrial Cosmogenic Nuclide production

1.2.1 Production processes

At the top of the Earth's atmosphere, high energy cosmic rays are composed of ~87% protons, ~12% α-particles and minor contributions from heavier nuclei, electrons and positrons (Masarik & Reedy, 1995). The energies of the cosmic rays range from a few MeV up to ~10^{20}eV (e.g., Simpson, 1983). Upon entering the atmosphere, cosmic ray particles react with air molecules in a process predominantly governed by spallation (the sputtering off of few nucleons from the target nucleus). In this process a cascade of secondary particles (having energies between 0.1 and 500 MeV) is produced as cosmic rays approach the Earth surface, changing the composition from proton-dominated to neutron-dominated flux (Figure 1; Lal and Peters, 1969).

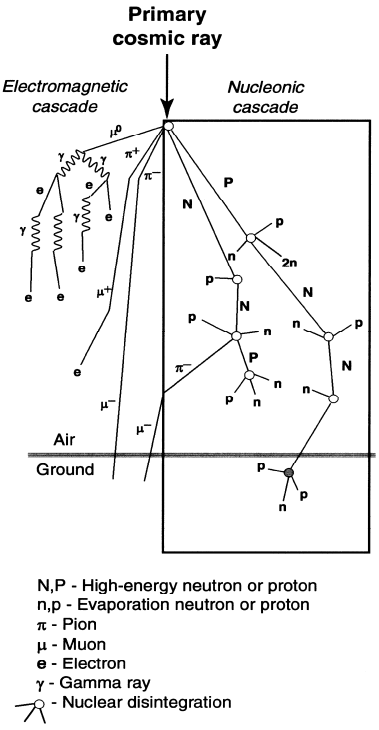

Fig. 1: Reactions of primary galactic and solar protons with the atmosphere and subsequent particle cascades (adapted from Simpson, 2000).

The secondary neutron species generated in the atmosphere can be divided into three types. So called fast neutrons have energies greater than 10 MeV and cause spallation reactions by

collision with atomic nuclei. When neutrons are slowed down (energies < 5 MeV), the epithermal and thermal neutrons can be captured by nuclei having large cross-sections. Thermal neutrons (~0.025 eV) are the main cause for capture reactions as their energy resembles the thermal vibration energy of target matrices (Gosse & Phillips, 2001 and references therein).

Muons occur in two species important for TCN production. Fast muons can cause spallation reactions similar to fast neutrons due to their high energy. Slow negative muons can be captured in the electron shells of nuclei and cause the production of secondary neutrons from the nuclei.

The main *in situ* TCN production processes are spallation, thermal neutron capture, negative muon capture and fast muon reactions. However, due to their low interaction with matter muons are at least an order of magnitude less important for *in situ* TCN production at the surface but their reaction rate decreases only slowly with depth compared to nucleons and therefore they produce more TCNs relative to other particles at great depths (Gosse & Phillips, 2001 and references therein). Spallation is the single most important production process for cosmogenic ^{3}He and ^{21}Ne (Niedermann, 2002) at Earth's surface.

1.2.2 Exposure age calculation

Given no erosion or burial of material exposed at the Earth' surface, TCNs accumulate over time according to Eq. 1.1:

$$C_{\cos} = P_{cos} \times t_{\exp} \qquad (1.1)$$

where C_{cos} is the measured concentration of the cosmogenic nuclide in the material, P_{cos} the production rate of the nuclide in the material and t_{exp} the exposure time of the material to secondary cosmic radiation.

Equation (2.1) is true for stable TCNs (^{3}He and ^{21}Ne); for the radionuclides (e.g, ^{10}Be, ^{26}Al and ^{36}Cl) equation (1.1) needs to be modified to:

$$C_{\cos} = (P_{\cos} - D_{\cos}) \times t_{\exp} \qquad (1.2)$$

where D_{cos} is the decay rate of the examined radionuclide. Over time, equilibrium will be reached between production and decay of the radionuclide of interest.

Burial and erosion of a surface decrease the apparent production rate and thus the concentration of the TCN. While constant erosion can be treated like decay of the TCN, burial is more complicated to assess, especially when it is not apparent at the site. To compensate for burial and erosion, equation 2.2 needs to be modified to:

$$C_{\cos} = (P_{\cos} - D_{\cos} - B(t_{bur}, d_{bur}) - E(t_{ero}, d_{ero})) \times t_{\exp} \qquad (1.3)$$

B (burial) and E (erosion) are functions of the duration of the respective process (t) and the depth of burial or erosion (d). For erosion average erosion rates can often be estimated from the preservation of the sample site. The duration and speed of burial is, however, more difficult to assess**.**

1.2.3 Spatial and temporal variation in cosmogenic nuclide production

In space, the flux and energy spectrum of cosmic rays is isotropic. Upon approaching the Earth, the flux and energy spectrum is modified and affected by the Earth magnetic field and adsorption in the atmosphere. This results in distinct variations in cosmic ray intensity and energy flux (and thus TCN production rates) at different positions on Earth (altitude, latitude and longitude).

Geomagnetic field variation

The geomagnetic field deflects incoming cosmic rays. Only rays exceeding a critical energy (cut-off rigidity, P_c) can reach the Earth's surface. In a dipole field, the cut off rigidity is defined as:

$$P_c = \frac{M\mu_0 c}{16\pi R^2} \cos^4 \lambda \qquad (1.4, \text{eq. 5 in Webber (1962)})$$

where M is the dipole moment, c the velocity of light, μ_0 the magnetic permeability of free space (1.256637×10^{-6} $N \times A^{-2}$), R the radius of the Earth (6371 km) and λ the geomagnetic latitude. Following equation 1.4 cut off rigidity increases from polar regions towards the equator and accordingly cosmic ray flux decreases. At latitudes >60°, the cut-off rigidity drops below the energy level of inbound cosmic particles resulting in a constant cosmic ray flux at latitudes >60°.

The geomagnetic field also changes its strength and geometry over time, and not necessarily in an easily predictable manner. Short term exposure histories up to approximately 10-20 ka (Dunai, 2001) are influenced to a great extent by changes in the local geomagnetic field and require detailed assessment of the geomagnetic field parameters. For long term exposure histories, geomagnetic variations average out and the magnetic field can be approximated by a global axial dipole field (Dunai, 2001; Masarik et al, 2001). To date the most detailed long term geomagnetic records span the last 2 Ma (Valet et al., 2005; Ziegler et al., 2011). Short term records are used depending on location and availability.

Atmospheric cosmic ray attenuation

Neutrons are attenuated by the atmosphere and on a first order the resulting decrease in neutron flux follows an exponential relationship:

$$N = N_0 \times e^{-z/\Lambda} \qquad \text{(1.5, e.g. Lal (1991))}$$

where N and N_0 are the neutron fluxes with and without atmospheric attenuation or at the location of the observer and at the top of the atmosphere respectively; z is the atmospheric depth and Λ is the attenuation length (both in g/cm^2). Λ is not a constant, but changes with latitude and to lesser extend with altitude (Lal, 1991). When passing through the atmosphere secondary cosmic rays continuously loose kinetic energy and the energy spectrum changes from high energies at the top of the atmosphere to lower energies towards the ground. For atmospheric conditions it is common practice to use the model of a standard atmosphere where the pressure, p, at sampling altitude, h, at a sampling point is:

$$p = p_0 \left(1 - \frac{\beta_0 h}{T_0}\right)^{\frac{g_0}{R_d \beta_0}} \qquad \text{(1.6; Iribane \& Godson, 1992)}$$

with p_0 being the mean annual pressure at sea level (standard pressure 1013.25 mbar), β_0 the temperature decrease with elevation (6.5 K/km), R_d the gas constant (287.05 J/kg/K), T_0 the temperature in Kelvin at sea level (dependent on the climatic region) and g_0 the standard sea level value of the acceleration due to gravity (9.80665 m/s^2). Recently, however, it has been shown that deviations from these conditions are common and in some cases

have a severe impact on TCN production rates (e.g, the Antarctic Low Pressure System, Stone, 2000). Recent work using artificial targets to measure altitude transects of production rates for cosmogenic ^{3}He and ^{21}Ne (Vermeesch et al., 2009) confirmed the ranges of attenuation lengths in the atmosphere.

Geometry of the surface and surrounding geomorphology

On a near-horizontal surface, the cosmic ray flux arrives uninterrupted from a 360° angle. Depending on the sample's geometry (e.g. inclined surface) and geomorphology of the sample site (e.g. presence of nearby mountains), part of the incoming cosmic ray flux is blocked out, resulting in lower TCN production rates. Consequently, this needs to be corrected for using the sample site dip angle of the surface and the horizon (Equation (1.7); eq. 1 in Vermeesch, 2007; Balco et al., 2008):

$$S_t = 1 - \int_0^{2\pi} \frac{\sin\left(h(\alpha)\right)^{3.5}}{2\pi} d\alpha \qquad (1.7)$$

where S_t is the topographic shielding factor, h(α) is the height h (in degrees or radians) of the horizon in the direction of azimuth α or the slope of the sample surface, whichever is greater.

Sample geometry corrections have been discussed with models including thin quadratic columns, hemispheric bodies, cubes and pyramids, all resting on a flat surface (Masarik & Wieler, 2003) and using natural targets (Lal & Chen, 2005). Self-shielding occurs in a similar way as attenuation in the atmosphere with materials having specific attenuation lengths (see Equation 1.5). While numeric simulations show a perturbed and rather flat neutron flux profile at shallow depths (Masarik & Reedy, 1995), strictly exponential self-shielding corrections without a surface layer of constant production rate are also in use (Vermeesch, 2007; Gosse & Phillips, 2001). A common practice is to ignore the shielding correction when sampling at the immediate surface (less than 10-12 g/cm^2; Masarik & Reedy, 1995) or low geomorphologic shielding (less than 15°; Dunne et al., 1999) as the effects of the shielding correction would have negligible effects when compared to the uncertainties of the final results.

1.2.4 Scaling of cosmic ray flux

In order to compare TCN concentration data from different locations on Earth scaling models are necessary to recalculate datasets to values at a reference site, commonly at sea level and high latitude (Gosse & Phillips, 2001; Niedermann, 2002; Lifton et al., 2008). These models are based on neutron global flux surveys and consist of datasets for lateral and vertical profiles.The first commonly used scaling model applicable to all altitudes and latitudes by Lal (1991) was a widely accepted standard method to convert production rates from one location to another. This method is based on third-order polynomials in altitude fitted to nuclear disintegration rates in the atmosphere (Lal and Peters 1968), which are given for geomagnetic latitudes from 0° to 60° with a 10° spacing. The production rate of any spallation-produced nuclide in a surface rock is expected to be proportional to the nuclear disintegration rate, so if the production rate at one location is known it can be scaled to any location.

Recognizing differences of atmospheric conditions from the standard atmosphere Stone (2000) improved this scaling model by using local air pressure rather than the altitude-pressure relationship of the standard atmosphere. Production by muons is also taken into account separately in this model.

Lal's (1991) scaling method was challenged by Dunai (2000), who claimed that some of the approximations inherent in Lal's procedure may lead to large systematic errors, especially for high altitudes and for latitudes around 30°. Among these approximations are the description of the geomagnetic field by an axial dipole and the extrapolation of attenuation path lengths from high to low altitudes. A different scaling method was proposed that avoided all these critical approximations. To include the non-dipole components, Dunai (2000) used the geomagnetic field inclination instead of the geomagnetic latitude as the parameter describing the field and then derives the dependence of the neutron flux on latitude and altitude by fitting two separate five-parameter sigmoidal functions to the observational data.

According to Desilets and Zreda (2001), both methods have shortcomings as they do not adequately appreciate the influence of effects such as energy-dependence of the nucleon attenuation length, energy sensitivity and background correction of instruments used for cosmic ray monitoring, parameters of the real geomagnetic field, and solar activity. Desilets and Zreda (2003) and Lifton et al. (2005) address these points by including attenuation models for single

cosmic particle species, more detailed geomagnetic models and solar activity data in their scaling models.

1.2.5 Sources of uncertainty

Analytic techniques for TCN applications are very refined and rarely a major source of uncertainty except for samples with short exposure histories or low TCN contents. Scaling models contribute most of the uncertainties associated with TCN results (Gosse & Phillips, 2001). The two major factors are the disagreement between production rates for individual TCNs and the uncertainties of existing scaling models. They alone account for most of the 5 – 10 % uncertainty common to exposure age dating.

2. Applications and methodology for *in situ* noble gas TCNs

2.1 Characteristics of noble gas TCNs

Stable TCNs (^{3}He, ^{21}Ne) continuously accumulate in surface rocks. When exposure is uninterrupted, they can be used to reconstruct exposure history durations from a few hundreds (Kurz et al., 1990) to millions of years (Schäfer et al., 1999). ^{3}He and ^{21}Ne are retained quantitatively in olivine and pyroxene crystals, ^{3}He in garnet (Gayer et al., 2004; Dunai & Roselieb, 1996) and ^{21}Ne in quartz crystals (Shuster & Farley, 2005), phenocrysts that are widely available in independently datable host rocks (e.g. ^{40}Ar/^{39}Ar on basalt flows). ^{3}He has the highest production rate of all TCNs (103 atoms/g/y in olivine; Dunai, 2001; 116 – 135 atoms/g/y depending on scaling model in olivine and pyroxene; Goehring et al., 2010) and has been widely used for production rate determinations (Goehring et al., 2010; Niedermann, 2002 and references therein). It was successfully analysed in an artificial quartz sample after one year of exposure (Vermeesch et al., 2009).

^{3}He is produced mainly by spallation reactions on oxygen, magnesium, silicon, calcium, iron and aluminium as well as by neutron capture of ^{6}Li. Muon capture reactions become important only at depths greater than a few meters (Gosse & Phillips, 2001). The limit on the application of cosmogenic ^{3}He is the contribution of non-cosmogenic helium components in sample material. The first and easiest component to determine is the magmatic helium trapped as inclusions in volcanic minerals.

^{3}He is also produced by the neutron capture reaction

$^{6}Li(n,\alpha)^{3}H$

which can be triggered by neutrons generated by α-reactions in nuclei (Dunai et al., 2007; Farley et al., 2006)).

^{4}He is produced in abundance by α decay of U, Th and Sm. The ^{4}He content within the sample has to be corrected for implanted and nucleogenic ^{4}He and this correction increases with sample age. (Dunai & Wijbrans, 2000; Williams et al., 2005; Farley et al., 2006; Blard & Farley, 2008). If exposure age and helium closure age for a sample are the same, then the ratio of the concentrations of cosmogenic ^{3}He and radiogenic ^{4}He is the same as the ratio of their production rates in time and can be used for correction (Blard & Farley, 2008).

2.2 Sampling strategies

For surface production rate and exposure studies one wants to sample the immediate surface of the studied rock in order to minimize the self shielding-correction. A flat surface is preferable in order to avoid correction for sample geometry. Erosion and ash cover can be avoided by sampling local geomorphological highs. They are less prone to a history with cover and might be more resistant to erosion.

Sample preparation for cosmogenic ^{3}He measurements only involves crushing the whole rock sample, sieving out the desired grain size fraction and mineral separation using density separation and picking of suitable phenocrysts under a binocular microscope. This is followed by superficial cleaning of the sample of weathered rims or adherent grains either by simple rinsing or treatment with dilute acid. In order to avoid implantation effects from the basaltic groundmass the outer 20 to 25 µm of the crystals can be etched away (Gayer et al., 2004; Farley et al., 1996).

2.3 Measurement routine

Normally an *in vacuo* crushing step is applied in order to extract magmatic helium from the the crystal. It is important not to over crush the sample and liberate cosmogenic ^{3}He from the crystal matrix (Blard et al., 2006; Scarsi, 2000; Hilton et al., 1993). The observed effects are small, however, and intensive crushing is necessary to observe this cosmogenic ^{3}He release (Blard et al., 2008).

Extraction of the residual magmatic and cosmogenic helium is done by heating using either furnace or laser heating (Foeken et al., 2006), often in several heating steps. The measurement is performed on a magnetic sector mass spectrometer with enough resolution to separate the mass peak of ^{3}He from that of HD. Cosmogenic ^{3}He ($^3He_{cos}$) is calculated from:

$$^3He_{cos}=^4He_{melt}((^3He/^4He)_{melt}-(^3He/^4He)_{crush}) \qquad (2.1, \text{Williams et al., 2005})$$

where $^4He_{melt}$ is the concentration of ^{4}He in the melt, and the isotopic composition of helium in the crushing step is $(^3He/^4He)_{crush}$ and in the fusion step $(^3He/^4He)_{melt}$. When necessary, $^4He_{melt}$ has to be corrected for implanted and ingrown ^{4}He as mentioned earlier. In the presence of nucleogenic ^{3}He the measured $^3He_{cos}$ needs to be corrected.

An alternative isochron method proposed by Blard and Pik (2008) can omit the crushing step as it uses a plot of the isotopic composition of the fusion step $(^3He/^4He)_{melt}$ against the inverse of the concentration of ^{4}He in the fusion step $^4He_{melt}$. When done for several aliquots of one sample the resulting points are aligned in a linear function and the slope of this function, $((^3He/^4He)_{melt}/^4He_{melt})$ is the concentration of cosmogenic ^{3}He in the sample. Here implanted and ingrown helium affect the slope of the isochron and need to be corrected for accordingly. The isochron method actually yields the non cosmogenic helium composition of the sample as intercept of the isochron with the ordinate of the plot.

3. *In situ* cosmogenic ^{3}He methodology and approach in this work

Sampling and sample preparation methods used in this study are described in Chapter II. Densities of the samples were determined by simple hydrostatic weighing of uncrushed sample blocks of at least 15 to 20 cm^3 in water. These blocks incorporated and therefore accounted for vesicles and their filling material. The irregular shape of the phenocrysts makes a numerical correction for implanted helium quite difficult. Therefore we chose to etch away the outermost rim of the crystals in a solution of 10% HNO_3 and 10% HF until enough sample weight was lost (in our case 40% for an average grain size of 375 µm) to safely assume the outermost 20 µm to be removed avoiding ^{4}He implanted from the matrix influencing the measurement (Farley et al.,

1996). During this process the acid bath was manually shaken to ensure a homogeneous exposure of all grain surfaces to the acid.

Magmatic was released by a manual hydraulic crushing device (Stuart et al., 1995). The blanks for both helium isotopes in the crushing steps were in the range of a few permil of the sample helium signals and were omitted in the later calculation. An 808 nm diode laser (Foeken et al., 2006) was used for the melting. The laser was linked to the same mass spectrometer line as the crushing device. The laser does not couple with partly transparent minerals like olivine. In this study basaltic groundmass and pyroxene from a recent eruption from Merapi was completely melted and ground to a powder before mixing with the olivine sample to facilitate melting. It was practically devoid of ^{3}He and had a low ^{4}He concentration even before the melting and grinding treatment. Complete melting of the olivine crystals was achieved with the diode laser after being mixed well with the degassed pyroxene. An electron multiplier and a Faraday cup were used for ^{3}He and ^{4}He detection respectively. Blanks for these measurements had intensities of 0.7 ± 0.5 cps and 0.11 ± 0.03 mV respectively and represented less than 5% of the total signal in an average sample. They were accounted for in the calculations. Drift and fractionation of the mass spectrometer were monitored using a helium standard from a manometrically calibrated gas bottle.

After measurement the raw data was regressed to the point of inlet time and then corrected for blanks. Then the cosmogenic ^{3}He concentration was calculated according to Equation (2.1) and corrected for self shielding and altitude using CosmoCalc 1.7 (Vermeesch, 2007) and the scaling factors of Dunai (2001) combined with the geomagnetic record from Guyodo and Valet (1999).

Volcanic landscape of Fuerteventura

V. Volcanic and exposure geochronology from Fuerteventura

Introduction

In young basalts the non-radiogenic argon component is large compared to the radiogenic $^{40}Ar^{*}$ fraction. Therefore, corrections for non-radiogenic argon - often made under the assumption of atmospheric argon composition – are critical for obtaining reliable ages and ultimately depend on the accuracy and precision of the measured ^{36}Ar signal.

Low potassium content results in low radiogenic $^{40}Ar^{*}$, and high calcium contents result in production of excess undesired argon isotopes during irradiation in the reactor. Further, alteration can have adverse effects on the $^{40}Ar/^{39}Ar$ method.

Numerous studies have explored using the K-Ar method (Gillot et al., 1992, Guillou et al., 1998, Lanphere, 2000, Quidelleur et al., 2001, Guillou et al., 2004) and the $^{40}Ar/^{39}Ar$ method (Mertz & Renne, 1995, Renne et al., 1997 and references therein, Lanphere, 2000, Sharp & Renne, 2005, Calvert et al., 2006, Wilson et al., 2007, Schneider et al., 2009) for dating Holocene and historic volcanic rocks. Most of these studies utilize mineral phases with high potassium contents and/or large sample amounts (sometimes more than 10 g) to achieve usable high analytical precision. Obtaining potassium rich material is, however, not always possible. In addition, recent studies have refined the atmospheric composition of argon (Lee et al., 2006) that affects age calculations at the young end of the spectrum (Valkiers et al., 2010; Renne et al., 2009) and so requires a re-evaluation of young data and how they are calculated. As in the case of radiogenic $^{40}Ar^{*}$, cosmogenic ^{3}He accumulates with time in a sample making it easier to detect in older material. Advantages of the cosmogenic ^{3}He method compared to the $^{40}Ar/^{39}Ar$ method are that lower amounts of material are generally required for sample preparation and the smaller natural background of ^{3}He compared to ^{40}Ar in many samples. The lower natural backgrounds also allow cosmogenic ^{3}He to be used for determining the age of younger samples than commonly dated with $^{40}Ar/^{39}Ar$.

Disadvantages compared to the $^{40}Ar/^{39}Ar$ method arise mainly from the less precise constraints on the production processes of cosmogenic ^{3}He. While for $^{40}Ar/^{39}Ar$ most process related constants are known very precisely and most of the uncertainty is derived from trapped argon or in some instances blanks. Most of the uncertainty for cosmogenic ^{3}He most comes from the uncertainty about the neutron flux constraints and related production rates. By the nature of the method the

application is bound to rock surfaces exposed to cosmic radiation. Furthermore, cover and erosion limit the use of ^{3}He for age determination.

Both methods, ^{40}Ar/^{39}Ar and cosmogenic ^{3}He, are viable tools for cross calibrating young lava flows as their application ranges overlap in the Upper Pleistocene. This chapter presents and discusses both argon incremental heating and cosmogenic ^{3}He exposure age data for samples gathered on Fuerteventura.

We present new ^{40}Ar/^{39}Ar incremental heating data obtained from late Pleistocene alkaline basalt lavas from Fuerteventura using the quadrupole mass spectrometer and furnace extraction line described in Chapter III. The youngest reported K-Ar age on Fuerteventura volcanic rocks is 400 ± 100 ka (Coello et al., 1992) while correlation of volcanic rocks with young sediments show Holocene ages (Coello et al., 1999). Our data reveal ages for some of the Series IV lava flows down to 52.7 ± 21.6 ka. Using a modified procedure for better coupling a diode laser with semi transparent minerals, *in situ* cosmogenic ^{3}He exposure dating of olivines yields exposure ages down to 65.2 ± 4.2 ka for these young flows. However, the data reported in this study are not sufficiently precise to yield meaningful production rates for *in situ* terrestrial cosmogenic ^{3}He.

1. Methodology

The reader is referred to Chapter II for all aspects of sampling and sample treatment for both ^{40}Ar/^{39}Ar geochronology and cosmogenic ^{3}He exposure dating. The measurement routine was used for argon isotope analysis is described in Chapter III.

1.1 ^{40}Ar/^{39}Ar geochronology

Cold blanks of the argon extraction system were stable for ^{36}Ar at 40 cps (~6.7x10^{-17} mol), for ^{37}Ar at 2 cps (~3.3x10^{-18} mol), for ^{38}Ar at 12 cps (~2x10^{-17} mol), for ^{39}Ar at 7 cps (~1.2x10^{-17} mol) and for ^{40}Ar at 14000 cps (~2.3x10^{-14} mol). Hot blanks for argon isotopes range for 700 ºC to 1200 ºC, respectively, from 62 to 125 cps (~2.1x10^{-16} mol) for ^{36}Ar, from 2 to 7 cps (~1.2x10^{-17} mol) for ^{37}Ar, from 10 to 27 cps (~4.5x10^{-17} mol) for ^{38}Ar, from 7 to 15 cps (~2.5x10^{-17} mol) for ^{39}Ar, from 16000 to 35000 cps (~5.8x10^{-14} mol) for ^{40}Ar for 700ºC to 1200ºC. Sample sizes ranged from 250 to 500 mg per analysis.

ArArCALC (version 2.40) (Koppers, 2002) was used to regress intensity data and calculate ^{40}Ar/^{39}Ar plateau ages and isochrons. Isochron intercepts were calculated using a linear fit (York-

2) over the plateau data points. All temperature steps of all replicate experiments were sorted by temperature and plateau and isochron ages were calculated from all data.

The generally accepted criteria for a geologically meaningful plateau age are a plateau over more than 50% of the released ^{39}Ar that includes a reasonable number of heating steps (in our case the minimum requirement was four steps), an isochron for the plateau gas fraction and concordant plateau and isochron ages (Lanphere and Dalrymple, 1978). In addition, we included heating steps in the plateau age only until the mean square weighted deviation (MSWD) was close to, but below 1.5 to further restrict outliers.

To assess the impact of the Steiger and Jäger (1977) recommended value for the atmospheric $^{40}Ar/^{36}Ar$ of 295.5 ± 0.5 derived from data in Nier (1950) versus the value in Lee et al. (2006) of 298.56 ± 0.31 we calculated our plateau ages including mass discrimination and standards based on both values. Plateau and isochron ages were calculated first using the $^{40}Ar/^{36}Ar$ value recommended by Steiger & Jäger (1977) and then using the value reported by Lee et al. (2006). In addition a third set of plateau ages was calculated using the data of Lee et al. (2006) in which we substituted the commonly assumed trapped $^{40}Ar/^{36}Ar$ air ration with the $^{40}Ar/^{36}Ar$ axis intercept value predicted by the isochrones, following Lanphere (2000). Plateau and isochron ages were based on the same set of steps/points wherever possible for each dataset.

As mentioned earlier the main uncertainty in dating young samples is the low amount of radiogenic ^{40}Ar and the corrections needed to calculate this amount. Therefore, we performed variance analysis to assess where in our experimental set-up the biggest improvements can be made to reduce analytical uncertainties.

In order to assess the contributions of all the variables involved in the age calculation process we split the variance analysis in two parts. First the uncertainties propagated into the plateau age were investigated according to equations laid out in Renne et al. (1998) and secondly we assessed the analytical uncertainties in the F_u (or $^{40}Ar^*/^{39}Ar_K$ of the unknown) for individual steps.

For the first part we used equation (1.1) for calculation of a plateau age

$$t = \frac{1}{\lambda}\ln\left[\frac{F_u}{F_{st}}\left(e^{\lambda T}-1\right)+1\right] = \frac{1}{\lambda}\ln[X] \qquad \text{(1.1; 1.9 in Chapter III)}$$

where F_u is the $^{40}Ar^*/^{39}Ar_K$ of the plateau, F_{st} the $^{40}Ar^*/^{39}Ar_K$ ratio of the standard and λ the decay constant of ^{40}K (compare eq. 16 and 17 in Koppers, 2002 and references therein). The error in this

equation is determined using the partial derivatives of each variable: error contributions from decay constant ^{40}K, age of standard, $^{40}Ar^*/^{39}Ar_K$ of the plateau and $^{40}Ar^*/^{39}Ar_K$ of the standard. Partial derivatives for these variables are found in the Appendix C.

$$\sigma_F^2 = \left(\frac{\partial t}{\partial \lambda}\right)^2 \sigma_\lambda^2 + \left(\frac{\partial t}{\partial T}\right)^2 \sigma_{t_{st}}^2 + \left(\frac{\partial t}{\partial F_u}\right)^2 \sigma_{F_u}^2 + \left(\frac{\partial t}{\partial F_{st}}\right)^2 \sigma_{F_{st}}^2 \qquad (1.2)$$

The second step is based on derivation of the analytical solution for the error equation of the age equation (1.3) based on McDougall & Harrison (1999).

$$F = \frac{^{40}Ar}{^{39}Ar_K} = \frac{^{40}Ar_{m'} - 295.5 \times ^{36}Ar_{m'} + 295.5 \times \left[^{36}Ar^{37}Ar\right]_{Ca} \times ^{37}Ar_{m'}}{^{39}Ar_{m'} - \left[^{39}Ar^{37}Ar\right]_{Ca} \times ^{37}Ar_{m'}} - \left[^{40}Ar^{39}Ar\right]_K$$

(1.3; 1.8 in Chapter III)

$^{X}Ar_{m'}$ is the measured signal for isotope X corrected for blank, mass discrimination and ^{37}Ar or ^{39}Ar decay. $[^{36}Ar/^{37}Ar]_{Ca}$, $[^{39}Ar/^{37}Ar]_{Ca}$ and $[^{40}Ar/^{39}Ar]_K$ are correction factors for neutron interference reactions.

For the VUA laboratory this can be converted to

$$F = \frac{\left\{\left(^{40}Ar_m - ^{40}Ar_{bl}\right) - D \times \left(^{36}Ar_m - ^{36}Ar_{bl}\right) + \frac{E \times \left[^{36}Ar^{37}Ar\right]_{Ca} \times \left(^{37}Ar_m - ^{37}Ar_{bl}\right) \times C_{37}}{\frac{0.75E}{D} + 0.25} + \frac{E \times \left[\frac{^{36}Cl}{^{38}Cl}\right]_P \times \lambda_{^{36}Cl} \times t_e \left(^{38}Ar_m - ^{38}Ar_{bl}\right)}{\frac{0.5E}{D} + 0.5}\right\}}{\left\{\frac{\left(^{39}Ar_m - ^{39}Ar_{bl}\right) C_{39}}{\frac{0.25E}{D} + 0.75} - \frac{\left[^{39}Ar^{37}Ar\right]_{Ca} \left(^{37}Ar_m - ^{37}Ar_{bl}\right) C_{37}}{\frac{0.75E}{D} + 0.25}\right\}} - \left[^{40}Ar^{39}Ar\right]_K$$

(1.4; 1.10 in Chapter III)

$^{X}Ar_m$ is the uncorrected measured signal for isotope X. $^{X}Ar_{bl}$ is the measured blank signal for isotope X, D is the $^{40}Ar/^{36}Ar$ ratio measured on air and E is the literature value for the $^{40}Ar/^{36}Ar$ ratio of air. $[^{36}Ar/^{37}Ar]_{Ca}$, $[^{39}Ar/^{37}Ar]_{Ca}$ and $[^{40}Ar/^{39}Ar]_K$ are correction factors for neutron interference reactions. $[^{36}Cl/^{38}Cl]_P$ is the production ratio of the Cl isotopes (from resp. ^{35}Cl and ^{37}Cl, ~316 reported by Roddick, 1983 and 262.8 ± 1.7 and 252.7 ± 1.8 for NaCl and KCl respectively reported by Renne et al., 2008), λ_{36Cl} is decay constant for decay ^{36}Cl to ^{36}Ar and t_e is time elapsed between irradiation and measurement. C_{37} and C_{39} are the correction factors for ^{37}Ar and ^{39}Ar decay and are defined as:

$$C_{37} = \frac{\lambda_{37} \times d \times e^{\lambda_{37} t_e}}{\left(1 - e^{-\lambda_{37} t_e}\right)} \qquad (1.5; 1.11 \text{ in Chapter III})$$

$$C_{39}=\frac{\lambda_{39}\times d\times e^{\lambda_{39}t_e}}{\left(1-e^{-\lambda_{39}t_e}\right)} \qquad (1.6;\ 1.12 \text{ in Chapter III})$$

where λ_{37} and λ_{39} are respectively the decay constants of ^{37}Ar (half life 35.1 d) and ^{39}Ar (half life 269.0 a), d is the duration of the irradiation. Note, that for longer, segmented irradiations the decay correction of Wijbrans and McDougall (1987) should be incorporated.

The variance can be calculated with the following equation. Note, that the uncertainties in duration of irradiation and of the time elapsed since the irradiation are not taken into account.

$$\sigma_F^2=\left(\frac{\partial F}{\partial {}^{40}Ar_m}\right)^2\sigma^2_{{}^{40}Ar_m}+\left(\frac{\partial F}{\partial {}^{39}Ar_m}\right)^2\sigma^2_{{}^{39}Ar_m}+\left(\frac{\partial F}{\partial {}^{37}Ar_m}\right)^2\sigma^2_{{}^{37}Ar_m}+\left(\frac{\partial F}{\partial {}^{36}Ar_m}\right)^2\sigma^2_{{}^{36}Ar_m}+$$
$$\left(\frac{\partial F}{\partial {}^{40}Ar_{bl}}\right)^2\sigma^2_{{}^{40}Ar_{bl}}+\left(\frac{\partial F}{\partial {}^{39}Ar_{bl}}\right)^2\sigma^2_{{}^{39}Ar_{bl}}+\left(\frac{\partial F}{\partial {}^{37}Ar_{bl}}\right)^2\sigma^2_{{}^{37}Ar_{bl}}+\left(\frac{\partial F}{\partial {}^{36}Ar_{bl}}\right)^2\sigma^2_{{}^{36}Ar_{bl}}+$$
$$\left(\frac{\partial F}{\partial D}\right)^2\sigma_D^2+\left(\frac{\partial F}{\partial\left[{}^{36}Ar/{}^{37}Ar\right]_{Ca}}\right)^2\sigma^2_{\left[{}^{36}Ar/{}^{37}Ar\right]_{Ca}}+\left(\frac{\partial F}{\partial\left[{}^{39}Ar/{}^{37}Ar\right]_{Ca}}\right)^2\sigma^2_{\left[{}^{39}Ar/{}^{37}Ar\right]_{Ca}}+$$
$$\left(\frac{\partial F}{\partial E}\right)^2\sigma_E^2+\left(\frac{\partial F}{\partial\left[{}^{40}Ar/{}^{39}Ar\right]_K}\right)^2\sigma^2_{\left[{}^{40}Ar/{}^{39}Ar\right]_K}+\left(\frac{\partial F}{\partial\lambda_{37}}\right)^2\sigma^2_{\lambda_{37}}+\left(\frac{\partial F}{\partial\lambda_{39}}\right)^2\sigma^2_{\lambda_{39}}+\left(\frac{\partial F}{\partial\lambda_{{}^{36}Cl}}\right)^2\sigma^2_{\lambda_{{}^{36}Cl}} \qquad (1.7)$$

The partial derivatives to determine the contribution of all these parameters are shown in the Appendix C.

Whole rock major element geochemistry of the samples was determined by XRF and trace elements were measured using ICP-MS at the faculty of Geosciences, Utrecht University.

1.2 Cosmogenic ^{3}He exposure dating

Olivine and clinopyroxene compositions were determined using a JEOL® JSM-6400 microprobe at the Vrije Universiteit Amsterdam. Helium measurements were conducted using a MAP 215-50 mass spectrometer at the noble gas facility at SUERC, Scotland. Approximately 500 mg of mineral

was crushed in an all metal hydraulic vacuum crusher in order to determine the magmatic $^3He/^4He$ in melt inclusions. The ^3He and ^4He blanks of the crushing procedure were $3.6*10^3$ and $5.6*10^8$ atoms, respectively, and were never more than 0.5 % of the crushed samples. Cosmogenic He was extracted using an 808 nm diode laser (Foeken et al, 2006; Foeken et al, 2009). Note that due to logistical constraints no helium data could be obtained for flow MN.

Olivine fragments (250-500 μm) were heated for 10–15 min in 1 cm diameter holes in a high purity Cu pan by rastering a 4 mm-diameter beam over the samples. Coupling of the 808 nm laser with the near-transparent olivine was poor so melting was achieved by addition of degassed pyroxene glass powder. Laser ^3He and ^4He blanks averaged to $4.5*10^3$ and $3.6*10^8$ atoms, respectively, with the ^3He blank contributing up to 10% of the ^3He signal in some samples and the ^4He blank staying below 5% and in most samples below 1% of the total ^4He signal. Gas clean up and mass spectrometric techniques are described by Williams et al. (2005). The concentration of cosmogenic ^3He was calculated from:

$$^3He_{cos} = {}^4He_{melt}\left(\left(\frac{^3He}{^4He}\right)_{melt} - \left(\frac{^3He}{^4He}\right)_{crush}\right) \qquad (1.8)$$

where $^3He_{cos}$ is the concentration of cosmogenic ^3He, $^4He_{melt}$ is the concentration of ^4He obtained in the melting step, $(^3He/^4He)_{melt}$ is the helium isotope ratio obtained from the melt and $(^3He/^4He)_{crush}$ is the helium isotope ratio obtained in the crushing step. CosmoCalc 1.7 (Vermeesch, 2007) and the scaling factors of Dunai (2001) and a production rate of 103 ± 4 atms/g/y were used for calculations of exposure ages. The following equations were used for cosmic ray flux scaling (see Appendix D for more details):

$$N_{1030}(P) = Y + \frac{A}{\left(1 + e^{-\left(\frac{P-X}{B}\right)}\right)^C} \qquad (1.9;\ \text{eq. 3 in Dunai (2001)})$$

with P being the cutoff rigidity and A=0.5221, B=-1.7211, C=0.3345, X=4.2822 and Y=0.4952.

$$\Lambda(P) = y + \frac{a}{\left(1 + e^{-\left(\frac{P-x}{b}\right)}\right)^c} \qquad (1.10;\ \text{eq. 4 in Dunai (2001)})$$

with a=17.183, b=2.060, c=5.9164, x=2.2964 and y=130.11.

The neutron flux as a function of atmospheric depth and cuttoff rigidity was calculated as

$$N(z,P) = N_{1030}(P)\, e^{z(h)/\Lambda(P)} \qquad \text{(1.11; eq. 5 in Dunai (2001))}$$

The paleomagnetic field reconstruction by Guyodo and Valet (1999) was used in the scaling model. Atmospheric conditions were estimated using the model by Iribane and Godson (1992; eq. 1.6 in Chapter II) and assuming an annual mean sea level temperature of 20° C.

$$p = p_0 \left(1 - \frac{\beta_0 h}{T_0}\right)^{\frac{g_0}{R_d \beta_0}} \qquad \text{(1.12; eq. 54 in Iribane \& Godson, 1992)}$$

where p_0 is the pressure at sea level (standard pressure 1013.25 mbar), β_0 the temperature decrease with elevation (6.5 mK/m), h is the altitude in meters, T_0 the temperature in Kelvin at sea level (standard temperature 15ºC = 288.15 K, use an appropriate value depending on the climatic region), g_0 the standard sea level value of the acceleration due to gravity (9.80665 m/s^2), R_d the gas constant (287.05 J/kg/K).

Shielding factors used include topographic shielding S_t and self shielding S_s:

$$S_t = 1 - \int_0^{2\pi} \frac{\sin(h(\alpha))^{3.5}}{2\pi} d\alpha \qquad \text{(1.13; eq. 1 in Vermeesch (2007))}$$

where h(α) is the height h (in radians) of the horizon in the direction of azimuth α or the slope of the sample surface, whichever is greater;

$$S_s = \frac{\Lambda}{\rho z}\left(1 - e^{\frac{\rho z}{\Lambda}}\right) \qquad \text{(1.14; eq. 2 in Vermeesch (2007))}$$

Where Λ is the attenuation length for high energy neutrons in rock (160 ± 10 g/cm^2), ρ is the rock density and z the thickness of the sample.

2. Results

2.1 $^{40}Ar/^{39}Ar$ incremental heating results

A summary of the $^{40}Ar/^{39}Ar$ analyses is given in Tables 1 and 2 as well as in Figure 1. In Table 1 age calculations using the $^{40}Ar/^{36}Ar_{air}$ of Steiger and Jäger (1977, based on Nier, 1950) and Lee et al (2006) are shown. Table 2 shows the replicate measurements of CA, MA, MC and MM using

atmospheric composition from Lee et al (2006). Age plateau data is available in Appendix E. All errors are given as 1 sigma including external errors.

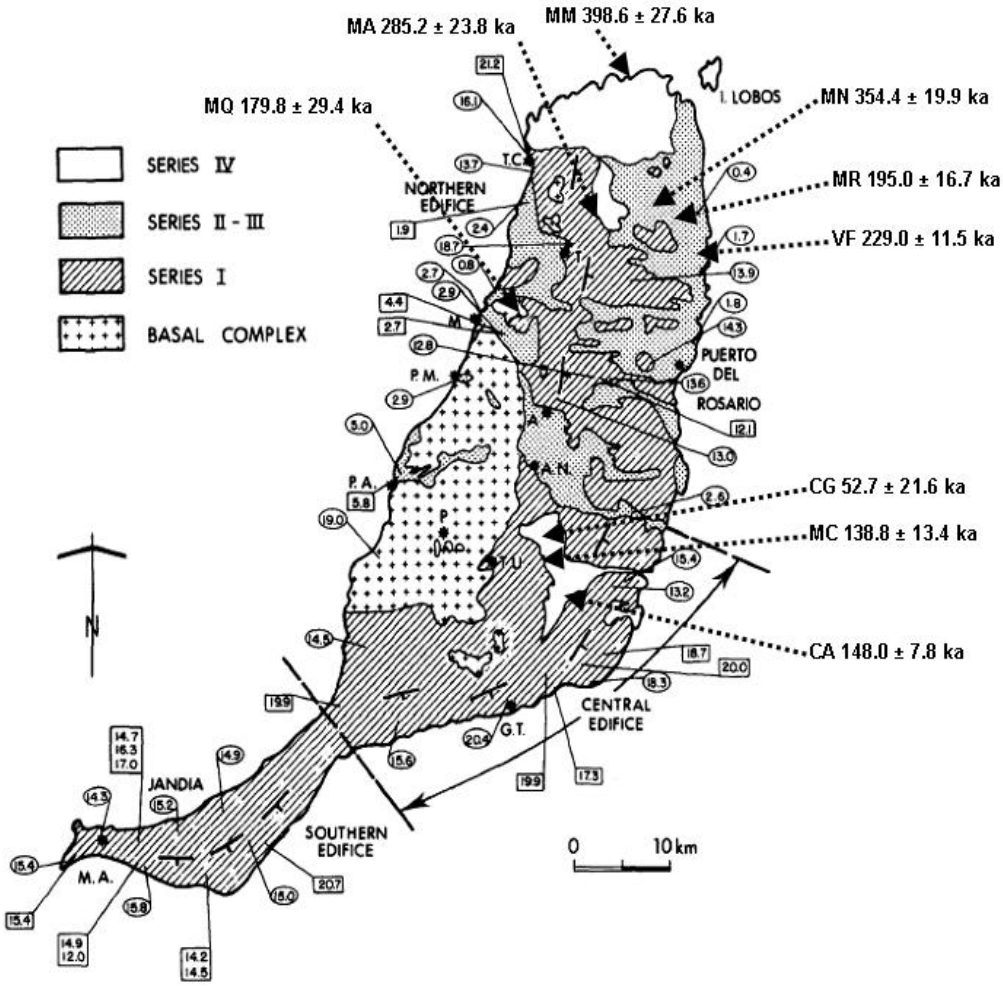

Figure 1: Schematic geological map of Fuerteventura after Coello et al. (1992). Locations of this study's sampling sites are indicated by arrows. Small numbers in ellipses and rectangles indicate ages in Ma (Coello et al., 1992 and references therein).

air (Steiger & Jäger, 1977)

	plateau and 1σ error [ka]		isochron from plateau data and 1σ error [ka]		40/36 Isochron Intercept and 1σ error	
CA	144.6	7.5	146.2	11.4	295.2	1
CG	53	18.6	52.6	34	295.5	0.8
MA	320.5	21	286.3	50.1	296	0.6
MC	108.5	12.2	138.6	21.1	294.1	0.8
MM	403.2	26.2	410.8	36	295.2	1
MN	370.2	17.1	352.6	26.3	296.7	1.4
MQ	272	20.4	179.4	61.4	299.1	2.2
MR	230.6	16.8	203	33.4	297.9	2.5
VF	236.7	10.7	221.3	29.8	298.7	5.9

air (Lee et al, 2006)

	plateau and 1σ error [ka]		isochron from plateau data (in case of sample CG best fitting points) and 1σ error [ka]		40/36 Isochron Intercept		plateau with substituted air composition and 1σ error [ka]		isochron from plateau data and 1σ error [ka]	
CA	***95.9***	***10.7***	***130.4***	***15.3***	294.5	1	148	7.8	147.3	11.5
CG	***---***	***---***	***50.7***	***21***	294.7	0.8	52.7	21.6	53	31.8
MA	***94.4***	***25.8***	***198.1***	***173.7***	295.2	0.6	285.2	23.8	285.9	45.7
MC	***69.6***	***18.2***	***92.4***	***36.3***	293.3	0.8	138.8	13.4	139.3	20.8
MM	348.7	29.2	375.3	77.6	295.7	0.9	398.6	27.6	396.8	35.1
MN	317.5	17.1	355.1	26.1	295.9	1.4	354.4	19.9	355.1	26.1
MQ	173.0	20.4	181.3	60.7	298.2	2.2	179.8	29.4	181.3	60.7
MR	185.9	15.7	195.1	24.8	298	1.1	195	16.7	195.1	24.8
VF	217.5	11.9	239.9	26.1	295.8	1.2	229	11.5	228.6	14.7

Table 1 (previous page): $^{40}Ar/^{39}Ar$ analysis results. All errors are 1 sigma including external errors. Bold values indicate samples which show great differences in plateau ages depending on the assumed composition of air and the trapped argon component.

Sample	Plateau age and 1 σ error [ka]		MSWD	% of total $^{39}Ar_K$ in plateau	steps used/total heating steps	Isochron age and 1 σ error [ka]		MS WD	$^{40}Ar/^{36}Ar$ Intercept and 1 σ error
CA-1	135.6	15.1	1.2	89.4	8/9	135.6	31.0	1.8	295.8
CA-2	163.1	10.3	0.3	80.5	7/9	163.5	14.2	0.4	292.2
$CA_{weighted\ mean\ of\ replicates}$	154.4	8.5							
$CA_{total\ plateau}$	148.0	7.8	0.8	79.7	14/18	147.3	11.5	1.0	294.5
MC-1	131.7	22.8	0.3	61.2	7/11	132.5	38.1	0.4	293.4
MC-2	139.9	18.9	0.2	60.2	5/8	139.8	32.2	0.3	293.4
$MC_{weighted\ mean\ of\ replicates}$	136.6	14.6							
$MC_{total\ plateau}$	138.8	13.4	0.2	60.9	12/19	139.3	20.8	0.3	293.3
MA-1	313.2	35.7	0.0	73.1	6/9	311.5	69.8	0.1	294.7
MA-2	272.6	37.3	0.2	82.8	6/8	275.0	70.8	0.4	295.4
$MA_{weighted\ mean\ of\ replicates}$	293.8	25.8							
$MA_{total\ plateau}$	285.2	23.8	0.1	77.6	12/17	285.9	45.7	0.2	295.2
MM-1	305.8	68.1	0.1	84.9	7/8	295.3	107.3	0.3	297.0
MM-2	415.1	31.7	0.6	89.9	5/6	413.9	37.2	0.9	295.0
$MM_{weighted\ mean\ of\ replicates}$	395.6	28.7							
$MM_{total\ plateau}$	398.6	27.6	0.6	93.9	13/14	396.8	35.1	0.8	295.7

Table 2: Comparison of replicate plateau ages with their error weighted mean and the plateau age obtained on the pooled data. Ages are based on the air composition reported by Lee et al. (2006) and the assumption that the trapped argon component is of a $^{40}Ar/^{36}Ar$ composition represented by the y-axis intercept of the respective isochron.

The data of sample CA show two replicate experiments on different aliquots of the sample yielding inverse variance weighted mean plateau and an isochron age of 144.6 ± 7.5 ka and 146.2 ± 11.4 ka respectively when using the $^{40}Ar/^{36}Ar$ value reported by Steiger and Jäger (1977). Using the value reported by Lee et al. (2006) yields a plateau and isochron age of 95.9 ± 10.7 ka and 130.4 ± 15.3

ka respectively. Using the $^{40}Ar/^{36}Ar$ intercept of the isochron as the trapped air component in the plateau calculation yielded a plateau age of 148.0 ± 7.8 ka.

Sample CG revealed a plateau age of 53 ± 18.6 ka and an isochron age of 52.6 ± 34 ka using the air argon composition of Steiger and Jäger (1977). No plateau age and an isochron age of 50.7 ± 21 ka were obtained with the value of Lee et al. (2006). However introducing the $^{40}Ar/^{36}Ar$ isochron intercept yielded a plateau age of 52.7 ± 21.6 ka.

Two aliquots of sample MC were dated. They reveal plateau and isochron ages of 108.5 ± 12.2 ka and 138.6 ± 21.1 ka respectively using Steiger and Jäger (1977) and 69.6 ± 18.2 ka and 92.4 ± 36.3 ka using Lee et al. (2006). Substitution of the trapped argon component with the isochron intercept value calculated to a plateau age of 138.8 ± 13.4 ka.

Sample MR yielded plateau and isochron ages of 230.6 ± 16.8 ka and 203.0 ± 33.4 ka using Steiger and Jäger (1977). Calculation with the $^{40}Ar/^{36}Ar$ value of Lee et al. (2006) yields ages of 185.9 ± 15.7 ka and 195.1 ± 24.8 ka respectively. The isochron intercept substitution gives a plateau age of 195.0 ± 16.7 ka.

On sample VF plateau and isochron ages of 236.7 ± 10.7 ka and 221.3 ± 29.8 ka were obtained using Steiger and Jäger (1977). Recalculating with Lee et al. (2006) yielded ages of 217.5 ± 11.9 ka and 239.9 ± 26.1 ka for the plateau and isochron, respectively. The isochron intercept substitution yielded a plateau age of 229.0 ± 11.5 ka.

Sample MQ yielded plateau and isochron ages of 272.0 ± 20.4 ka and 179.4 ± 61.4 ka when assuming the atmospheric argon composition reported by Steiger and Jäger (1977) and 173.0 ± 20.4 ka and 181.3 ± 60.7 ka when assuming the composition reported by Lee et al. (2006). Isochron intercept substitution yielded a plateau age of 179.8 ± 29.4 ka.

Sample MA was dated using 2 aliquots that yielded plateau and isochron ages of 320.5 ± 21 ka and 286.3 ± 50.1 ka, respectively, using Steiger and Jäger (1977). Recalculation using Lee et al. (2006) yielded plateau and isochron ages of 94.4 ± 25.8 ka and 198.1 ± 173.7 ka, respectively. Recalculation with isochron intercept substitution gave a plateau age of 285.2 ± 23.8 ka.

Sample MN yielded plateau and isochron ages of 370.2 ± 17.1 ka and 352.6 ± 26.3 ka after Steiger and Jäger (1977). Calculating with Lee et al. (2006) gave ages of 317.5 ± 17.1 ka and 355.1 ± 26.1 ka. Isochron intercept substitution yielded a plateau age of 354.4 ± 19.9 ka.

Sample MM was dated using two aliquots from two different irradiations. Using the atmospheric composition from Steiger and Jäger (1977) yielded plateau and isochron ages of 403.2 ± 26.2 ka

and 410.8 ± 36 ka, respectively. Using the atmospheric composition from Lee et al. (2006) plateau and isochron ages of 348.7 ± 29.2 ka and 375.3 ± 77.6 ka were obtained. Furthermore, the isochron intercept substitution yielded a plateau age of 398.6 ± 27.6 ka.

The results of the variance analysis are summarized in Table 3 and Figure 2. In Table 3 the percentage of variance caused by the parameters of eq. (1) (λ, T_{st},F_{sample} and F_{st}) are reported for all dated samples. In all cases F_{sample} contributes more than 97 % of the total variance. Figure 2 shows variance contributions to F_{sample} for one representative heating step for each experiment. The full dataset can be found in the supplementary dataset. 85% and more of the variance of F_{sample} are contributed by $^{36}Ar_{bl}$, $^{36}Ar_{m}$ and $^{40}Ar_{bl}$. This shows the high influence of ^{36}Ar on the measurements of these samples. Surprisingly the literature value for air argon composition does not have a significant impact on the uncertainty.

	CA	CG	MA	MC	MM	MN	MQ	MR	VF
% variance by									
λ	0.00%	0.00%	0.00%	0.00%	0.00%	0.00%	0.00%	0.00%	0.00%
T_{st}	1.17%	0.02%	0.47%	0.36%	0.69%	1.04%	0.12%	0.62%	1.30%
F_{sample}	97.52%	99.96%	98.99%	99.23%	98.79%	97.76%	99.74%	98.66%	97.19%
F_{st}	1.31%	0.02%	0.53%	0.41%	0.52%	1.20%	0.14%	0.72%	1.51%

Table 3: Variance analysis of main age equation.

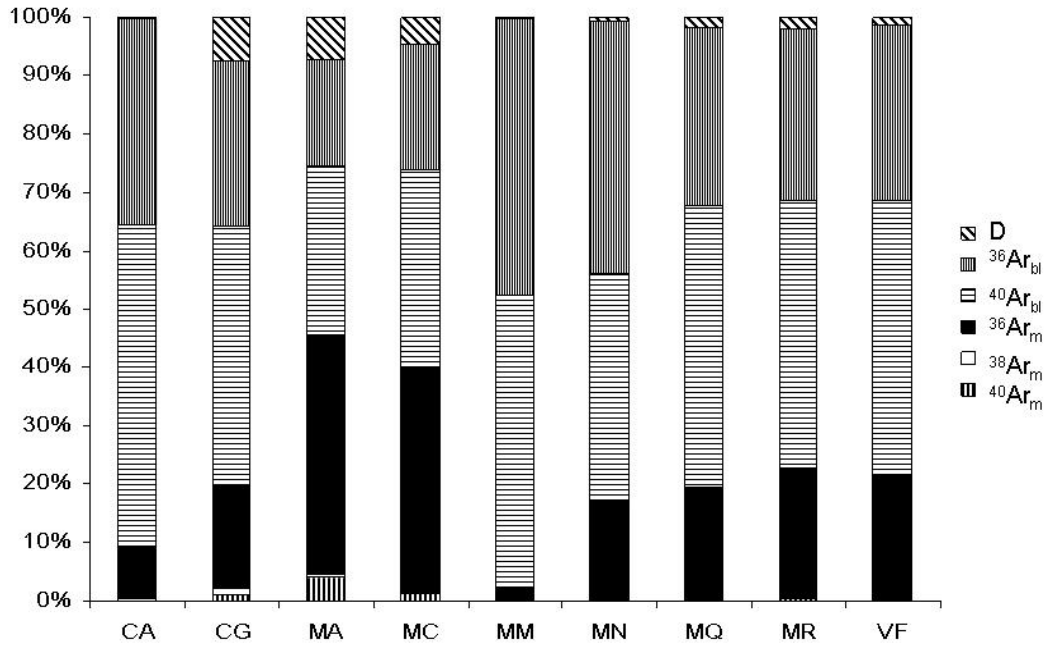

Figure 2: Parameters of significant contributions to single step F-ratios. Only parameters with a relative contribution of 1% or more are shown. Please note that only one representative heating step per sample is shown. The full results are available in the supplementary dataset.

2.2 Cosmogenic ^{3}He exposure dating

The sampled olivine phenocrysts contained 15.5 ± 1.6 wt. % FeO and 44.7 ± 1.2 wt. % MgO with the standard deviation including core to rim variations. This composition equals Fo_{85}. Clinopyroxene compositions from flow CA were equally uniform yielding MgO 13 ± 1 wt.%, CaO 22 ± 1 wt.%, FeO 7 ± 1 wt.%, Al_2O_3 7 ± 2 wt.% and TiO_2 3 ± 1 wt.%.

Topographic shielding (calculated from eq. 1 in Vermeesch, 2007) was less than 0.1 % for all samples and was therefore neglected. Self shielding (calculated from eq. 2 in Vermeesch, 2007) was on average 8% and at maximum 15% for sample CG 05/04 (see Appendix F). Shielding corrected ^{3}He concentrations were scaled to sea level at 28.5º N using the scaling factors of Dunai (2001) and exposure ages were calculated based on a production rate of 103 ± 4 atms/g/y (Dunai, 2001). Exposure ages are summarized in Table 4 and a comparison between exposure and argon

isotope ages is given in Figure 3. Full analytical data is reported in Appendix F. Note that only cosmogenic ages obtained from the flows CG, MR, MQ and VF are within or close to the uncertainty of the $^{40}Ar/^{39}Ar$ ages, while for the rest of the samples exposure ages were significantly younger than corresponding $^{40}Ar/^{39}Ar$ ages. The volcanic flows with cosmogenic helium and argon age agreement show an argon age of less than 250 ka. It seems that problems arise with one or the other of these methods for samples with an apparent radiogenic age >250 ka and also for a substantial number of data younger than 250 ka. Figure 3 shows that exposure ages show great variation, especially for flows CA, MR and VF. For flow CA exposure ages from olivine cluster around younger ages between 36.3 to 54.2 ka compared to exposure ages from clinopyroxenes that cluster around 53.9 to 90 ka resulting in two populations. MR and VF also show a high spread of exposure ages. The maximum exposure ages of 199.9 ± 14.9 ka for MR and 203.8 ± 14.5 ka for VF agree with the radiogenic ages of 195.0 ± 16.7 ka and 229.0 ± 11.5 ka, respectively. However exposure ages as low as half these values were obtained in our measurements on the thinnest samples. This leads to the conclusion that undetected contamination must have caused at least some of these low outliers as replicate measurements from flow MR show a similar spread as measurements from individual samples of flow VF. Incomplete mixing of our samples during sample preparation and a resulting over representation of minerals from lower parts of the sampled boulder could explain a maximum of only ~ 11 % exposure age underestimation compared to up to 50 % underestimation.

Sample	elevation [m]	Mineral	analytical cosmogenic ^{3}He concentration [atoms/g] and uncertainty, no scaling applied		sample material [g/cm^{2}] and uncertainty		^{40}Ar/^{39}Ar age [ka] and uncertainty (based on Lee et al.(2006))		exposure age [ka] and uncertainty (Dunai, 2001)	
CA05/01	127	cpx	3.56E+06	2.94E+05	31.78	2.38	148.0	7.8	53.9	7.5
CA05/01 40%			3.79E+06	5.12E+05	31.78	2.38	148.0	7.8	57.3	10.9
CA05/02			4.48E+06	2.91E+05	34.95	2.45	148.0	7.8	68.5	8.3
CA05/03 part B			4.81E+06	2.41E+05	34.65	1.58	148.0	7.8	73.4	7.6
CA05/04			5.76E+06	4.17E+05	42.67	1.52	148.0	7.8	90.0	11.5
CA05/05			4.78E+06	2.71E+05	38.92	2.87	148.0	7.8	73.8	8.5
CA05/06			4.49E+06	3.28E+05	29.25	1.30	148.0	7.8	67.3	8.4
CA05/07			5.81E+06	4.77E+05	34.72	1.64	148.0	7.8	88.7	12.1
CA05/01	127	olv	2.79E+06	3.88E+05	31.78	2.38	148.0	7.8	40.1	7.7
CA05/03B			2.74E+06	2.91E+05	34.65	1.58	148.0	7.8	39.8	6.3
CA05/05			3.68E+06	2.50E+05	38.78	2.86	148.0	7.8	54.2	6.7
CA05/06			2.54E+06	2.12E+05	29.25	1.30	148.0	7.8	36.3	4.8
CG05/01	213	olv	6.09E+06	2.40E+05	15.15	2.35	52.7	21.6	78.9	7.0
CG 05/02			*-8.95E+05*	*-1.01E+04*			0.0	0.0	0.0	0.0
CG05/04			3.47E+06	8.91E+04	45.90	2.70	52.7	21.6	49.3	4.1
CG05/07			5.11E+06	1.18E+05	19.68	1.29	52.7	21.6	67.2	4.8
MA05/03	185	olv	1.86E+06	2.52E+04	30.55	2.44	285.2	23.8	22.0	1.6
MA05/05			8.80E+05	1.19E+04	34.44	1.42	285.2	23.8	10.6	0.7
MA05/06			1.64E+06	2.39E+04	23.10	1.19	285.2	23.8	19.0	1.3
MA05/08			2.34E+06	2.01E+04	19.32	1.00	285.2	23.8	26.9	1.5
MC05/07surf	199	olv	3.75E+06	1.33E+05	12.50	0.79	138.8	13.4	47.6	3.8
MM05/02	24	olv	9.21E+06	1.25E+05	34.02	2.53	398.6	27.6	116.3	7.9
MM05/03			1.06E+07	1.95E+05	27.95	1.34	398.6	27.6	132.1	9.0
MM05/04			1.02E+07	8.70E+04	41.28	1.52	398.6	27.6	131.2	8.0
MM05/04 surf			8.78E+06	3.30E+05	12.90	0.81	398.6	27.6	104.0	8.5
MM05/05			9.94E+06	1.35E+05	32.16	1.47	398.6	27.6	124.9	8.0
MM05/05 surf			8.12E+06	3.35E+05	13.40	0.84	398.6	27.6	96.4	8.3
MM05/06			9.56E+06	4.70E+05	24.64	1.25	398.6	27.6	117.4	11.5
MM05/06surf			8.36E+06	2.88E+05	11.20	0.72	398.6	27.6	98.5	7.7
MQ05/01surf	167	olv	1.29E+07	4.54E+05	13.15	0.83	179.8	29.4	157.0	12.5
MR05/01	185	olv	1.50E+07	6.72E+05	15.90	1.36	195.0	16.7	169.9	15.6
MR05/01 A			1.70E+07	7.53E+05	15.90	1.36	195.0	16.7	193.3	17.6
MR05/01 B			1.76E+07	4.90E+05	15.90	1.36	195.0	16.7	200.0	14.9
MR05/01 C			1.71E+07	8.59E+05	15.90	1.36	195.0	16.7	194.1	18.8
MR05/01 D			1.29E+07	5.67E+05	15.90	1.36	195.0	16.7	146.6	13.3
MR05/05 A			1.08E+07	8.02E+05	10.90	0.70	195.0	16.7	120.5	14.2
MR05/05 B			1.34E+07	6.95E+05	10.90	0.70	195.0	16.7	149.6	14.3
MR05/05 C			8.12E+06	3.58E+05	10.90	0.70	195.0	16.7	90.7	8.0
VF05/01	56	olv	1.46E+07	1.72E+05	38.40	3.69	229.0	11.5	203.8	14.5
VF05/02			9.62E+06	1.36E+05	30.94	4.80	229.0	11.5	131.6	9.9
VF05/03			1.39E+07	1.96E+05	36.64	2.43	229.0	11.5	193.1	13.4
VF05/05			1.39E+07	1.19E+05	24.80	2.53	229.0	11.5	186.0	11.4
VF05/07			1.01E+07	1.19E+05	26.40	2.69	229.0	11.5	136.6	8.9

Table 4 (last page): Summary of cosmogenic data compared to ^{40}Ar/^{39}Ar data. The index 'surf' in the sample description designates surface slices cut from bigger samples.

Shaded samples are for replicate measurements. See table 1 in Appendix A for sample locations.

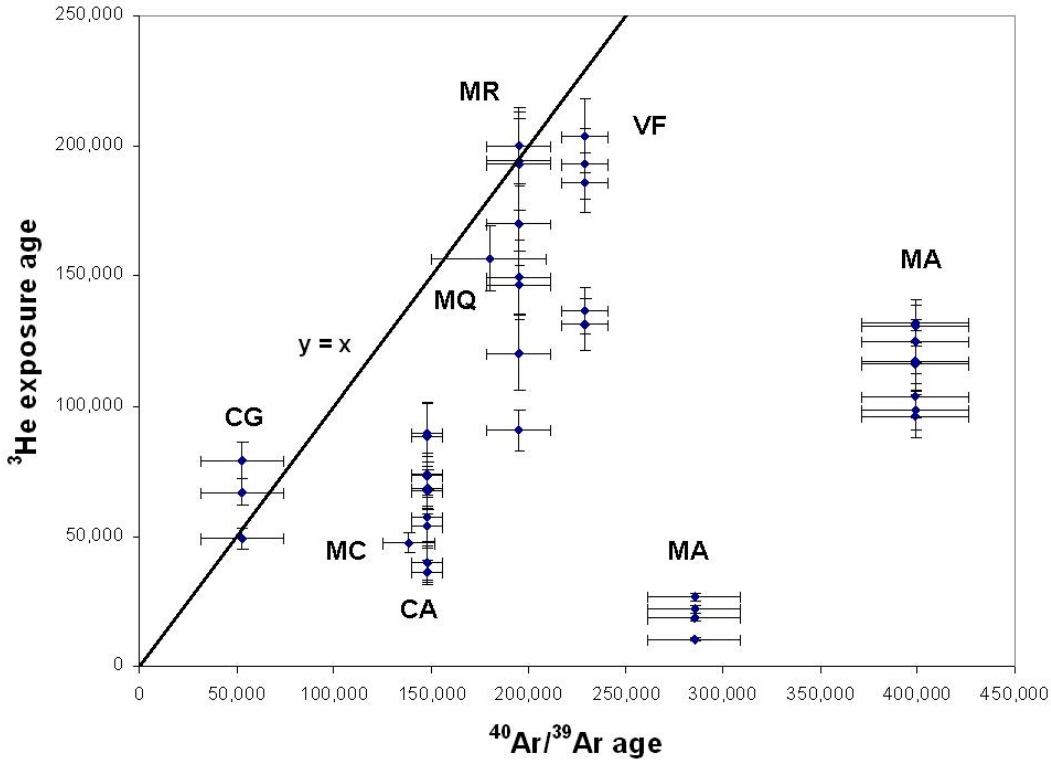

Figure 3: Cosmogenic ^{3}He exposure ages plotted against ^{40}Ar/^{39}Ar ages.

Many samples however did not yield exposure ages comparable to the ^{40}Ar/^{39}Ar results While four (CG, MR, MQ, VF) of six samples younger than 250 ka yield maximum exposure ages within or in the case of VF close to the uncertainty of the radiogenic argon ages, the other two and the older samples yield substantially lower ^{40}Ar/^{39}Ar-^{3}He age ratios of 0.5 or less. Due to the good preservation of the samples direct erosion can be ruled out. Volcanism could be a natural source for cover in the form of ash, but no evidence was found in the field. This would leave excess ^{40}Ar as the problem influencing the ^{40}Ar/^{39}Ar data. Given the low radiogenic ^{40}Ar* content in the young

samples excess argon could easily increase drastically the apparent age even though our samples had been leached.

3. Discussion

3.1 Argon data

3.1.1 Definition and calculation of plateaus

The criteria used to define a valid plateau are described in the methods section. Due to potential disequilibrium between lavas and atmospheric argon (Renne et al., 2009) the $^{40}Ar/^{36}Ar$ isochron intercept was used as substitute for the commonly assumed trapped air component to calculate a third plateau age dataset in Table 2 (e.g. Lanphere, 2000). Chlorine does not contribute significant amounts of argon to the measurement based on ^{38}Ar values so there was no opportunity to check the influence of the chlorine production ratios reported by Roddick (1983) and Renne et al. (2008). More than 50% of the released ^{39}Ar was incorporated into the plateau age determinations for all samples. Except for CG (58%) and MC (61%), more than two thirds of the released ^{39}Ar were incorporated into the plateaus. The smallest number of heating steps obtained in a single experiment was 6 (MM-2, Table 3). In all experiments, except for sample MC (still >50%), more than two third of the obtained heating steps could be incorporated into the plateau. The MSWD values for tha ages are around 1 or lower indicating that the analytical errors for individual heating steps used in calculating the plateau and isochron ages account for (MSWD ~1) or are overestimated (MSWD<1) to explain the observed scatter in the data. A comparison between ages calculated on the basis of the different atmospheric $^{40}Ar/^{36}Ar$ values shows that many agree within uncertainty while those with higher amounts of trapped argon do not. The consistent yielding of $^{40}Ar/^{36}Ar$ isochron intercepts below 298.53 ± 0.31 (Lee et al., 2006), mostly around 295, needs to be addressed. A potential explanation could be kinetic fractionation of air argon that was not completely equilibrated with the fast cooling lava (Renne et al., 2009). The common assumption that the ratio of air argon is the same as the trapped component in the system seems to be incorrect in the case of our samples. While substituting the $^{40}Ar/^{36}Ar$ value indicated by the isochron as the trapped argon composition in the plateau age eliminates the need for an assumption, it sacrifices the quality criterion of concordant plateau and isochron ages as both methods contribute to calculating the plateau age. The plateau age has a lower error than the isochron age when calculated using the same dataset and the isochron value for the trapped argon component.

However, both calculations should include the same set of steps and data points respectively otherwise the trapped component calculated from the isochron might no longer reflect the trapped component in the plateau.

In order to combine two replicate measurements for samples CA, MA, MC and MM we combined all incremental heating data for two experiments in ArArCALC, sorted them according to temperature, and calculated a plateau age using the previously mentioned criteria. In order to validate our approach we also calculated the error weighted mean and the weighted standard deviation of the two individual replicate plateau ages (Taylor, 1997). These weighted mean ages (Table 2). The weighted means of the replicate ages are statistically indistinguishable from the combined plateau ages with similar uncertainties.

The inverse variance weighted mean of the two replicate measurements of CA, MA, MC and MM also statistically identical to the plateau age obtained by combining all data into one plateau (Table 2). The error of the mean of the replicates is, however, slightly higher than the error of the plateau age.

3.1.2 Variance analysis

Variance analysis shows clearly that the error terms for the decay constant ^{40}K, the age of the standard and the F-ratio of the standard do not make a significant contribution to the error of the total plateau age compared to the that of the F-ratio of the unknown sample so the issue of decay value is not relevant at present for dating very young samples. The dominant contributors to the variance in F_u are measurement of the ^{36}Ar and ^{40}Ar blanks. In some cases the uncertainty of the instrument's mass discrimination factor is also a minor contributor. It is not surprising, however, in a system using a large volume furnace for the analytical error to be dominated by the blank contribution. We recommend therefore that future work to improve the method should focus on reducing the system blank and improving the precision in measuring the ^{36}Ar beam. While the blank on the furnace has been reduced already as far as possible it should be possible to reduce the blank on the laser extraction system 50 % or more. The fact that the literature value of the isotopic composition of argon did not significantly impact uncertainties is also linked to the high analytical uncertainty contributions from ^{36}Ar from. Chlorine was present in very low concentrations in our samples so there is no basis for comparing the impacts of the old (Roddick, 1983) and new (Renne et al., 2008) production rate ratios of argon isotopes from chlorine during irradiation in the reactor.

3.2 Cosmogenic Helium

Exposure geochronology supports the results of the $^{40}Ar/^{39}Ar$ analyses younger than about 250 ka. However, many samples yielded exposure ages lower than their apparent $^{40}Ar/^{39}Ar$ age. Furthermore, samples from lava flows for which exposure and $^{40}Ar/^{39}Ar$ ages agree show a tendency for the exposure ages to be lower. The effect of vesicular systems being filled with sand was taken into account during density measurement as the vesicle infilling was not removed prior to the measurement. Tumbling is one of the simplest things that can influence a loose sample boulder. Assuming that the boulder is shaped like a disk it could end up resting on either of its two flat sides so of the measured cosmogenic nuclide concentration over the whole boulder would be the same as for an undisturbed sample. Most samples were measured over the whole boulder thickness and the maximum sample thickness was around 45 g/cm^2. The most extreme case for a tumbling scenario would be if it occurred a short time before sampling. This lead to an underestimation of the surface exposure age by about 27 % for a sample 45 g/cm^2 thick and assuming an attenuation length for spallogenic neutrons of 160 g/cm^2 and sampling only the top of the boulder afterwards. If the sample tumbles in a way such that it is irradiated on both sides for exactly half the exposure time then the observed surface exposure age would be 14 % smaller than the expected value. Biased selection of target minerals from the deeper parts of a sample has the same quantitative effects. Sampling primarily the middle of a 45 g/cm^2 boulder reduces the exposure age by 14% while sampling the bottom results in an underestimation of about 27 %. For samples MC, MM, MR, MQ the top 5 cm where measured: results from MR and MQ are comparable to the $^{40}Ar/^{39}Ar$ data while MM results are similar to the total age integration. Exposure ages for samples MC and MM show an underestimation of 64 to 70 % compared to the $^{40}Ar/^{39}Ar$ method, which much more than could be caused by the effects tumbling alone.

The shape of a sample can also influence the observed production of cosmogenic nuclides. Masarik and Wieler (2003) discuss a variety of sample shapes and their corresponding loss in neutron flux. One of these shapes is a column of variable height with a cross section of 5 × 5 cm, which is rooted on a flat infinite surface. A 20 cm high column would yield a production rate of 0.98 relative to a flat surface integrated over the uppermost 5 cm of sample. However, our samples have a disk like shape and are less than 20 cm thick with a cross section in the range of 15 times 15 to 20 times 20 cm or larger. This would result in a factor even closer to 1 for a production rate

correction. Furthermore, most of our samples were partially embedded in the substratum or surrounded by other clasts, decreasing further the possibility of neutron leakage.

Erosion also could not have affected samples directly. In order to decrease the original surface production rate by 5 % a layer 8.2 g/cm^2 thick has to be removed. This equals more than 2.5 cm of basalt. However the sampled boulders did not show evidence of such extensive erosion as sample surface details were sometimes still preserved to the sub centimetre to millimetre scale. One other possible explanation for the observed underestimation of production rates is burial. A ratio of 0.5 for observed production rate to expected production rate would equal cover material with a thickness of 111 g/cm^2. This would amount to about 30 cm of basalt (3 g/cm^3) or about 1 m of moderately compacted ash (1.2 g/cm^3). As the lava flows themselves look very well preserved an erosion mechanism affecting basaltic rocks does not seem likely to have taken place. Frequent ash cover on the other side of the sample could cause the observed low production rates and also protect older lava flows from extensive erosion. Ash is also easier to erode than solid basalt.

Thermal neutron capture of ^{6}Li and production of ^{3}H and subsequently ^{3}He could result in excess ^{3}He being attributed to spallation production and therefore overestimation of the exposure. Sources for this are implantation from the rock matrix and in situ production in the crystal matrix. A conservative estimate using 1) a production of 1.5 atoms/g/y of ^{3}He from a Li concentration of 5 ppm (Dunai et al., 2007), 2) considering only increasing factors such as the maximum Li concentration of 9.55 ppm measured in our samples, and 3) that the maximum thickness of boulders is at the maximum of the thermal neutron flux bulge gives us a production rate of 4.3 atoms/g/y throughout the sample. This is about 5% of the total production rate used to calculate our exposure ages and does not consider the high incompatibility of Li in olivine and pyroxene (partition coefficients of 0.1 and 0.2; Brenan et al., 1998). So effects from ^{6}Li derived ^{3}He can be neglected as a source of error.

Contamination with ^{4}He rich material such as pieces of groundmass or similar materials containing high amounts of U and Th was minimised by hand picking the sample minerals under the binocular microscope and etching off the outer grain rims of olivine phenocrysts. However, a few data points cannot be explained by a natural mechanism. Samples MR and VF show some low ages of only half the maximum exposure age. And in the case of MR sample MR05/05 C was separated from a 5 cm thick section cut from the morphological top of a boulder. These findings

can only be explained by undetected contamination either from mineral inclusions or during the sample loading stage.

Implanted ^{4}He was a concern in this study and the main reason to etch away the phenocrysts outer rim. The samples were shaken in their acid baths by hand to promote a homogeneous etching process and not have preferred areas with material removed. Due to the irregular shape of phenocrysts weight control had to be used to assess the etching progress so implanted ^{4}He can not be ruled out as a contributor to exposure age underestimation. But it should not be a major contributor to the underestimation given the extend of etching to 40 % weight loss of a sample.

Whatever causes the unexplained low exposure ages in some samples does not influence the maximum values obtained for each lava flow. Cosmogenic ^{36}Cl in the whole rock shows concentrations similar to the expected concentrations.

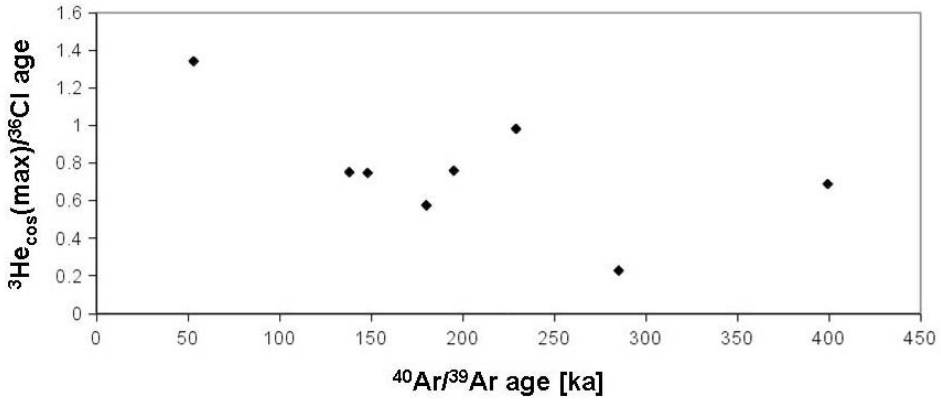

Figure 4: Ratio of Cosmogenic ^{3}He exposure age and cosmogenic ^{36}Cl data (Mai, 2009) plotted against $^{40}Ar/^{39}Ar$ age. See Mai (2009) for chlorine data. A general negative trend indicates decreasing cosmogenic ^{3}He production in samples with older argon ages.

Figure 4 shows the ratios of maximum cosmogenic ^{3}He ages in this study and ^{36}Cl data on whole rock samples for the same lava flows (Mai, 2009). It shows a general negative trend indicating a problem with the cosmogenic helium which would normally be attributed to implanted ^{4}He. Given the convergence of our exposure ages and radiogenic ages at ages younger than 250 ka and the low radiogenic ^{40}Ar concentrations measured during $^{40}Ar/^{39}Ar$ incremental heating experiments influence of the radiogenic ages by excess ^{40}Ar is very likely to have caused the discrepancy for

older radiogenic ages. Although sample burial by volcanic ash is not improbable no evidence for this was found in the field.

4. Conclusions

We have shown $^{40}Ar/^{39}Ar$ incremental heating data from basaltic lavas including a very high proportion of trapped argon. It is obvious that this trapped component deviates from recent determinations of the composition of atmospheric argon (Lee et al., 2006), challenging the basic assumption used for $^{40}Ar/^{39}Ar$ plateau geochronology of the trapped argon component being of atmospheric composition. Therefore it seems logical to derive the composition of the trapped argon component from the $^{40}Ar/^{36}Ar$ isochron intercept wherever possible when dealing with plateau ages of samples containing a high amount of trapped argon.

Variance analysis shows that in our case most of the uncertainty contributed by the many parameters used in $^{40}Ar/^{39}Ar$ geochronology was derived from furnace blanks and measurements of low intensity. Improvements in blank determination and minimization or switching to laser extraction attached to high gettering capacity extraction line might dramatically improve the precision of the method. The low radiogenic ^{40}Ar content in the young samples remains as a limiting factor.

The youngest ages obtained from Fuerteventura volcanic rocks so far (400 ± 100 ka, K-Ar, obtained on olivine basalt, Coello et al., 1992) reflect more the difficulty to date this kind of young material with low potassium content than the actual end of activity. Our age determinations support ongoing activity on Fuerteventura until at least 50 ka in accordance with the ongoing historic and recent activity in the Archipelago. Intercalibration with exposure dating further validates the $^{40}Ar/^{39}Ar$ results for flows of 200 ka and younger age. Holocene activity is documented by volcanic rocks interbedded with dated Holocene sediments (Coello et al., 1999) but more work is necessary to date young volcanic rocks independently to better constrain the history of most recent volcanism on Fuerteventura,

From a cosmogenic point of view the Canary Islands – especially the Eastern Canary Islands with their dry climate and abundance of well preserved lava flow tops appear to have a great potential as calibration sites for cosmogenic nuclides. The findings from Dunai and Wijbrans (2000) already showed the great potential on Lanzarote. However care has to be taken when assessing seemingly fresh and undisturbed samples as cover of presumably volcanic origin might influence the results

especially for older samples. These results indicate that work concerning the improvement of cosmogenic nuclide production systematics should also take place on Fuerteventura. Future work should focus on establishing a long term continuous production rate record at this site which would be helpful to assess influences of the geomagnetic field in more detail. The Canary Islands are one of the few sites which offer potential for a continuous production rate record at one location.

We need more samples…

Synthesis and Conclusion

1. This study and the Marie Curie initial training network

The aim of the Marie Curie CRONUS-EU initial training network was the transfer of knowledge between scientists, teaching young scientists in TCN application and improving TCN systematics. This study was designed to transfer TCN competence between researchers and address the key objective the CRONUS-EU initial training network of assessing the potential of the islands of the Canary archipelago as calibration sites for TCN production rates.. Another aim of this study was to establish a new $^{40}Ar/^{39}Ar$ measurement routine for a triple filter quadrupole mass spectrometer and furnace extraction line. Furthermore, new measurements of the composition of atmospheric argon by Lee et al. (2006) were used to evaluate the implications of these new data for $^{40}Ar/^{39}Ar$ age calculations, especially for young samples. During his PhD study Björn Schneider contributed to several research groups and projects within and outside of the CRONUS-EU network.

1) Fenton, C.R., Niedermann, S., Goethals, M.M., Schneider, B., Wijbrans, J.R., (2009). Evaluation of cosmogenic ^{3}He and ^{21}Ne production rates in olivine and pyroxene from a Pleistocene basalt flow, western Grand Canyon, AZ, USA. Quaternary Geochronology 4(6), 475-492.

2) Schimmelpfennig, I., Williams, A., Pik, R., Burnard, P., Samuel Niedermann, S., Finkel, R., Schneider, B., Benedetti, L. (2011). Inter-comparison of cosmogenic in-situ ^{3}He, ^{21}Ne and ^{36}Cl at low latitude along an altitude transect on the SE slope of Kilimanjaro volcano (3º S, Tanzania). Quaternary Geochronology 6 (5), 425-436.

3) Schneider, B., Kuiper, K.F., Postma, O., Wijbrans, J.R. (2009). $^{40}Ar/^{39}Ar$ geochronology using a quadrupole mass spectrometer. Quartenary Geochronology 4 (6), 508-516.

4) **Wijbrans, J.R., Schneider, B., Kuiper, K.F., Calvari, S., Branca, S., De Beni, E., Norini, G., Corsaro, R., Miraglia, L. (2011).** $^{40}Ar/^{39}Ar$ geochronology of Holocene basalts; examples from Stromboli, Italy. Quaternary Geochronology 6, 223-232.

2. Synthesis

2.1 Fuerteventura as a sampling site

Geological and geographical setting and sampling strategy are of great importance for both radiometric dating using the $^{40}Ar/^{39}Ar$ and TCN techniques

Chapter I summarizes the geology of the Canary Islands and Fuerteventura and presents the main theories about their origin.. This is followed by a review of the current geochronological data and a description of the climatic conditions in the archipelago, which is particularly important for cosmogenic studies.

Chapter II describes the practical aspects of fieldwork including the search for sampling sites and the sampling strategy. It also gives a description of the individual sampling sites and the samples themselves including petrographic descriptions as well as mineralogical and chemical rock composition.

The arid climate and the well preserved lava flows provided favourable fundamental conditions for undertaking this study. Nine lava flows were sampled, taking 7 to 9 samples for cosmogenic nuclide analysis. Although not all of these samples could be analysed due to logistical and time constraints this sampling strategy compensated in part for the many unexpected measurement results. A different approach for a larger scale sampling would be to initially take only 2 or 3 samples per flow such that more sites could be sampled with less material collected needing to be analysed. A second stage of the survey could then focus on the promising sampling sites indicated by in the first batch of results.

2.2 Testing a quadrupole mass spectrometer for argon geochronology

While multi collector magnetic sector mass spectrometers are now being used in many argon geochronology laboratories, a different technical approach using a triple filter quadrupole mass spectrometer was explored in this study.

In Chapter III general theoretical and practical aspects of $^{40}Ar/^{39}Ar$ geochronology are presented before moving on to testing of the quadrupole mass spectrometer and development of a working measurement routine. Reference gas measurements were used to show that the characteristics of this instrument are suitable compared to contemporary standard magnetic sector instruments. Standards and samples of known and unknown age spanning an age range between 25 Ma and 10 ka, demonstrated the flexibility of the mass spectrometer but also showed that it has limits when measuring young samples, samples otherwise low in radiogenic argon, or much enriched in trapped argon. Collaborative work on samples from other members of the CRONUS-EU network are also presented in this context as the instrument was used in the absolute dating of samples from these network members (Fenton et al., 2009; Schimmelpfennig et al., 2011). We demonstrated that

an industry grade triple filter quadrupole mass spectrometer equipped with a single electron multiplier linked to a furnace gas extraction line is capable of doing routine $^{40}Ar/^{39}Ar$ analyses. Performance of the system in the age range of upper Pleistocene to Holocene is very promising, although sample characteristics can influence significantly the quality of the results and the blanks of the furnace system also set limits. Collaborative work with other scientific groups helped to improve the understanding of young and active volcanic systems and demonstrated that the instrument is suitable for samples in the (Sub) Holocene age range (Branca et al., 2009; Wijbrans et al., 2011).

2.3 Intercalibration of argon geochronology with in situ terrestrial cosmogenic ^{3}He

Chapter IV summarizes the theoretical and practical aspects of in situ TCN application with focus on noble gas TCNs and particularly ^{3}He. It finishes by describing the analytical approach in study of using a diode laser and degassed basaltic groundmass as optical coupling medium for olivine melting.

Finally Chapter V reported $^{40}Ar/^{39}Ar$ and cosmogenic ^{3}He ages for Fuerteventura basalts spanning the complete interval between previously dated young volcanic rocks of the upper Pleistocene and volcanic rocks interbedded with Holocene sediments. The impact of minor variations in the composition of atmospheric argon on the $^{40}Ar/^{39}Ar$ data is discussed, as well as treatment of the plateau data, including the merging of replicate experiments. A variance analysis showed that the potential weaknesses of the method are associated with young or otherwise problematic samples. Cosmogenic ^{3}He data from olivine phenocrysts showed good agreement between maximum exposure ages (< 250 ka) and radiogenic ages. This intercalibration exercise also pointed out the possible presence of excess argon in some samples.

As part of the CRONUS-EU network this study contributed to the improvement of TCN systematics by characterizing the potential of Fuerteventura as a natural target calibration site. However, two factors limited the quality of the results to such a degree that they cannot be used to directly improve the precision of existing production rates. As field evidence for burial or significant erosion of the lava flows is missing, the influence of excess argon on the radiogenic ages is the most likely cause for these discrepancies. Radiogenic argon ages also suffered from low radiogenic ^{40}Ar concentrations resulting in poor uncertainties, particularly below 150 ka.

Furthermore, cosmogenic ages reported in this study show a pronounced scatter, most likely due to inhomogeneous sampling of phenocrysts from the sample column during sample preparation.

In conclusion, the most promising calibration sites on Fuerteventura should ideally have an age between 100 ka and 200 ka. For younger samples a precise enough independent age constraint via $^{40}Ar/^{39}Ar$ geochronology might be difficult to obtain, at least for groundmass separates. However, using a 'cleaner' (i.e., lower blank) extraction method (e.g. laser extraction) and finding lava flows with suitable single mineral phases might help to improve precision. The presence of excess argon in samples may further complicate the search for good sites given the low radiogenic ^{40}Ar content found in the youngest samples used in this study.

The upper Pleistocene volcanic history of Northern Fuerteventura could be improved by filling the gap in ages between 400 ka (Coello et al., 1992) and the Holocene (Coello et al., 1999). $^{40}Ar/^{39}Ar$ results show evenly distributed ages between 50 ka and 400 ka, although radiogenic ages older than 250 ka in our study have to be considered carefully. The geochronology record presented here is, at best, only a semi quantitative record of volcanic activity as the focus of this study was on intercalibration of two isotope dating techniques rather than on the spatial and temporal distribution of ocean island volcanism. The error analyses of radiogenic argon age data in Chapter V show that improvements in production rate calibration would result mostly from improved independent age constraints. Most of this improvement could be achieved by decreasing system blanks in the quadrupole mass spectrometer line. The use of laser extraction has already helped in analysing helium isotopic compositions in small amounts of olivine phenocrysts and is common practice in $^{40}Ar/^{39}Ar$ geochronology. However, a laser extraction system was not available for attachment to the quadrupole mass spectrometer line during this study. Furthermore, the assumption that sample material prepared for cosmogenic nuclide analysis was well mixed proved incorrect and caused spread in the cosmogenic data, which can be easily avoided in the future by sampling strictly from the uppermost surface.

In order to further verify Fuerteventura's potential as calibration site the focus of future works should be on finding sampling sites between 100 ka and 200 ka to refine long term production rate behaviour. Sampling sites younger than 100 ka down to Holocene ages would allow for the simultaneous measurement of long term and short term production rates and for their comparison with geomagnetic models used in cosmogenic scaling models. Nearby Lanzarote has shown already its potential as a calibration site (Dunai & Wijbrans, 2000) and both islands would

complement each other in establishing geochronological records, especially given that Lanzarotes has been volcanically active in historical times.

3. Perspectives

As this thesis reaches completion it is clear that calculating ages from $^{40}Ar/^{39}Ar$ plateaus for very young samples has some potential weaknesses. The composition of the trapped argon component should be known and not assumed; otherwise it leads potentially to erroneous results. The effects of this assumption need to be further evaluated in order to determine the viability of plateau calculations compared to isochron calculations.

The TCN method has changed dramatically in the last two decades. While the first models developed could yield scaling factors differing by up to 30 % (Dunai 2000; Lal, 1991) the ongoing refinement process has led to a substantial increase in the consensus about scaling factors. Most efforts now focus on improvements in geomagnetical models and records. CRONUS-Earth and CRONUS-EU were initiatives to improve TCN applications on a broad scale, including artificial and natural target calibration attempts, and the modelling and development of calculation tools to allow for a wider introduction to the scientific community. A major step forward would be the establishment of continuous production rate records from (sub-)historic to prehistoric times at single sampling sites in order to test geomagnetic models. So far, only spatially separated records of either short term (<20-50 ka) or long term (>20-50 ka) production rates exist so making it more difficult to link records and allow for only a limited testing of geomagnetic models.

The efforts to intercalibrate and improve two noble gas geochronometers undertaken in this study support several aspects of geochronology. Cosmogenic helium and argon geochronology are both used to date volcanic rocks. Improvements in this area will lead to the ability of drawing a more complete and also more recent picture of volcanism and help to better understand volcanic mechanisms and potential risks. The development of new mass spectrometry techniques primarily aims at pushing geochronology to its limits. Our example of developing a measurement method for argon geochronology around a cost effective industry grade mass spectrometer shows new opportunities for a larger group of research institutions. While state of the art equipped laboratories would be able to focus more on the forefront of high precision research the more cost effective laboratories would do research in technically less demanding but still important areas.

References

Ackert, R.P., Singer, B.S., Guillou, H., Kaplan, M.R. (2003). Long-term cosmogenic ^{3}He production rates from ^{40}Ar/^{39}Ar and K-Ar dated Patagonian lava flows at 47°S. EPSL 210, 119-136.

Acosta, J., Uchupi, E., Muñoz, A., Herranz, P., Palomo, C.,Ballesteros, M. , ZEE Working Group (2003). Geologic evolution of the Canarian Islands of Lanzarote, Fuerteventura, Gran Canaria and La Gomera and comparison of landslides at these islands with those at Tenerife, La Palma and El Hierro. Marine Geophysical Researches 24, 1–40.

Amidon, W.H., Hood, D.H., Farley, K.A. (2009). Cosmogenic ^{3}He and ^{21}Ne production rates calibrated against ^{10}Be in minerals from the Coso volcanic field. EPSL 280(1-4), 194-204.

Amidon, W.H., Farley, K.A., Burbank, D.W., Pratt-Sitaula, B. (2008). Anomalous cosmogenic ^{3}He production and elevation scaling in the high Himalaya. Earth and Planetary Science Letters 265, 287–301.

Ancochea, E., Brändle, J.L., Cubas, C.R., Hernán, F. and Huertas, M.J. (1996). Volcanic complexes in the eastern ridge of the Canary Islands: the Miocene activity of the island of Fuerteventura. J. Vol. Geoth. Res., 70, 183–204.

Anguita, F., Hernan, F. (2000). The Canary Islands origin: a unifying model. Journal of Volcanology and Geothermal Research 103, 1-26.

Anguita, F., Hernan, F. (1975). A propagating fracture model versus a hot-spot origin for the Canary Islands. EPSL 27, 11-19.

Arana, V., Ortiz, R. (1986). Marco geodinamico del volcanismo canario. An. Fisica, Vol. Esp. 82, 202-231.

Balco, G., Stone, J.O., Lifton, N.A., Dunai, T.J. (2008). A complete and easily accessible means of calculating surface exposure ages or erosion rates from ^{10}Be and ^{26}Al measurements. Quaternary Geochronology 3(3), 174-195.

Baur, H. (1999). A Noble-Gas Mass Spectrometer Compressor Source With two Orders of Magnitude Improvement in Sensitivity. AGU Fall meeting.

Baur, H., Signer, P. (1980). Numerical-Simulation of Ion-Source for Gas Mass-Spectrometer. Helvetica Physica Acta 52 (3), 395.

Blard, P.-H., Farley, K.A. (2008). The influence of radiogenic ^{4}He on cosmogenic ^{3}He determinations in volcanic olivine and pyroxene. EPSL 376, 20-29.

Blard, P.H., Pik, R. (2008). An alternative isochron method for measuring cosmogenic ^{3}He in lava flows. Chemical Geology 251, 20-32.

Blard, P.-H., Pik, R., Lave. J., Bourles, D., Burnard, P.G., Yockochi, R., Marty, B., Trussdell, F. (2006). Cosmogenic ^{3}He production rates revisited from evidences of grain size dependent release of matrix-sited helium. Earth and Planetary Science Letters 247, 222–234.

Blard, P.-H., Lave, J., Pik, R., Quidelleur, X., Bourles, D., Kieffer, G. (2005). Fossil cosmogenic ^{3}He record from K–Ar dated basaltic flows of Mount Etna volcano (Sicily, 388N): evaluation of a new paleoaltimeter. Earth and Planetary Science Letters 236 (3-4), 613–631.

Branca, S., Del Carlo, P., Lo Castro, M. D., De Beni, E., Wijbrans, J. (2009). The occurrence of Mt Barca flank eruption in the evolution of the NW periphery of Etna volcano (Italy). Bulletin of Vulcanology 71 (1), 79-94.

Brenan, J.M., Neroda, E., Lundstrom, C.C., Shaw, H.F., F.J. Ryerson, F.J., Phinney, D.L. (1998). Behaviour of boron, beryllium, and lithium during melting and crystallization: constraints

from mineral-melt partitioning experiments. Geochimica et Cosmochimica Acta 62 (12), 2129-2141.

Calvert, A.T., Moore, R.B., McGeehin, J.P., Rodrigues da Silva, A.M. (2006). Volcanic history and $^{40}Ar/^{39}Ar$ and ^{14}C geochronology of Terceira Island, Azores, Portugal. Journal of Volcanology and Geothermal Research 156, 103-115.

Cantagrel, J.M., Cendrero, A., Fuster, J.M., Ibarolla, E., Jamond, C. (1984). K-Ar chronology of the volcanic eruptions in the Canarian archipelago: Island of La Gomera. Bull. of Vul. 47(3), 597-609.

Carracedo, J.C., Day, S., Guillou, H., Rodriguez, E., Canas, J.A., Perez, F.J. (1998). Hotspot volcanism close to a passive continental margin. Geol. Mag. 135, 591-604.

Carracedo, J.C. (1994). The Canary Islands: an example of structural control on the growth of large oceanic-island volcanoes. Journal of Volcanology and Geothermal Research 60, 225-241.

Carracedo, J.C., Rodriguez-Badiola, E. (1993). Evolución geológica y magmática de la isla de Lanzarote (Islas Canarias). Rev. Acad. Canar. Cienc., V, 25–58.

Cassignol, C., Gillot, P.-Y. (1982). Range and Effectiveness of Unspiked Potassium–Argon Dating: Experimental Groundwork and Applications, John Wiley, New York.

Coble, M.A., Grove, M., Calvert, A.T. (2011). Calibration of Un-Instruments Noblesse multicollector mass spectrometers for argon isotopic measurements using a newly developed reference gas. Chemical Geology 290, 75-87.

Coello, J.J., Castillo, C., Gonzalez, E.M. (1999). Stratigraphy, Chronology, and Paleoenvironmental Reconstruction of the Quaternary Sedimentary Infilling of a Volcanic Tube in Fuerteventura, Canary Islands. Quaternary Research 52, 360–368.

Coello, J., Cantagrel, J.M., Hernan, F., Fuster, J.M., Ibarrola, E., Ancochea, E., Casquet, C., Jamond, C., Diaz, J.R., Cendrero, R. (1992). Evolution of the eastern volcanic ridge of the Canary Islands base don new K-Ar data. Journal of Volcanology and Geothermal Research 53, 251-274.

Coulie, E., Quidelleur, X., Lefevre, J.C., Gillot, P.Y. (2004). Exploring the multicollection approach for the $^{40}Ar/^{39}Ar$ dating technique. Geochemistry Geophysics Geosystems 5 (11).

Dalrymple, G. B. (1989). The GLM continuous laser system for $^{40}Ar/^{39}Ar$ dating: Description and performance characteristis, U.S. Geol. Survey Prof. Paper, 89–96.

Desilets, D., Zreda, M. (2003). Spatial and temporal distribution of secondary cosmic-ray nucleon intensities and applications to in situ cosmogenic dating. Earth Planet. Sci. Lett. 206, 21–42.

Desilets, D., Zreda, M. (2001). On scaling cosmogenic nuclide production rates for altitude and latitude using cosmic-ray measurements. Earth and Planetary Science Letters 193, 213-225.

Dunai, T.J. (2010). Cosmogenic Nuclides: Principles, Concepts and Applications in the Earth Surface Sciences. Cambridge University Press, 187 pp.

Dunai, T.J., Stuart, F.M., Pik, R., Burnard, P., Gayer, E. (2007). Production of ^{3}He in crustal rocks by cosmogenic thermal neutrons. Earth and Planetary Science Letters 258 228–236.

Dunai, T. (2001). Influence of secular variation of the geomagnetic field on production rates of in situ produced cosmogenic nuclides. Earth Planet. Sci. Lett. 193, 197–212.

Dunai, T. (2000). Scaling factors for production rates of in situ produced cosmogenic nuclides: a critical reevaluation. Earth Planet. Sci. Lett. 176, 157–169.

Dunai, T.J., Wijbrans, J.R. (2000). Long-term cosmogenic 3He production rates (152 ka – 1.35 Ma) from 40Ar/39Ar dated basalt flows at 29ºN latitude. Earth and Planetary Science Letters 176, 147-156.

Dunai, T.J., Roselieb, K. (1996). Sorption and diffusion of helium in garnet: implications for volatile tracing and dating. EPSL 139(3-4), 411-421.
Dunne, J., Elmore, D., Muzikar, P. (1999). Scaling factors for the rates of production of cosmogenic nuclides for geometric shielding and attenuation at depth on sloped surfaces. Geomorphology 27, 3-11.
Farley, K.A., Libarkin, J., Mukhopadhyay, S., Amidon, W. (2006). Cosmogenic and nucleogenic 3He in apatite, titanite, and zircon. EPSL 248, 451-461.
Farley, K.A., Wolf, R.A., Silver, L.T. (1996). The effects of long alpha-stopping distances on (U-Th)/He ages. Geochimica et Cosmochimica Acta 60 (21), 4223-4229.
Fenton, C.R., Niedermann, S., Goethals, M.M., Schneider, B., Wijbrans, J.R., (2009). Evaluation of cosmogenic ^{3}He and ^{21}Ne production rates in olivine and pyroxene from a Pleistocene basalt flow, western Grand Canyon, AZ, USA. Quaternary Geochronology 4(6), 475-492.
Fenton, C.R., Webb, R.H., Pearthree, P.A., Cerling, T.E., Poreda, R.J. (2001). Displacement rates on the Toroweap and Hurricane faults: implications for Quaternarydowncutting in Grand Canyon. Geology 29, 1035–1038.
Foeken, J.P.T., Day, S., Stuart, F.M. (2009). Cosmogenic ^{3}He exposure dating of the Quaternary basalts from Fogo, Cape Verdes: Implications for rift zone and magmatic reorganisation. Quaternary Geochronology 4, 37–49.
Foeken, J.P.T., Stuart, F.M., Dobson, K.J., Persano, C., Vilbert, D. (2006). A diode laser system for heating minerals for (U-Th)/He Chronometry. Geochemistry Geophysics Geosystems 7(4), 1-9.
Fuster, J.M. (1975). Las Islas Canarias: un ejemplo de evolucion temporal y espacial del volcanismo oceanico. Est. Geol. 31, 439-463.
Garner, E.L., Murphy, T.J., Gramlich, J.W., Paulsen, P.J., Barnes, I.L. (1975). Absolute Isotopic abundance ratios and the atomic weight of a reference sample of potassium. Journal of Research and National Bureau of Standards 79A, 713-725.
Gayer, E., Pik, R., Lave, J., France-Lanord, C., Bourles, D., Marty, B. (2004). Cosmogenic ^{3}He in Himalayan garnets indicating an altitude dependence of the ^{3}He/^{10}Be production ratio. Earth and Planetary Science Letters 229, 91-104.
Geldmacher, J., Hoernle, K., Boogard, P.v.d., Duggen, S., Werner, R. (2005). New ^{40}Ar/^{39}Ar age and geochemical data from seamounts in the Canary and Madeira volcanic provinces: Support for the mantle plume hypothesis. EPSL 237, 85-101.
Gillot, P.Y., Cornette, Y., Max, Nathalie (1992). Two reference materials, trachytes MDO-G and ISH-G, for argon dating (K-Ar and ^{40}Ar/^{39}Ar) of Pleistocene and Holocene rocks. Geostandards Newsletter 16(1), 55-60.
Goehring, B.M., Kurz, M.D., Balco, G., Schaefer, J.M., Licciardi, J., Lifton, N. (2010). A reevaluation of in situ cosmogenic ^{3}He production rates. Quaternary Geochronology 5(4), 410-418. doi: 10.1016/j.quageo.2010.03.001
Gosse, J. C., F. M. Phillips (2001). Terrestrial in situ cosmogenic nuclides: Theory and application. Quat. Sci. Rev., 20, 1475–1560.
Granger, D. E., Muzikar, P.F. (2001). Dating sediment burial with in situ-roduced cosmogenic nuclides: Theory, techniques, and limitations, Earth Planet. Sci. Lett., 188, 269–281.
Grasty, R.L., Miller, J.A. (1965). The omegatron: a useful tool for argon isotope investigation: Nature 207, 1146-1148.

Guillou, H., Torrado, F.J.P., Machin, A.R.H., Carracedo, J.C., Gimeno, D. (2004). The Plio–Quaternary volcanic evolution of Gran Canaria based on new K–Ar ages and magnetostratigraphy. Journal of Volcanology and Geothermal Research 135, 221–246.

Guillou, H., Carracedo, J.C., Day, S.J. (1998). Dating of the Upper Pleistocene-Holocene volcanic activity of La Palma using the unspiked K-Ar technique. Journal of Volcanology and Geothermal Research 86, 137-149.

Guyodo, Y.; Valet, J.-P. (1999). Global changes in intensity of the Earth'smagnetic field during the past 800kyr. Nature 399, 249-252.

Hamme, R.C., Emerson, S.R. (2004). Measurement of dissolved neon by isotope dilution using a quadrupole mass spectrometer. Marine Chemistry 91, 53-64.

Hess, J.C., Lippolt, H.J. (1994). Compilation of K–Ar measurements on HD-B1 standard biotite — 1994 status report. In: G.S. Odin, Editor, Phanerozoic Time Scale. Bull. Liasis. Inform. IUGS Subcom. Geochronol. vol. 12**,** Offset Paris (1994), pp. 19–23.

Hilton, D.R., Hammerschmidt, K., Teufel, S., Friedrichsen, H. (1993). Helium isotope characteristics of Andean geothermal fluids and lavas. EPSL 120(3-4), 265-282.

Hoernle, K., Zhang, Y.S., Graham, D. (1995). Seismic and geochemical evidence for large-scale mantle upwelling beneath the eastern Atlantic and western and central Europe. Nature 374, 34-39.

Hoernle, K., Schmincke, H.U. (1993). The role of partial melting in the 15-Ma geochemical evolution of Gran Canaria: a blob model for the Canary hotspot. Journal of Petrology 34, 599-626.

Holik, J.S., Rabinowitz, P.D., Austin, J.A. (1991). Effects of Canary hotspot volcanism on structure of oceanic crust off Morocco. Journal of Geophysical Research 96 (12), 39-67.

Holmes, R.D., Best, M.G., Hamblin, W.K., (1978). Calculated strain rates and their implications for the development of the Hurricane and Toroweap faults, Utah and northern Arizona. U.S. In: Geological Survey Technical Report Summaries, Earthquake Hazards Reduction Program VII, pp. 44–50.

Iribane, J.V., Godson, W.L. (1992). Atmospheric Thermodynamics. D. Reidel, Dordrecht, 259 pp.

Irvine, T.N., Baragar, W.R.A. (1971). A Guide to the Chemical Classification of the Common Volcanic Rocks. Can. J. Earth Sci. 8(5), 523–548.

Konenkov, N.V., Cousins, L.M., Baranov, V.I. (2001). Quadrupole mass filter operation with auxiliary quadrupolar excitation: theory and experiment. Int. Journ. of Mass Spec. 208(1-3), 17-27.

Koppers, A.A.P. (2002). ArArCALC - software for $^{40}Ar/^{39}Ar$ age calculations. Computers & Geosciences 28 (5), 605-619.

Koppers, A.A.P. (1998). $^{40}Ar/^{39}Ar$ Geochronology and Isotope Geochemistry of the West Pacific Seamount Province: implications for absolute Pacific plate motions of hotspots. PhD thesis, Vrije Universiteit Amsterdam.

Kuiper, K.F., Deino, A., Hilgen, F.J., Krijgsman, W., Renne, P.R., Wijbrans, J.R. (2008). Synchronizing Rock Clocks of Earth History. Science 320(5875), 500-504.

Kulongoski, J.T., Hilton, D.R. (2002). A quadrupole-based mass spectrometric system for the determination of noble gas abundances in fluids. Geochem. Geophys. Geosyst., 3(6), 1032.

Kurz, M.D., Colodner, D., Trull, T.W., Moore, R.B., O'Brien, K. (1990). Cosmic ray exposure dating with in situ produced cosmogenic 3He: results from young Hawaiian lava flows. EPSL 97, 177-189.

Kurz, M.D. (1986). In situ production of terrestrial cosmogenic helium and some applications to geochronology. Geochimica et Cosmochimica Acta 50, 2855-2862.

Lal, D., Chen, J. (2005). Cosmic ray labeling of erosion surfaces II: Special cases of exposure histories of boulders, soils and beach terraces. Earth and Planetary Science Letters 3-4, 797-813.
Lal, D., (1991). Cosmic ray labelling of erosion surfaces: in situ nuclide production rates and erosion models. Earth Planet. Sci. Lett. 104, 424–439.
Lal, D., Peters, B. (1968). Cosmic ray produced radioactivity on the earth. In: Handbuch der Physik, Vol. XLVI/2, Springer, Berlin, pp. 551-612.
Lanphere, M.A. (2000). Comparison of Conventional K-Ar and $^{40}Ar/^{39}Ar$ Dating of Young Mafic Volcanic Rocks. Quaternary Research 53, 294-301.
Lanphere, M. A., Dalrymple, G. B. (1978). The Use of 40Ar/39Ar Data in Evaluation of Disturbed K–Ar Systems. U.S. Geological Survey Open-File Report 78-701, 241–243.
Layer, P.W., Hall, C.M., York, D. (1987). The Derivation of $^{40}Ar/^{39}Ar$ age spectra of single grains of Hornblende and Biotite by laser step-heating. Geophysical Research Letters 14(7), 757-760.
Le Bas, M.J., Rex, D.C., Stillman, C.J. (1986). The early magmatic chronology of Fuerteventura, Canary Islands. Geol. Mag., 123, 287-298.
Lee, J.-Y., Marti, K., Severinghaus, J.P., Kawamura, K., Yoo, H.-S., Lee, J.B., Kim, J.S. (2006). A redetermination of the isotopic abundances of atmospheric Ar. Geochimica et Cosmochimica Acta 70, 4507–4512.
Licciardi, J.M., Kurz, M.D., Clark, P.U., Brook., E.J. (1999). Calibration of cosmogenic 3He production rates from Holocene lava flows in Oregon, USA, and effects of the Earth's magnetic field. Earth and Planetary Science Letters 172, 261–271.
Lifton, N., Smart, D.F., Shea, M.A. (2008). Scaling time-integrated in situ cosmogenic nuclide production rates using a continuous magnetic model. Earth and Planetary Science Letters 268, 190–201.
Lifton, N. A., Bieber, J.W., Clem, J.M., Dulding, M.L., Evenson, P., Humble, J.E., Pyle, R. (2005). Addressing solar modulation and long-term uncertainties in scaling secondary cosmic rays for in situ cosmogenic nuclide applications. Earth Planet. Sci. Lett., 239, 140–161.
Ludwig, K.R., Renne, P.R. (2000). Geochronology on the paleoanthropological time scale. Evolutionary Anthropology: Issues, News, and Reviews 9(2), 101–110.
Mai. K. (2009). Production rates of 36Cl in basalts from the calibration site of Fuerteventura, Canary Islands. PhD Thesis, University of Utrecht.
Mark et al. 2011!!!!!
Mark, D.F., Barford, D., Stuart, F.M., Imlach, J. (2009). The ARGUS multicollector noble gas mass spectrometer: Performance for 40Ar/39AR geochronology. Geochemistry Geophysics Geosystems 10, Q0AA02, doi:10.1029/2009GC002643.
Marty, B., Lenoble, M., Vassard, N. (1995). Nitrogen, helium and argon in basalt: a static mass spectrometry study. Chemical Geology 120, 183-195.
Masarik, J., Wieler, R. (2003). Production rates of cosmogenic nuclides in boulders. Earth and Planetary Science Letters 216, 201-208.
Masarik, J., Frank, M., Schäfer, J.M., Wieler, R. (2001). Correction of in situ cosmogenic nuclide production rates for geomagnetic field intensity variations during the past 800,000 years. Geochimica et Cosmochimica Acta 65(17), 2995-3003.
Masarik, J., Reedy, R.C. (1995). Terrestrial cosmogenic-nuclide production systematics calculated from numerical simulations. Earth and Planetary Science Letters 136, 381–395.
McDougall, I., Harrison, M.T. (1999). Geochronology and Thermochronology by the $^{40}Ar/^{39}Ar$ Method. Oxford University Press.

Merrihue, C., Turner, G. (1966). Potassium-Argon Dating by Activation with Fast Neutrons. Journal of Geophys. Res. 71, pp. 2852.
Mertz, D.F., Renne, Paul, P.R. (1995). Quaternary multi-stage alkaline volcanism at Vesteris seamount (Norwegian-Greenland Sea): Evidence from laser step heating $^{40}Ar/^{39}Ar$ experiments. Journal of Geodynamics 19 (1), 79-95.
Middlemost, E.A.K. (1994). Naming materials in the magma/igneous rock system. Earth-Science Reviews 37 (3-4), 215-224.
Min et al., 2000!!!!!
Morgan, W.J. (1971). Convection plumes in the lower mantle. Nature 230, 42-43.
Niedermann, S. (2002). Cosmic-Ray-Produced Noble Gases in Terrestrial Rocks: Dating Tools for Surface Processes. Reviews in Mineralogy and Geochemistry, 47 (1), 731-784.
Nier, A.O. (1950). A redetermination of the relative abundances of the isotopes of carbon, nitrogen, oxygen, agron and potassium. Physical Review 77 (6), 789-793.
Nier, A.O. (1947). A mass spectrometer for isotope and gas analysis: Rev. Sci. Inst. 18, 398-411.
Nishiizumi, K., D. Lal, J. Klein, R. Middleton, J. R. Arnold (1986). Production of ^{10}Be and ^{26}Al by cosmic rays in terrestrial quartz in situ and implications for erosion rates. Nature, 319, 134–135.
Pearce, T. H., Gorman, B. E., Birkett, T. C. (1977). The relationship between major element geochemistry and tectonic environment of basic and intermediate volcanic rocks. Earth and Planetary Science Letters 36, 121–132.
Persano, C., Stuart, F.M., Bishop. P., Barfod, D.N. (2002). Apatite (U-Th)/He age constraints on the development of the Great Escarpment on the southeastern Australian passive margin. EPSL 200(1-2), 79-90.
Phillips, F. M., Leavy, B.D., Jannik, N.O., Elmore, D., Kubik, P.W. (1986). The accumulation of cosmogenic chlorine in rocks: A method for surface exposure dating. Science, 231, 41–43.
Pigati, J. S., and N. A. Lifton (2004). Geomagnetic effects on time-integrated cosmogenic nuclide production with emphasis on in situ ^{14}C and ^{10}Be, Earth Planet. Sci. Lett., 226, 193–205.
Pinti, D.L., Hashizume, K., Matsuda, J. (2001). Nitrogen and argon signatures in 3.8 to 2.8 Ga metasediments: Clues on the chemical state of the Archean ocean and the deep biosphere. Geochimica et Cosmochimica Acta 65(14), 2301–2315.
Quidelleur, X., Gillot, P.-Y., Soler, V., Lefevre, J.C. (2001). K/Ar dating extended into the last millenium: application to the youngest effusive episode of the Teide volcano (Spain). Geophysical Research Letters, 28(16), 3067-3070.
Renne, P.R., Cassata, W.S., Morgan, L.E., (2009). The isotopic Composition of atmospheric argon and 40Ar. Quaternary Geochronology 4(4), 288-298.
Renne, P.R., Sharp, Z.D., Heizler, M.T., (2008). Cl-derived argon isotope production in the CLICIT facility of OSTR reactor and the effects of the Cl-correction in 40Ar/39Ar geochronology. Chemical Geology 255, 463–466.
Renne, P.R., Swisher, C.C., Deino, A.L., Karner, D.B., Owens, T.L., DePaolo, D.J. (1998). Intercalibration of standards, absolute ages and uncertainties in Ar-40/Ar-39 dating. Chemical Geology 145, 117-152.
Renne, P.R., Sharp, W.D., Deino, A.L., Orsi, G., Civetta, L. (1997). $^{40}Ar/^{39}Ar$ Dating into the Historical Realm: Calibration against Pliny the Younger. Science 277, 1279-1280.
Rex, D.C. & Dodson, M.H. (1970). Improved Resolution and Precision of Argon Analysis Using an MS 10 Mass Spectrometer. Eclogae geol. Helv. 63(1), 275-280.

Reynolds, J.H. (1956). High sensitivity mass spectrometer for noble gas analysis. Rev. Sci. Inst. 27, 928-934.
Roddick, J.C., (1983). High precision intercalibration of 40Ar–39Ar standards. Geochimica et Cosmochimica Acta 47, 887-898.
Rothe, P. (1996). Kanarische Inseln, Gebr. Bornträger, Berlin.
Rouchon, V., Lefevre, J.-C., Quidelleur, X., Guerin, G., Gillot, P.-Y. (2008). Nonspiked ^{40}Ar and ^{36}Ar quantification using a quadrupole mass spectrometer: A potential for K-Ar geochronology. International Journal of Mass Spectrometry 270, 52-61.
Sano, Y. & Takahata, N. (2005). Measurement of Noble Gas Solubility in Seawater Using a Quadrupole Mass Spectrometer. Journal of Oceanography 61, 465-473.
Scarsi, P. (2000). Fractional extraction of helium by crushing of olivine and clinopyroxene phenocrysts: Effects on the $^{3}He/^{4}He$ measured ratio. Geochim. Cosmochim. Acta 64, 3751–3762.
Schaefer, J.M., Ivy-Ochs, S.,Wieler, R., Leya, I., Baur, H., Denton, G.H., Schluechter, C. (1999). Cosmogenic noble gas studies in the oldest landscape on Earth: Surface exposure ages of the Dry Valleys, Antarctica, Earth Planet. Sci. Lett. 167, 215–226.
Schimmelpfennig, I., Williams, A., Pik, R., Burnard, P., Samuel Niedermann, S., Finkel, R., Schneider, B., Benedetti, L. (2011). Inter-comparison of cosmogenic in-situ ^{3}He, ^{21}Ne and ^{36}Cl at low latitude along an altitude transect on the SE slope of Kilimanjaro volcano (3º S, Tanzania). Quaternary Geochronology 6(5), 425-436.
Schneider, B., Kuiper, K.F., Postma, O., Wijbrans, J.R. (2009). $^{40}Ar/^{39}Ar$ geochronology using a quadrupole mass spectrometer. Quartenary Geochronology 4 (6), 508-516.
Schuster, D.L., Farley, K.A. (2005). Diffusion kinetics of proton-induced ^{21}Ne, ^{3}He and ^{4}He in quartz. Geochimica et Cosmochimica Acta 69(9), 2349-2359.
Sharp, W.D., Renne, P.R. (2005). The 40Ar/39Ar dating of core recovered by the Hawaii Scientific Drilling Project (phase 2), Hilo, Hawaii. Geochemistry Geophysics Geosystems 6(4), 1-18.
Shervais, J.W. (1982). Ti-V plots and the petrogenesis of modern and ophiolitic lavas. Earth and Planetary Science Letters 59, 101-118.
Shuster, D.L., Farley, K.A. (2005). Diffusion kinetics of proton-induced ^{21}Ne, ^{3}He and ^{4}He in quartz. Geochimica et Cosmochimica Acta 69(9), 2349-2359.
Simpson, J.A. (2000). The cosmic ray nucleonic component: the invention and scientific uses of the neutron monitor, Space Sci. Rev. 93 11-32.
Simpson, J. A. (1983). Elemental and isotopic composition of the galactic cosmic rays. Ann. Rev. Nucl. Part. Sci., 33, 323-381.
Stacey, J.S., Sherrill, N.D., Dalrymple, G.B., Lamphere, M.A., Carpenter, N.V. (1981). A Five-collector System for the simultaneous Measurement of Argon Isotopic Ratios in a static Mass Spectrometer. International Journal of Mass Spectrometry and Ion Physics 39, 167-180.
Staudacher, T., Jessberger, E.K., Dorflinger, D., Kiko, J. (1978). A refined ultrahigh-vacuum furnace for rare gas analysis. Journal of Physics E: Scientific instruments 11, 781-784.
Steiger, R.H., Jäger, E. (1977). Subcommission on geochronology: Convention on the use of decay constants in geo- and cosmochronology. Earth and Planetary Science Letters 36(3), 359-362.
Stillman, C.J. (1999). Giant Miocene landslides and the evolution of Fuerteventura, Canary Islands. Journal of Volcanology and Geothermal Research 94, 89–104
Stone, J.O., (2000). Air pressure and cosmogenic isotope production. J. Geophys. Res. 105, 23,753–23,759.

Storey, M., Duncan, R.A., Swisher, C.C. (2007). Paleocene-Eocene Thermal Maximum and the Opening of the Northeast Atlantic. Science 27 (316, 5824), 587-589.
Stuart, F.M., Burnard, P.G., Taylor, R.P., Turner, G. (1995). Resolving mantle and crustal contributions to ancient hydrothermal fluids: He–Ar isotopes in fluid inclusions from Dae Hwa W–Mo mineralisation, S. Korea. Geochimica et Cosmochimica Acta 59, 4663–4673.
Sun, S.S., McDonough, W.F. (1989). Chemical and isotopic systematics of ocean basalts: Implications for mantle composition and processes. In Saunders, A.D., Norry, M.J. (editors): Magmatism in the Ocean Basins. Geol. Soc. London Spec. Pub., 42, 313-345.
Taylor, J.R. (1997). An Introduction to Error Analysis. The Study of Uncertainties in Physical Measurements. University Science Books, Mill Valley, California.
Turner, G. (1971). Argon 40 – argon 39 dating: the optimization of irradiation parameters. Earth and Planetary Science Letters 10, 227-234.
Valet, J.P., Meynadier, L., Guyodo, Y. (2005). Geomagnetic dipole strength and reversal rate over the past two million years. Nature 435, 802-805.
Valkiers, S., Vendelbo, D., Berglund, M., de Podesta, M. (2010). Preparation of argon primary measurement Standards for the calibration of íon current ratios measured in argon. Int. J. Mass Spectrom. 291, 41-47.
Vermeesch, P., Baur, H., Heber, V.S., Kober, F., Oberholzer, P., Schäfer, J.M., Schluechter, C., Strasky, S., Wieler, R. (2009). Cosmogenic ^{3}He and ^{21}Ne measured in quartz targets after one year of exposure in the Swiss Alps. Earth and Planetary Science Letters 284, 417-425.
Vermeesch, P. (2007). CosmoCalc: An Excel add-in for cosmogenic nuclide calculations. Volume 8(8), 1-14.
Webber, W.R. (1962). Time variations of low-rigidity cosmic rays during the recent sunspot cycle, in: J.G. Wilson, S.A. Wouthuysen (Eds.), Progress in Elementary Particle and Cosmic Ray Physics, Vol. 6, North Holland, Amsterdam, 1962, pp. 77-243.
Wijbrans, J.R., McDougall, I. (1987). On the metamorphic history of an Archaean granitoid greenstone terrane, East Pilbara, Western Australia, using the ^{40}Ar/^{39}Ar age spectrum technique. Earth and Planetary Science Letters 84 (2-3), 226-242.
Wijbrans, J.R., Pringle, M.S., Koppers, A.A.P., Scheveers, R. (1995). Argon geochronology of small samples using the Vulkaan argon laser probe. Proc. Kon. Ned. Akad. V. Wetensch. 98, 185-218.
Wijbrans, J.R., Schneider, B., Kuiper, K.F., Calvari, S., Branca, S., De Beni, E., Norini, G., Corsaro, R., Miraglia, L. (2011). ^{40}Ar/^{39}Ar geochronology of Holocene basalts; examples from Stromboli, Italy. Quaternary Geochronology 6, 223-232.
Williams, A.J., Stuart, F.M., Day, S.J., Phillips, W.M. (2005). Using pyroxene microphenocrysts to determine cosmogenic ^{3}He concentrations in old volcanic rocks: an example of landscape development in central Gran Canaria. Quaternary Science Reviews 24, 211–222.
Wilson, C.J.N., Rhoades, D.A., Lanphere, M.A., Calvert, A.T., Houghton, B.F., Weaver, S.D., Cole, J.W. (2007). A multiple-approach radiometric age estimate for the Rotoiti and Earthquake Flat eruptions, New Zealand, with implications for the MIS 4/3 boundary. Quaternary Science Reviews 26, 1861-1870.
Winkler, H.G.F. (1962). Viel Basalt und wenig Gabbro – wenig Rhyolit und viel Granit. Beiträge zur Mineralogie und Petrographie 8, 222-231.

Woodhead, J.D. (1992). Temporal geochemical evolution in oceanic intra-plate volcanics: a case study from the Marquesas (French Polynesia) and comparison with other hotspots. Contrib. Mineral. Petrol. 111, 458-467.

Zazo, C., Goy, J.L., Hillaire-Marcel, C., Gillot, P.-Y., Soler, V., González, J.A., Dabrio, C.J., Ghaleb, B. (2002). Raised marine sequences of Lanzarote and Fuerteventura revisited—a reappraisal of relative sea-level changes and vertical movements in the eastern Canary Islands during the Quaternary. Quaternary Science Reviews 21 (18–19) 2019-204.

Ziegler, L.B., Constable, C.G., Johnson, C.L., Tauxe, L. (2011). PADM2M: a penalized maximum likelihood model of the 0-2 Ma palaeomagnetic axial dipole moment. Geophysical Journal Internationa 184(3), 1069–1089.

Acknowledgements

When I began my PhD at the Vrije Universiteit Amsterdam I could hardly grasp how it would transform me. After I left the quiet university city of Bonn, had unloaded my last moving box from the car and seat quietly in my new and empty flat I realized that I was making the leap into the international environment where a new chapter of my life had started and eventually evolved into this thesis. During this time many people in one way or another took part in my life and work and therefore contributed to my thesis. And while typing these lines many memories resurface and make me wonder about the way that is behind me and the way yet to take.

I would like to start by thanking the reading committee Leah Morgan, Tibor Dunai, Anthony Hildenbrand, John O'Connor and Fin Stuart for their quick replies on my thesis manuscript even around holiday time. I found the comments very helpful and encouraging. This work improved greatly thanks to the scrutinizing reviews.

I thank my supervisor and promotor Paul Andriessen and my co-supervisor Jan Wijbrans for their support, patience and the inspirational pointers they gave me when I was seemingly stuck somewhere. I want to specially thank Jan for daring to leave me alone with a whole mass spectrometer line. This was a great encouragement for me. Paul I want to thank for encouraging me to write a proper thesis next to the articles. I hope someone can profit from my experience in the future.

I owe many thanks to Fenny Bosse, our secretary and good soul of the department. She made the potentially confusing process of getting my papers much easier and on one occasion arranged for a critical paper for me while I was on fieldwork in the Canary Islands.

Many thanks go to Katrin Mai for all the help along the road of the Fuerteventura work. Her organization of the door-to-door transport of the samples from our hotel on Fuerteventura to the Vrije Universiteit – including the design of the sample container – was a remarkable feat considering the often less than optimal circumstances.

Klaudia Kuiper led me on the journey through the argon age calculation equations and their numerous derivatives and made the perfect tandem with Jan in minimizing supervising downtime.

Bert, Onno and Roel helped me to get started in the labs and were there when things did not go exactly as planned.

Thanks go to the morning coffee round for teaching me Dutch.

I want to thank my PhD fellows for showing me Amsterdam and having many good times together. A very special thank you goes to Ibrahim Barrie who shared the office and many things beyond that with me. Also he and Frank Beunk translated my summary into proper Dutch.

To the members of the CRONUS-EU network I owe more than one thank you for the great team spirit and much collaboration. In particular I want to acknowledge the organizers of the workshops who made these occasions something that will be a nice memory for me – also besides the educational value.

Thanks to Tibor Dunai for his great support in our field campaign on Fuerteventura and his good nose for restaurants. He also was responsible for the CRONUS-EU Initial Training Network so without him many people (including me) would not be where they are right now.

Fin Stuart and Jurgen Foeken greatly supported me in all things concerning cosmogenic nuclides and still found time to introduce me to Scottish culture during my stays at SUERC. I owe them many thanks because without them some of this work would not have been possible.

I thank Margret and Terry Donnelly for their hospitality during may stays in Scotland, particularly Margret who showed me only the best of local cuisine.

Thanks go to Rainer Wieler for providing me with a working place at ETH Zurich after I left the Netherlands. Those extra months at a proper desk with fellow scientists helped quite a lot.

Ich möchte meiner Familie in Deutschland für ihre bedingungslose Unterstützung und Geduld danken. Es war immer wieder eine Herausforderung, ihnen zu erklären, was ich eigentlich genau mache. Besonderer Dank geht an meine Eltern Hannelore und Klaus, die meine Neugier und mein Bedürfnis, neue Territorien zu erkunden gefördert haben, wo sie nur konnten.

I am grateful to little sister Inken for joining me as one of my paranymphs.

And last but most I owe thanks to Glenda and our little daughter Dido Annelie. Without Glenda's support this thesis simply would not exist and she also sat by my side as paranymph during the defense. One could not ask for a more caring, patient and supporting partner than her. All the time in Zurich she was the solid rock in my stormy ocean of life. Little Dido finally made me a better person just by coming into my life. Few people keep this talent until adulthood but I think it is an important part of human existence.

Appendices

APPENDIX A

Sample Chemistry

Sample name	coordinates (GPS, UTM WGS84)	flow type	SiO_2	Al_2O_3	TiO_2	Fe_2O_3	CaO	MgO	Na_2O	K_2O	P_2O_5	MnO	LOI	sum
CA	28R 0599491/3131878	pahoehoe	41.54	11.07	3.35	14.00	10.75	12.15	3.00	***1.16***	0.76	0.19	0.15	98.12
CG	28R 0597494/3138100	pahoehoe	39.90	10.44	3.50	14.22	10.66	12.57	3.03	***1.38***	0.92	0.18	0.08	96.90
MA	28R 0603142/3168401	aa	43.55	10.70	3.12	12.90	10.13	12.09	2.74	***1.08***	0.73	0.16	0.53	97.74
MC	28R 0596995/3135947	pahoehoe	39.91	10.14	3.54	14.59	10.85	13.28	2.97	***1.31***	0.95	0.20	0.03	97.80
MN	28R 0609388/3168817	aa	44.33	11.02	3.25	13.88	9.58	12.77	2.45	***1.02***	0.48	0.20	0.83	99.82
MQ	28R 0597389/3160187	pahoehoe	41.90	9.84	2.89	14.24	10.22	14.59	2.68	***0.71***	0.71	0.19	0.12	98.10
MR	28R 0611020/3167587	pahoehoe	45.00	12.52	3.49	12.84	10.36	8.41	2.94	***1.13***	0.54	0.16	0.24	97.63
VF	28R 0613361/3163377	aa	46.84	12.76	3.02	13.11	9.34	8.46	3.02	***0.83***	0.53	0.16	0.07	98.15
MM	28R 0607317/3180737	pahoehoe	43.83	11.87	2.85	13.35	10.37	11.63	2.86	***0.88***	0.69	0.18	0.33	98.84

Table 1: Sample locations as well as major and minor element oxide concentrations in weight percent (wt.%). Note that sums deviate from 100% due to uncertainties of individual measurements.

	CA	CG	MA	MC	MN	MQ	MR	VF	MM
Li	6.23	6.59	7.15	7.06	9.55	5.55	6.74	8.33	7.59
Be	1.40	1.57	1.29	1.53	1.09	1.05	1.29	1.13	1.09
B	1.21	1.51	0.81	1.35	1.02	0.71	1.02	1.00	0.82
Sc	25	23	23	23	25	21	28	25	23
V	259	255	222	255	210	204	249	226	214
Cr	304	411	442	421	457	435	324	356	393
Co	89	88	80	88	85	78	98	80	81
Ni	299	347	298	365	371	349	197	240	317
Cu	60	67	69	73	93	76	62	53	98
Zn	124	121	111	123	114	99	119	129	137
Ga	17	17	15	17	15	13	19	18	16
As	2.18	2.34	1.80	2.44	2.04	1.59	1.86	1.85	2.08
Se	0.44	0.44	0.38	0.44	0.35	0.36	0.46	0.38	0.39
Rb	25	29	22	28	18	9.85	22	13	18
Sr	774	816	570	824	511	621	617	518	711
Y	24	25	20	24	20	19	24	22	22
Zr	239	273	214	274	227	198	262	243	205
Nb	60	79	45	79	53	56	61	48	50
Mo	1.89	2.50	1.48	2.50	1.12	1.21	1.40	0.94	1.76
Ag	3.67	5.39	3.13	3.45	3.28	2.53	3.53	2.61	3.09
Cd	0.41	0.39	0.35	0.40	0.55	0.29	0.42	0.38	0.39

	CA	CG	MA	MC	MN	MQ	MR	VF	MM
Sn	2.18	2.43	2.36	2.88	1.95	1.68	2.02	2.42	2.08
Sb	0.12	0.11	0.07	0.11	0.09	0.07	0.07	0.18	0.07
Te	0.04	0.03	0.03	0.03	0.04	0.02	0.02	0.02	0.03
Cs	0.22	0.37	0.38	0.34	0.28	0.20	0.27	0.13	0.22
Ba	454	524	309	502	410	390	464	267	398
La	47	62	30	63	32	45	35	25	39
Ce	94	121	66	123	71	88	74	54	78
Pr	12	14	8.24	15	8.46	10	9.43	7.05	9.39
Nd	48	57	35	58	35	40	39	30	38
Sm	9.22	10	7.13	10	7.03	7.35	8.03	6.61	7.39
Eu	2.88	3.10	2.24	3.15	2.21	2.24	2.58	2.18	2.39
Gd	8.34	8.98	6.60	9.15	6.48	6.54	7.56	6.46	6.87
Tb	1.01	1.06	0.83	1.08	0.82	0.79	0.96	0.84	0.85
Dy	5.60	5.71	4.62	5.77	4.56	4.29	5.39	4.73	4.79
Ho	0.89	0.89	0.75	0.90	0.74	0.69	0.88	0.79	0.78
Er	2.25	2.20	1.90	2.22	1.88	1.74	2.24	2.00	2.00
Tm	0.27	0.26	0.23	0.26	0.23	0.21	0.27	0.25	0.24
Yb	1.61	1.52	1.39	1.51	1.40	1.25	1.65	1.48	1.47
Lu	0.22	0.21	0.19	0.20	0.19	0.17	0.23	0.20	0.20
Hf	5.68	6.35	5.22	6.37	5.39	4.47	6.29	5.61	4.73
Ta	4.20	5.46	3.49	5.59	4.18	3.73	4.69	3.72	3.60
W	561	633	592	531	431	411	1135	464	444
Hg	1.76	2.05	2.17	2.11	1.73	1.73	4.96	2.16	2.12
Tl	0.03	0.02	0.07	0.02	0.09	0.02	0.04	0.03	0.03
Pb	2.99	3.36	2.84	3.52	2.73	2.24	1.93	2.25	3.73
Bi	0.01	0.02	0.03	0.02	0.02	0.01	0.01	0.02	0.01
Th	4.33	6.04	2.94	6.10	3.12	4.13	3.11	2.12	3.54
U	0.97	1.33	0.68	1.30	0.61	0.83	0.70	0.43	0.88

Table 2: Trace element concentrations. Concentrations are given in parts per million (ppm).

APPENDIX B

Safety settings for semi automatic mode

Furnace		
name	**desired action**	**necessary conditions valve/relais/vacuum**
TPFUR	start	VFUR2 is open pressure at RPFUR is OK
	stop	VFUR1 is closed
RLFUR	on	outer furnace vacuum is OK VFUR1 is open UHV is OK cooling water is OK
Furnace main switch	stop	VFUR2 is closed
VFUR1	open	outer furnace vacuum is OK TPFUR is running
	close	Furnace main switch is off
VFUR2	open	RPFUR is on pressure at RPFUR is OK
	close	VFUR1 is closed TPFUR is not running

Pump line		
name	**desired action**	**necessary conditions valve/relais/vacuum**
TP2	stop	VPL5 is closed
TP1	start	Pressure at TP1 is OK
	stop	not allowed
DP	stop	VPL6 is closed
VPL4	open	forevacuum pressure is OK
VPL1	open	UHV is OK pressure between VL1 and 2 is OK
VPL5	open	VPL4 is closed TP2 is running
VPL2	open	ion gauge pressure (UHV) is OK VPL5 is closed
	close	ion gauge pressure (UHV) is OK pressure between VL1 and 2 is OK

Purification line		
name	**desired action**	**necessary conditions valve/relais/vacuum**
VGP2	open	UHV is OK

Pipette system/MS		
name	**desired action**	**necessary conditions valve/relais/vacuum**
V381	open	V382 is closed VAIR1 is closed
V382	open	V381 is closed
VAIR1	open	VAIR2 is closed V381 is closed
VAIR2	open	VAIR1 is closed

APPENDIX C

Equations used for error analysis on single heating steps of $^{40}Ar/^{39}Ar$ data

Partitial derivatives of equation (3):

$$\frac{\partial T}{\partial \lambda} = \frac{-\ln X}{\lambda^2} + \frac{F_u \times t \times e^{\lambda t_{st}}}{F_{st} \times \lambda \times X}$$

$$\frac{\partial T}{\partial t_{st}} = \frac{F_u \times e^{\lambda t_{st}}}{F_{st} \times X}$$

$$\frac{\partial T}{\partial F_u} = \frac{\left(e^{\lambda t_{st}} - 1\right)}{\lambda \times F_{st} \times X}$$

$$\frac{\partial T}{\partial F_{st}} = \frac{-F_u \times \left(e^{\lambda t_{st}} - 1\right)}{\lambda \times X \times F_{st}^2}$$

Based on equation (1.4) used at the VUA

$$F = \frac{\left\{ \left({}^{40}Ar_m - {}^{40}Ar_{bl}\right) - D \times \left({}^{36}Ar_m - {}^{36}Ar_{bl}\right) + \frac{E \times \left[{}^{36}Ar/{}^{37}Ar\right]_{Ca} \times \left({}^{37}Ar_m - {}^{37}Ar_{bl}\right) \times C_{37}}{\frac{0.75E}{D} + 0.25} + \frac{E \times \left[\frac{{}^{36}Cl}{{}^{38}Cl}\right]_P \times \lambda_{{}^{36}Cl} \times t_e \times \left({}^{38}Ar_m - {}^{38}Ar_{bl}\right)}{\frac{0.5E}{D} + 0.5} \right\}}{\left\{ \frac{\left({}^{39}Ar_m - {}^{39}Ar_{bl}\right) \times C_{39}}{\frac{0.25E}{D} + 0.75} - \frac{\left[{}^{39}Ar/{}^{37}Ar\right]_{Ca} \times \left({}^{37}Ar_m - {}^{37}Ar_{bl}\right) \times C_{37}}{\frac{0.75E}{D} + 0.25} \right\}} - \left[{}^{40}Ar/{}^{39}Ar\right]_K$$

which can be written as

$$F = \frac{P}{Q} - \left[{}^{40}Ar/{}^{39}Ar\right]_K$$

with

$$P = \left({}^{40}Ar_m - {}^{40}Ar_{bl}\right) - D \times \left({}^{36}Ar_m - {}^{36}Ar_{bl}\right) + \frac{E \times \left[{}^{36}Ar^{37}Ar\right]_{Ca} \times \left({}^{37}Ar_m - {}^{37}Ar_{bl}\right) \times C_{37}}{\frac{0.75E}{D} + 0.25} +$$

$$\frac{E \times \left(\frac{{}^{36}Cl}{{}^{38}Cl}\right)_P \times \lambda_{{}^{36}Cl} \times t_e \left({}^{38}Ar_m - {}^{38}Ar_{bl}\right)}{\frac{0.5E}{D} + 0.5}$$

and

$$Q=\frac{\left({}^{39}Ar_m-{}^{39}Ar_{bl}\right)\times C_{39}}{\frac{0.25E}{D}+0.75}-\frac{\left[{}^{39}Ar/{}^{37}Ar\right]_{Ca}\times\left({}^{37}Ar_m-{}^{37}Ar_{bl}\right)\times C_{37}}{\frac{0.75E}{D}+0.25}$$

variance can be calculated using the partitial derivatives:

$$\frac{\partial F}{\partial {}^{40}Ar_m}=\frac{1}{Q}$$

$$\frac{\partial F}{\partial {}^{39}Ar_m}=\frac{-P\times C_{39}}{Q^2\times\left(\frac{0.25E}{D}+0.75\right)}$$

$$\frac{\partial F}{\partial {}^{37}Ar_m}=\frac{\left\{E\times\left[{}^{36}Ar/{}^{37}Ar\right]_{Ca}\times C_{37}\times Q\right\}+\left\{\left[{}^{39}Ar/{}^{37}Ar\right]_{Ca}\times C_{37}\times P\right\}}{Q^2}$$

$$\frac{\partial F}{\partial {}^{36}Ar_m}=\frac{-D}{Q}$$

$$\frac{\partial F}{\partial {}^{40}Ar_{bl}}=\frac{-1}{Q}$$

$$\frac{\partial F}{\partial {}^{39}Ar_{bl}}=\frac{P\times C_{39}}{Q^2\times\left(\frac{0.25E}{D}+0.75\right)}$$

$$\frac{\partial F}{\partial {}^{37}Ar_{bl}}=\frac{\left\{-E\times\left[{}^{36}Ar/{}^{37}Ar\right]_{Ca}\times C_{37}\times Q\right\}-\left\{\left[{}^{39}Ar/{}^{37}Ar\right]_{Ca}\times C_{37}\times P\right\}}{Q^2}$$

$$\frac{\partial F}{\partial {}^{36}Ar_{bl}}=\frac{D}{Q}$$

$$\frac{\partial F}{\partial\left[{}^{36}Ar/{}^{37}Ar\right]_{Ca}}=\frac{E\times C_{37}\times\left({}^{37}Ar_m-{}^{37}Ar_{bl}\right)}{Q\times\left(\frac{0.75E}{D}+0.25\right)}$$

$$\frac{\partial F}{\partial\left[{}^{39}Ar/{}^{37}Ar\right]_{Ca}}=\frac{P\times\left({}^{37}Ar_m-{}^{37}Ar_{bl}\right)\times C_{37}}{Q^2\times\left(\frac{0.75E}{D}+0.25\right)}$$

$$\frac{\partial F}{\partial\left[{}^{40}Ar/{}^{39}Ar\right]_{K}}=-1$$

$$\frac{\partial F}{\partial\lambda_{39}}=-\frac{P}{Q^2}\times d\times\left({}^{39}Ar_m-{}^{39}Ar_{bl}\right)\times\frac{\left\{\left(\frac{0.25E}{D}+0.75\right)-e^{-\lambda_{39}t_e}\left(\frac{0.25E}{D}+0.75\right)\right\}\times\left(\lambda_{39}e^{\lambda_{39}t_e}t_e+e^{\lambda_{39}t_e}\right)+\left(\lambda_{39}e^{\lambda_{39}t_e}e^{-\lambda_{39}t_e}t_e\left(\frac{0.25E}{D}+0.75\right)\right)}{\left(\left(\frac{0.25E}{D}+0.75\right)-e^{-\lambda_{39}t_e}\left(\frac{0.25E}{D}+0.75\right)\right)^2}$$

$$\frac{\partial F}{\partial\lambda_{37}}=\frac{Q\times P'-P\times Q'}{Q^2}$$

with

$$P'=E\times\left[{}^{36}Ar{}^{37}Ar\right]_{Ca}\times\left({}^{37}Ar_m-{}^{37}Ar_{bl}\right)\times d\times$$

$$\frac{\left\{\left(\frac{0.75E}{D}+0.25\right)-e^{-\lambda_{37}t_e}\left(\frac{0.75E}{D}+0.25\right)\right\}\times\left(e^{\lambda_{37}t_e}+\lambda_{37}e^{\lambda_{37}t_e}t_e\right)-\lambda_{37}e^{\lambda_{37}t_e}e^{-\lambda_{37}t_e}t_e\left(\frac{0.75E}{D}+0.25\right)}{\left\{\left(\frac{0.75E}{D}+0.25\right)-e^{-\lambda_{37}t_e}\left(\frac{0.75E}{D}+0.25\right)\right\}^2}$$

and

$$Q'=-\left[{}^{39}Ar{}^{37}Ar\right]_{Ca}\times\left({}^{37}Ar_m-{}^{37}Ar_{bl}\right)\times d\times$$

$$\frac{\left\{\left(\frac{0.75E}{D}+0.25\right)-e^{-\lambda_{37}t_e}\left(\frac{0.75E}{D}+0.25\right)\right\}\times\left(e^{\lambda_{37}t_e}+\lambda_{37}e^{\lambda_{37}t_e}t_e\right)-\lambda_{37}e^{\lambda_{37}t_e}e^{-\lambda_{37}t_e}t_e\left(\frac{0.75E}{D}+0.25\right)}{\left\{\left(\frac{0.75E}{D}+0.25\right)-e^{-\lambda_{37}t_e}\left(\frac{0.75E}{D}+0.25\right)\right\}^2}$$

$$\frac{\partial F}{\partial D}=\frac{Q\times P'-Q'\times P}{Q^2}$$

with

$$P' = -\left({}^{36}Ar_m - {}^{36}Ar_{bl}\right) + \frac{0.75E^2 \times \left[{}^{36}Ar^{37}Ar\right]_{Ca} \times \left({}^{37}Ar_m - {}^{37}Ar_{bl}\right) \times C_{37}}{D^2 \times \left(\frac{0.75E}{D} + 0.25\right)^2} +$$

$$\frac{0.5E^2 \times \left(\frac{{}^{36}Cl}{{}^{38}Cl}\right)_P \times \lambda_{{}^{36}Cl} \times t_e \left({}^{38}Ar_m - {}^{38}Ar_{bl}\right)}{D^2 \left(\frac{0.5E}{D} + 0.5\right)^2}$$

and

$$Q' = \frac{0.25E \times \left({}^{39}Ar_m - {}^{39}Ar_{bl}\right) \times C_{39}}{D^2 \times \left(\frac{0.25E}{D} + 0.75\right)^2} -$$

$$\frac{0.75E \times \left[{}^{39}Ar^{37}Ar\right]_{Ca} \times \left({}^{37}Ar_m - {}^{37}Ar_{bl}\right) \times C_{37}}{D^2 \times \left(\frac{0.75E}{D} + 0.25\right)^2}$$

$$\frac{\partial F}{\partial E} = \frac{Q \times P' - Q' \times P}{Q^2}$$

with

$$P' = \frac{0.25 \times \left[{}^{36}Ar^{37}Ar\right]_{Ca} \times \left({}^{37}Ar_m - {}^{37}Ar_{bl}\right) \times C_{37}}{\left(\frac{0.75E}{D} + 0.25\right)^2} + \frac{0.5 \times \left(\frac{{}^{36}Cl}{{}^{38}Cl}\right)_P \times \lambda_{{}^{36}Cl} \times t_e \left({}^{38}Ar_m - {}^{38}Ar_{bl}\right)}{\left(\frac{0.5E}{D} + 0.5\right)^2}$$

and

$$Q' = -\frac{\frac{0.25}{D} \times \left({}^{39}Ar_m - {}^{39}Ar_{bl}\right) \times C_{39}}{\left(\frac{0.25E}{D} + 0.75\right)^2} + \frac{\frac{0.75}{D}\left[{}^{39}Ar/{}^{37}Ar\right]_{Ca} \times \left({}^{37}Ar_m - {}^{37}Ar_{bl}\right) \times C_{37}}{\left(\frac{0.75E}{D} + 0.25\right)^2}$$

$$\frac{\partial F}{\partial \lambda_{{}^{36}Cl}} = \frac{E \times \left(\frac{{}^{36}Cl}{{}^{38}Cl}\right)_P \times t_e \times \left({}^{38}Ar_m - {}^{38}Ar_{bl}\right)}{Q \times \left(\frac{0.5E}{D} + 0.5\right)}$$

APPENDIX D

Equations used for cosmogenic nuclide calculations

Self shielding correction (Vermeesch, 2007)

$$S_s = \frac{\Lambda}{\rho z}\left(1 - e^{\frac{\rho z}{\Lambda}}\right)$$ (Eq. 2 in Vermeesch (2007))

Neutron flux scaling factor

$$N_{1030}(P) = Y + \frac{A}{\left(1 + e^{-\left(\frac{P-X}{B}\right)}\right)^C}$$ (eq. 3 in Dunai,2001)

with P being the cutoff rigidity and A=0.5221, B=-1.7211, C=0.3345, X=4.2822 and Y=0.4952.

$$\Lambda(P) = y + \frac{a}{\left(1 + e^{-\left(\frac{P-x}{b}\right)}\right)^c}$$ (eq. 4 in Dunai(2001)

with a=17.183, b=2.060, c=5.9164, x=2.2964 and y=130.11.

$$N(z, P) = N_{1030}(P)\, e^{z(h)/\Lambda(P)}$$ (eq. 5 in Dunai (2001))

with

$$z(h) = d_0 - d$$ (appendix in Dunai(2000)

with atmospheric depths d (sampling site) and d_0 (sea level)

$$d = 10\, p / g_0$$ (appendix in Dunai(2000)

$$d_0 = 10\, p_0 / g_0$$ (appendix in Dunai(2000)

the long term average sea level pressure p at the sampling site

$$p = p_0\left(1 - \frac{\beta_0 h}{T_0}\right)^{\frac{g_0}{R_d \beta_0}}$$

where p_0 is the pressure at sea level (standard pressure 1013.25 mbar), β_0 the temperature decrease with elevation (6.5 mK/m), h is the altitude in meters, T_0 the temperature in Kelvin at sea level (standard temperature 15ºC = 288.15 K, use an appropriate value depending on the climatic region), g_0 the standard sea level value of the acceleration due to gravity (9.80665 m/s^2), R_d the gas constant (287.05 J/kg/K).

APPENDIX E

Argon incremental heating data from Fuerteventura showing ages calculated using air composition from Steiger & Jäger (1977) as well as Lee et al. (2006, using isochron data to determine trapped component composition)

Incremental Heating			36Ar(a)	37Ar(ca)	38Ar(cl)	39Ar(k)	40Ar(r)	Age ± 1σ (Ka)	40Ar(r) (%)	39Ar(k) (%)	K/Ca ± 1σ
07MQ009	750 °C		0.013716	0.169479	0.000000	0.231624	0.205277	458.8 ± 41.2	4.82	5.18	0.588 ± 0.026
07MQ198	750 °C		0.007427	0.093955	0.000000	0.124717	0.112425	466.7 ± 66.9	4.87	2.79	0.571 ± 0.036
07MQ010	775 °C		0.004409	0.156939	0.000000	0.230808	0.089446	200.6 ± 28.6	6.42	5.17	0.632 ± 0.029
07MQ199	780 °C		0.001277	0.188120	0.000000	0.318462	0.140653	228.7 ± 17.1	27.13	7.13	0.728 ± 0.038
07MQ011	800 °C	X	0.003696	0.147245	0.000000	0.258163	0.085053	170.6 ± 25.5	7.22	5.78	0.754 ± 0.037
07MQ200	810 °C	X	0.000727	0.179595	0.000000	0.334478	0.104108	161.2 ± 16.5	32.57	7.49	0.801 ± 0.042
07MQ012	825 °C	X	0.003982	0.151107	0.000000	0.279093	0.056677	105.1 ± 22.9	4.59	6.25	0.794 ± 0.037
07MQ201	840 °C	X	0.001066	0.126847	0.000000	0.223771	0.064047	148.2 ± 24.8	16.88	5.01	0.759 ± 0.045
07MQ202	840 °C	X	0.000902	0.080873	0.000000	0.130925	0.042295	167.3 ± 42.0	13.68	2.93	0.696 ± 0.041
07MQ013	850 °C	X	0.003954	0.082269	0.000000	0.149669	0.039916	138.1 ± 47.3	3.30	3.35	0.782 ± 0.037
07MQ014	900 °C	X	0.004914	0.127784	0.000000	0.208864	0.043454	107.7 ± 40.1	2.90	4.68	0.703 ± 0.035
07MQ203	900 °C	X	0.001888	0.143965	0.000000	0.230001	0.073684	165.9 ± 26.6	11.66	5.15	0.687 ± 0.036
07MQ015	950 °C	X	0.005259	0.120646	0.000000	0.144150	0.024005	86.2 ± 49.2	1.52	3.23	0.514 ± 0.023
07MQ204	950 °C	X	0.001661	0.112944	0.000000	0.159074	0.043186	140.6 ± 36.4	8.08	3.56	0.606 ± 0.037
07MQ016	1050 °C	X	0.007843	0.204363	0.000000	0.200276	0.072659	187.8 ± 41.1	3.04	4.48	0.421 ± 0.019
07MQ205	1050 °C	X	0.003280	0.224285	0.000000	0.227077	0.047644	108.6 ± 29.3	4.68	5.08	0.435 ± 0.023
07MQ017	1200 °C	X	0.026401	2.353517	0.000000	0.487610	0.156673	166.4 ± 29.5	1.97	10.92	0.089 ± 0.004
07MQ206	1200 °C	X	0.013783	2.375418	0.000000	0.528493	0.134944	132.2 ± 20.5	3.21	11.83	0.096 ± 0.005
		□	0.106185	7.039351	0.000000	4.467256	1.536145				

Information on Analysis	Results	40(r)/39(k) ± 1σ	Age ± 1σ (Ka)	MSWD	39Ar(k) (%,n)	K/Ca ± 1σ
sample CA using air composition from Steiger & Jäger	**Weighted Plateau**	0.2794 ± 0.0143 ± 5.12%	144.6 ± 7.5 ± 5.16%	0.91	79.73 14	0.143 ± 0.044
			External Error ± 7.5	0.97	Statistical T Ratio	
			Analytical Error ± 7.4	1.0000	Error Magnification	
Project = Fuerte05	**Total Fusion Age**	0.3439 ± 0.0143 ± 4.15%	178.0 ± 7.5 ± 4.19%		18	0.014 ± 0.000
Irradiation = VU61			External Error ± 7.5			
J = 0.0002870 ± 0.0000018			Analytical Error ± 7.4			
DRA 1 = 25.260 ± 0.076 Ma						

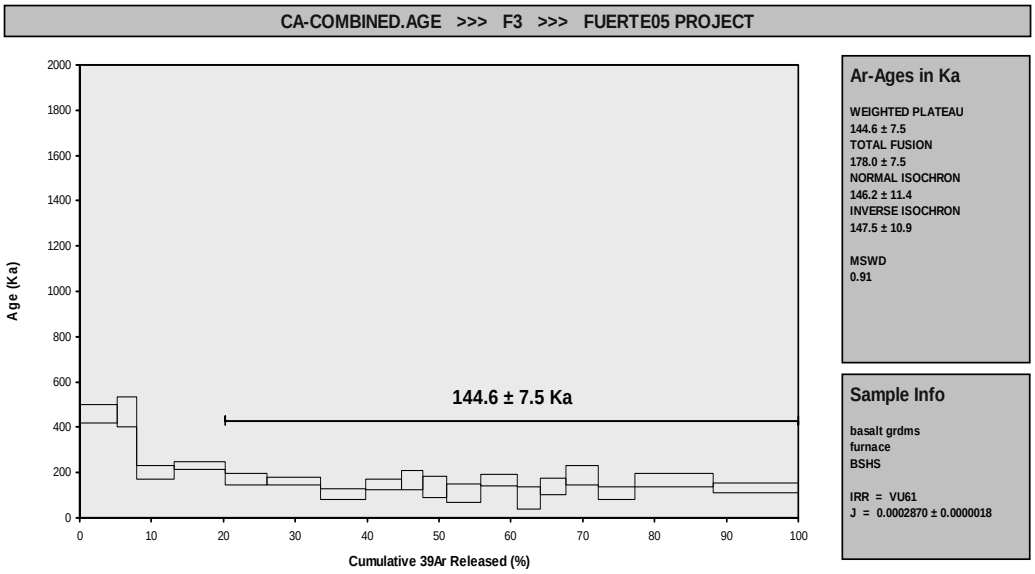

CA-COMBINED.AGE >>> F3 >>> FUERTE05 PROJECT

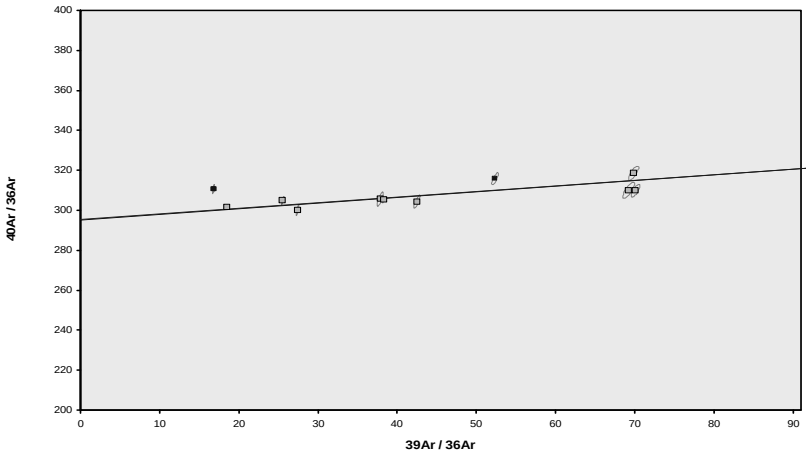

Ar-Ages in Ka

WEIGHTED PLATEAU
144.6 ± 7.5
TOTAL FUSION
178.0 ± 7.5
NORMAL ISOCHRON
146.2 ± 11.4
INVERSE ISOCHRON
147.5 ± 10.9

MSWD
0.98

40AR/36AR INTERCEPT
295.2 ± 1.0

Sample Info

basalt grdms
furnace
BSHS

IRR = VU61
J = 0.0002870 ± 0.0000018

CA-COMBINED.AGE >>> F3 >>> FUERTE05 PROJECT

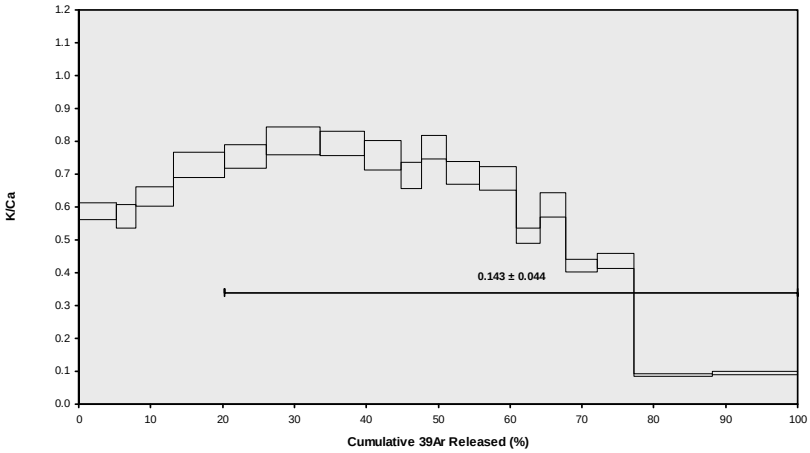

Ar-Ages in Ka

WEIGHTED PLATEAU
144.6 ± 7.5
TOTAL FUSION
178.0 ± 7.5
NORMAL ISOCHRON
146.2 ± 11.4
INVERSE ISOCHRON
147.5 ± 10.9

Sample Info

basalt grdms
furnace
BSHS

IRR = VU61
J = 0.0002870 ± 0.0000018

Incremental Heating			36Ar(a)	37Ar(ca)	38Ar(cl)	39Ar(k)	40Ar(r)	Age ± 1σ (Ka)	40Ar(r) (%)	39Ar(k) (%)	K/Ca ± 1σ
07MQ009	750 °C		0.013754	0.169868	0.000000	0.231795	0.207870	471.7 ± 48.3	4.88	5.18	0.587 ± 0.006
07MQ198	750 °C		0.007448	0.094275	0.000000	0.124814	0.113542	478.5 ± 73.6	4.92	2.79	0.569 ± 0.022
07MQ010	775 °C		0.004421	0.157237	0.000000	0.230977	0.090208	205.4 ± 30.4	6.48	5.17	0.632 ± 0.011
07MQ199	780 °C		0.001280	0.188517	0.000000	0.318722	0.140819	232.4 ± 17.6	27.16	7.13	0.727 ± 0.012
07MQ011	800 °C	X	0.003707	0.147591	0.000000	0.258364	0.085661	174.4 ± 26.9	7.27	5.78	0.753 ± 0.018
07MQ200	810 °C	X	0.000729	0.180049	0.000000	0.334737	0.104312	163.9 ± 16.8	32.63	7.49	0.799 ± 0.014
07MQ012	825 °C	X	0.003993	0.151425	0.000000	0.279313	0.057322	108.0 ± 24.3	4.65	6.25	0.793 ± 0.016
07MQ201	840 °C	X	0.001070	0.127179	0.000000	0.223947	0.064005	150.3 ± 25.4	16.86	5.01	0.757 ± 0.024
07MQ202	840 °C	X	0.000905	0.081110	0.000000	0.131026	0.042346	170.0 ± 43.1	13.70	2.93	0.695 ± 0.021
07MQ013	850 °C	X	0.003965	0.082409	0.000000	0.149786	0.040562	142.4 ± 49.6	3.36	3.35	0.782 ± 0.015
07MQ014	900 °C	X	0.004927	0.128080	0.000000	0.209022	0.044304	111.5 ± 42.4	2.96	4.68	0.702 ± 0.017
07MQ203	900 °C	X	0.001893	0.144311	0.000000	0.230171	0.074232	169.6 ± 27.4	11.74	5.15	0.686 ± 0.011
07MQ015	950 °C	X	0.005273	0.120914	0.000000	0.144263	0.024995	91.1 ± 52.8	1.58	3.23	0.513 ± 0.007
07MQ204	950 °C	X	0.001666	0.113205	0.000000	0.159203	0.043424	143.5 ± 37.8	8.13	3.56	0.605 ± 0.022
07MQ016	1050 °C	X	0.007865	0.204844	0.000000	0.200438	0.073877	193.9 ± 45.5	3.09	4.48	0.421 ± 0.006
07MQ205	1050 °C	X	0.003289	0.224684	0.000000	0.227244	0.048415	112.1 ± 30.6	4.76	5.08	0.435 ± 0.008
07MQ017	1200 °C	X	0.026476	2.358691	0.000000	0.487990	0.160912	173.5 ± 36.6	2.02	10.92	0.089 ± 0.001
07MQ206	1200 °C	X	0.013823	2.380741	0.000000	0.528908	0.137109	136.4 ± 21.3	3.26	11.83	0.096 ± 0.001
		□	0.106485	7.055130	0.000000	4.470719	1.553913				

Information on Analysis

sample CA using air composition from

Project = Fuerte05
Irradiation = VU61
J = 0.0002909 ± 0.0000018
DRA 1 = 25.420 ± 0.076 Ma

Results	40(r)/39(k) ± 1σ	Age ± 1σ (Ka)	MSWD	39Ar(k) (%,n)	K/Ca ± 1σ
Weighted Plateau	0.2814 ± 0.0148 ± 5.29%	148.0 ± 7.8 ± 5.29%	0.81	79.73 14	0.105 ± 0.022
		External Error ± 7.9	0.97	Statistical T Ratio	
		Analytical Error ± 7.8	1.0000	Error Magnification	
Total Fusion Age	0.3476 ± 0.0155 ± 4.46%	182.8 ± 8.2 ± 4.50%		18	0.014 ± 0.000
		External Error ± 8.4			
		Analytical Error ± 8.1			

CA-NEW.AGE >>> CA >>> FUERTE05 PROJECT

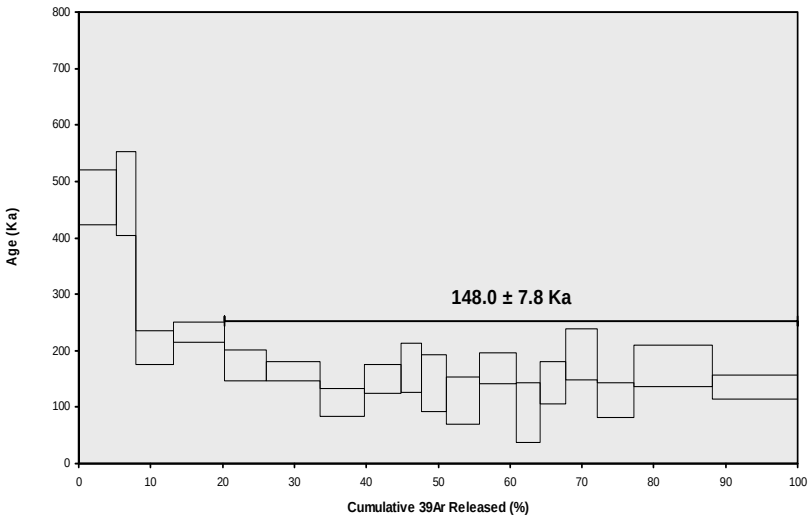

Ar-Ages in Ka

WEIGHTED PLATEAU
148.0 ± 7.8
TOTAL FUSION
182.8 ± 8.2
NORMAL ISOCHRON
147.3 ± 11.5
INVERSE ISOCHRON
148.7 ± 10.9

MSWD
0.81

Sample Info

groundmass
furnace
BSHS

IRR = VU61
J = 0.0002909 ± 0.0000018

CA-NEW.AGE >>> CA >>> FUERTE05 PROJECT

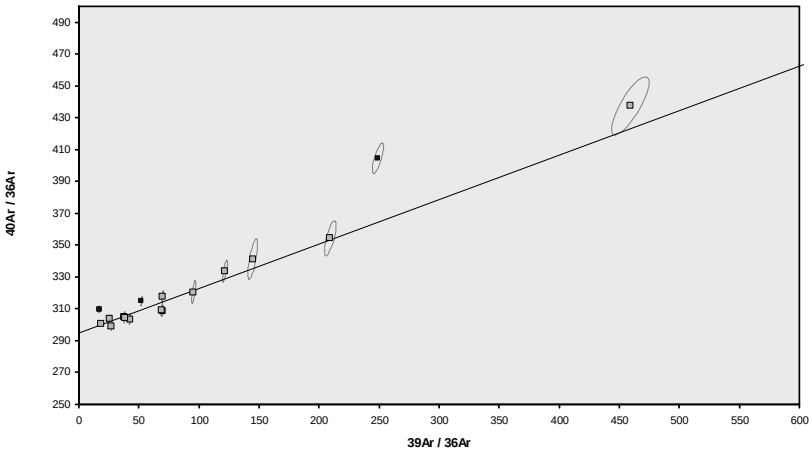

Ar-Ages in Ka

WEIGHTED PLATEAU
148.0 ± 7.8
TOTAL FUSION
182.8 ± 8.2
NORMAL ISOCHRON
147.3 ± 11.5
INVERSE ISOCHRON
148.7 ± 10.9

MSWD
0.99

40AR/36AR INTERCEPT
294.5 ± 1.0

Sample Info

groundmass
furnace
BSHS

IRR = VU61
J = 0.0002909 ± 0.0000018

CA-NEW.AGE >>> CA >>> FUERTE05 PROJECT

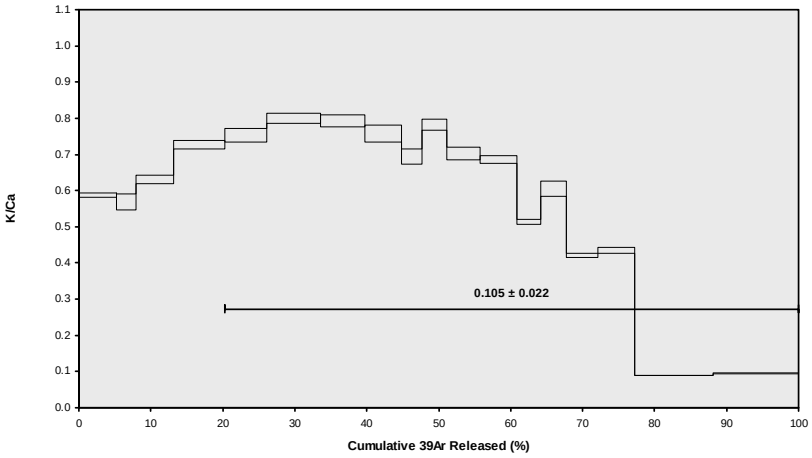

Ar-Ages in Ka

WEIGHTED PLATEAU
148.0 ± 7.8
TOTAL FUSION
182.8 ± 8.2
NORMAL ISOCHRON
147.3 ± 11.5
INVERSE ISOCHRON
148.7 ± 10.9

Sample Info

groundmass
furnace
BSHS

IRR = VU61
J = 0.0002909 ± 0.0000018

Incremental Heating			36Ar(a)	37Ar(ca)	38Ar(cl)	39Ar(k)	40Ar(r)	Age ± 1σ (Ka)	40Ar(r) (%)	39Ar(k) (%)	K/Ca ± 1σ
07MQ063	750 °C		0.023602	0.031956	0.001061	0.104973	0.047405	235.4 ± 116.4	0.68	4.61	1.413 ± 0.089
07MQ064	775 °C	X	0.008752	0.036345	0.001140	0.131561	0.006258	24.8 ± 59.5	0.24	5.78	1.557 ± 0.087
07MQ065	800 °C	X	0.011778	0.042331	0.001172	0.139009	0.002875	10.8 ± 71.7	0.08	6.11	1.412 ± 0.086
07MQ066	825 °C	X	0.059656	0.039024	0.001296	0.125626	0.021672	89.9 ± 187.3	0.12	5.52	1.384 ± 0.083
07MQ067	850 °C	X	0.015131	0.062522	0.001541	0.214983	0.030776	74.6 ± 45.0	0.68	9.44	1.479 ± 0.086
07MQ068	875 °C	X	0.012557	0.074151	0.001866	0.261624	0.037180	74.1 ± 34.9	0.99	11.49	1.517 ± 0.078
07MQ069	900 °C	X	0.012651	0.072001	0.001706	0.241767	0.019874	42.9 ± 38.2	0.53	10.62	1.444 ± 0.076
07MQ070	925 °C	X	0.016222	0.061491	0.001463	0.201032	0.014455	37.5 ± 50.8	0.30	8.83	1.406 ± 0.072
07MQ071	975 °C		0.032721	0.064455	0.001453	0.198263	0.085868	225.8 ± 68.6	0.88	8.71	1.323 ± 0.068
07MQ072	1075 °C		0.195504	0.135667	0.005528	0.187508	0.020482	56.9 ± 184.6	0.04	8.24	0.594 ± 0.028
07MQ073	1300 °C		0.238839	6.819210	0.011783	0.469900	0.000000	0.0 ± 0.0	0.00	20.64	0.030 ± 0.001
		Π	0.627412	7.439152	0.030010	2.276245	0.286844				

Information on Analysis
sample CG using air composition from Steiger & Jäger (1977)
Project = Fuerte05 Irradiation = VU61 J = 0.0002890 ± 0.0000018 DRA 1 = 25.260 ± 0.076 Ma

Results	40(r)/39(k) ± 1σ	Age ± 1σ (Ka)	MSWD	39Ar(k) (%,n)	K/Ca ± 1σ
Weighted Plateau	0.1016 ± 0.0357 ± 35.09%	53.0 ± 18.6 ± 35.10%	0.23	57.80 7	1.454 ± 0.031
		External Error ± 18.6	1.01	Statistical T Ratio	
		Analytical Error ± 18.6	1.0000	Error Magnification	
Total Fusion Age	0.1260 ± 0.0431 ± 34.18%	65.7 ± 22.5 ± 34.19%		11	0.007 ± 0.000
		External Error ± 22.5			
		Analytical Error ± 22.5			

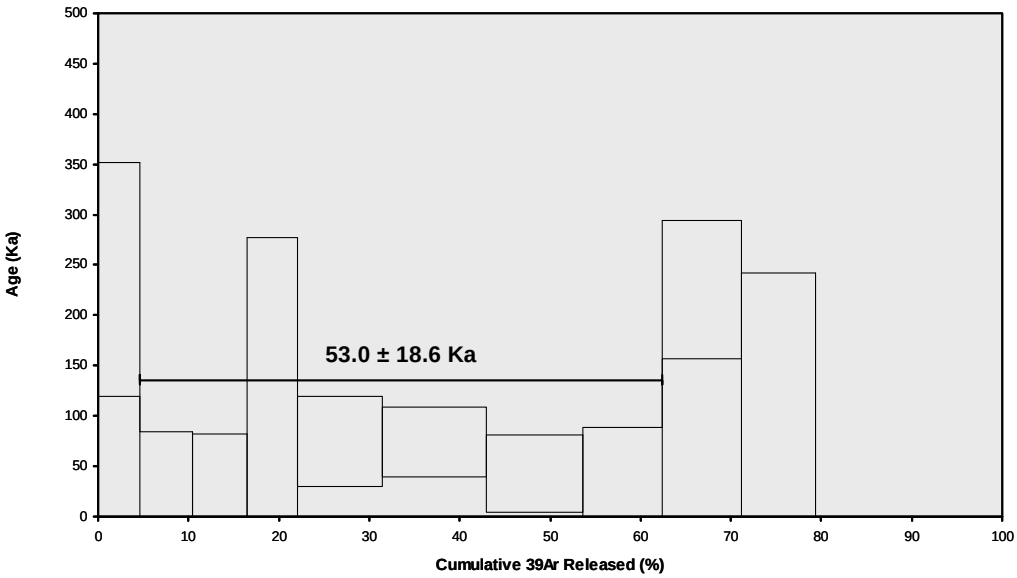

CG.AGE >>> F11 >>> FUERTE05 PROJECT

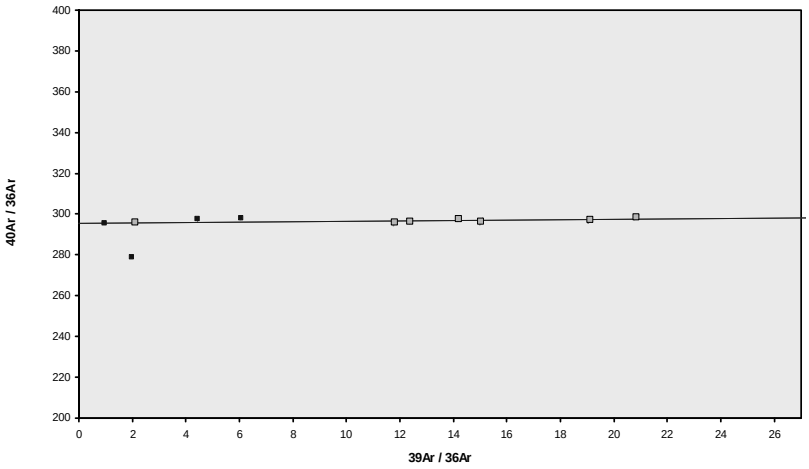

Ar-Ages in Ka

WEIGHTED PLATEAU
53.0 ± 18.6
TOTAL FUSION
65.7 ± 22.5
NORMAL ISOCHRON
52.6 ± 34.0
INVERSE ISOCHRON
52.7 ± 27.1

MSWD
0.27

40AR/36AR INTERCEPT
295.5 ± 0.8

Sample Info

basalt grdms
furnace
BSHS

IRR = VU61
J = 0.0002890 ± 0.0000018

CG.AGE >>> F11 >>> FUERTE05 PROJECT

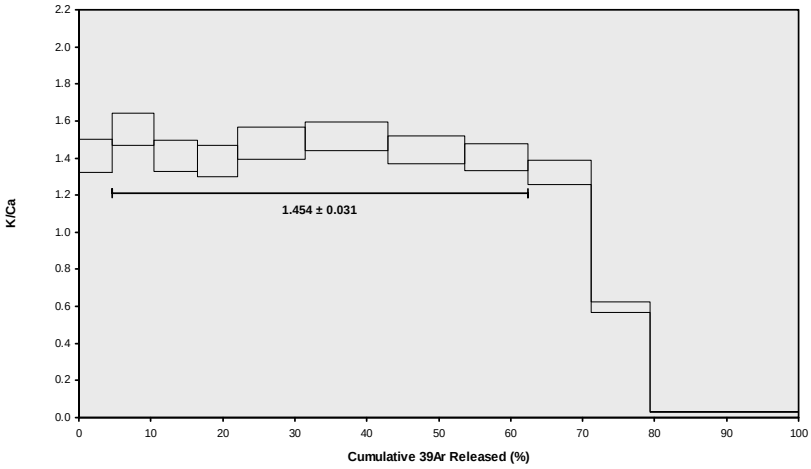

Ar-Ages in Ka

WEIGHTED PLATEAU
53.0 ± 18.6
TOTAL FUSION
65.7 ± 22.5
NORMAL ISOCHRON
52.6 ± 34.0
INVERSE ISOCHRON
52.7 ± 27.1

Sample Info

basalt grdms
furnace
BSHS

IRR = VU61
J = 0.0002890 ± 0.0000018

Incremental Heating			36Ar(a)	37Ar(ca)	38Ar(cl)	39Ar(k)	40Ar(r)	Age ± 1σ (Ka)	40Ar(r) (%)	39Ar(k) (%)	K/Ca ± 1σ
07MQ063	750 °C		0.023663	0.032081	0.001059	0.105046	0.048330	242.0 ± 157.7	0.69	4.61	1.408 ± 0.062
07MQ064	775 °C	X	0.008777	0.036460	0.001142	0.131663	0.005969	23.8 ± 67.6	0.23	5.78	1.553 ± 0.052
07MQ065	800 °C	X	0.011810	0.042383	0.001173	0.139116	0.002622	9.9 ± 79.7	0.08	6.11	1.411 ± 0.060
07MQ066	825 °C	X	0.059818	0.039116	0.001287	0.125722	0.021581	90.3 ± 280.3	0.12	5.52	1.382 ± 0.057
07MQ067	850 °C	X	0.015171	0.062631	0.001543	0.215141	0.030895	75.5 ± 53.6	0.69	9.44	1.477 ± 0.056
07MQ068	875 °C	X	0.012591	0.074284	0.001869	0.261820	0.037157	74.7 ± 40.1	0.99	11.49	1.516 ± 0.039
07MQ069	900 °C	X	0.012686	0.072192	0.001710	0.241949	0.019882	43.2 ± 43.8	0.53	10.62	1.441 ± 0.040
07MQ070	925 °C	X	0.016266	0.061681	0.001464	0.201183	0.014428	37.7 ± 60.8	0.30	8.83	1.403 ± 0.035
07MQ071	975 °C		0.032816	0.064611	0.001451	0.198422	0.084059	222.8 ± 103.5	0.86	8.71	1.321 ± 0.033
07MQ072	1075 °C		0.195980	0.135919	0.005502	0.187656	0.036683	102.8 ± 508.2	0.06	8.24	0.594 ± 0.008
07MQ073	1300 °C		0.239190	6.827473	0.011772	0.470131	0.000000	0.0 ± 0.0	0.00	20.64	0.030 ± 0.000
		◊	0.628768	7.448830	0.029972	2.277849	0.301607				

Information on Analysis

sample CG using air composition from Lee et al. (2006)

Project = Fuerte05
Irradiation = VU61
J = 0.0002909 ± 0.0000018
DRA 1 = 25.420 ± 0.076 Ma

Results	40(r)/39(k) ± 1σ	Age ± 1σ (Ka)	MSWD	39Ar(k) (%,n)	K/Ca ± 1σ
Weighted Plateau	0.1002 ± 0.0410 ± 40.89%	52.7 ± 21.6 ± 40.89%	0.18	57.80 7	1.454 ± 0.023
		External Error ± 21.6	1.01	Statistical T Ratio	
		Analytical Error ± 21.6	1.0000	Error Magnification	
Total Fusion Age	0.1324 ± 0.0904 ± 68.29%	69.7 ± 47.6 ± 68.29%		11	0.007 ± 0.000
		External Error ± 47.6			
		Analytical Error ± 47.6			

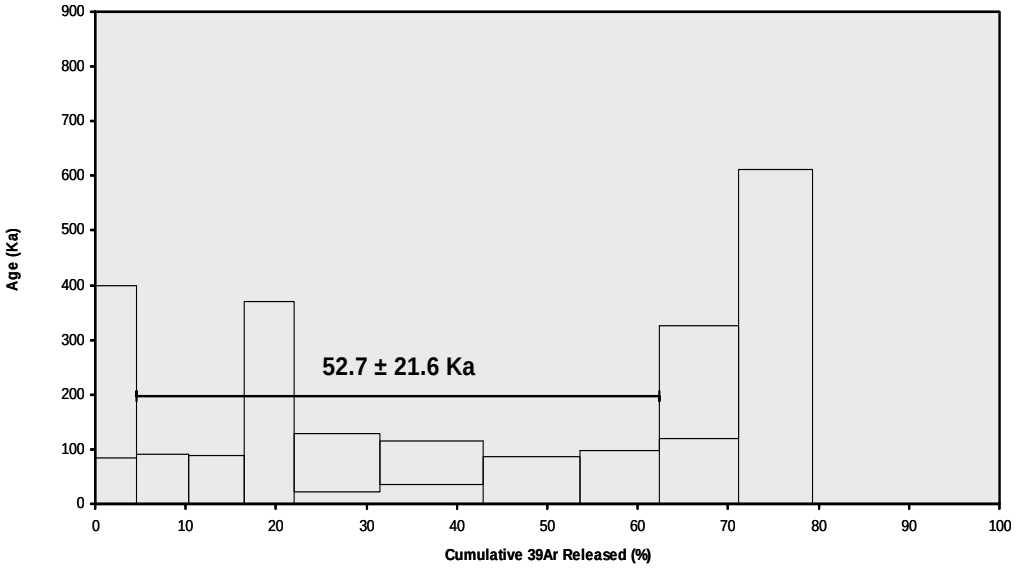

CG-NEW.AGE >>> CG >>> FUERTE05 PROJECT

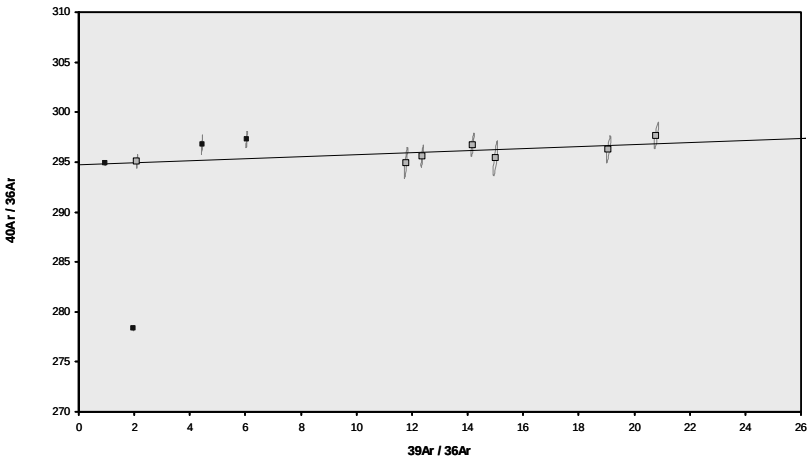

Ar-Ages in Ka

WEIGHTED PLATEAU
52.7 ± 21.6
TOTAL FUSION
69.7 ± 47.6
NORMAL ISOCHRON
53.0 ± 31.8
INVERSE ISOCHRON
53.2 ± 25.5

MSWD
0.31

40AR/36AR INTERCEPT
294.7 ± 0.8

Sample Info

groundmass
furnace
BSHS

IRR = VU61
J = 0.0002909 ± 0.0000018

CG-NEW.AGE >>> CG >>> FUERTE05 PROJECT

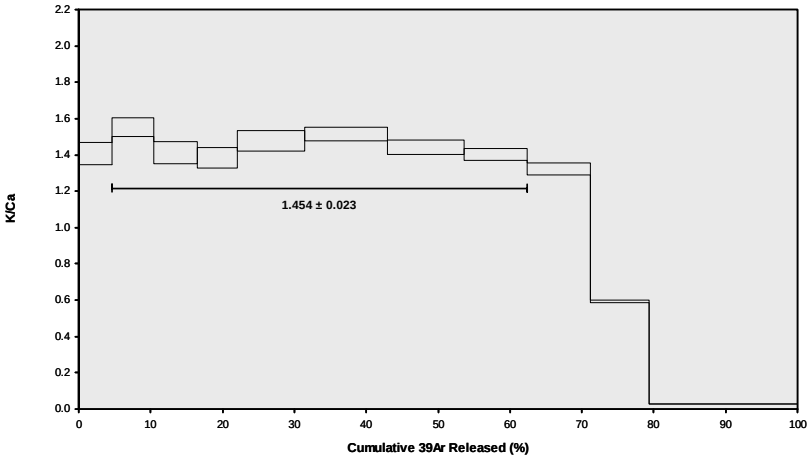

Ar-Ages in Ka

WEIGHTED PLATEAU
52.7 ± 21.6
TOTAL FUSION
69.7 ± 47.6
NORMAL ISOCHRON
53.0 ± 31.8
INVERSE ISOCHRON
53.2 ± 25.5

Sample Info

groundmass
furnace
BSHS

IRR = VU61
J = 0.0002909 ± 0.0000018

Incremental Heating			36Ar(a)	37Ar(ca)	38Ar(cl)	39Ar(k)	40Ar(r)	Age ± 1σ (Ka)	40Ar(r) (%)	39Ar(k) (%)	K/Ca ± 1σ
07MQ234	750 °C		0.026458	0.072196	0.000874	0.083676	0.155268	967.2 ± 158.4	1.95	3.12	0.498 ± 0.030
07MQ074	750 °C		0.044631	0.139722	0.001591	0.163870	0.286927	912.7 ± 113.6	2.13	6.11	0.504 ± 0.024
07MQ075	775 °C	X	0.022401	0.218209	0.001370	0.215015	0.139196	337.5 ± 55.5	2.06	8.01	0.424 ± 0.021
07MQ235	775 °C	X	0.026063	0.178770	0.001301	0.183188	0.137099	390.2 ± 72.3	1.75	6.83	0.441 ± 0.025
07MQ076	800 °C	X	0.019083	0.208322	0.001351	0.195151	0.113583	303.4 ± 53.2	1.97	7.27	0.403 ± 0.019
07MQ236	800 °C	X	0.023339	0.203338	0.000991	0.186000	0.108338	303.7 ± 64.1	1.55	6.93	0.393 ± 0.022
07MQ237	825 °C	X	0.017180	0.122034	0.000829	0.123690	0.076720	323.4 ± 85.7	1.49	4.61	0.436 ± 0.026
07MQ077	825 °C	X	0.020055	0.183660	0.001457	0.186959	0.105553	294.3 ± 87.8	1.75	6.97	0.438 ± 0.021
07MQ078	850 °C	X	0.012965	0.080986	0.001014	0.119015	0.069915	306.3 ± 83.1	1.79	4.43	0.632 ± 0.040
07MQ238	850 °C	X	0.027229	0.154381	0.001313	0.180035	0.102029	295.4 ± 72.0	1.25	6.71	0.501 ± 0.031
07MQ079	900 °C	X	0.034227	0.171073	0.001307	0.233899	0.138156	307.9 ± 56.6	1.35	8.72	0.588 ± 0.029
07MQ239	900 °C	X	0.052284	0.167517	0.001653	0.251797	0.157159	325.4 ± 73.8	1.01	9.38	0.646 ± 0.036
07MQ080	950 °C	X	0.037187	0.116062	0.000716	0.101098	0.056626	292.0 ± 157.6	0.51	3.77	0.375 ± 0.018
07MQ240	950 °C	X	0.061259	0.099823	0.000741	0.107518	0.105160	509.9 ± 189.6	0.58	4.01	0.463 ± 0.026
07MQ081	1050 °C		0.091668	0.115731	0.000904	0.047426	0.154523	1698.0 ± 502.9	0.57	1.77	0.176 ± 0.009
07MQ241	1200 °C		0.272065	1.195873	0.008877	0.130342	0.000000	0.0 ± 0.0	0.00	4.86	0.047 ± 0.002
07MQ082	1250 °C		0.170148	4.173029	0.004146	0.174869	0.000000	0.0 ± 0.0	0.00	6.52	0.018 ± 0.001
		□	0.958241	7.600726	0.030437	2.683547	1.906252				

Information on Analysis
sample MA using air composition from Steiger & Jäger (1977)
Project = Fuerte05 Irradiation = VU60 J = 0.0002890 ± 0.0000018 DRA 1 = 25.260 ± 0.076 Ma

Results	40(r)/39(k) ± 1σ	Age ± 1σ (Ka)	MSWD	39Ar(k) (%,n)	K/Ca ± 1σ
Weighted Plateau	0.6147 ± 0.0402 ± 6.53%	320.5 ± 21.0 ± 6.56%	0.23	77.63 12	0.445 ± 0.022
		External Error ± 21.0	0.98	Statistical T Ratio	
		Analytical Error ± 20.9	1.0000	Error Magnification	
Total Fusion Age	0.7103 ± 0.0423 ± 5.95%	370.3 ± 22.2 ± 5.98%		17	0.008 ± 0.000
		External Error ± 22.2			
		Analytical Error ± 22.0			

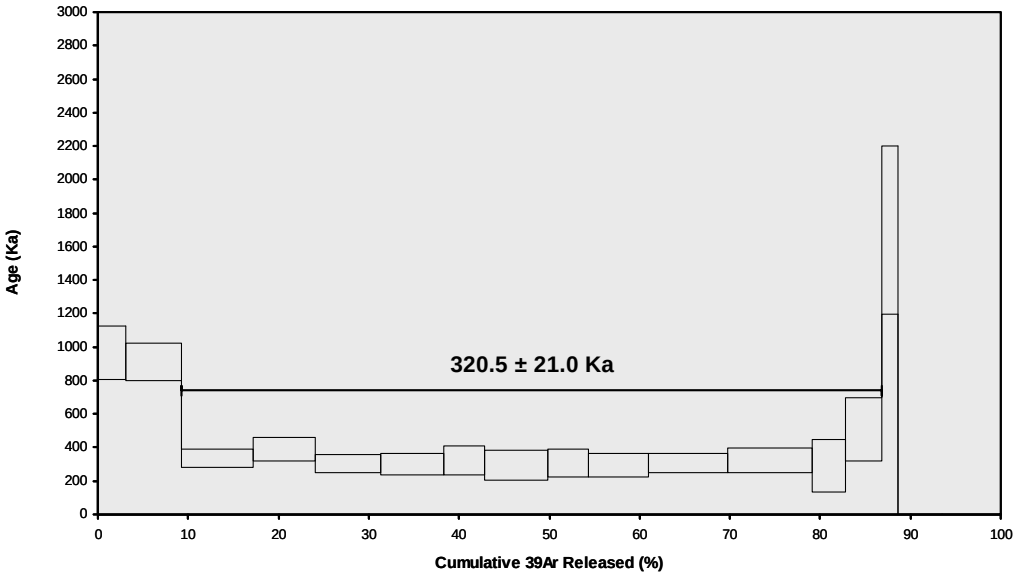

MA-COMBINED.AGE >>> F12 >>> FUERTE05 PROJECT

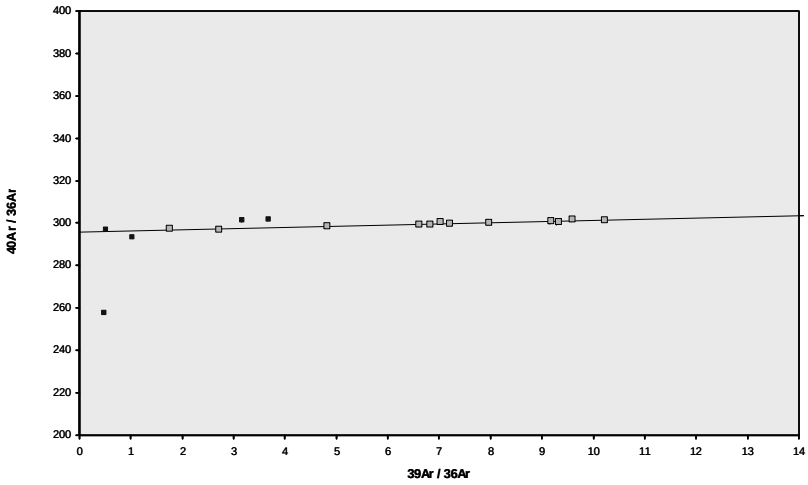

Ar-Ages in Ka

WEIGHTED PLATEAU
320.5 ± 21.0
TOTAL FUSION
370.3 ± 22.2
NORMAL ISOCHRON
286.3 ± 50.1
INVERSE ISOCHRON
286.3 ± 48.6

MSWD
0.19

40AR/36AR INTERCEPT
296.0 ± 0.6

Sample Info

basalt grdmass
furnace
BSHS

IRR = VU60
J = 0.0002890 ± 0.0000018

MA-COMBINED.AGE >>> F12 >>> FUERTE05 PROJECT

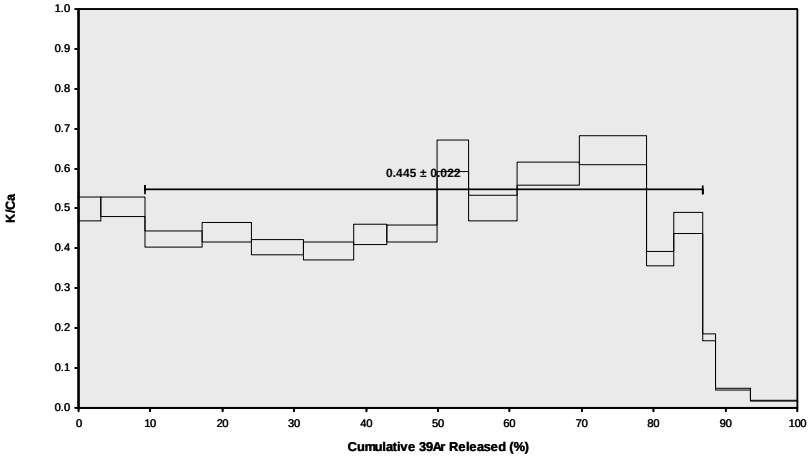

Ar-Ages in Ka

WEIGHTED PLATEAU
320.5 ± 21.0
TOTAL FUSION
370.3 ± 22.2
NORMAL ISOCHRON
286.3 ± 50.1
INVERSE ISOCHRON
286.3 ± 48.6

Sample Info

basalt grdmass
furnace
BSHS

IRR = VU60
J = 0.0002890 ± 0.0000018

Incremental Heating			36Ar(a)	37Ar(ca)	38Ar(cl)	39Ar(k)	40Ar(r)	Age ± 1σ (Ka)	40Ar(r) (%)	39Ar(k) (%)	K/Ca ± 1σ
07MQ074	750 °C		0.044746	0.140037	0.001586	0.163987	0.266259	853.9 ± 133.5	1.98	6.11	0.504 ± 0.009
07MQ234	750 °C		0.026528	0.072339	0.000870	0.083736	0.142541	895.2 ± 176.7	1.79	3.12	0.498 ± 0.016
07MQ075	775 °C	X	0.022467	0.218693	0.001370	0.215187	0.126448	309.1 ± 60.7	1.87	8.01	0.423 ± 0.008
07MQ235	775 °C	X	0.026135	0.179184	0.001300	0.183324	0.123896	355.5 ± 80.4	1.58	6.83	0.440 ± 0.010
07MQ076	800 °C	X	0.019134	0.208710	0.001352	0.195293	0.104218	280.7 ± 58.0	1.81	7.27	0.402 ± 0.006
07MQ236	800 °C	X	0.023400	0.203744	0.000990	0.186134	0.097314	275.0 ± 75.6	1.39	6.93	0.393 ± 0.008
07MQ077	825 °C	X	0.020113	0.184090	0.001457	0.187107	0.094648	266.1 ± 91.9	1.57	6.97	0.437 ± 0.008
07MQ237	825 °C	X	0.017229	0.122270	0.000828	0.123787	0.067135	285.3 ± 96.8	1.30	4.61	0.435 ± 0.013
07MQ078	850 °C	X	0.013003	0.081093	0.001014	0.119110	0.062593	276.4 ± 90.6	1.60	4.43	0.632 ± 0.028
07MQ238	850 °C	X	0.027308	0.154653	0.001312	0.180178	0.086828	253.5 ± 81.1	1.07	6.71	0.501 ± 0.018
07MQ079	900 °C	X	0.034322	0.171420	0.001304	0.234080	0.120096	269.9 ± 67.9	1.17	8.72	0.587 ± 0.011
07MQ239	900 °C	X	0.052438	0.167910	0.001646	0.252003	0.127583	266.3 ± 92.4	0.82	9.38	0.645 ± 0.014
07MQ080	950 °C	X	0.037268	0.116270	0.000712	0.101158	0.044090	229.3 ± 183.8	0.40	3.77	0.374 ± 0.007
07MQ240	950 °C	X	0.061437	0.100115	0.000729	0.107605	0.071012	347.1 ± 243.5	0.39	4.01	0.462 ± 0.012
07MQ081	1050 °C		0.091908	0.115961	0.000885	0.047461	0.111186	1231.9 ± 737.5	0.41	1.77	0.176 ± 0.003
07MQ241	1200 °C		0.273101	1.199620	0.008826	0.130513	0.000000	0.0 ± 0.0	0.00	4.86	0.047 ± 0.000
07MQ082	1250 °C		0.170976	4.189329	0.004098	0.175129	0.000000	0.0 ± 0.0	0.00	6.52	0.018 ± 0.000
			0.961512	7.625437	0.030279	2.685794	1.645845				

Information on Analysis

sample MA using air composition from Lee et al. (2006)

Project = Fuerte05
Irradiation = VU60
J = 0.0002909 ± 0.0000018
DRA 1 = 25.420 ± 0.076 Ma

Results	40(r)/39(k) ± 1σ	Age ± 1σ (Ka)	MSWD	39Ar(k) (%,n)	K/Ca ± 1σ
Weighted Plateau	0.5421 ± 0.0451 ± 8.32%	285.2 ± 23.8 ± 8.34%	0.13	77.63 12	0.435 ± 0.021
		External Error ± 23.9	0.98	Statistical T Ratio	
		Analytical Error ± 23.7	1.0000	Error Magnification	
Total Fusion Age	0.6128 ± 0.0512 ± 8.36%	322.3 ± 27.0 ± 8.38%		17	0.008 ± 0.000
		External Error ± 27.2			
		Analytical Error ± 26.9			

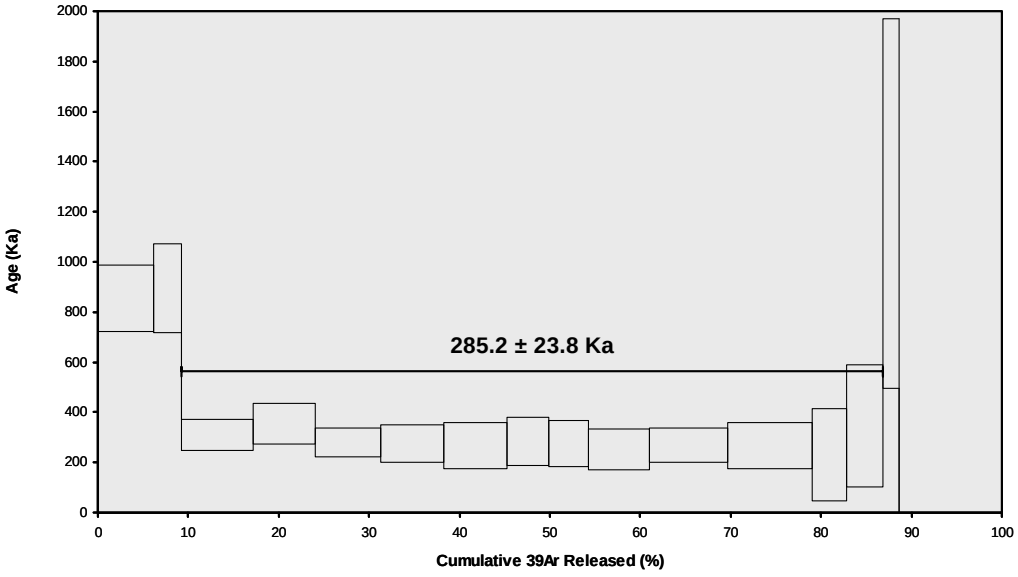

MA-NEW.AGE >>> MA >>> FUERTE05 PROJECT

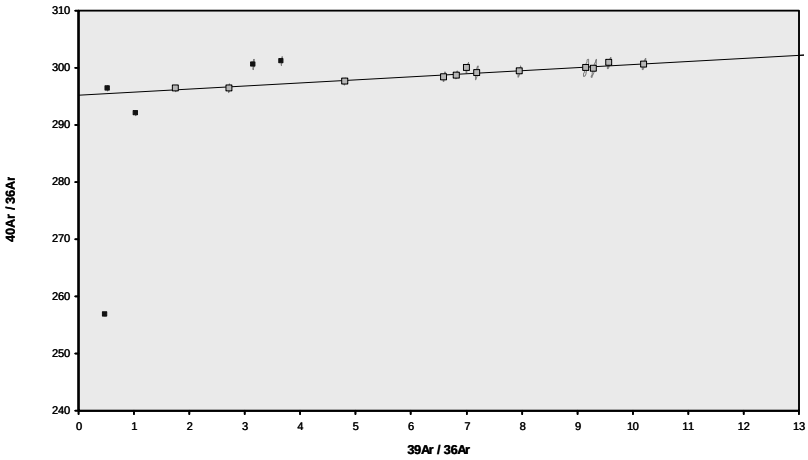

Ar-Ages in Ka

WEIGHTED PLATEAU
285.2 ± 23.8
TOTAL FUSION
322.3 ± 27.0
NORMAL ISOCHRON
285.9 ± 45.7
INVERSE ISOCHRON
286.0 ± 44.5

MSWD
0.21

40AR/36AR INTERCEPT
295.2 ± 0.6

Sample Info

groundmass
furnace
BSHS

IRR = VU60
J = 0.0002909 ± 0.0000018

MA-NEW.AGE >>> MA >>> FUERTE05 PROJECT

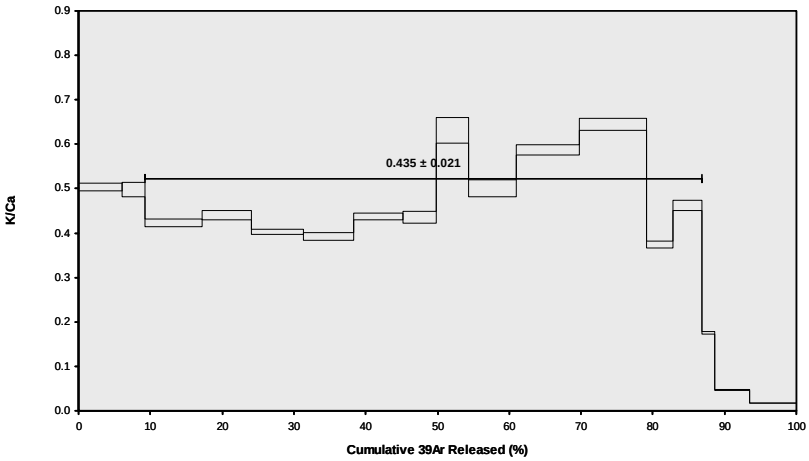

Ar-Ages in Ka

WEIGHTED PLATEAU
285.2 ± 23.8
TOTAL FUSION
322.3 ± 27.0
NORMAL ISOCHRON
285.9 ± 45.7
INVERSE ISOCHRON
286.0 ± 44.5

Sample Info

groundmass
furnace
BSHS

IRR = VU60
J = 0.0002909 ± 0.0000018

Incremental Heating			36Ar(a)	37Ar(ca)	38Ar(cl)	39Ar(k)	40Ar(r)	Age ± 1σ (Ka)	40Ar(r) (%)	39Ar(k) (%)	K/Ca ± 1σ
07MQ217	750 °C		0.006650	0.023182	0.000519	0.063430	0.045756	373.5 ± 122.9	2.28	1.64	1.177 ± 0.106
07MQ036	750 °C		0.008459	0.023463	0.000813	0.087942	0.043959	258.8 ± 92.9	1.73	2.27	1.612 ± 0.091
07MQ037	800 °C	X	0.007251	0.044748	0.001387	0.189842	0.034138	93.1 ± 43.4	1.57	4.90	1.824 ± 0.093
07MQ218	800 °C	X	0.008125	0.061882	0.001599	0.279299	0.065310	121.1 ± 28.5	2.65	7.20	1.941 ± 0.123
07MQ038	825 °C	X	0.007535	0.037947	0.001163	0.163335	0.033602	106.5 ± 50.1	1.49	4.21	1.851 ± 0.131
07MQ219	830 °C	X	0.003013	0.049196	0.001162	0.206373	0.057449	144.1 ± 29.4	6.06	5.32	1.804 ± 0.133
07MQ039	850 °C	X	0.006504	0.029205	0.000886	0.163650	0.022033	69.7 ± 50.5	1.13	4.22	2.410 ± 0.167
07MQ220	860 °C	X	0.005316	0.042437	0.001086	0.215062	0.041795	100.6 ± 32.6	2.59	5.55	2.179 ± 0.201
07MQ040	875 °C	X	0.028042	0.033743	0.000646	0.168877	0.009422	28.9 ± 77.2	0.11	4.35	2.152 ± 0.115
07MQ221	890 °C	X	0.017775	0.053642	0.001529	0.252119	0.050528	103.8 ± 46.2	0.95	6.50	2.021 ± 0.132
07MQ041	900 °C	X	0.008240	0.041415	0.001424	0.183303	0.051059	144.2 ± 43.1	2.05	4.73	1.903 ± 0.119
07MQ222	920 °C	X	0.012594	0.065743	0.001400	0.264541	0.049564	97.0 ± 40.8	1.31	6.82	1.730 ± 0.119
07MQ042	925 °C	X	0.017138	0.034760	0.000841	0.152140	0.015377	52.3 ± 76.7	0.30	3.92	1.882 ± 0.107
07MQ043	950 °C	X	0.011222	0.028084	0.000710	0.113822	0.006467	29.4 ± 80.8	0.19	2.94	1.743 ± 0.091
07MQ223	950 °C		0.012291	0.046259	0.001274	0.194705	0.094877	252.3 ± 50.2	2.55	5.02	1.810 ± 0.138
07MQ044	1000 °C		0.015871	0.035502	0.000544	0.092964	0.111743	622.3 ± 111.1	2.33	2.40	1.126 ± 0.062
07MQ045	1150 °C		0.267308	0.684543	0.003217	0.234501	0.000000	0.0 ± 0.0	0.00	6.05	0.147 ± 0.007
07MQ224	1200 °C		0.236486	2.131902	0.011758	0.546534	0.000000	0.0 ± 0.0	0.00	14.09	0.110 ± 0.006
07MQ046	1300 °C		0.048845	6.539782	0.005677	0.305521	1.004409	1701.4 ± 66.6	6.51	7.88	0.020 ± 0.001
		¬	0.728665	10.007434	0.037633	3.877959	1.737491				

Information on Analysis
sample MC using air composition from Steiger & Jäger (1977)
Project = Fuerte05
Irradiation = VU61
J = 0.0002870 ± 0.0000018
DRA 1 = 25.260 ± 0.076 Ma

Results	40(r)/39(k) ± 1σ	Age ± 1σ (Ka)	MSWD	39Ar(k) (%,n)	K/Ca ± 1σ
Weighted Plateau	0.2096 ± 0.0235 ± 11.22%	108.5 ± 12.2 ± 11.24%	0.52	60.66 12	1.906 ± 0.050
		External Error ± 12.2	0.98	Statistical T Ratio	
		Analytical Error ± 12.2	1.0000	Error Magnification	
Total Fusion Age	0.4480 ± 0.0211 ± 4.72%	232.0 ± 11.0 ± 4.76%		19	0.009 ± 0.000
		External Error ± 11.0			
		Analytical Error ± 10.9			

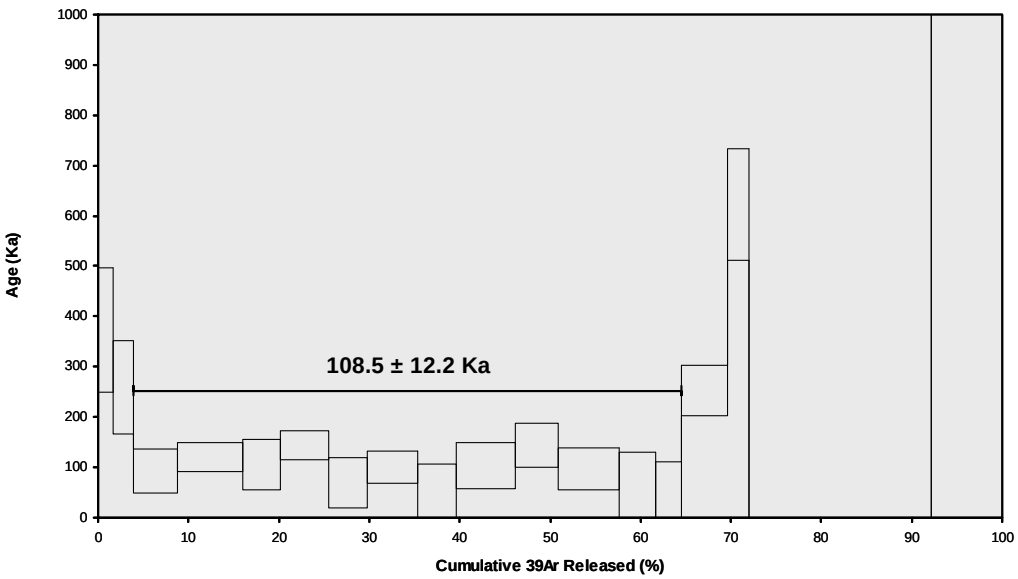

MC-COMBINED.AGE >>> F7 >>> FUERTE05 PROJECT

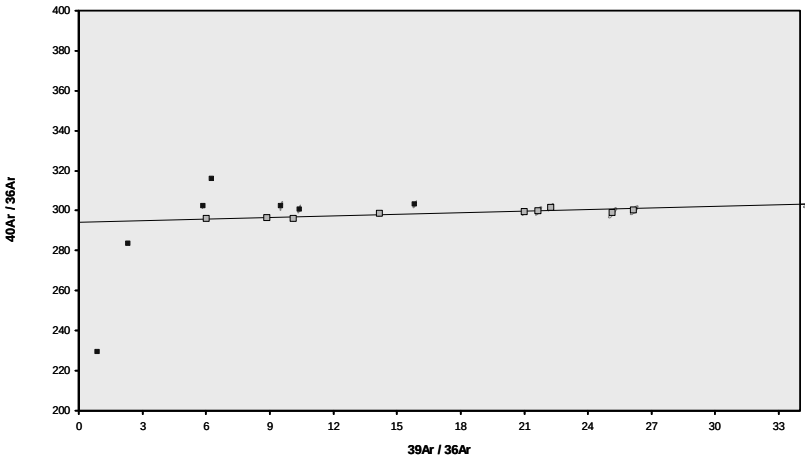

Ar-Ages in Ka

WEIGHTED PLATEAU
108.5 ± 12.2
TOTAL FUSION
232.0 ± 11.0
NORMAL ISOCHRON
138.6 ± 21.1
INVERSE ISOCHRON
138.9 ± 20.4

MSWD
0.27

40AR/36AR INTERCEPT
294.1 ± 0.8

Sample Info

basalt grdmass
furnace
BSHS

IRR = VU61
J = 0.0002870 ± 0.0000018

MC-COMBINED.AGE >>> F7 >>> FUERTE05 PROJECT

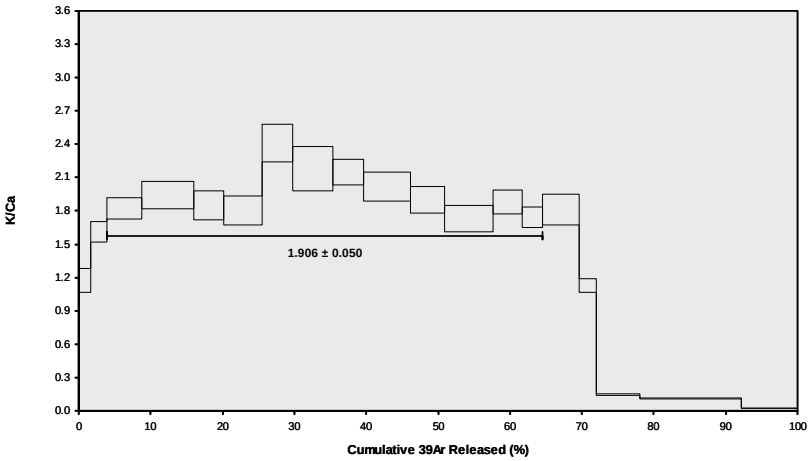

Ar-Ages in Ka

WEIGHTED PLATEAU
108.5 ± 12.2
TOTAL FUSION
232.0 ± 11.0
NORMAL ISOCHRON
138.6 ± 21.1
INVERSE ISOCHRON
138.9 ± 20.4

Sample Info

basalt grdmass
furnace
BSHS

IRR = VU61
J = 0.0002870 ± 0.0000018

Incremental Heating			36Ar(a)	37Ar(ca)	38Ar(cl)	39Ar(k)	40Ar(r)	Age ± 1σ (Ka)	40Ar(r) (%)	39Ar(k) (%)	K/Ca ± 1σ
07MQ036	750 °C		0.008483	0.023528	0.000813	0.088007	0.055653	330.3 ± 103.6	2.19	2.28	1.608 ± 0.059
07MQ217	750 °C		0.006670	0.023349	0.000520	0.063481	0.054560	448.9 ± 133.0	2.71	1.64	1.169 ± 0.090
07MQ037	800 °C	X	0.007271	0.044868	0.001390	0.189984	0.044371	122.0 ± 45.9	2.04	4.92	1.821 ± 0.048
07MQ218	800 °C	X	0.008147	0.062028	0.001603	0.279504	0.076875	143.7 ± 31.8	3.12	7.23	1.938 ± 0.073
07MQ038	825 °C	X	0.007556	0.038039	0.001165	0.163461	0.044092	140.9 ± 53.5	1.95	4.23	1.848 ± 0.103
07MQ219	830 °C	X	0.003022	0.049342	0.001166	0.206541	0.061438	155.4 ± 30.5	6.48	5.35	1.800 ± 0.099
07MQ039	850 °C	X	0.006523	0.029268	0.000889	0.163777	0.030922	98.6 ± 53.9	1.59	4.24	2.406 ± 0.128
07MQ220	860 °C	X	0.005331	0.042494	0.001090	0.215231	0.048961	118.8 ± 34.7	3.04	5.57	2.178 ± 0.166
07MQ040	875 °C	X	0.028119	0.033859	0.000642	0.169006	0.048511	149.9 ± 103.7	0.58	4.37	2.146 ± 0.066
07MQ221	890 °C	X	0.017824	0.053713	0.001530	0.252311	0.075253	155.8 ± 56.8	1.42	6.53	2.020 ± 0.082
07MQ041	900 °C	X	0.008262	0.041510	0.001426	0.183438	0.062858	179.0 ± 48.2	2.53	4.75	1.900 ± 0.084
07MQ222	920 °C	X	0.012628	0.065923	0.001403	0.264741	0.067213	132.6 ± 45.1	1.78	6.85	1.727 ± 0.082
07MQ042	925 °C	X	0.017186	0.034869	0.000840	0.152255	0.039181	134.4 ± 92.8	0.77	3.94	1.878 ± 0.070
07MQ043	950 °C	X	0.011254	0.028149	0.000710	0.113913	0.021519	98.7 ± 90.0	0.65	2.95	1.740 ± 0.051
07MQ223	950 °C		0.012325	0.046420	0.001276	0.194851	0.112063	300.4 ± 56.3	3.01	5.04	1.805 ± 0.105
07MQ044	1000 °C		0.015915	0.035530	0.000542	0.093033	0.133792	751.1 ± 131.1	2.79	2.41	1.126 ± 0.037
07MQ045	1150 °C		0.205810	0.555919	0.007082	0.216692	0.987224	2378.3 ± 463.4	1.61	5.61	0.168 ± 0.001
07MQ224	1200 °C		0.237466	2.139198	0.011729	0.547303	0.000000	0.0 ± 0.0	0.00	14.17	0.110 ± 0.001
07MQ046	1300 °C		0.048955	6.551213	0.005678	0.305707	1.079427	1843.5 ± 87.3	6.99	7.91	0.020 ± 0.000
		□	0.668747	9.899217	0.041495	3.863237	3.043912				

Information on Analysis
sample MC using air composition from Lee et al. (2006)
Project = Fuerte05 Irradiation = VU61 J = 0.0002889 ± 0.0000018 DRA 1 = 25.420 ± 0.076 Ma

Results	40(r)/39(k) ± 1σ	Age ± 1σ (Ka)	MSWD	39Ar(k) (%,n)	K/Ca ± 1σ
Weighted Plateau	0.2658 ± 0.0255 ± 9.60%	138.8 ± 13.4 ± 9.62%	0.21	60.94 12	1.891 ± 0.047
		External Error ± 13.4	0.98	Statistical T Ratio	
		Analytical Error ± 13.3	1.0000	Error Magnification	
Total Fusion Age	0.7879 ± 0.0558 ± 7.08%	411.5 ± 29.3 ± 7.11%		19	0.009 ± 0.000
		External Error ± 29.5			
		Analytical Error ± 29.2			

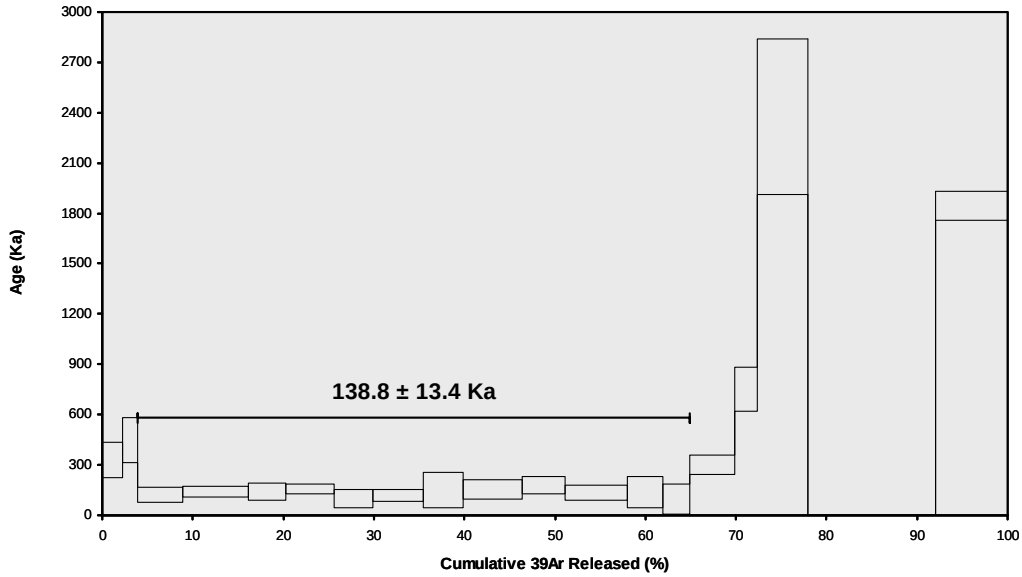

MC-NEW.AGE >>> MC >>> FUERTE05 PROJECT

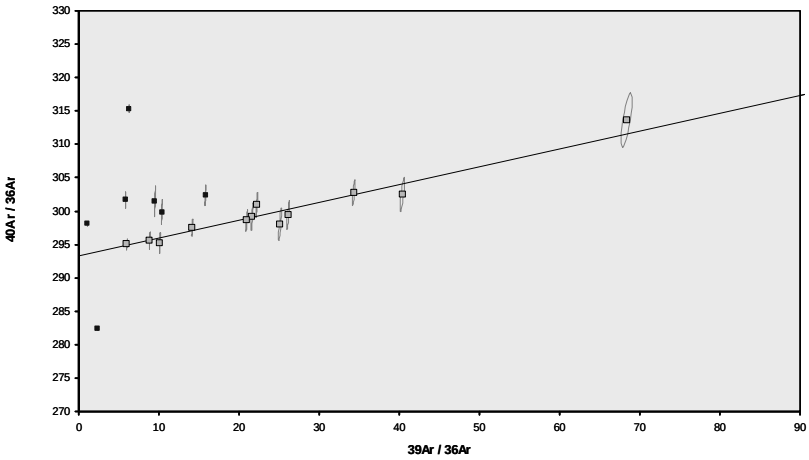

Ar-Ages in Ka

WEIGHTED PLATEAU
138.8 ± 13.4
TOTAL FUSION
411.5 ± 29.3
NORMAL ISOCHRON
139.3 ± 20.8
INVERSE ISOCHRON
139.6 ± 20.2

MSWD
0.28

40AR/36AR INTERCEPT
293.3 ± 0.8

Sample Info

groundmass
furnace
BSHS

IRR = VU61
J = 0.0002889 ± 0.0000018

MC-NEW.AGE >>> MC >>> FUERTE05 PROJECT

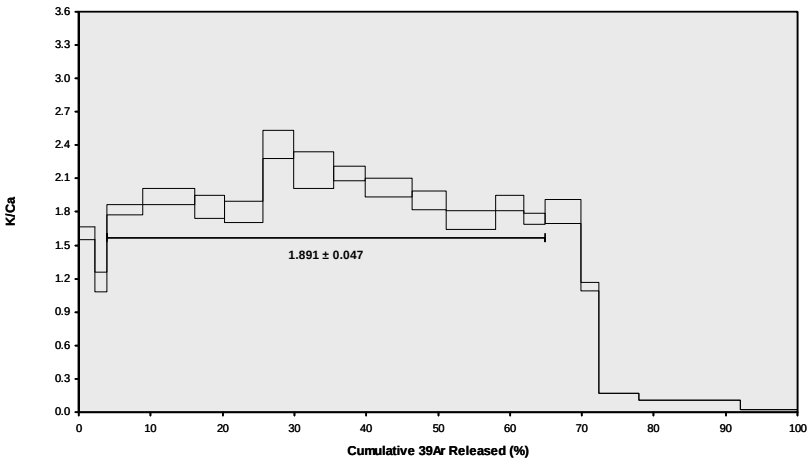

Ar-Ages in Ka

WEIGHTED PLATEAU
138.8 ± 13.4
TOTAL FUSION
411.5 ± 29.3
NORMAL ISOCHRON
139.3 ± 20.8
INVERSE ISOCHRON
139.6 ± 20.2

Sample Info

groundmass
furnace
BSHS

IRR = VU61
J = 0.0002889 ± 0.0000018

Incremental Heating			36Ar(a)	37Ar(ca)	38Ar(cl)	39Ar(k)	40Ar(r)	Age ± 1σ (Ka)	40Ar(r) (%)	39Ar(k) (%)	K/Ca ± 1σ
07MQ047	750 °C	X	0.011336	0.218349	0.001531	0.220266	0.177283	416.7 ± 116.6	5.03	6.73	0.434 ± 0.020
08MQ057	750 °C	X	0.021953	0.359348	0.005101	0.747202	0.615446	426.4 ± 36.7	8.66	22.83	0.894 ± 0.026
07MQ048	775 °C	X	0.006490	0.255671	0.000978	0.190105	0.133578	363.8 ± 133.5	6.51	5.81	0.320 ± 0.015
08MQ058	775 °C	X	0.003848	0.235795	0.001004	0.295173	0.188075	329.9 ± 84.8	14.19	9.02	0.538 ± 0.016
07MQ049	800 °C	X	0.006685	0.273904	0.000762	0.163763	0.102355	323.6 ± 154.3	4.93	5.00	0.257 ± 0.012
08MQ059	800 °C	X	0.003115	0.313922	0.000569	0.254480	0.170253	346.4 ± 98.0	15.60	7.77	0.349 ± 0.010
07MQ050	850 °C	X	0.010894	0.275714	0.000583	0.166559	0.113466	352.7 ± 154.5	3.40	5.09	0.260 ± 0.012
08MQ060	850 °C	X	0.062798	0.476092	0.000436	0.271047	0.097612	186.5 ± 119.5	0.52	8.28	0.245 ± 0.007
07MQ051	925 °C	X	0.024587	0.417449	0.000866	0.227278	0.150402	342.6 ± 119.0	2.03	6.94	0.234 ± 0.011
08MQ061	925 °C	X	0.008247	0.546769	0.000000	0.196678	0.202655	533.4 ± 129.4	7.68	6.01	0.155 ± 0.004
07MQ052	1000 °C	X	0.016630	0.202541	0.000230	0.083517	0.086028	533.3 ± 311.2	1.72	2.55	0.177 ± 0.008
07MQ053	1150 °C	X	0.017039	0.341639	0.000003	0.060567	0.112064	957.7 ± 438.7	2.18	1.85	0.076 ± 0.003
08MQ062	1200 °C	X	0.027596	1.871741	0.000036	0.198428	0.248921	649.4 ± 137.5	2.96	6.06	0.046 ± 0.001
07MQ054	1300 °C		0.080515	4.845197	0.001845	0.198502	1.968634	5127.7 ± 164.0	7.64	6.06	0.018 ± 0.001
		□	0.301733	10.634131	0.013944	3.273565	4.366774				

Information on Analysis
sample MM using air composition from Steiger & Jäger (1977)
Project = Fuerte05 Irradiation = VU61 J = 0.0002870 ± 0.0000018 DRA 1 = 25.260 ± 0.076 Ma

Results	40(r)/39(k) ± 1σ	Age ± 1σ (Ka)	MSWD	39Ar(k) (%,n)	K/Ca ± 1σ
Weighted Plateau	0.7789 ± 0.0504 ± 6.47%	403.2 ± 26.2 ± 6.50%	0.96	93.94 13	0.080 ± 0.024
		External Error ± 26.2	0.97	Statistical T Ratio	
		Analytical Error ± 26.1	1.0000	Error Magnification	
Total Fusion Age	1.3340 ± 0.0597 ± 4.48%	690.5 ± 31.2 ± 4.52%		14	0.007 ± 0.000
		External Error ± 31.2			
		Analytical Error ± 30.9			

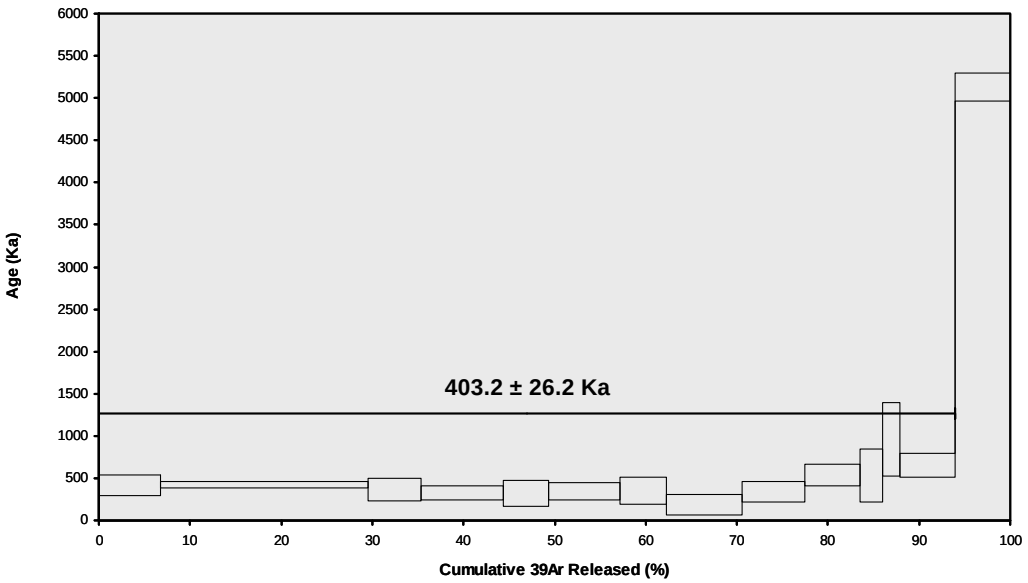

MM-COMBINED.AGE >>> F8 >>> FUERTE05 PROJECT

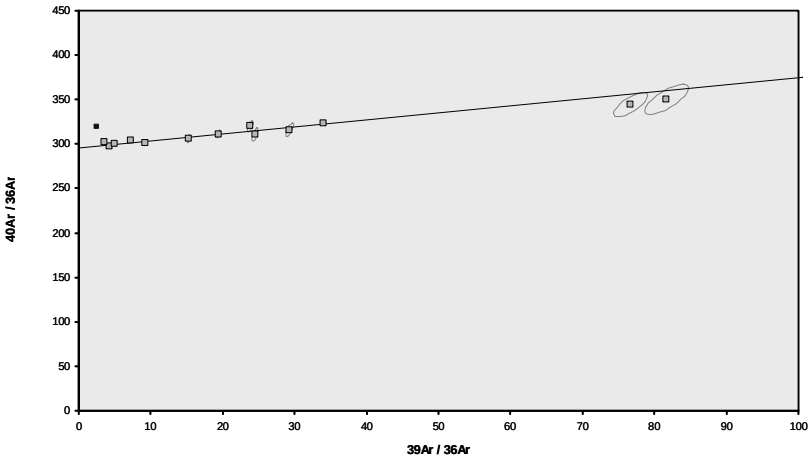

Ar-Ages in Ka

WEIGHTED PLATEAU
403.2 ± 26.2
TOTAL FUSION
690.5 ± 31.2
NORMAL ISOCHRON
410.8 ± 36.0
INVERSE ISOCHRON
412.8 ± 34.9

MSWD
1.03

40AR/36AR INTERCEPT
295.2 ± 1.0

Sample Info

basalt grdms
furnace
BSHS

IRR = VU61
J = 0.0002870 ± 0.0000018

MM-COMBINED.AGE >>> F8 >>> FUERTE05 PROJECT

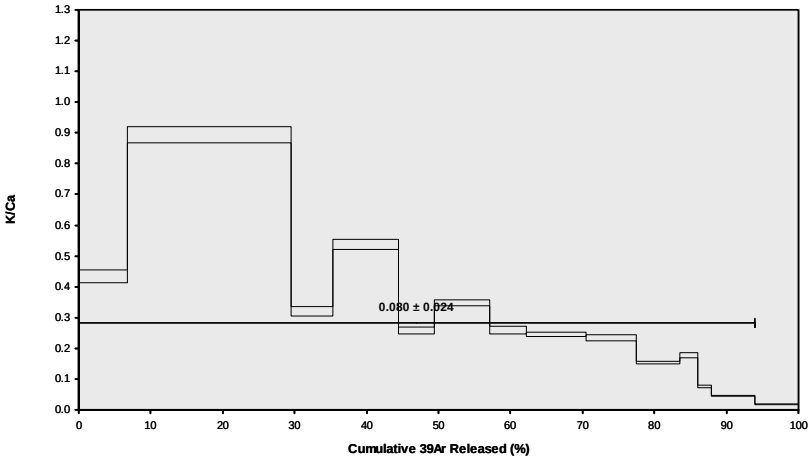

Ar-Ages in Ka

WEIGHTED PLATEAU
403.2 ± 26.2
TOTAL FUSION
690.5 ± 31.2
NORMAL ISOCHRON
410.8 ± 36.0
INVERSE ISOCHRON
412.8 ± 34.9

Sample Info

basalt grdms
furnace
BSHS

IRR = VU61
J = 0.0002870 ± 0.0000018

Incremental Heating			36Ar(a)	37Ar(ca)	38Ar(cl)	39Ar(k)	40Ar(r)	Age ± 1σ (Ka)	40Ar(r) (%)	39Ar(k) (%)	K/Ca ± 1σ
07MQ047	750 °C	X	0.011368	0.218823	0.001534	0.220437	0.165629	392.4 ± 119.4	4.70	6.73	0.433 ± 0.005
08MQ057	750 °C	X	0.021968	0.359543	0.005105	0.747362	0.606540	423.9 ± 38.9	8.54	22.82	0.894 ± 0.012
07MQ048	775 °C	X	0.006507	0.256196	0.000981	0.190241	0.127363	349.7 ± 135.7	6.21	5.81	0.319 ± 0.004
08MQ058	775 °C	X	0.003861	0.236379	0.001011	0.295436	0.183632	324.7 ± 85.9	13.85	9.02	0.537 ± 0.007
07MQ049	800 °C	X	0.006704	0.274507	0.000764	0.163883	0.095562	304.6 ± 156.9	4.60	5.00	0.257 ± 0.002
08MQ059	800 °C	X	0.003126	0.314700	0.000573	0.254708	0.166498	341.4 ± 99.2	15.26	7.78	0.348 ± 0.004
07MQ050	850 °C	X	0.010923	0.276278	0.000584	0.166679	0.102669	321.7 ± 158.2	3.08	5.09	0.259 ± 0.004
08MQ060	850 °C	X	0.062541	0.474595	0.000451	0.270742	0.160964	310.5 ± 150.6	0.86	8.27	0.245 ± 0.003
07MQ051	925 °C	X	0.024656	0.418352	0.000865	0.227452	0.125193	287.5 ± 128.3	1.69	6.95	0.234 ± 0.003
08MQ061	925 °C	X	0.008270	0.547981	0.000000	0.196834	0.194153	515.2 ± 131.7	7.35	6.01	0.154 ± 0.002
07MQ052	1000 °C	X	0.016678	0.203004	0.000228	0.083581	0.068715	429.4 ± 327.7	1.37	2.55	0.177 ± 0.002
07MQ053	1150 °C	X	0.017085	0.342358	0.000000	0.060613	0.095063	819.1 ± 461.7	1.85	1.85	0.076 ± 0.001
08MQ062	1200 °C	X	0.027596	1.871786	0.000036	0.198433	0.243395	640.6 ± 149.9	2.90	6.06	0.046 ± 0.001
07MQ054	1300 °C		0.080681	4.852969	0.001836	0.198616	1.903578	4999.6 ± 239.4	7.39	6.06	0.018 ± 0.000
		J	0.301962	10.647470	0.013967	3.275018	4.238955				

Information on Analysis

sample MM using air composition from Lee et al. (2006)

Project = Fuerte05
Irradiation = VU61
J = 0.0002889 ± 0.0000018
DRA 1 = 25.420 ± 0.076 Ma

Results	40(r)/39(k) ± 1σ	Age ± 1σ (Ka)	MSWD	39Ar(k) (%,n)	K/Ca ± 1σ
Weighted Plateau	0.7632 ± 0.0526 ± 6.89%	398.6 ± 27.6 ± 6.92%	0.63	93.94 13	0.089 ± 0.025
		External Error ± 27.8	0.97	Statistical T Ratio	
		Analytical Error ± 27.5	1.0000	Error Magnification	
Total Fusion Age	1.2943 ± 0.0660 ± 5.10%	676.0 ± 34.7 ± 5.13%		14	0.007 ± 0.000
		External Error ± 35.2			
		Analytical Error ± 34.4			

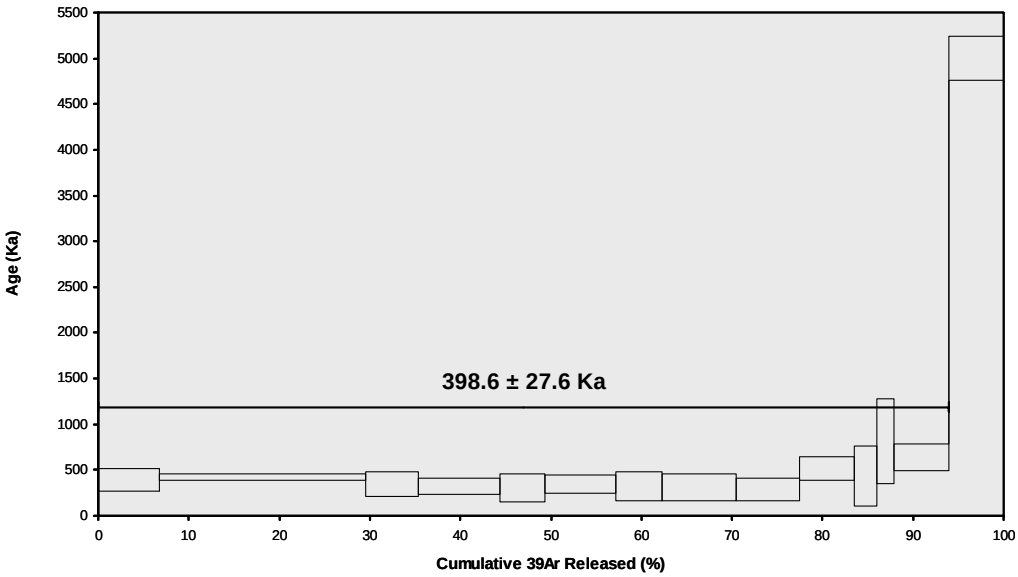

MM-NEW.AGE >>> MM >>> FUERTE05 PROJECT

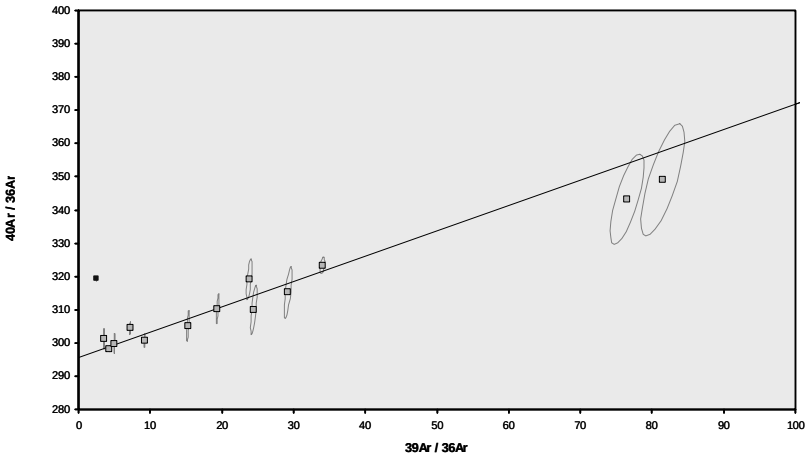

Ar-Ages in Ka

WEIGHTED PLATEAU
398.6 ± 27.6
TOTAL FUSION
676.0 ± 34.7
NORMAL ISOCHRON
396.8 ± 35.1
INVERSE ISOCHRON
398.9 ± 34.1

MSWD
0.80

40AR/36AR INTERCEPT
295.7 ± 0.9

Sample Info

groundmass
furnace
BSHS

IRR = VU61
J = 0.0002889 ± 0.0000018

MM-NEW.AGE >>> MM >>> FUERTE05 PROJECT

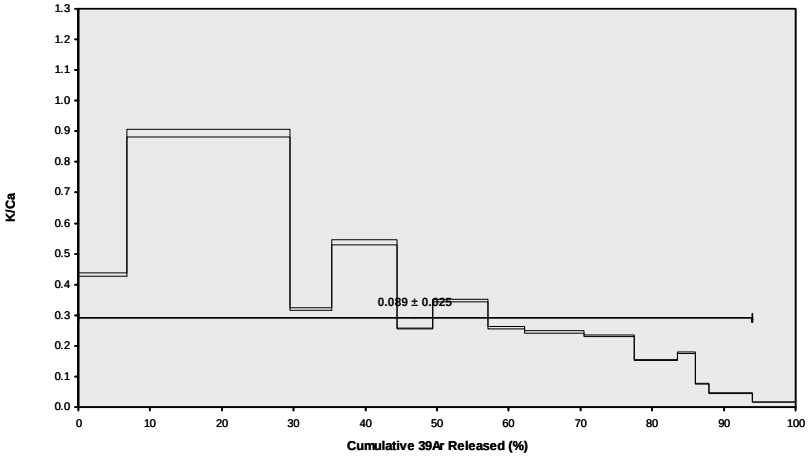

Ar-Ages in Ka

WEIGHTED PLATEAU
398.6 ± 27.6
TOTAL FUSION
676.0 ± 34.7
NORMAL ISOCHRON
396.8 ± 35.1
INVERSE ISOCHRON
398.9 ± 34.1

Sample Info

groundmass
furnace
BSHS

IRR = VU61
J = 0.0002889 ± 0.0000018

Incremental Heating			36Ar(a)	37Ar(ca)	38Ar(cl)	39Ar(k)	40Ar(r)	Age ± 1σ (Ka)	40Ar(r) (%)	39Ar(k) (%)	K/Ca ± 1σ
07MQ001	750 °C	X	0.029412	0.190338	0.002223	0.413835	0.332570	416.0 ± 54.0	3.69	15.27	0.935 ± 0.043
07MQ002	800 °C	X	0.014332	0.786017	0.000000	0.862220	0.609355	365.9 ± 20.5	12.57	31.82	0.472 ± 0.020
07MQ003	825 °C	X	0.005145	0.124473	0.000000	0.128987	0.072889	292.6 ± 130.2	4.57	4.76	0.446 ± 0.022
07MQ004	875 °C	X	0.009640	0.479609	0.000000	0.351903	0.238220	350.5 ± 48.0	7.72	12.99	0.316 ± 0.014
07MQ005	925 °C	X	0.010782	0.562401	0.000000	0.269614	0.199008	382.1 ± 68.2	5.88	9.95	0.206 ± 0.009
07MQ006	1000 °C	X	0.013585	0.385085	0.000000	0.135515	0.117705	449.7 ± 138.1	2.85	5.00	0.151 ± 0.007
07MQ007	1100 °C	X	0.016632	0.292167	0.000000	0.085144	0.066559	404.7 ± 208.9	1.34	3.14	0.125 ± 0.005
07MQ008	1300 °C		0.139888	8.215431	0.000657	0.462232	1.154688	1293.0 ± 72.3	2.72	17.06	0.024 ± 0.001
		\	0.239415	11.035520	0.002880	2.709450	2.790994				

Information on Analysis
sample MN using air composition from Steiger & Jäger (1977)
Project = Fuerte05 Irradiation = VU61 J = 0.0002870 ± 0.0000018 DRA 1 = 25.260 ± 0.076 Ma

Results	40(r)/39(k) ± 1σ	Age ± 1σ (Ka)	MSWD	39Ar(k) (%,n)	K/Ca ± 1σ
Weighted Plateau	0.7150 ± 0.0326 ± 4.57%	370.2 ± 17.1 ± 4.61%	0.28	82.94 7	0.183 ± 0.044
		External Error ± 17.1	1.01	Statistical T Ratio	
		Analytical Error ± 16.9	1.0000	Error Magnification	
Total Fusion Age	1.0301 ± 0.0422 ± 4.10%	533.3 ± 22.1 ± 4.14%		8	0.005 ± 0.000
		External Error ± 22.1			
		Analytical Error ± 21.8			

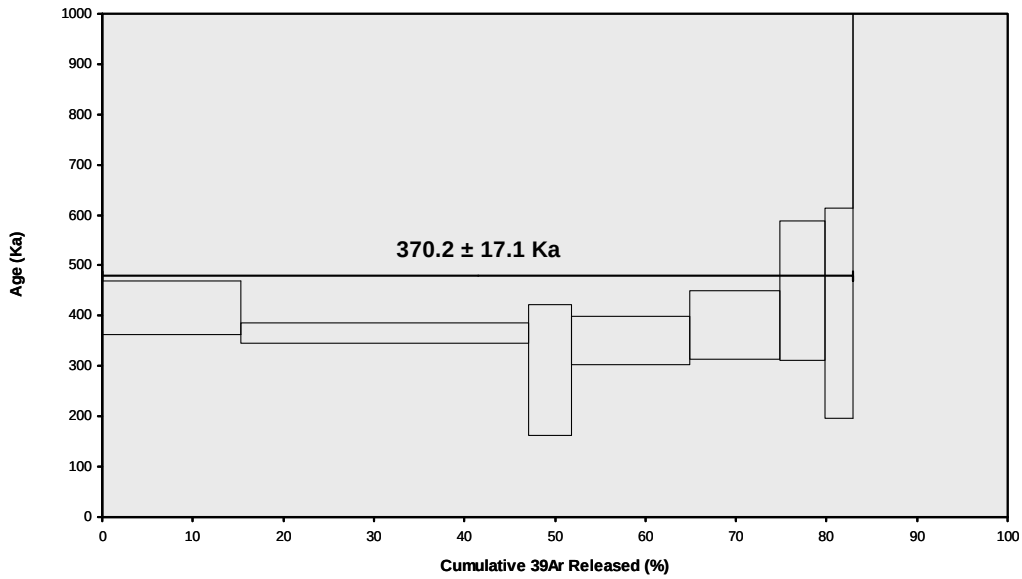

MN.AGE >>> F2 >>> FUERTE05 PROJECT

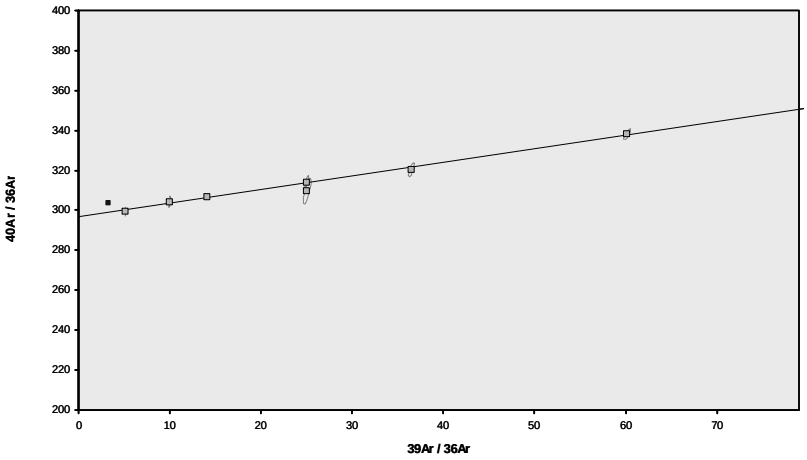

Ar-Ages in Ka

WEIGHTED PLATEAU
370.2 ± 17.1
TOTAL FUSION
533.3 ± 22.1
NORMAL ISOCHRON
352.6 ± 26.3
INVERSE ISOCHRON
352.6 ± 26.3

MSWD
0.18

40AR/36AR INTERCEPT
296.7 ± 1.4

Sample Info

basalt grdmass
furnace
BSHS

IRR = VU61
J = 0.0002870 ± 0.0000018

MN.AGE >>> F2 >>> FUERTE05 PROJECT

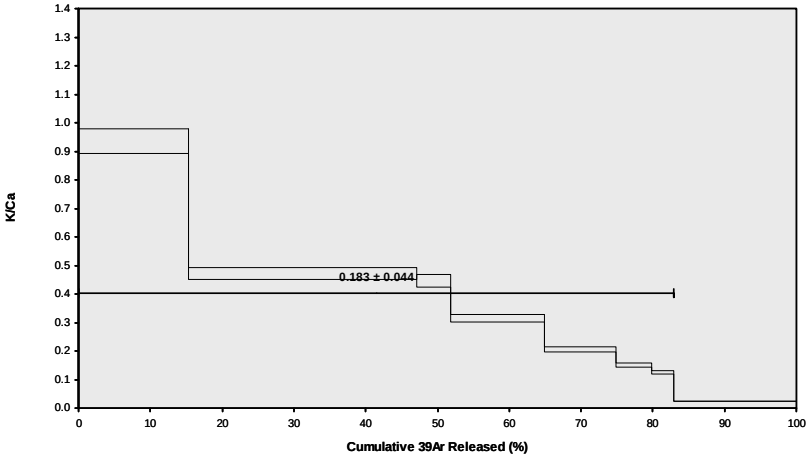

Ar-Ages in Ka

WEIGHTED PLATEAU
370.2 ± 17.1
TOTAL FUSION
533.3 ± 22.1
NORMAL ISOCHRON
352.6 ± 26.3
INVERSE ISOCHRON
352.6 ± 26.3

Sample Info

basalt grdmass
furnace
BSHS

IRR = VU61
J = 0.0002870 ± 0.0000018

Incremental Heating			36Ar(a)	37Ar(ca)	38Ar(cl)	39Ar(k)	40Ar(r)	Age ± 1σ (Ka)	40Ar(r) (%)	39Ar(k) (%)	K/Ca ± 1σ
07MQ001	750 °C	X	0.029493	0.190728	0.002225	0.414150	0.296791	374.3 ± 76.2	3.29	15.27	0.934 ± 0.016
07MQ002	800 °C	X	0.014373	0.787707	0.000000	0.862886	0.591475	358.0 ± 24.0	12.21	31.82	0.471 ± 0.004
07MQ003	825 °C	X	0.005160	0.124707	0.000000	0.129088	0.066299	268.3 ± 134.9	4.16	4.76	0.445 ± 0.012
07MQ004	875 °C	X	0.009665	0.480616	0.000000	0.352159	0.226850	336.5 ± 52.9	7.35	12.99	0.315 ± 0.004
07MQ005	925 °C	X	0.010811	0.563558	0.000000	0.269808	0.186281	360.6 ± 74.8	5.50	9.95	0.206 ± 0.002
07MQ006	1000 °C	X	0.013623	0.385929	0.000000	0.135621	0.100777	388.1 ± 159.8	2.44	5.00	0.151 ± 0.002
07MQ007	1100 °C	X	0.016676	0.292812	0.000000	0.085206	0.046801	286.9 ± 259.6	0.94	3.14	0.125 ± 0.001
07MQ008	1300 °C		0.140093	8.225021	0.000645	0.462434	1.038115	1172.3 ± 243.1	2.44	17.06	0.024 ± 0.000
		–	0.239894	11.051077	0.002870	2.711351	2.553390				

Information on Analysis	Results	40(r)/39(k) ± 1σ	Age ± 1σ (Ka)	MSWD	39Ar(k) (%,n)	K/Ca ± 1σ
sample MN using air composition from Lee et al. (2006)	**Weighted Plateau**	0.6785 ± 0.0379 ± 5.59%	354.4 ± 19.9 ± 5.62%	0.12	82.94 7	0.190 ± 0.040
			External Error ± 20.2	1.01	Statistical T Ratio	
			Analytical Error ± 19.8	1.0000	Error Magnification	
Project = Fuerte05 Irradiation = VU61 J = 0.0002889 ± 0.0000018 DRA 1 = 25.420 ± 0.076 Ma	**Total Fusion Age**	0.9417 ± 0.0896 ± 9.51%	491.9 ± 46.9 ± 9.53%		8	0.005 ± 0.000
			External Error ± 47.1			
			Analytical Error ± 46.8			

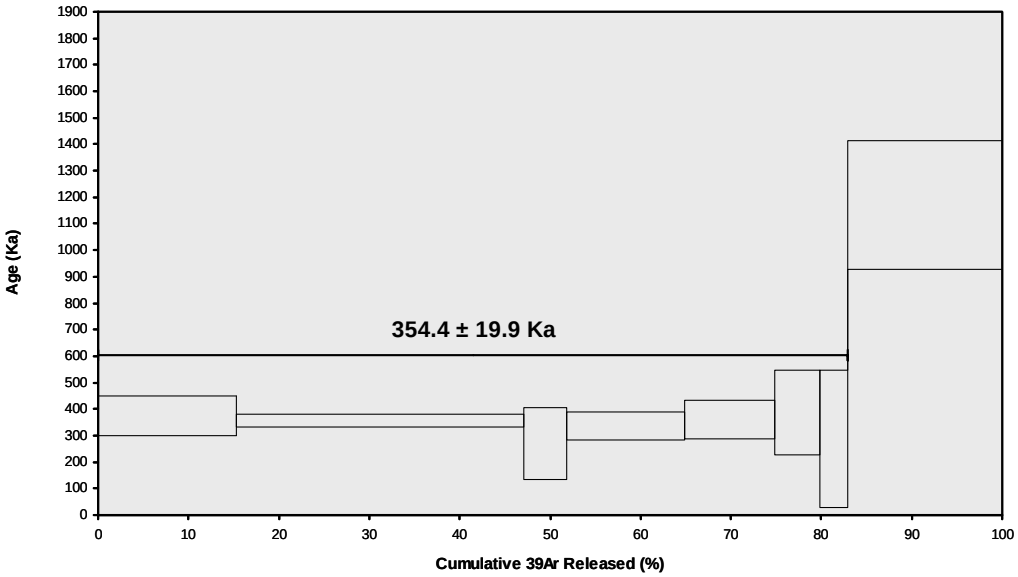

MN-NEW.AGE >>> MN >>> FUERTE05 PROJECT

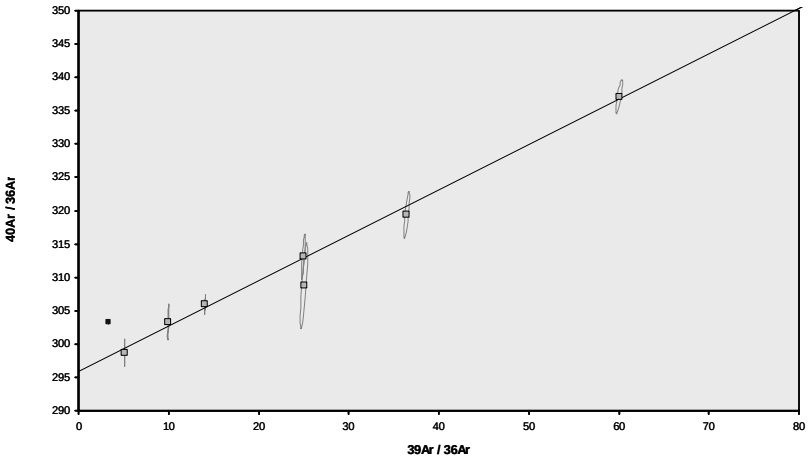

Ar-Ages in Ka

WEIGHTED PLATEAU
354.4 ± 19.9
TOTAL FUSION
491.9 ± 46.9
NORMAL ISOCHRON
355.1 ± 26.1
INVERSE ISOCHRON
355.1 ± 26.0

MSWD
0.18

40AR/36AR INTERCEPT
295.9 ± 1.4

Sample Info

groundmass
furnace
BSHS

IRR = VU61
J = 0.0002889 ± 0.0000018

MN-NEW.AGE >>> MN >>> FUERTE05 PROJECT

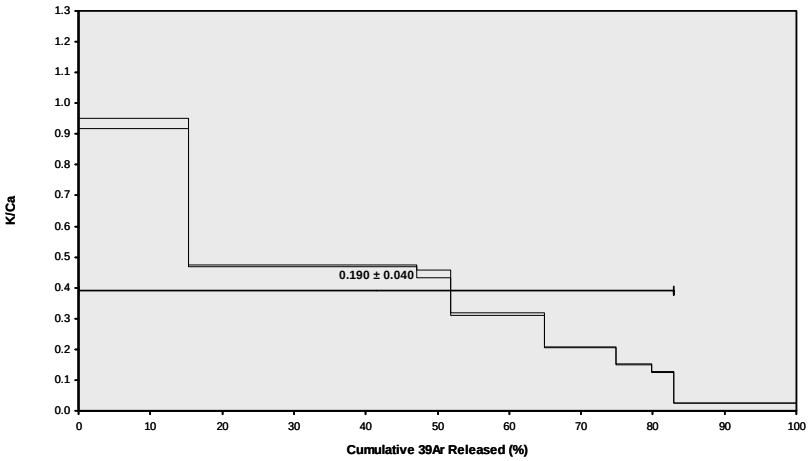

Ar-Ages in Ka

WEIGHTED PLATEAU
354.4 ± 19.9
TOTAL FUSION
491.9 ± 46.9
NORMAL ISOCHRON
355.1 ± 26.1
INVERSE ISOCHRON
355.1 ± 26.0

Sample Info

groundmass
furnace
BSHS

IRR = VU61
J = 0.0002889 ± 0.0000018

Incremental Heating			36Ar(a)	37Ar(ca)	38Ar(cl)	39Ar(k)	40Ar(r)	Age ± 1σ (Ka)	40Ar(r) (%)	39Ar(k) (%)	K/Ca ± 1σ
07MQ055	750 °C	X	0.015476	0.165385	0.000000	0.252120	0.090076	186.3 ± 70.8	1.91	21.66	0.656 ± 0.030
07MQ056	775 °C	X	0.005608	0.143334	0.000000	0.182243	0.065450	187.2 ± 50.7	3.75	15.66	0.547 ± 0.026
07MQ057	800 °C	X	0.003236	0.088123	0.000000	0.091296	0.026054	148.8 ± 79.1	2.62	7.84	0.445 ± 0.022
07MQ058	850 °C	X	0.007496	0.216701	0.000000	0.171825	0.061737	187.3 ± 60.0	2.68	14.76	0.341 ± 0.016
07MQ059	900 °C	X	0.006339	0.170089	0.000000	0.114543	0.035740	162.7 ± 81.8	1.85	9.84	0.290 ± 0.013
07MQ060	975 °C	X	0.005998	0.191636	0.000000	0.093841	0.027374	152.1 ± 97.6	1.50	8.06	0.211 ± 0.010
07MQ061	1125 °C	X	0.008541	0.298527	0.000000	0.078165	0.028363	189.2 ± 143.7	1.10	6.72	0.113 ± 0.005
07MQ062	1500 °C		0.049275	7.079622	0.002516	0.179735	0.666548	1932.5 ± 283.9	4.33	15.44	0.011 ± 0.000
		Π	0.101967	8.353417	0.002516	1.163768	1.001341				

Information on Analysis
sample MQ using air composition from Steiger & Jäger (1977)
Project = Fuerte05 Irradiation = VU60 J = 0.0002890 ± 0.0000018 DRA 1 = 25.260 ± 0.076 Ma

Results	40(r)/39(k) ± 1σ	Age ± 1σ (Ka)	MSWD	39Ar(k) (%,n)	K/Ca ± 1σ
Weighted Plateau	0.3395 ± 0.0526 ± 15.49%	177.0 ± 27.4 ± 15.50%	0.05	84.56 7	0.191 ± 0.050
		External Error ± 27.4	1.01	Statistical T Ratio	
		Analytical Error ± 27.4	1.0000	Error Magnification	
Total Fusion Age	0.8604 ± 0.0971 ± 11.28%	448.6 ± 50.7 ± 11.30%		8	0.003 ± 0.000
		External Error ± 50.7			
		Analytical Error ± 50.6			

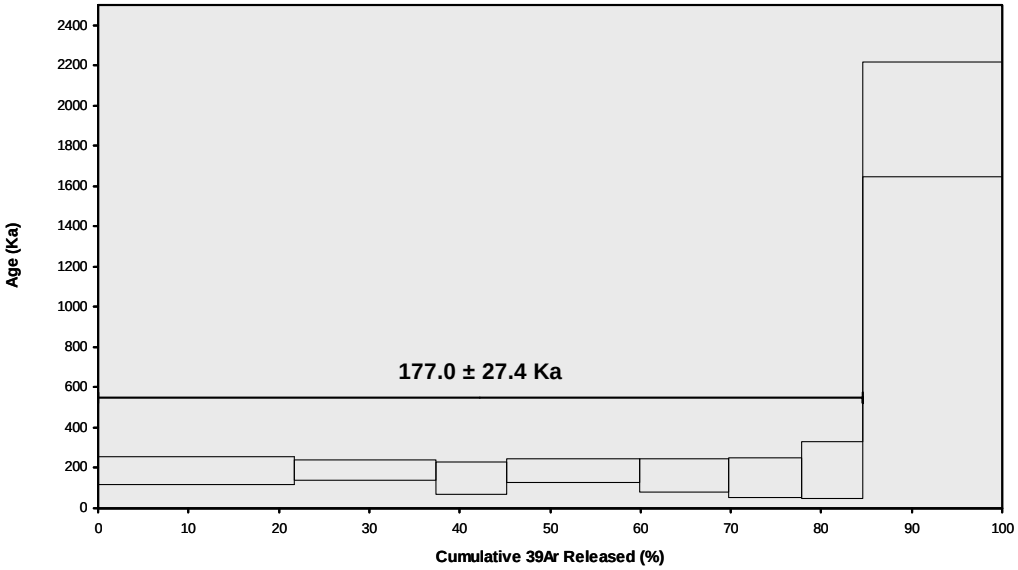

MQ-INTERCEPT.AGE >>> F10 >>> FUERTE05 PROJECT

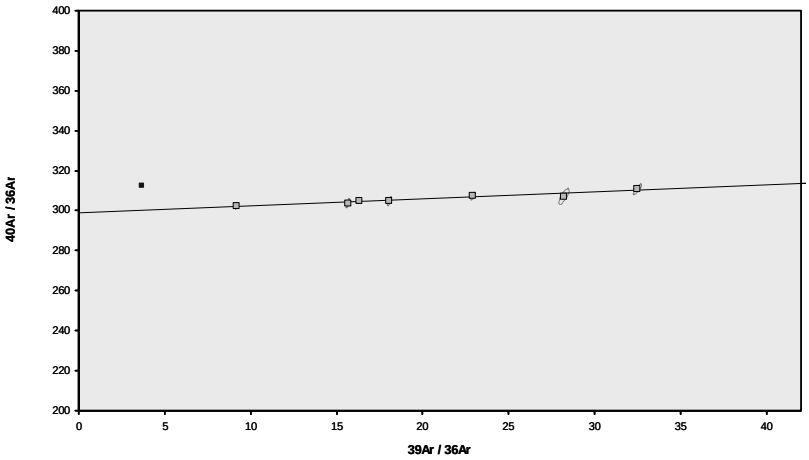

Ar-Ages in Ka

WEIGHTED PLATEAU
177.0 ± 27.4
TOTAL FUSION
448.6 ± 50.7
NORMAL ISOCHRON
179.4 ± 61.4
INVERSE ISOCHRON
179.6 ± 59.7

MSWD
0.10

40AR/36AR INTERCEPT
299.1 ± 2.2

Sample Info

basalt grdms
furnace
BSHS

IRR = VU60
J = 0.0002890 ± 0.0000018

MQ-INTERCEPT.AGE >>> F10 >>> FUERTE05 PROJECT

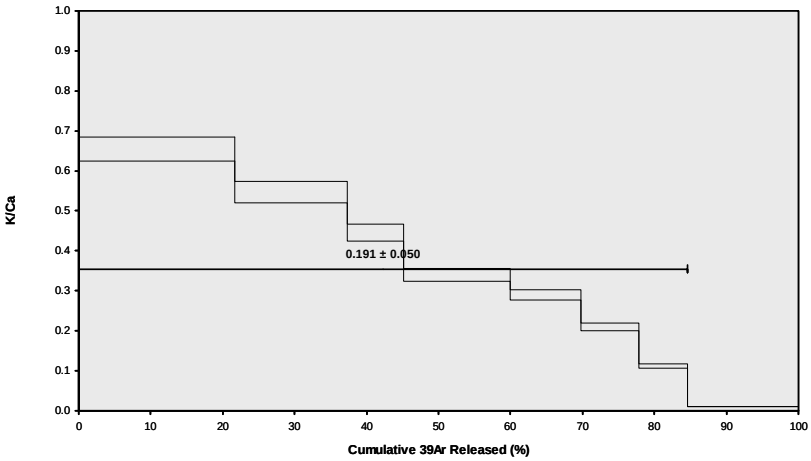

Ar-Ages in Ka

WEIGHTED PLATEAU
177.0 ± 27.4
TOTAL FUSION
448.6 ± 50.7
NORMAL ISOCHRON
179.4 ± 61.4
INVERSE ISOCHRON
179.6 ± 59.7

Sample Info

basalt grdms
furnace
BSHS

IRR = VU60
J = 0.0002890 ± 0.0000018

Incremental Heating			36Ar(a)	37Ar(ca)	38Ar(cl)	39Ar(k)	40Ar(r)	Age ± 1σ (Ka)	40Ar(r) (%)	39Ar(k) (%)	K/Ca ± 1σ
07MQ055	750 °C	X	0.015517	0.165742	0.000000	0.252297	0.091968	191.7 ± 78.1	1.95	21.66	0.655 ± 0.007
07MQ056	775 °C	X	0.005623	0.143625	0.000000	0.182374	0.065944	190.2 ± 54.0	3.78	15.66	0.546 ± 0.011
07MQ057	800 °C	X	0.003245	0.088269	0.000000	0.091362	0.026285	151.3 ± 82.3	2.64	7.84	0.445 ± 0.010
07MQ058	850 °C	X	0.007518	0.217112	0.000000	0.171960	0.061895	189.3 ± 64.2	2.69	14.77	0.341 ± 0.006
07MQ059	900 °C	X	0.006356	0.170470	0.000000	0.114632	0.036120	165.7 ± 88.4	1.87	9.84	0.289 ± 0.003
07MQ060	975 °C	X	0.006015	0.192019	0.000000	0.093911	0.027690	155.1 ± 103.2	1.52	8.06	0.210 ± 0.003
07MQ061	1125 °C	X	0.008566	0.299176	0.000000	0.078226	0.028513	191.7 ± 154.8	1.10	6.72	0.112 ± 0.001
07MQ062	1500 °C		0.049407	7.094309	0.002511	0.179863	0.671260	1962.0 ± 313.5	4.36	15.44	0.011 ± 0.000
		–	0.102247	8.370723	0.002511	1.164625	1.009675				

Information on Analysis

sample MQ using air composition from Lee et al. (2006)

Project = Fuerte05
Irradiation = VU60
J = 0.0002909 ± 0.0000018
DRA 1 = 25.420 ± 0.076 Ma

Results	40(r)/39(k) ± 1σ	Age ± 1σ (Ka)	MSWD	39Ar(k) (%,n)	K/Ca ± 1σ
Weighted Plateau	0.3419 ± 0.0558 ± 16.32%	179.8 ± 29.4 ± 16.33%	0.05	84.56 7	0.177 ± 0.048
		External Error ± 29.4	1.01	Statistical T Ratio	
		Analytical Error ± 29.4	1.0000	Error Magnification	
Total Fusion Age	0.8670 ± 0.1057 ± 12.19%	456.0 ± 55.7 ± 12.21%		8	0.003 ± 0.000
		External Error ± 55.8			
		Analytical Error ± 55.6			

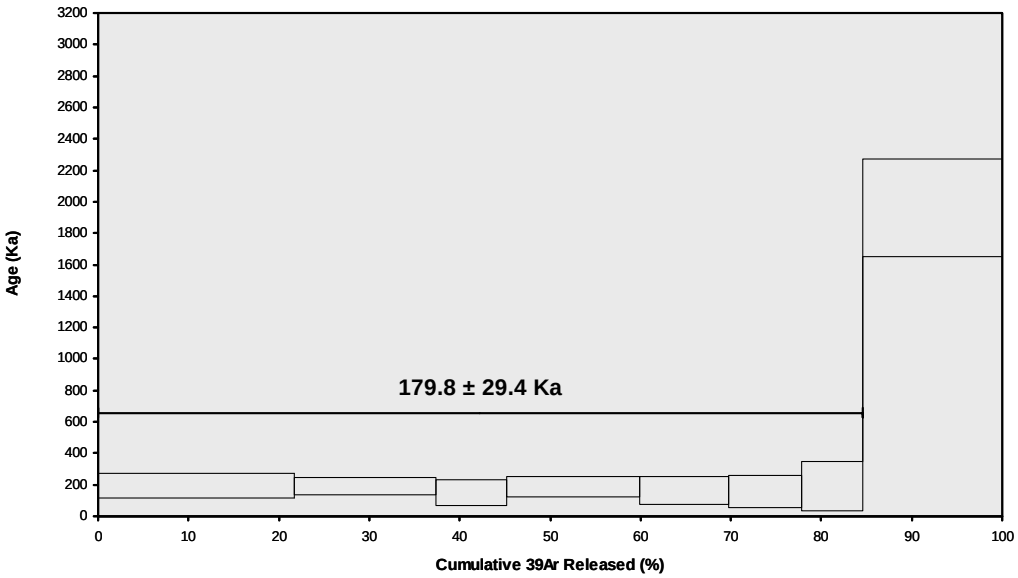

MQ-NEW.AGE >>> MQ >>> FUERTE05 PROJECT

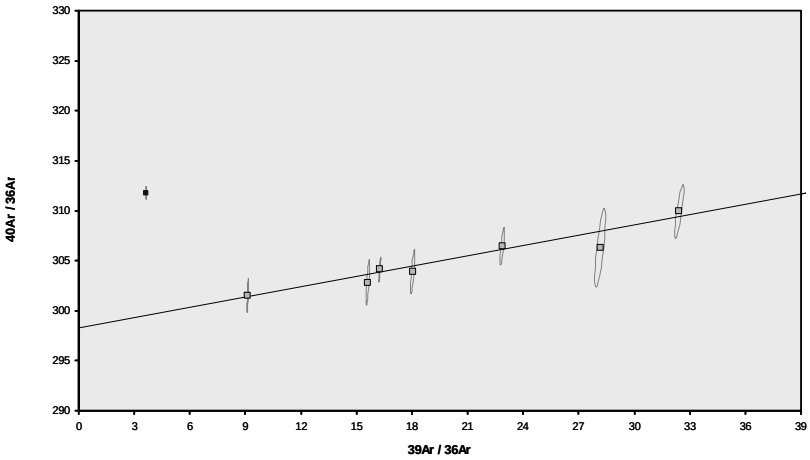

Ar-Ages in Ka

WEIGHTED PLATEAU
179.8 ± 29.4
TOTAL FUSION
456.0 ± 55.7
NORMAL ISOCHRON
181.3 ± 60.7
INVERSE ISOCHRON
181.5 ± 59.0

MSWD
0.10

40AR/36AR INTERCEPT
298.2 ± 2.2

Sample Info

groundmass
furnace
BSHS

IRR = VU60
J = 0.0002909 ± 0.0000018

MQ-NEW.AGE >>> MQ >>> FUERTE05 PROJECT

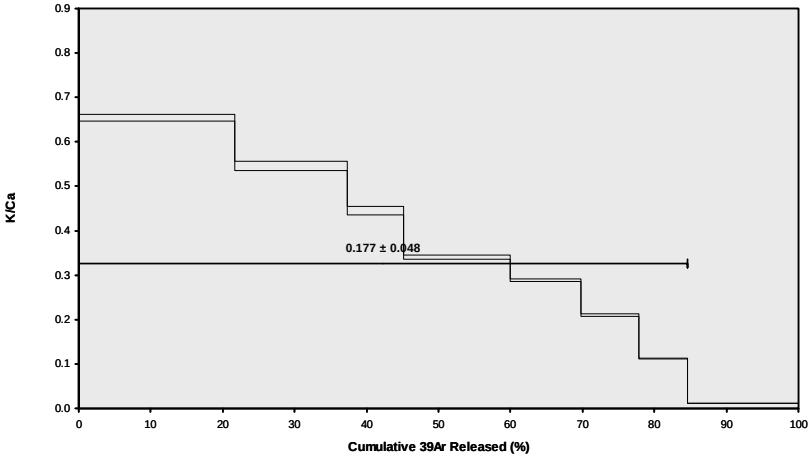

Ar-Ages in Ka

WEIGHTED PLATEAU
179.8 ± 29.4
TOTAL FUSION
456.0 ± 55.7
NORMAL ISOCHRON
181.3 ± 60.7
INVERSE ISOCHRON
181.5 ± 59.0

Sample Info

groundmass
furnace
BSHS

IRR = VU60
J = 0.0002909 ± 0.0000018

Incremental Heating			36Ar(a)	37Ar(ca)	38Ar(cl)	39Ar(k)	40Ar(r)	Age ± 1σ (Ka)	40Ar(r) (%)	39Ar(k) (%)	K/Ca ± 1σ
07MQ018	750 °C		0.010401	0.216266	0.000569	0.338712	0.211584	323.4 ± 24.7	6.44	21.13	0.673 ± 0.030
07MQ019	775 °C	X	0.003785	0.226916	0.000000	0.239946	0.099120	213.9 ± 32.0	8.14	14.97	0.455 ± 0.021
07MQ020	800 °C	X	0.002869	0.274669	0.000000	0.201439	0.089683	230.5 ± 30.9	9.56	12.57	0.315 ± 0.014
07MQ021	825 °C	X	0.002963	0.213765	0.000000	0.148843	0.068958	239.9 ± 40.4	7.30	9.29	0.299 ± 0.014
07MQ022	875 °C	X	0.004120	0.207370	0.000000	0.147370	0.062394	219.2 ± 45.8	4.87	9.19	0.306 ± 0.014
07MQ023	950 °C	X	0.005817	0.245936	0.000000	0.147625	0.071414	250.5 ± 53.0	3.99	9.21	0.258 ± 0.012
07MQ024	1050 °C	X	0.005817	0.160483	0.000000	0.071048	0.044403	323.6 ± 100.4	2.52	4.43	0.190 ± 0.009
07MQ025	1200 °C		0.025720	1.612690	0.000000	0.307893	0.201543	338.9 ± 40.4	2.58	19.21	0.082 ± 0.004
		Σ	0.061492	3.158094	0.000569	1.602876	0.849099				

Information on Analysis
sample MR using air composition from Steiger & Jäger (1977)
Project = Fuerte05 Irradiation = VU61 J = 0.0002870 ± 0.0000018 DRA 1 = 25.260 ± 0.076 Ma

Results	40(r)/39(k) ± 1σ	Age ± 1σ (Ka)	MSWD	39Ar(k) (%,n)	K/Ca ± 1σ
Weighted Plateau	0.4454 ± 0.0323 ± 7.26%	230.6 ± 16.8 ± 7.28%	0.28	59.66 6	0.267 ± 0.031
		External Error ± 16.8	1.03	Statistical T Ratio	
		Analytical Error ± 16.7	1.0000	Error Magnification	
Total Fusion Age	0.5297 ± 0.0274 ± 5.17%	274.3 ± 14.3 ± 5.21%		8	0.011 ± 0.000
		External Error ± 14.3			
		Analytical Error ± 14.2			

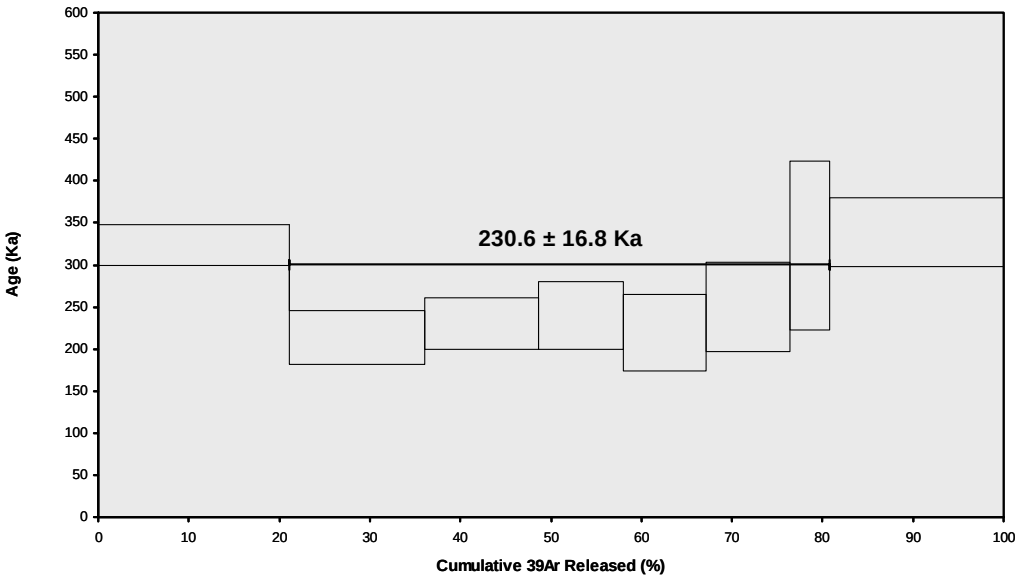

MR.AGE >>> F4 >>> FUERTE05 PROJECT

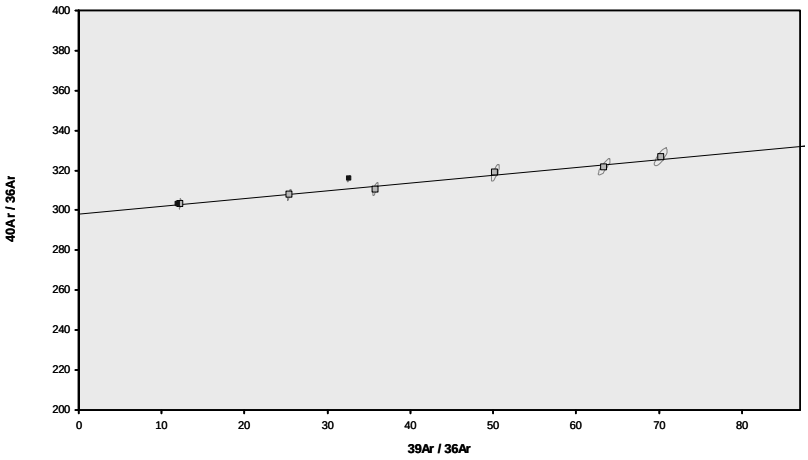

Ar-Ages in Ka

WEIGHTED PLATEAU
230.6 ± 16.8
TOTAL FUSION
274.3 ± 14.3
NORMAL ISOCHRON
203.0 ± 33.4
INVERSE ISOCHRON
203.1 ± 33.1

MSWD
0.11

40AR/36AR INTERCEPT
297.9 ± 2.5

Sample Info

basalt grdmass
furnace
BSHS

IRR = VU61
J = 0.0002870 ± 0.0000018

MR.AGE >>> F4 >>> FUERTE05 PROJECT

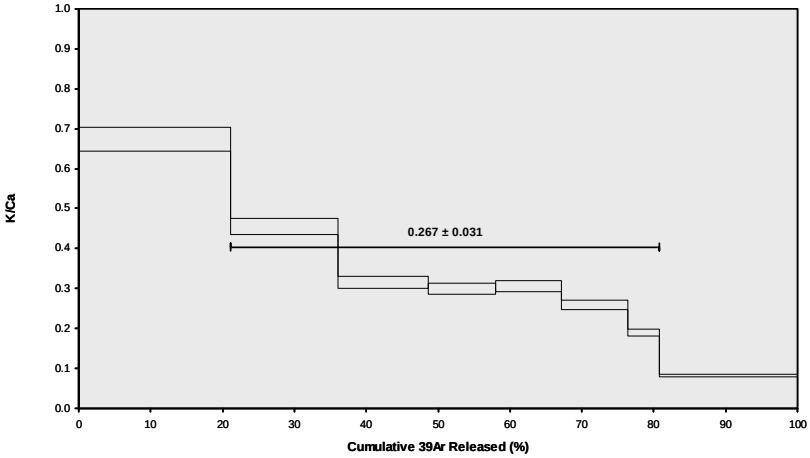

Ar-Ages in Ka

WEIGHTED PLATEAU
230.6 ± 16.8
TOTAL FUSION
274.3 ± 14.3
NORMAL ISOCHRON
203.0 ± 33.4
INVERSE ISOCHRON
203.1 ± 33.1

Sample Info

basalt grdmass
furnace
BSHS

IRR = VU61
J = 0.0002870 ± 0.0000018

Incremental Heating			36Ar(a)	37Ar(ca)	38Ar(cl)	39Ar(k)	40Ar(r)	Age ± 1σ (Ka)	40Ar(r) (%)	39Ar(k) (%)	K/Ca ± 1σ
07MQ018	750 °C		0.010432	0.216746	0.000573	0.338980	0.176428	271.9 ± 27.9	5.37	21.13	0.672 ± 0.008
07MQ019	775 °C	X	0.003796	0.227450	0.000000	0.240134	0.086369	187.9 ± 33.5	7.09	14.97	0.454 ± 0.006
07MQ020	800 °C	X	0.002878	0.275303	0.000000	0.201602	0.079840	206.9 ± 32.2	8.51	12.57	0.315 ± 0.005
07MQ021	825 °C	X	0.002972	0.214267	0.000000	0.148964	0.059022	207.0 ± 42.2	6.25	9.29	0.299 ± 0.005
07MQ022	875 °C	X	0.004132	0.207871	0.000000	0.147488	0.048559	172.0 ± 48.3	3.79	9.19	0.305 ± 0.004
07MQ023	950 °C	X	0.005833	0.246428	0.000000	0.147734	0.052114	184.3 ± 57.1	2.91	9.21	0.258 ± 0.003
07MQ024	1050 °C	X	0.005832	0.160834	0.000000	0.071100	0.025316	186.0 ± 109.0	1.44	4.43	0.190 ± 0.003
07MQ025	1200 °C	X	0.025783	1.615775	0.000000	0.308101	0.118519	200.9 ± 53.3	1.52	19.21	0.082 ± 0.001
		0	0.061657	3.164674	0.000573	1.604102	0.646167				

Information on Analysis

sample MR using air composition from Lee et al. (2006)

Project = Fuerte05
Irradiation = VU61
J = 0.0002889 ± 0.0000018
DRA 1 = 25.420 ± 0.076 Ma

Results	40(r)/39(k) ± 1σ	Age ± 1σ (Ka)	MSWD	39Ar(k) (%,n)	K/Ca ± 1σ
Weighted Plateau	0.3733 ± 0.0320 ± 8.56%	195.0 ± 16.7 ± 8.58%	0.09	78.87 7	0.109 ± 0.029
		External Error ± 16.8	1.01	Statistical T Ratio	
		Analytical Error ± 16.7	1.0000	Error Magnification	
Total Fusion Age	0.4028 ± 0.0313 ± 7.77%	210.4 ± 16.4 ± 7.79%		8	0.011 ± 0.000
		External Error ± 16.5			
		Analytical Error ± 16.3			

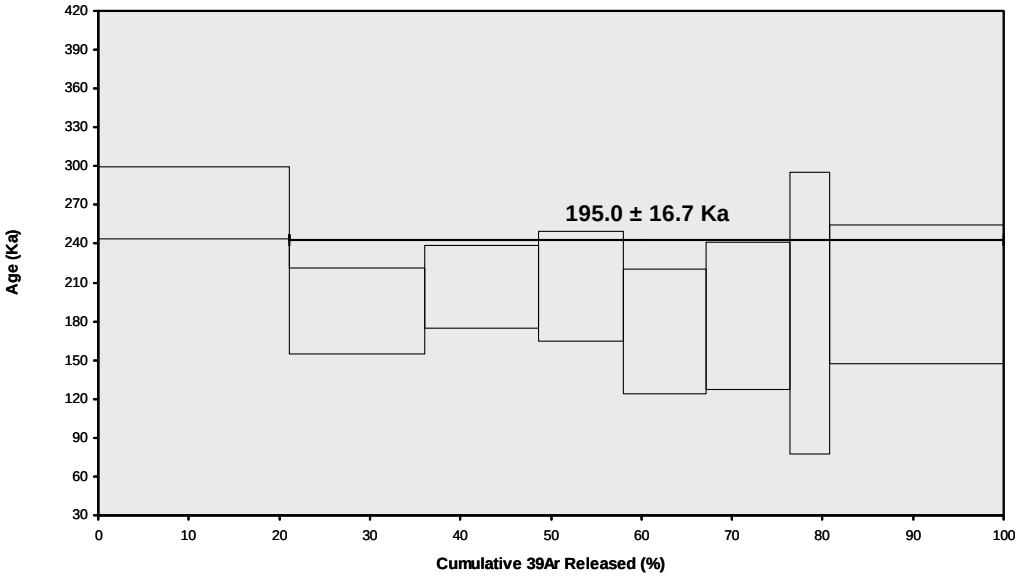

MR-NEW.AGE >>> MR >>> FUERTE05 PROJECT

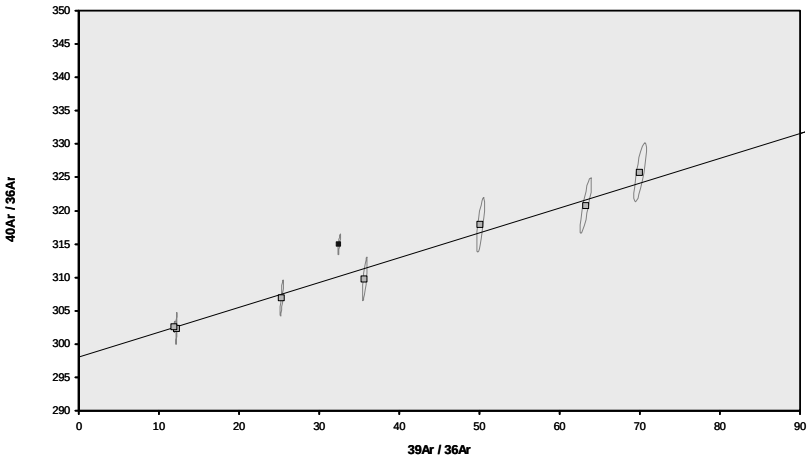

Ar-Ages in Ka

WEIGHTED PLATEAU
195.0 ± 16.7
TOTAL FUSION
210.4 ± 16.4
NORMAL ISOCHRON
195.1 ± 24.8
INVERSE ISOCHRON
195.3 ± 24.6

MSWD
0.12

40AR/36AR INTERCEPT
298.0 ± 1.1

Sample Info

groundmass
furnace
BSHS

IRR = VU61
J = 0.0002889 ± 0.0000018

MR-NEW.AGE >>> MR >>> FUERTE05 PROJECT

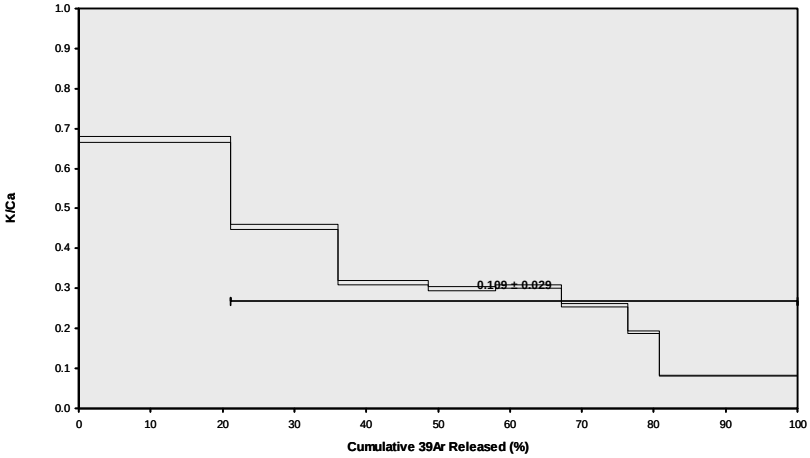

Ar-Ages in Ka

WEIGHTED PLATEAU
195.0 ± 16.7
TOTAL FUSION
210.4 ± 16.4
NORMAL ISOCHRON
195.1 ± 24.8
INVERSE ISOCHRON
195.3 ± 24.6

Sample Info

groundmass
furnace
BSHS

IRR = VU61
J = 0.0002889 ± 0.0000018

Incremental Heating			36Ar(a)	37Ar(ca)	38Ar(cl)	39Ar(k)	40Ar(r)	Age ± 1σ (Ka)	40Ar(r) (%)	39Ar(k) (%)	K/Ca ± 1σ
07MQ026	700 °C		0.004423	0.033492	0.000000	0.015806	0.025565	837.3 ± 413.8	1.92	0.92	0.203 ± 0.012
07MQ027	750 °C		0.004170	0.194998	0.000000	0.097339	0.111670	593.9 ± 70.0	8.31	5.70	0.215 ± 0.010
07MQ028	800 °C	X	0.002555	0.415845	0.000000	0.228368	0.123254	279.4 ± 27.8	14.03	13.36	0.236 ± 0.011
07MQ029	825 °C	X	0.001956	0.466417	0.000000	0.229302	0.110401	249.3 ± 26.8	16.03	13.42	0.211 ± 0.010
07MQ030	850 °C	X	0.003385	0.302738	0.000000	0.174861	0.074271	219.9 ± 36.0	6.91	10.23	0.248 ± 0.011
07MQ031	900 °C	X	0.002649	0.499696	0.000000	0.431402	0.183666	220.4 ± 15.1	18.99	25.24	0.371 ± 0.017
07MQ032	950 °C	X	0.002358	0.187581	0.000000	0.206116	0.098038	246.3 ± 28.3	12.33	12.06	0.472 ± 0.022
07MQ033	1000 °C		0.002709	0.084989	0.000000	0.095440	0.030240	164.0 ± 66.6	3.64	5.58	0.483 ± 0.023
07MQ034	1100 °C		0.005065	0.153876	0.000000	0.107737	0.028522	137.1 ± 66.3	1.87	6.30	0.301 ± 0.014
07MQ035	1300 °C		0.023179	3.869161	0.000000	0.122520	0.093803	396.4 ± 115.8	1.35	7.17	0.014 ± 0.001
		□	0.052447	6.208792	0.000000	1.708891	0.879429				

Information on Analysis
sample VF using air composition from Steiger & Jäger (1977)
Project = Fuerte05
Irradiation = VU61
J = 0.0002870 ± 0.0000018
DRA 1 = 25.260 ± 0.076 Ma

Results	40(r)/39(k) ± 1σ	Age ± 1σ (Ka)	MSWD	39Ar(k) (%,n)	K/Ca ± 1σ
Weighted Plateau	0.4572 ± 0.0204 ± 4.47%	236.7 ± 10.7 ± 4.51%	1.02	74.32 5	0.261 ± 0.036
		External Error ± 10.7	1.06	Statistical T Ratio	
		Analytical Error ± 10.6	1.0089	Error Magnification	
Total Fusion Age	0.5146 ± 0.0271 ± 5.27%	266.4 ± 14.1 ± 5.31%		10	0.006 ± 0.000
		External Error ± 14.2			
		Analytical Error ± 14.0			

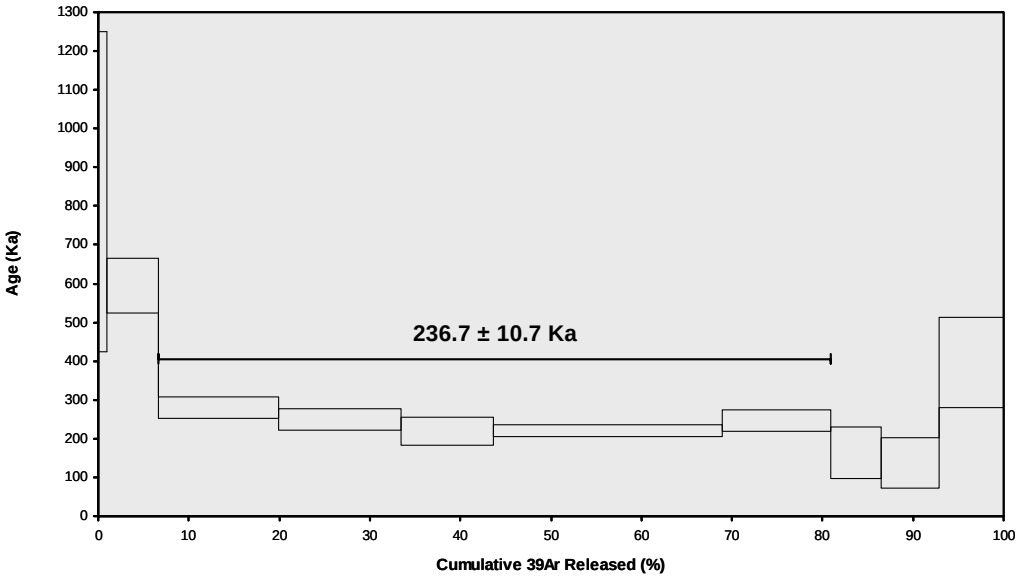

VF.AGE >>> F6 >>> FUERTE05 PROJECT

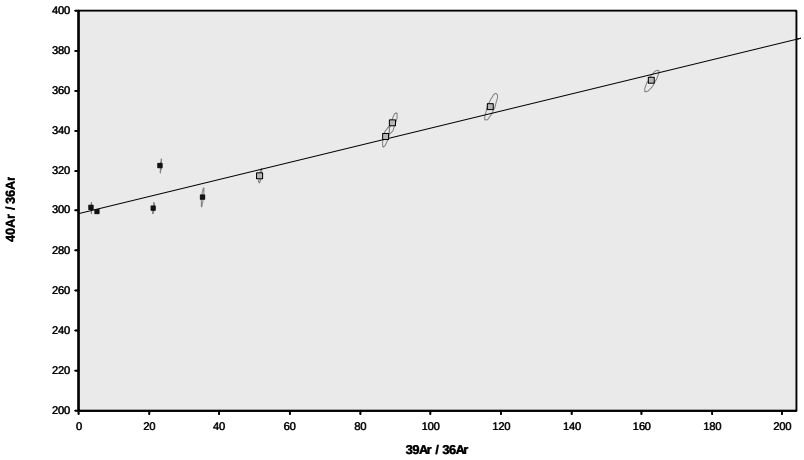

Ar-Ages in Ka

WEIGHTED PLATEAU
236.7 ± 10.7
TOTAL FUSION
266.4 ± 14.1
NORMAL ISOCHRON
221.3 ± 29.8
INVERSE ISOCHRON
221.2 ± 29.4

MSWD
1.22

40AR/36AR INTERCEPT
298.7 ± 5.9

Sample Info

basalt grdms
furnace
BSHS

IRR = VU61
J = 0.0002870 ± 0.0000018

VF.AGE >>> F6 >>> FUERTE05 PROJECT

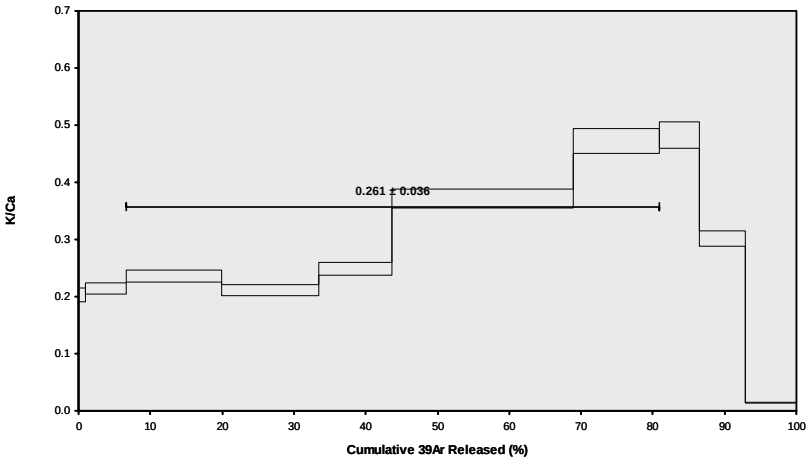

Ar-Ages in Ka

WEIGHTED PLATEAU
236.7 ± 10.7
TOTAL FUSION
266.4 ± 14.1
NORMAL ISOCHRON
221.3 ± 29.8
INVERSE ISOCHRON
221.2 ± 29.4

Sample Info

basalt grdms
furnace
BSHS

IRR = VU61
J = 0.0002870 ± 0.0000018

Incremental Heating			36Ar(a)	37Ar(ca)	38Ar(cl)	39Ar(k)	40Ar(r)	Age ± 1σ (Ka)	40Ar(r) (%)	39Ar(k) (%)	K/Ca ± 1σ
07MQ026	700 °C		0.004436	0.033543	0.000000	0.015819	0.020374	672.7 ± 439.2	1.53	0.92	0.203 ± 0.008
07MQ027	750 °C		0.004182	0.195481	0.000000	0.097418	0.106739	572.3 ± 73.6	7.94	5.70	0.214 ± 0.003
07MQ028	800 °C	X	0.002562	0.416767	0.000000	0.228550	0.120250	274.8 ± 28.7	13.69	13.36	0.236 ± 0.003
07MQ029	825 °C	X	0.001962	0.467407	0.000000	0.229475	0.108175	246.2 ± 27.4	15.70	13.42	0.211 ± 0.003
07MQ030	850 °C	X	0.003394	0.303339	0.000000	0.174992	0.070521	210.5 ± 37.9	6.56	10.23	0.248 ± 0.004
07MQ031	900 °C	X	0.002656	0.500752	0.000000	0.431713	0.180778	218.7 ± 15.4	18.69	25.24	0.371 ± 0.004
07MQ032	950 °C	X	0.002365	0.187984	0.000000	0.206277	0.095462	241.7 ± 29.3	12.00	12.06	0.472 ± 0.007
07MQ033	1000 °C	X	0.002717	0.085163	0.000000	0.095515	0.026936	147.3 ± 69.0	3.24	5.59	0.482 ± 0.008
07MQ034	1100 °C		0.005079	0.154177	0.000000	0.107821	0.022678	109.9 ± 70.6	1.49	6.30	0.301 ± 0.004
07MQ035	1300 °C		0.023246	3.877793	0.000000	0.122613	0.066953	285.2 ± 128.7	0.96	7.17	0.014 ± 0.000
		(	0.052599	6.222406	0.000000	1.710191	0.818868				

Information on Analysis
sample VF using air composition from Lee et al. (2006)
Project = Fuerte05 Irradiation = VU61 J = 0.0002889 ± 0.0000018 DRA 1 = 25.420 ± 0.076 Ma

Results	40(r)/39(k) ± 1σ	Age ± 1σ (Ka)	MSWD	39Ar(k) (%,n)	K/Ca ± 1σ
Error Plateau	0.4428 ± 0.0207 ± 4.68%	231.3 ± 10.9 ± 4.73%	1.03	79.90 6	0.267 ± 0.036
		External Error ± 11.1	1.03	Statistical T Ratio	
		Analytical Error ± 10.8	1.0169	Error Magnification	
Total Fusion Age	0.4788 ± 0.0287 ± 6.00%	250.1 ± 15.1 ± 6.03%		10	0.006 ± 0.000
		External Error ± 15.2			
		Analytical Error ± 15.0			

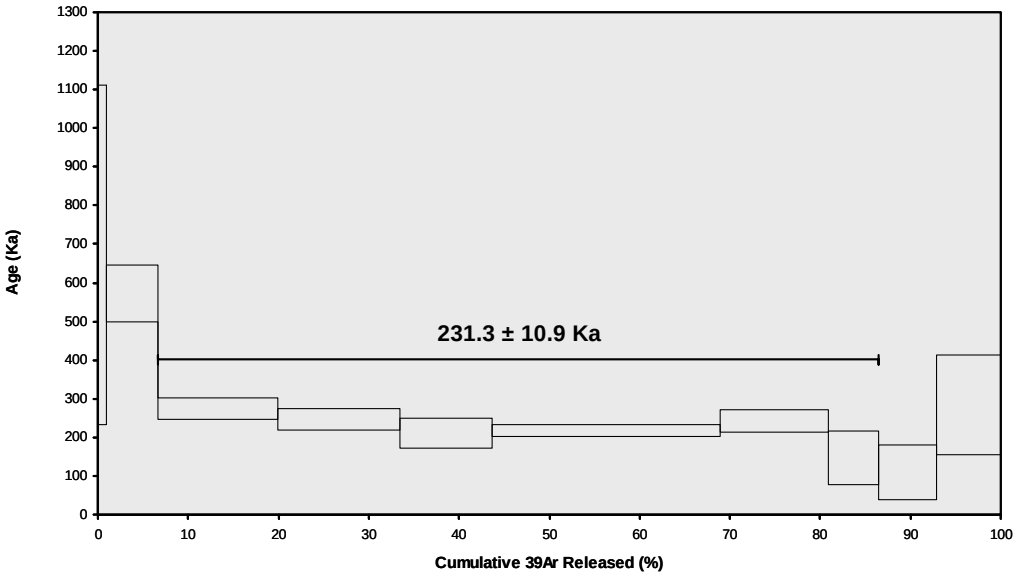

VF-NEW.AGE >>> VF >>> FUERTE05 PROJECT

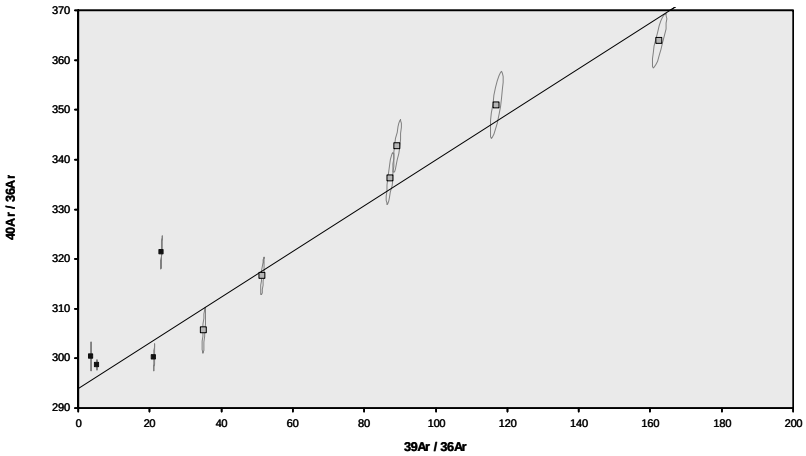

Ar-Ages in Ka

WEIGHTED PLATEAU
231.3 ± 10.9
TOTAL FUSION
250.1 ± 15.1
NORMAL ISOCHRON
239.9 ± 26.1
INVERSE ISOCHRON
240.4 ± 25.9

MSWD
1.28

40AR/36AR INTERCEPT
293.9 ± 4.7

Sample Info

groundmass
furnace
BSHS

IRR = VU61
J = 0.0002889 ± 0.0000018

VF-NEW.AGE >>> VF >>> FUERTE05 PROJECT

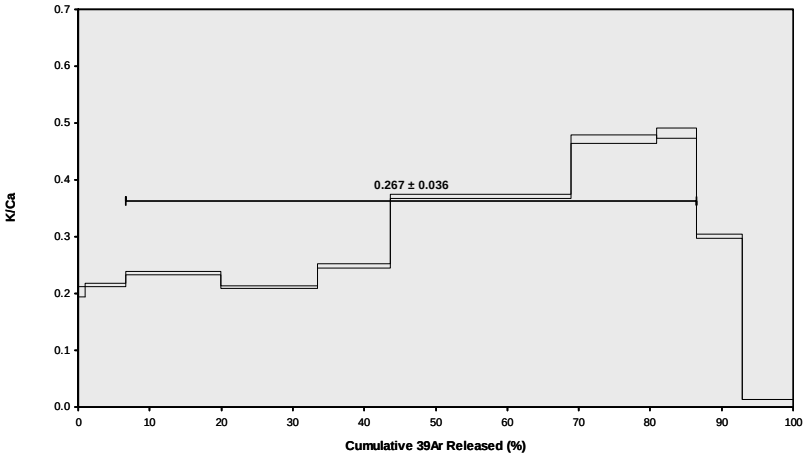

Ar-Ages in Ka

WEIGHTED PLATEAU
231.3 ± 10.9
TOTAL FUSION
250.1 ± 15.1
NORMAL ISOCHRON
239.9 ± 26.1
INVERSE ISOCHRON
240.4 ± 25.9

Sample Info

groundmass
furnace
BSHS

IRR = VU61
J = 0.0002889 ± 0.0000018

APPENDIX F

Cosmogenic ^{3}He data

Sample	elevation [m]	Mineral	analytical cosmogenic ^{3}He concentration [atoms/g] and uncertainty, no scaling applied		density [g/cm2]	error	sample thickness [cm]	error	^{40}Ar/^{39}Ar age [ka] and uncertainty (based on Lee et al.(2006))		exposure age [ka] and uncertainty (Dunai, 2001)	
CA05/01			3.56E+06	2.94E+05	2.27	0.05	14	1	148.0	7.8	53.9	7.5
CA05/01 40%			3.79E+06	5.12E+05	2.27	0.05	14	1	148.0	7.8	57.3	10.9
CA05/02			4.48E+06	2.91E+05	2.33	0.05	15	1	148.0	7.8	68.5	8.3
CA05/03 part B	127	cpx	4.81E+06	2.41E+05	2.31	0.05	15	0.6	148.0	7.8	73.4	7.6
CA05/04			5.76E+06	4.17E+05	2.51	0.05	17	0.5	148.0	7.8	90.0	11.5
CA05/05			4.78E+06	2.71E+05	2.78	0.05	14	1	148.0	7.8	73.8	8.5
CA05/06			4.49E+06	3.28E+05	2.25	0.05	13	0.5	148.0	7.8	67.3	8.4
CA05/07			5.81E+06	4.77E+05	2.48	0.05	14	0.6	148.0	7.8	88.7	12.1
CA05/01			2.79E+06	3.88E+05	2.27	0.05	14	1	148.0	7.8	40.1	7.7
CA05/03B	127	olv	2.74E+06	2.91E+05	2.31	0.05	15	0.6	148.0	7.8	39.8	6.3
CA05/05			3.68E+06	2.50E+05	2.77	0.05	14	1	148.0	7.8	54.2	6.7
CA05/06			2.54E+06	2.12E+05	2.25	0.05	13	0.5	148.0	7.8	36.3	4.8
CG05/01			6.09E+06	2.40E+05	2.33	0.05	6.5	1	52.7	21.6	78.9	7.0
CG 05/02	213	olv	*-8.95E+05*	*-1.01E+04*					0.0	0.0	0.0	0.0
CG05/04			3.47E+06	8.91E+04	2.55	0.05	18	1	52.7	21.6	49.3	4.1
CG05/07			5.11E+06	1.18E+05	2.46	0.05	8	0.5	52.7	21.6	67.2	4.8
MA05/03			1.86E+06	2.52E+04	2.35	0.05	13	1	285.2	23.8	22.0	1.6
MA05/05	185	olv	8.80E+05	1.19E+04	2.46	0.05	14	0.5	285.2	23.8	10.6	0.7
MA05/06			1.64E+06	2.39E+04	2.1	0.05	11	0.5	285.2	23.8	19.0	1.3
MA05/08			2.34E+06	2.01E+04	1.61	0.05	12	0.5	285.2	23.8	26.9	1.5
MC05/07surf	199	olv	3.75E+06	1.33E+05	2.5	0.05	5	0.3	138.8	13.4	47.6	3.8
MM05/02			9.21E+06	1.25E+05	2.43	0.05	14	1	398.6	27.6	116.3	7.9
MM05/03			1.06E+07	1.95E+05	2.43	0.05	11.5	0.5	398.6	27.6	132.1	9.0
MM05/04			1.02E+07	8.70E+04	2.58	0.05	16	0.5	398.6	27.6	131.2	8.0
MM05/04 surf	24	olv	8.78E+06	3.30E+05	2.58	0.05	5	0.3	398.6	27.6	104.0	8.5
MM05/05			9.94E+06	1.35E+05	2.68	0.05	12	0.5	398.6	27.6	124.9	8.0
MM05/05 surf			8.12E+06	3.35E+05	2.68	0.05	5	0.3	398.6	27.6	96.4	8.3
MM05/06			9.56E+06	4.70E+05	2.24	0.05	11	0.5	398.6	27.6	117.4	11.5
MM05/06surf			8.36E+06	2.88E+05	2.24	0.05	5	0.3	398.6	27.6	98.5	7.7
MQ05/01surf	167	olv	1.29E+07	4.54E+05	2.63	0.05	5	0.3	179.8	29.4	157.0	12.5
MR05/01			1.50E+07	6.72E+05	2.65	0.05	6	0.5	195.0	16.7	169.9	15.6
MR05/01 A			1.70E+07	7.53E+05	2.65	0.05	6	0.5	195.0	16.7	193.3	17.6
MR05/01 B			1.76E+07	4.90E+05	2.65	0.05	6	0.5	195.0	16.7	200.0	14.9
MR05/01 C	185	olv	1.71E+07	8.59E+05	2.65	0.05	6	0.5	195.0	16.7	194.1	18.8
MR05/01 D			1.29E+07	5.67E+05	2.65	0.05	6	0.5	195.0	16.7	146.6	13.3
MR05/05 A			1.08E+07	8.02E+05	2.18	0.05	5	0.3	195.0	16.7	120.5	14.2
MR05/05 B			1.34E+07	6.95E+05	2.18	0.05	5	0.3	195.0	16.7	149.6	14.3
MR05/05 C			8.12E+06	3.58E+05	2.18	0.05	5	0.3	195.0	16.7	90.7	8.0
VF05/01			1.46E+07	1.72E+05	2.4	0.05	16	1.5	229.0	11.5	203.8	14.5
VF05/02			9.62E+06	1.36E+05	2.38	0.05	13	2	229.0	11.5	131.6	9.9
VF05/03	56	olv	1.39E+07	1.96E+05	2.29	0.05	16	1	229.0	11.5	193.1	13.4
VF05/05			1.39E+07	1.19E+05	2.48	0.05	10	1	229.0	11.5	186.0	11.4
VF05/07			1.01E+07	1.19E+05	2.64	0.05	10	1	229.0	11.5	136.6	8.9